Biological Research Centre, Szeged

Institute of Plant Biology

Petar H. Lambrev

On the role of light-harvesting complex II in regulating the excitation energy flow

Dissertation

Szeged, 2022

dc_1987_22

TABLE OF CONTENTS

Abbreviations

2DES	two-dimensional electronic spectroscopy
ACD	anisotropic CD
BBO	beta barium borate (β-BaB_2O_4)
BBY	photosystem II-enriched grana fragments
Car	carotenoid
CD	circular dichroism
Chl	chlorophyll
CT	charge transfer
(α/β)-DDM	n-dodecyl-(α/β)-D-maltoside
DAS (DAES)	decay-associated (emission) spectrum
DGDG	digalactosyldiacylglycerol
DiI	1,1′-dioctadecyl-3,3,3′,3′-tetramethylindocarbocyanine-5,5′-perchlorate
DMPC	dimyristoylphosphatidylcholine
EDTA	2,2′,2″,2‴-(ethane-1,2-diyldinitrilo)tetraacetic acid
EET	excitation energy transfer
ESA	excited-state absorption
GSB	ground-state bleaching
HEPES	2-[4-(2-hydroxyethyl)piperazin-1-yl]ethanesulfonic acid
IRF	instrument response function
LD	linear dichroism
LHC(I/II)	light-harvesting complex (I/II)
L/P	lipid/protein
MGDG	monogalactosyldiacylglycerol
NPQ	non-photochemical quenching
OPA	optical parametric amplifier
PAA	polyacrylamide
PC	phosphatidylcholine
PG	phosphatidylglycerol
PQ	plastoquinone
PS(I/II)	photosystem (I/II)
RC	reaction centre
RT	room temperature
SAS (SAES)	species-associated (emission) spectrum
SE	stimulated emission
SQDG	sulfoquinovosyldiacylglycerol
SR	synchrotron radiation
TA	transient absorption
TM	thylakoid membrane
TCSPC	time-correlated single-photon counting
TRF	time-resolved fluorescence

1. INTRODUCTION

Nearly all life on Earth is fundamentally sustained by energy from the Sun stored in the process of photosynthesis. Intensifying research in photosynthesis is a logical and necessary step to overcome serious challenges that humankind is facing today – satisfying the increasing demands for food and energy, while simultaneously reducing carbon and other greenhouse gas emissions. On one hand, further significant improvements of crop productivity are only possible through enhanced photosynthetic efficiency (Long et al., 2006; Kromdijk et al., 2016). On the other hand, there is a vast potential for developing biotechnological and artificial solutions for solar energy conversion that exceed the solar-to-mass efficiency of natural photosynthesis (Tachibana et al., 2012; Dogutan and Nocera, 2019). Detailed, molecular-level understanding of the photophysical and photochemical mechanisms of photosynthesis that identifies the various bottlenecks and limitations existing in natural photosynthetic systems is a prerequisite to achieve either of these goals.

Photosynthesis begins with the absorption of light by pigments in the photosynthetic light-harvesting antenna complexes and the creation of electronic excited states. The successful conversion of the absorbed energy into chemical form relies on the ability of the antenna system to transfer the excitations over many molecules to the photochemical reaction centres – of PSI and PSII in plants and algae. Achieving high quantum efficiency of photochemistry is only possible if together excitation energy transfer and the photochemical reaction are much faster than radiative or nonradiative excitation losses (Blankenship, 2014). The biological structures supporting these processes are honed and over more than 2 billion years of evolution (Nelson, 2011). In the past several years, advances in structural biology have greatly enriched our knowledge on the structure of the photosynthetic machinery, including atomic or near-atomic resolution structures of most important photosynthetic pigment–protein complexes (Lambrev and Akhtar, 2019). However, direct prediction of photophysical functions in terms of quantum chemistry and quantum electrodynamic theory is not possible for these systems consisting of millions of atoms. Despite decades of intense research, gaps of our understanding and controversial views still exist about the mechanisms and dynamics of the primary photosynthetic reactions. Fortunately, the arsenal of available spectroscopic tools to probe

the molecular responses to light and the theoretical framework to understand them and their structural basis have been steadily improving (Croce and van Amerongen, 2020).

Light-harvesting complex II (LHCII) is the main photosynthetic antenna complex of plants and green algae that binds about half of all chlorophylls (Chls) in the TM (van Amerongen and Croce, 2013). The transfer of excitation energy in and between LHCII complexes determines the efficiency of PSII. LHCII also plays important roles in maintaining the macroorganization of the TM and regulating the photosynthetic process in response to the physiological conditions. Under excess light conditions LHCII can switch from its light-harvesting function to a light-dissipation function (non-photochemical quenching) and it can balance the excitation of the two photosystems in the process of state transitions. These functions are based on and controlled by the inherent structural flexibility of the complex and on intermolecular interactions in the TM. The goal of the present work was to elucidate structure-function relationships in LHCII, especially regarding excited-state dynamics and its dependence on interactions between the complex and its molecular surroundings. To this end, we performed investigations on isolated LHCII complexes in solution and in the form of aggregates, as well as in native and artificial (model) lipid membranes, employing steady-state and ultrafast time-resolved optical spectroscopy to probe changes in the pigment excited states and excitation dynamics.

The results of this work revealed a remarkable sensitivity of the photophysical function of LHCII to the environment – circular dichroism (CD) spectroscopy identified excited states sensitive to aggregation or lipid and detergent interactions, activation of strong non-photochemical quenching was demonstrated not only in LHCII aggregates but also in lipid membranes and a common physical mechanism was proposed based on its fluorescence signature, the ultrafast energy transfer, measured with great detail by two-dimensional electronic spectroscopy (2DES), was shown to markedly depend on temperature, aggregation and the substitution of specific pigments. Finally, the ability and the limits of long-range energy transfer between multiple LHCII and between LHCII and PSI were determined quantitatively. Thanks to these studies we have a more detailed knowledge of the dynamics of energy transfer in the natural photosynthetic membranes, the mechanisms of photoprotective non-photochemical quenching, and fundamental principles and limits of the design of photosynthetic light harvesting. Technological advances made in the course of this work, for example regarding the techniques of

anisotropic CD and synchrotron-radiation CD spectroscopy and purely absorptive 2DES, will find applications on other systems and help solve further problems in photosynthesis research in the future.

This dissertation is organized as the following. Chapter 2 outlines the scientific background and current problems regarding photosynthetic light harvesting, briefly describes the structure and functions of LHCII, PSI and PSII, the general organization of the TM and fundamentals of CD spectroscopy and 2DES. Chapters 3 and 4 summarize the aims and experimental methodology. Chapter 5 presents the results on structural and functional plasticity of LHCII – changes in the excited states in different molecular environments and mechanisms of non-photochemical quenching. Chapter 6 is devoted to the ultrafast dynamics of energy transfer in LHCII and its dependence on the environment. This is followed by a short summary (thesis points), acknowledgements and a list of literature sources.

2. BACKGROUND

2.1. Fundamentals of light harvesting

2.1.1. Photosynthetic pigments

All oxygenic photosynthetic organisms employ Chls as the primary photosynthetic pigments. Anoxygenic phototrophic bacteria use closely related molecules, bacteriochlorophylls. Most Chls contain a chlorin ring (Figure 2.1) – a heterocyclic macrocycle, similar to the tetrapyrrole ring of porphyrins, which coordinates a central Mg atom (Grimm et al., 2007). Pheophytin *a*, the metal-free form of Chl *a*, is essential part of the electron-transport chain in PSII. Functional Chls are always bound to proteins, where the Mg atom is usually coordinated by an amino acid.

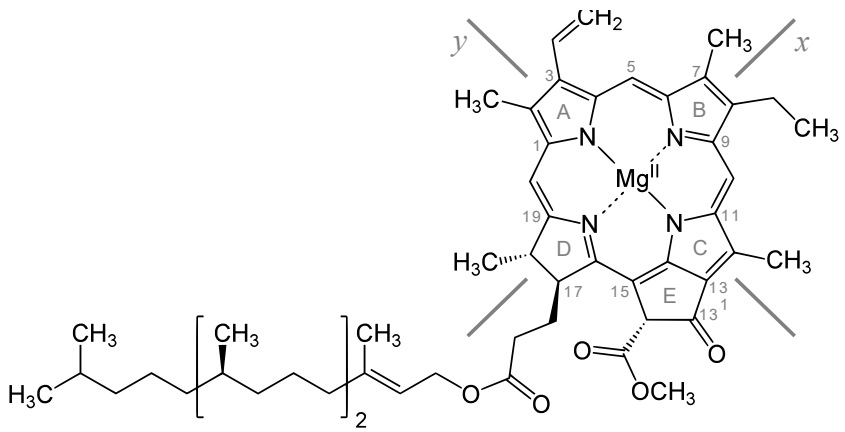

Figure 2.1. Chemical structure of Chl *a* with ring and atom numbering according to IUPAC. In Chl *b*, the methyl group (–CHO) at position C7 is replaced by a formyl group (–CHO). Chls *a* and *b* are the only Chl types found in plants and green algae. Other algae may contain Chl *c*, *d*, *f*.

Chls are remarkably versatile molecules, able to perform virtually all kinds of photochemical reactions, in part thanks to their strong absorption, long excitation lifetime and redox reactivity. The basic optical properties (electronic absorption spectra) of Chls are understood in terms of Gouterman's four-orbital model (Gouterman et al., 1963). According to it, electron transitions from one of the two highest occupied π orbitals of the macrocycle (HOMO–1 and HOMO, a_{1u} and a_{2u}) to the lowest unoccupied π* orbitals (LUMO, e_g) give rise to two optical bands in the visible region, Q and B (Soret). They correspond to the $Q_{(x,y)}$ and $B_{(x,y)}$ transitions with electronic transition dipole moments within the macrocycle plane. For Chl *a* dissolved in acetone, the main Q and B absorption maxima are at 663 and 436 nm, respectively. More complete quantum chemical

calculations, usually employing time-dependent density functional theory, predict a variety of electronic and vibronic transitions making up for complex optical spectra (König and Neugebauer, 2012; Curutchet and Mennucci, 2017). In addition, the excited-state (quantum eigenstate) energies are strongly influenced by ring deformations, interactions with the solvent and especially with the protein environment (Curutchet and Mennucci, 2018). The microenvironment also largely determines the redox properties of the Chls, potentially stabilizing their anions or cations as well as mixed states with excited and charge-transfer (CT) character (Frese et al., 2002; Wahadoszamen et al., 2014; Novoderezhkin et al., 2016). The primary photochemical reactions in PSI and PSII are in fact oxidation-reduction reactions where both the electron donor and acceptors are Chl *a* molecules, resulting in a primary radical ion pair $Chl_D^{\bullet+}$ $Chl_A^{\bullet-}$.

Singlet excited Chls can undergo intersystem crossing and relax to a metastable low-energy triplet state, $^3Chl^*$ (Figure 2.2). The triplet excited Chls are potent sensitizers of singlet oxygen; this reaction is the major cause of photodamage under excess light conditions (Triantaphylides et al., 2008; Vass, 2011; Pospíšil, 2012; Fischer et al., 2013). Formation of radical pairs, CT and triplet states, interaction with oxygen and any other non-radiative excited-state decay pathways all shorten the excited-state lifetime of Chl and respectively reduce the fluorescence yield and lifetime and can be generally referred to as fluorescence quenching mechanisms.

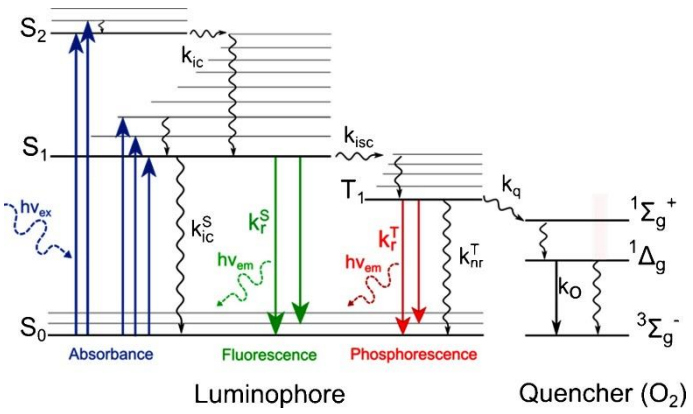

Figure 2.2. Perrin-Jablonski diagram summarizing the principal electronic and vibrational energy eigenstates and electronic transitions in pigments (luminophores) such as Chls and their interaction with molecular oxygen to form singlet oxygen. The arrows and symbols indicate internal conversion (with rate constant k_{ic}), fluorescence emission (k_r), intersystem crossing (k_{ics}), and oxygen quenching (k_q). Reproduced from Quaranta et al. (2012).

Carotenoids (Cars) are another class of pigments ubiquitous in photosynthetic organisms. They strongly absorb visible light in the blue-green to orange region of the spectrum and are thus well suited as accessory pigments filling the gap between the Q- and B-band absorption of Chls. Apart from that, the highly hydrophobic Car molecules have structure-stabilizing role in the pigment–protein complexes and their peculiar photophysical properties make them key photoprotective agents. Other pigments that play role in certain taxonomic groups of photosynthetic microorganisms, such as bilins in red algae and cyanobacteria, will not be discussed here.

2.1.2. Excitonic interactions

In photosynthetic complexes, pigment molecules are located at close distances, often less than 10 Å, and interact with each other via electrostatic (Coulomb) interactions. Such ensembles of interacting chromophores are not mere sums of individual chromophores but their properties are modified by interaction forces. The photophysical and spectroscopic properties can be described by the theory of molecular excitons (Cantor and Schimmel, 1980; van Amerongen et al., 2000). The basics of the theory are given for a dimer of identical two-level (ground and excited state) systems. The total wave function can be described as a product of the wave functions of the monomers. There are two single-excitation wave functions, with excitations residing on each of the monomers:

$$\begin{aligned} \Psi_1 &= \phi_1' \phi_2 \\ \Psi_2 &= \phi_1 \phi_2' \end{aligned} \tag{2.1.1}$$

where ϕ and ϕ' represent ground- and excited-state monomer wave functions. The Hamiltonian of the system is:

$$H = H_1 + H_2 + V \tag{2.1.2}$$

where V is the interaction energy arising from Coulombic coupling of the electric transition dipoles $\boldsymbol{\mu_1}$ and $\boldsymbol{\mu_2}$ connected by the space vector $\boldsymbol{r}$:

$$V = -\frac{1}{4\pi\varepsilon_0 r^3}\left[\boldsymbol{\mu_1} \cdot \boldsymbol{\mu_2} - \frac{3(\boldsymbol{\mu_1} \cdot \boldsymbol{r})(\boldsymbol{\mu_2} \cdot \boldsymbol{r})}{r^2}\right], \tag{2.1.3}$$

The excited wave functions and energies can be found by diagonalizing the Hamiltonian. The energy eigenvalues are

$$E^{\alpha} = E \pm V \tag{2.1.4}$$

and the eigenfunctions are

$$\Psi^{\alpha} = \frac{1}{\sqrt{2}}(\Psi_1 \pm \Psi_2). \tag{2.1.5}$$

Thus, the excited states of the dimer, called exciton states, are linear superpositions of the monomer excited states. For both exciton states, the excitation is *delocalized* between the two monomers. The energies of the exciton states are split by a magnitude of 2V.

The transition dipole moments of the exciton states are also linear combinations of the monomer transition dipole moments:

$$\boldsymbol{\mu}^{\alpha} = \frac{1}{\sqrt{2}}(\boldsymbol{\mu}_1 \pm \boldsymbol{\mu}_2). \tag{2.1.6}$$

Thus, the transition dipole moment magnitudes, or the dipole strengths of the two transitions will depend on the geometry of the dimer.

For an aggregate of N chromophores, there are N exciton states Ψ^{α}, which are linear superpositions of monomeric states:

$$\Psi_m^{\alpha} = \sum_{n=1}^{N} c_{mn}\Psi_n \tag{2.1.7}$$

where Ψ_n is a state where the nth chromophore is excited and all other are in their ground state. The coefficients c_{mn} of each product component of the summation represent the contribution of each component to the exciton's structure. For a system of identical monomers, c_{mn} are also identical, which means that exciton states are fully delocalized — equally distributed among all chromophores. However, if the monomer energy levels, called *site energies*, are not degenerate, the coefficients c_{mn} are not equal and the excitations are localized or partly delocalized. Excited states can be expressed both in terms of monomer basis states Ψ_n and in exciton basis states Ψ_m^{α} — called site representation and exciton representation, respectively.

The theory summarized above considers only electronic degrees of freedom. For any dynamic description of excited-state processes, the interaction of the electron system with the nuclear environment must also be included. In general, the coupling of the electronic excited states with nuclear motions (system–bath coupling or electron–phonon coupling) tends to localize the excitations on monomeric chromophores.

2.1.3. Excitation energy transfer

The principal role of light-harvesting antenna pigments in photosynthesis is to deliver the absorbed energy to the RC via excitation energy transfer (EET), wherein the excited donor molecule interacting with an acceptor molecule returns to the ground state and the acceptor is excited instead:

$$D^* + A \rightarrow D + A^* \tag{2.1.8}$$

If there is molecular orbital overlap between D and A, EET can occur via electron exchange mechanism (Dexter, 1953). At longer distances EET is driven by Coulombic interactions. Based on the strength of coupling, three scenarios can be distinguished, as proposed by T. Förster (1965). In the ***weak electronic coupling limit***, i.e. the intermolecular coupling term is weaker compared to the interaction between the electronic and nuclear motions within the molecule, EET is described with Förster's theory of resonance energy transfer (FRET). Conversely, in the ***strong coupling limit***, the delocalized excited states are best treated in exciton basis as described in the previous section and EET dynamics is quantitated by Redfield theory.

Förster theory

Förster theory (Förster, 1965) describes the hopping of excitation energy between localized and thermally equilibrated excited states. The efficiency of transfer W is given by:

$$W = \frac{R_0^6}{R_0^6 + r^6}, \tag{2.1.9}$$

where R_0 is the Förster radius — the distance at which half of the excitation energy of the donor D is transferred to the acceptor A. The Förster radius depends on the fluorescence quantum yield of the donor in the absence of acceptor $f_D(v)$, the refractive index of the solution n, the dipole angular orientation factor κ^2, and the spectral overlap integral, in frequency space, v, of the fluorescence $f_D(v)$ of D and the $\varepsilon_A(v)$ of the A as given by the following equation:

$$R_0^6 = C\kappa^2 n^{-4} \int f_D(v)\varepsilon_A(v)v^{-4}dv \tag{2.1.10}$$

Förster's equation is accurate in many experimental systems and conditions, but its validity is limited by a number of assumptions:

- The interaction is between two molecules only, isolated from the environment.
- The molecules are sufficiently separated so that there is no overlap between their electronic wave functions.
- The wavelength corresponding to the electronic transitions is significantly longer than the distance of FRET (near field).

The Förster equation is not sufficient to describe EET in photosynthetic systems, where due to the very close distances between the pigment molecules, the point-dipole approximation is inaccurate and, more importantly, strong electronic couplings (excitonic interactions) violate the weak-coupling condition holding that EET occurs from thermally equilibrated states.

Excitonic energy transfer

Redfield theory (Redfield, 1957) is used for the case of strong excitonic coupling and weak exciton-vibrational coupling. The system is described in exciton state basis (excitations are delocalized among all pigments). The weak exciton-vibrational interactions are described by perturbation theory. Coupling of the individual transitions with uncorrelated vibrational motions leads to uncorrelated fluctuations in the individual site energies. These site energy fluctuations interact with different exciton levels and allow transitions between them. If the site energies are identical, the excitations are delocalized over all chromophores, but if the site energies are not identical the delocalization is only partial and transitions between exciton energy levels are equivalent to transfer of energy in space. Redfield theory helps to describe the efficiency of energy exchange between proteins and pigments in photosynthetic pigment–protein complexes. The protein can either accept energy, in the case of downhill exciton relaxation (dissipation of excess energy) or provide energy, for uphill exciton relaxation (thermal activation).

Modified Redfield theory (Zhang et al., 1998; Yang and Fleming, 2002; Renger and Marcus, 2003) describe the dynamics of EET in systems of strong excitonic and strong excitonic-vibrational coupling. For such system, it is necessary to include both types of couplings into theory non-perturbatively. Modified Redfield theory describes the transitions between delocalized excited states, while including nuclear reorganization effects without invoking perturbation. Because the electronic charge density is different for the different excitonic states, the nuclei, which are not in equilibrium with the electrons in the final exciton state, relax toward new equilibrium positions. The diagonal elements of

the exciton-vibrational coupling are used to introduce potential energy surfaces of exciton states (Renger and Marcus, 2002). Then the excitonic potential energy surfaces are mutually shifted along the vibrational coordinates to describe the nuclear reorganization effect. The standard Redfield theory neglects these nuclear reorganization effects.

Modified Redfield theory has been successfully applied to model the EET in a number of pigment–protein complexes – bacterial light-harvesting antenna LH2 (Novoderezhkin et al., 2006), LHCII (Novoderezhkin et al., 2004) and the water-soluble Chl binding protein (Renger et al., 2007). The authors concluded that if the energy gap between the exciton states is larger than approximately 200 cm^{-1}, the modified Redfield theory should be used. However, this theory does not describe coherence dynamics, unlike the full Redfield approach, as it is based on a diagonal projection operator approach. This limits its applications to population dynamics in the exciton basis.

Generalized Förster theory (Sumi, 1999; Scholes and Fleming, 2000) can be applied for large photosynthetic pigment–protein complexes, in which not all pigments are coupled strongly. Such system can be described by formation of delocalized states in certain domains of strongly coupled pigments. The exciton relaxation within the domains of excitonically coupled molecules can be described by Redfield or modified Redfield theory, and the EET between the exciton states in different domains is described as incoherent hopping (Förster regime).

2.2. Spectroscopy techniques to probe exciton states and dynamics

2.2.1. Circular dichroism spectroscopy

Excitonic CD basics

CD spectroscopy is an extension of absorption spectroscopy. Absorption of light causes an electronic transition in the optical material to an excited state of higher energy corresponding to the photon energy. The probability of the transition, W_{ge}, is proportional to the squared scalar product of the electric field vector of the light and the electric transition dipole moment

$$W_{ge} \propto |\boldsymbol{E} \cdot \boldsymbol{\mu}|^2 \propto |\boldsymbol{E}|^2 \cdot |\boldsymbol{\mu}|^2 \cdot \cos^2 \theta \tag{2.2.1}$$

Hence, absorption is maximal if the light polarization is parallel to the transition dipole moment. The squared transition dipole moment, called dipole strength, is proportional to the spectrally integrated absorption coefficient:

$$D_{ge} = \langle \Psi_g | \hat{\boldsymbol{\mu}} | \Psi_e \rangle \cdot \langle \Psi_e | \hat{\boldsymbol{\mu}} | \Psi_g \rangle = |\boldsymbol{\mu}|^2 = 9.18 \cdot 10^{-3} \cdot \int \frac{\varepsilon(\omega)}{\omega} d\omega \tag{2.2.2}$$

This relates to the famous Beer-Lambert law

$$A = \varepsilon c l \tag{2.2.3}$$

where c and l are the chromophore concentration and the pathlength, respectively.

CD is the difference in absorption of left and right circularly polarized light

$$\mathrm{CD} = A_{\mathrm{L}} - A_{\mathrm{R}} = \Delta A \tag{2.2.4}$$

Defined as such, CD is a unitless quantity but can also be expressed in terms of molar absorption coefficients

$$\Delta\varepsilon = \varepsilon_L - \varepsilon_R = \frac{\Delta A}{cl} \; [\mathrm{M}^{-1}\mathrm{cm}^{-1}] \tag{2.2.5}$$

In analogy to the dipole strength, the CD can be expressed via the rotational strength, which is proportional to the spectrally integrated differential extinction coefficient

$$R \propto \int \frac{\Delta\varepsilon(\omega)}{\omega} d\omega \tag{2.2.6}$$

As CD is essentially absorption, the same rules and conditions governing absorption apply to CD as well. In addition, CD requires that the transition is associated with circular movement of electrons, i.e. the orbital angular momentum, which enters the rotational strength via the magnetic dipole operator $\hat{\boldsymbol{m}} = (e/2mc)(\hat{\boldsymbol{r}} \times \hat{\boldsymbol{p}})$:

$$R_{ge} \propto -\mathrm{Im}\left(\langle \Psi_{\mathrm{g}} | \hat{\boldsymbol{\mu}} | \Psi_e \rangle \cdot \langle \Psi_e | \hat{\boldsymbol{m}} | \Psi_g \rangle\right) \propto -\mathrm{Im}(\boldsymbol{m} \cdot \boldsymbol{\mu}) \tag{2.2.7}$$

The scalar product means that the circularly polarized electromagnetic field induces a helical oscillation of charges, which is only possible if the optical material is asymmetric, or chiral, and explains why helical biological macromolecules and assemblies typically have intense CD. We refer to the CD of individual chiral molecules as *intrinsic* CD.

Molecular aggregates can exhibit CD even if they are composed of molecules that are not themselves chiral, as long as there is *excitonic* coupling between their transition dipole

moments (Tinoco Jr, 1963). The excitonically coupled transitions of the amide backbone of polypeptides have made CD spectroscopy an indispensable tool in the analysis of protein folding and secondary structure (Woody, 2005; Siligardi and Hussain, 2015). In the simplest case, the rotational strength of an excitonically coupled dimer of chromophores (Figure 2.3) contains a term dependent only on the distance vector connecting the two, $\boldsymbol{r}_{12}$, and the respective electric transition dipole moments:

$$\mathrm{CD} \propto \pm \boldsymbol{r}_{12} \cdot \boldsymbol{\mu}_1 \times \boldsymbol{\mu}_2 \tag{2.2.8}$$

This scalar triple product is often the dominant term for excitonically coupled molecules. The $\pm$ sign denotes that the dimer has two CD bands of opposite sign but equal rotational strength (spectrally integrated intensity), i.e. a conservative spectrum. Because the excitonic transition energies are split apart by a gap equal to twice the interaction energy, the oppositely signed CD bands do not (completely) cancel each other and the excitonic CD spectrum of many photosynthetic antenna complexes is at least an order of magnitude stronger than the CD arising from the chirality of the photosynthetic pigments (termed intrinsic CD). In section 5.1 the excitonic CD of light-harvesting complexes in different molecular environments will be examined.

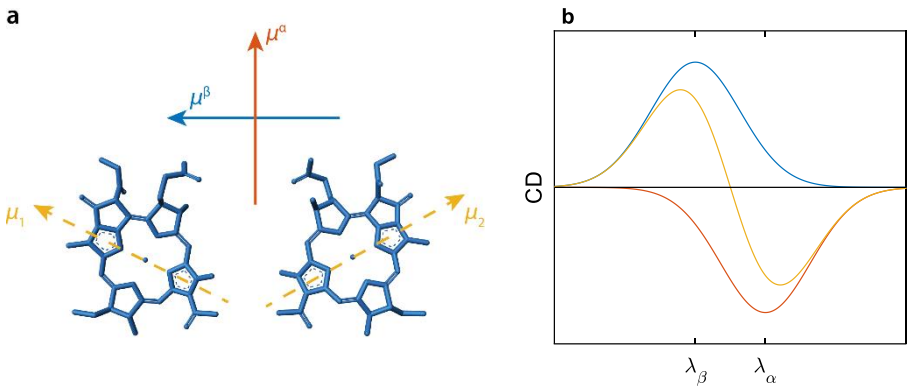

Figure 2.3. Excitonic CD. a: geometry of a dimer of two identical bacteriochlorophyll molecules with the monomeric transition dipole moments represented by dashed yellow arrows and the excitonic transition dipole moments with red/blue arrows; b: CD of the exciton dimer: the two exciton transitions have CD of equal magnitude but opposite sign (blue and red), which combined produce the isotropic CD spectrum of the dimer (yellow); measurements on aligned molecules can, in principle, probe the two transitions separately. Adapted from ref. (Lindorfer and Renger, 2018).

Psi-type CD

The excitonic CD is extremely sensitive to the interaction energy and to the mutual geometry of the coupled chromophores and a useful structural probe for multi-chromophore aggregates. It is the dominant contribution to the visible-range CD of isolated photosynthetic pigment–protein complexes. However, in large three-dimensional assemblies of densely packed and structurally ordered chromophores, such as DNA condensates, viruses, and especially TM, intense CD can be generated, exceeding in magnitude both the intrinsic CD of the chromophores and the short-range excitonic CD of the pigment–protein complexes (Keller and Bustamante, 1986; Garab, 1992). This type of induced CD, termed "giant" or "*psi-type*" (polymer- or salt-induced), is an emergent property of the supramolecular organization of the assembly and cannot be represented by merely the sum CD of its constituent parts. Intact leaves, chloroplasts and isolated stacked TM contain all three types of CD (intrinsic, excitonic and psi-type) superimposed on each other, with characteristic psi-type CD bands in the Chl Q_y and in the blue-green wavelength region (Garab and van Amerongen, 2009; Lambrev and Akhtar, 2019). Although the psi-type CD contains some contribution from circular intensity differential scattering, especially giving rise to characteristic long tails flanking the absorption bands (Garab et al., 1988; Garab et al., 1988), it is not merely an optical artefact but an intrinsic spectroscopic signature uniquely depending on the three-dimensional macroorganization and therefore carries meaningful physical information (Garab and van Amerongen, 2009). The psi-type CD, as a sensitive and accessible probe for the macroorganization and flexibility of the TM, has been used to assess the response to physiological conditions and abiotic stress (Garab, 2016; Lambrev and Akhtar, 2019).

Anisotropic CD

The CD signal of excitonic systems depends simultaneously on the geometry, the transition energies of the uncoupled chromophores and the strength of coupling (the interaction energy). Different combinations between these parameters can result in nearly indistinguishable CD spectra, making it difficult to derive the structure from the spectra. Even if the basic structure is known, as is the case for the major plant photosynthetic complexes, because of the delocalised nature of the excitonic states, the spectral bands have contributions from multiple coupled chromophores (Georgakopoulou et al., 2007). Finally, each chromophore contributes with multiple excited states with mixed electronic

and vibrational nature – some of which may lie outside the measured wavelength region, tremendously complicating the energy landscape (Dinh and Renger, 2015).

An extension of CD spectroscopy, the anisotropic CD (ACD) of oriented samples, also termed oriented CD (OCD), can potentially help with these problems. ACD has been elaborated for large molecules and liquid crystals (Kuball and Höfer, 2000; Kuball, 2002; Kuball et al., 2005) but not frequently used for photosynthetic systems. Conceptually ACD is simple – if the molecules of interest can be macroscopically aligned or oriented, the measured ACD can give additional information about the spatial orientation of the transitions giving rise to the CD signal, hence about the molecular configuration. In the simplest terms, we can interpret the ACD of the excitonic dimer illustrated in Figure 2.3, by only considering the electric transition dipole coupling, which gives rise to two excitonic states with transition dipole moments $\boldsymbol{\mu}_{\alpha,\beta} = \boldsymbol{\mu}_1 \pm \boldsymbol{\mu}_2$, i.e. perpendicular to each other. From Eq. 2.2.1 it follows that absorption is zero if the light polarization and the transition dipole moment are orthogonal, which will be the case for light propagating parallel to the transition dipole moment. Therefore, if the molecules have fixed orientation in the laboratory frame of reference, we can find such measurement beam angles where one or the other excitonic transition is selectively suppressed. For example, with light propagating parallel to the μ_α direction (Figure 2.3a), only the β exciton transition is probed. Generally, if the measuring light is parallel to vector $\boldsymbol{n}$, the ACD of the dimer is (Hansen, 2005; Lindorfer and Renger, 2018)

$$\mathrm{CD}_n \propto (\boldsymbol{r_{12}} \cdot \boldsymbol{n})(\boldsymbol{\mu}_1 \times \boldsymbol{\mu}_2) \cdot \boldsymbol{n} + \left((Q_1' \cdot \boldsymbol{n}) \times \boldsymbol{\mu}_2\right) \cdot \boldsymbol{n} \tag{2.2.9}$$

where Q_1' is the electric quadrupole moment calculated from the three-dimensional transition density of the pigment. For isotropic, or random solutions, the quadrupole terms cancel out and Eq. 2.2.9 reduces to the Rosenfeld equation (2.2.8). In practice, the measurement of ACD can be problematic because of distortions from linear dichroism and birefringence, which can be much more intense than the CD signal. However, this is not an issue of ACD if the sample has rotational symmetry along the measurement axis (so linear dichroism is zero).

ACD allows for independent measurement of the excitonic CD bands (Figure 2.3b), which brings valuable information, otherwise lost by rotational averaging, such as the exact peak positions and hence the excitonic split. More importantly, ACD "labels" the

excitonic CD bands with orientations of the underlying transitions, which dramatically reduces the possible geometries that can fit the spectra and the degrees of freedom in model fitting. A simple and clear example of using ACD to separately probe exciton transitions is the CsmA baseplate protein found in the chlorosome antenna of green-sulfur photosynthetic bacteria, where bacteriochlorophyll *a* effectively forms exciton dimers (Nielsen et al., 2016). The ACD spectra of the CsmA protein were theoretically calculated following the molecular exciton approach (Hansen, 2005). Based on these data the NMR structure of the protein could be validated (Nielsen et al., 2016). In the ACD calculations, an earlier theory by Hansen (2005) was used that includes the full spatial variation of the electromagnetic field and is referred to as fully retarded description. Recently, Lindorfer and Renger (2018) presented simplified formalism to calculate the ACD spectra of chlorosome baseplate that can be applied to describe the ACD of molecular aggregates.

Membrane and lamellar structures are naturally amenable to ACD spectroscopy because of their planar geometry. ACD of membranes and membrane-embedded complexes can be easily measured with light perpendicular to the membrane plane, which is termed face-aligned position (Garab, 1996; Garab and van Amerongen, 2009). In the edge-aligned position, with light parallel to the membrane plane, the measurement of ACD is more difficult because of crosstalk with linear dichroism (Kuball et al., 2005). The isotropic CD is a linear combination of the face- and edge-aligned contributions (Kuball et al., 2005; Miloslavina et al., 2012):

$$\mathrm{CD} = \frac{1}{3}\left(\mathrm{ACD}_{\mathrm{face}} + 2\mathrm{ACD}_{\mathrm{edge}}\right) \tag{2.2.10}$$

The two right-hand side terms are a basis set that fully determines the ACD of uniaxial samples (Kuball et al., 2005). Alignment of membranes in the laboratory frame of reference can be achieved by a variety of methods – by orienting in magnetic field (if they have sufficient diamagnetic anisotropy), Langmuir-Blodget films, surface-supported bilayers, or in compressed gels (Garab and van Amerongen, 2009). Section 5.3 deals with the ACD of plant TM and light-harvesting complexes.

UV-ACD

The UV CD of peptides and proteins is widely used to study their structure, folding, and conformational dynamics; membrane insertion; and effects of ligand binding (Towell

and Manning, 1994; Woody, 2005; Siligardi and Hussain, 2015). The far-UV CD spectra of α-helices, aromatic peptides and β-sheets has specific characteristics below 240 nm that have made CD spectroscopy a standard tool for monitoring the secondary structures of proteins. Below 240 nm the spectra are dominated by n–π* and π–π* transitions of the peptide backbone (Woody and Tinoco Jr., 1967; Woody, 1968). The n–π* transition gives rise to a negative peak in the CD spectrum at about 224 nm. According to Moffitt's theory (1956) excitonic interactions in α-helices result in three π–π* transitions with split energies: one gives rise to the negative peak at around 210 nm and the other two are degenerate, at around 190 nm, with amplitudes strongly depending on the probing direction. The ACD of oriented polypeptides can provide additional information regarding the angle of orientation of the secondary structures (Wu et al., 1990; Dave et al., 2005; Bürck et al., 2008; Bürck et al., 2016). Helical peptides inserted into lipid bilayers exhibit a specific ACD spectrum. As the 210 nm transition is polarized parallel to the helix principal axis, a distinguishing feature of the ACD of α-helices is the presence or absence of 210 nm negative band, being indicative of surface or transmembrane helix alignment, respectively (Wu et al., 1990). For polytopic transmembrane proteins, the average inclination angle of the transmembrane helices can be extrapolated.

2.2.2. Two-dimensional electronic spectroscopy

Principles of 2DES

Two-dimensional electronic spectroscopy and its related techniques have become an important and essential tool in the study of various physical, chemical, and biological systems (Jonas, 2003; Fassioli et al., 2014; Fuller and Ogilvie, 2015; Oliver, 2018; Petti et al., 2018; Gelzinis et al., 2019). Here I will summarize the principles of the method, as outlined in (Lambrev et al., 2020).

A 2DES spectrum $S(\omega_\tau, T_w, \omega_t)$ is typically presented as a contour map spread in two frequency axes ω_τ and ω_t for a certain waiting time, or population time, T_w. 2DES can be considered as an extension of the pump-probe or transient absorption (TA) spectroscopy. In TA, an ultrashort pump pulse excites a system, and the differential absorption of an ultrashort broadband probe pulse with delay time T_w after the pump pulse is then measured (Figure 2.4) to give a TA spectrum $S_{\mathrm{TA}}(T_w, \omega_t)$ along frequency axis ω_t. Due

to the inherent broad bandwidth of the ultrashort pump pulse, there is no frequency resolution in the excitation.

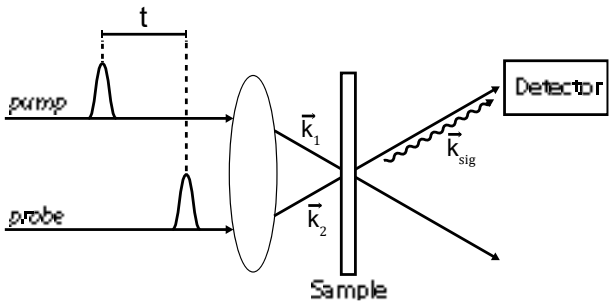

Figure 2.4. Scheme of pump-probe transient absorption spectroscopy. The output from an ultra-short-pulse laser is split into two beams, pump and probe. The probe pulse trains are delayed, and the two beams are focused on the sample at different incident angles. The transmitted probe beam is detected by a wavelength-sensitive detector.

2DES's enhancement of the TA technique is its ability to provide an extra frequency axis ω_τ that represents the frequency resolution in the excitation pulse. This allows experimentalists to have frequency-resolved correlation between excitation and detection and is particularly important for complex systems with multiple donor and acceptor exciton states with overlapping absorption profiles that often cannot be resolved during excitation in TA spectroscopy. Hence, 2DES has advantage over conventional pump-probe spectroscopy providing separate spectral information of donor and acceptor molecules involved in the EET process.

A schematic illustration of a 2D spectrum is presented in Figure 2.5, for a hypothetical system of two coupled chromophores with exciton energies corresponding to the frequencies a and b ($a > b$). In simplified terms, the 2D signal intensity reflects the conditional population of excited states absorbing at the *detection frequency* ω_t, if the initially excited states are ones absorbing at the *excitation frequency* ω_τ. The two cross-peaks ($\omega_t \neq \omega_\tau$) indicate coupling between the electronic transitions. The cross-peak at $\omega_\tau = a$ and $\omega_t = b$ indicates that upon initial excitation of the exciton level a, after waiting time T_w, the system can be found in the state corresponding to frequency b.

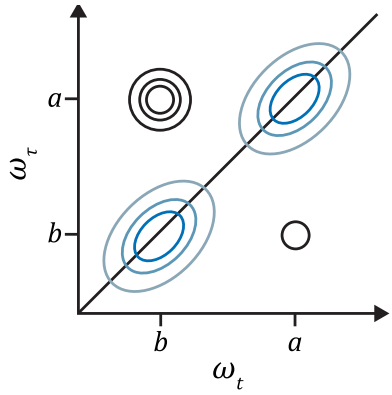

Figure 2.5. Schematic illustration of the 2D spectrum of two coupled electronic transitions. Diagonal peaks appear at the absorption frequencies of the two transitions and cross-peaks reflect their coupling. The cross-peak at excitation frequency *a* and detection frequency *b* reflects the population of electronic energy level *b* upon initial excitation of the level *a*.

The 2D spectra contain all information recorded by conventional TA spectroscopy – the *projection-slice theorem* (Gallagher Faeder and Jonas, 1999; Jonas, 2003) holds that the 2D spectrum $S(\omega_\tau, T_w, \omega_t)$ integrated over ω_τ is identical to the pump-probe TA spectrum $S_{\mathrm{TA}}(T_w, \omega_t)$ (Hamm and Zanni, 2011). The 2D spectrum also provides valuable information about the fundamental inhomogeneous/homogeneous lineshapes of the transitions. Inhomogeneously broadened absorption bands (in an ensemble of molecules with energy disorder persisting over the course of the measurement) result in 2D peaks elongated along the diagonal, since the excitation and detection frequencies are correlated. The inhomogeneous and homogeneous broadening can be determined from the anti-diagonal and diagonal width of the 2D peak. *Spectral diffusion* induced by random fluctuations of the transition energies, cause the diagonal elongation to disappear over time as the system loses memory of the initial excitation frequency.

Time-domain Fourier-transform 2DES

In a 2DES experiment, the sample interacts with three pulses as illustrated in Figure 2.6 – the first pulse creates coherence between the ground state and an electronic excited state. If the second pulse at time delay τ (sometimes denoted t_1) is in phase with the coherent oscillation, it creates population. The third (probe) pulse causes the emission of a photon echo signal, which will generally oscillate in time t (also denoted t_3) with the same frequency as the initial excitation frequency. However, during the waiting time T_w (t_2), the system may undergo changes, or population transfer to a different state, causing a frequency shift of the echo signal.

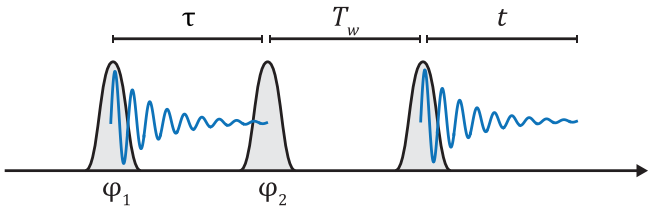

Figure 2.6. Pulse sequence in 2DES — two 'pump' pulses at defined coherence time τ and phase followed by a third pulse ('probe') after waiting time T_w.

The optical signal is described in terms of nonlinear response theory. The laser pulses transiently alter the *polarization* state of the medium $P(t)$, which is the electric dipole moment per unit volume. In the case of linear response, the polarization is proportional to the electric field:

$$P(t) = \varepsilon_0 \cdot \chi \cdot E(t) \tag{2.2.11}$$

where χ is known as linear optical susceptibility. In nonlinear optics, the polarization is generalized as power series in the field strength:

$$P(t) = \varepsilon_0\left(P^{(1)}(t) + P^{(2)}(t) + P^{(3)}(t) + \cdots\right), \tag{2.2.12}$$

where:

$$P^{(n)}(t) = \chi^{(n)} \cdot E^n(t) \tag{2.2.13}$$

The nonlinear optical response of the system can be theoretically calculated by equating polarization with the expectation value of the quantum-mechanical electric transition dipole operator $\hat{\mu}$:

$$P(t) = \langle \mu \rangle = \langle \Psi(t) | \hat{\mu} | \Psi(t) \rangle \tag{2.2.14}$$

In time-domain Fourier-transform 2DES, the emitted signal is a third-order nonlinear polarization signal, which is a convolution of the three laser fields and the *third-order nonlinear optical response function* (Mukamel, 1995; Hamm and Zanni, 2011):

$$P^{(3)}(t) = \int_0^\infty dt_3 \int_0^\infty dt_2 \int_0^\infty dt_1 E_3(t - t_3) E_2(t - t_3 - t_2) E_1(t - t_3 - t_2 - t_1) R^{(3)}(t_3, t_2, t_1) \tag{2.2.15}$$

The nonlinear optical response can be calculated by equating polarization with the expectation value of the quantum-mechanical electric transition dipole operator $\hat{\mu}$:

$$P(t) = \langle \mu \rangle = \langle \Psi(t) | \hat{\mu} | \Psi(t) \rangle \tag{2.2.16}$$

This is the basis for the *theory of nonlinear spectroscopy* used to describe various spectroscopic techniques (Mukamel, 1995).

In the frequency domain, the polarization is determined by the *third-order nonlinear susceptibility*, which is the Fourier transform of the response function:

$$\chi^{(3)}(\omega_1, \omega_2, \omega_3) = \int_{-\infty}^{\infty} dt_1 \int_{-\infty}^{\infty} dt_2 \int_{-\infty}^{\infty} dt_3 R^{(3)}(t_3, t_2, t_1) e^{i(\omega_1 t_1 + \omega_2 t_2 + \omega_3 t_3)} \tag{2.2.17}$$

The frequency-domain 2D electronic spectrum is the Fourier transform of the emitted signal with respect to τ (t_1) and t (t_3) at a fixed waiting time T_w (t_2). In practice, Fourier transformation with respect to t is done physically by a spectrometer (diffraction grating). Transformation with respect to τ is done numerically after scanning over a range of τ values. It is necessary that the first two interaction pulses have very well-defined phase, and the signal is *heterodyne-detected*. The 2D signal must also be separated from all other background signals, including the interacting laser pulses and other responses, such as TA. There are generally two approaches to this purpose – *phase matching* and *phase cycling* (see below), which are applied depending on the beam geometry used in the 2DES experiment.

The most common 2DES implementation is the noncollinear beam geometry, wherein all three interacting pulses arrive at the sample at different angles of incidence. Due to the phase matching condition, the desired nonlinear signal emits in a distinct direction different from the three interacting pulses. In order to measure the full amplitude and phase profile of the signal, a fourth "measurement" pulse, known as a local oscillator pulse, is introduced collinearly with the emitted signal before being detected in a spectrometer with a square-law detector. This detection process is known as heterodyne detection (Jonas, 2003). An alternative 2DES approach is to use pulses in a collinear beam geometry. In this approach, the relative phases of the first two collinear pulses are manipulated to extract the desired signal in a procedure known as phase cycling (Keusters et al., 1999; Tan, 2008), whereby one repeats an experiment with a series of different pulse phases $\varphi_{12} = \varphi_2 - \varphi_1$. Using the analogy of pump-probe spectroscopy, one can view the first two collinear pulses as a two-pulse "pump". A third "probe" pulse, noncollinear with the first two and delayed by T_w, provides the third interaction. The third pulse also acts as a local oscillator to give a heterodyne-detected frequency-resolved signal $S(\varphi_{12}; \tau, T_w, \omega_t)$. By using a 1×2 phase cycling scheme, $S(\varphi_{12}; \tau, T_w, \omega_t)$ is collected at $\varphi_{12} = 0°, 180°$, which are then processed to yield the 2D spectrum.

2.3. Photosynthetic pigment–protein complexes

2.3.1. Photosystem II

PSII is called "the engine of life" (Barber, 2006) as it is the enzyme mainly responsible for the presence of oxygen in the Earth's atmosphere, released as a bioproduct of water photolysis. PSII acts as water:plastoquinone oxidoreductase, whereby the energy of four absorbed light quanta (photons) is used to power the reaction:

$$2H_2O + 2PQ \rightarrow O_2 + 2PQH_2$$

where PQ stands for plastoquinone (oxidised) and PQH_2 for plastoquinol. Thus, each absorbed photon extracts one electron and one proton – ultimately used for carbon fixation.

PSII is a large multisubunit transmembrane pigment–protein complex. In plants and green algae, PSII is found in the chloroplast TM as a PSII–LHCII supercomplex, which consists of a dimeric core complex surrounded by several peripheral antenna complexes LHCII. The crystal structure of the core complex (from a thermophyllic cyanobacterium) has been determined to 1.9 Å (Umena et al., 2011) and cryo-electronic microscopy has recently allowed the structural determination of various PSII–LHCII supercomplexes (Wei et al., 2016; Su et al., 2017; van Bezouwen et al., 2017; Cao et al., 2018), of which the so-called $C_2S_2M_2$, shown in (Figure 2.7), is the most commonly found functional PSII unit in plants (Dekker and Boekema, 2005; Caffarri et al., 2009; Kouřil et al., 2013). Each of the two RCs in this supercomplex is served by about 200 light-harvesting pigments (Chls and Cars) who work in concert to deliver the absorbed solar energy to the RC. Even larger algal PSII–LHCII supercomplexes have been resolved recently (Shen et al., 2019). As seen in the figure, the pigment density is very high in the peripheral antenna whereas the protein density is higher in the core complex, which supports the electron transport reactions.

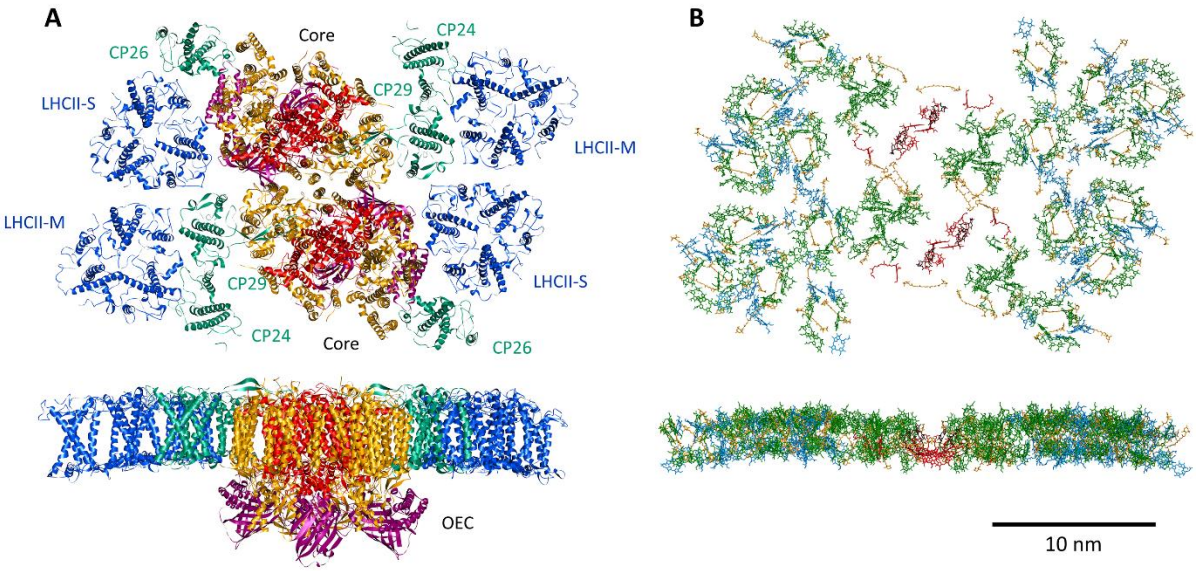

Figure 2.7. Structure of the PSII–LHCII supercomplex (top and side views). A. Protein subunits: core complex subunits in yellow and red, oxygen-evolving complex in purple, monomeric LHCII in green, trimeric LHCII in blue. B. Pigment cofactors: Chl *b* in blue, Chl *a* in green, Cars in yellow, RC cofactors in red. Images created in Discovery Studio from PDB ID 5XNL.

The core complex encompasses the RC, the core antenna complexes, CP47 and CP43, and the oxygen-evolving complex. Its composition and structure is highly conserved among all oxygenic photosynthetic organisms, from cyanobacteria to higher plants (Hankamer et al., 2001). The monomeric core complex contains 25 or more protein subunits (PsbA–Z) binding in total 35 Chls *a*, 2 pheophytins, 11 β-carotenes, 2 plastoquinones, inorganic ions (Ca^{2+}, Cl^{-}, HCO^{3-}, Fe^{3+}, Mn^{2+}) as well as lipids (Umena et al., 2011; Suga et al., 2015).

Two homologous polypeptides, PsbA and PsbD (D1 and D2), each having five transmembrane α-helices, arranged in a pseudo-symmetric heterodimer, bind the cofactors that carry out the photoinduced charge separation and electron transfer (Figure 2.8). The D1/D2 RC proteins are flanked by the core light-harvesting antenna proteins CP43 (PsbC) and CP47 (PsbE) and cytochrome b_{559} (PsbF). CP43 protrudes toward the lumen and, together with D1 and several membrane-extrinsic proteins (PsbO, PsbP and PsbQ in higher plants), participates in the formation of the oxygen-evolving complex (OEC), providing ligands to its inorganic catalytic centre — Mn_4CaO_n (Vinyard et al., 2013), located on the donor side of PSII (Figure 2.8).

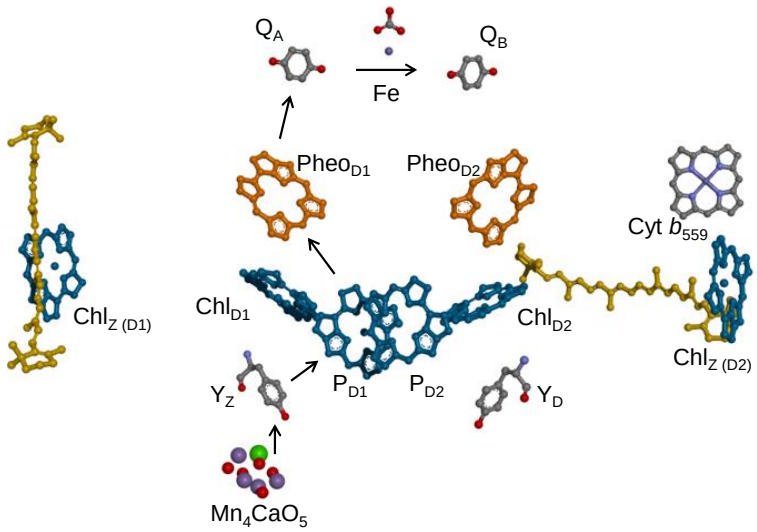

Figure 2.8. Structural arrangement of the cofactors involved in the primary reactions of PSII and pathway of electron transfer (Umena et al., 2011). Created in Discovery studio using PDB ID 3WU2.

Photoexcitation of the RC Chls, collectively named P_{680}, results in rapid (within a few ps) reduction of $Pheo_{D1}$ and creation of a strong oxidant, $P_{680}^{\bullet+}$, with the highest mid-point potential in nature of about +1.2 V – capable of extracting electrons from water. On the acceptor side of PSII, electrons are transferred from Pheo to Q_A in 200–300 ps and then to the two quinones, Q_A and Q_B on a timescale of 200–800 µs (Renger and Renger, 2008). The exact kinetics, rate-limiting steps and mechanisms of the primary photochemical events are still under debate (van Amerongen and Croce, 2013) and may involve quantum phenomena such as CT state mixing and vibronic coherence (Romero et al., 2014; Romero et al., 2017).

2.3.2. Light-harvesting complex II

The majority of Chls associated with PSII are bound to the peripheral antenna subunits, LHCII. LHCII binds up to 50% of the total Chl in the plant chloroplasts and is the most abundant membrane protein in the biosphere (van Amerongen and Croce, 2007). The nuclear genome of higher plants contains six genes, *lhcb1–6,* encoding homologous proteins of the Lhc superfamily (Jansson, 1999). Lhcb1–3 constitute the heterotrimers termed major LHCII, LHCIIb or simply LHCII. Lhcb4–6 are the so-called minor (or LHCIIa) antenna complexes CP29, CP26 and CP24, respectively. These monomeric complexes are located between the core complex and the LHCII trimers (Figure 2.7) mediating the transfer of energy (Boekema et al., 1999; Nield and Barber, 2006; Wei et al., 2016).

Structure of plant LHCII

Apart from the cryo-EM structures of PSII, the high-resolution structures of the trimeric LHCII (Liu et al., 2004; Standfuss et al., 2005) and CP29 (Pan et al., 2011) have been obtained by X-ray crystallography. All Lhc complexes share a common framework with three transmembrane α-helices in a characteristic IX shape, connected by loops and smaller amphipathic helices (Figure 2.9).

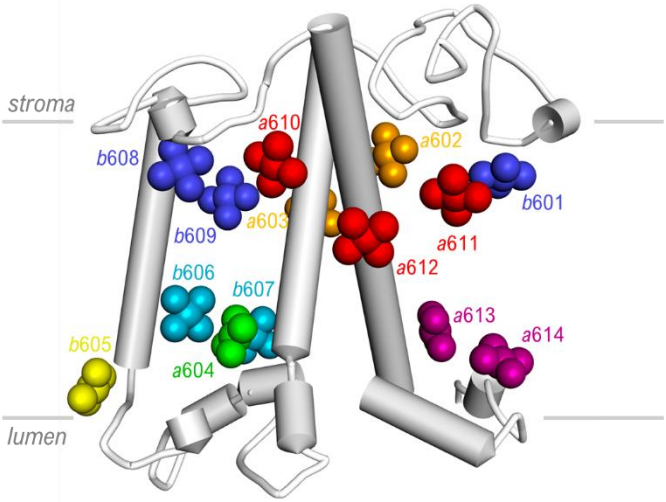

Figure 2.9. Schematic structure of the LHCII monomer – the positions of the Mg and N atoms of the 14 Chls are indicated in colour and the apoprotein in white. Similar colours indicate groups consisting of Chls *a* or *b* at Mg–Mg distances less than 12 Å (including an inter-monomeric 601–608 pair). Created in Discovery Studio from PDB ID 1RWT (Liu et al., 2004).

Each monomeric subunit of the major LHCII noncovalently binds eight Chl *a*, six Chl *b* and four xanthophylls. The transmembrane part of the protein complex has high structural rigidity (Standfuss et al., 2005; Dockter et al., 2012) ensuring strict geometry and electrostatic environment of the pigments, which in turn determine the excited-state properties of the complex. The Chls are arranged in two layers – eight Chls near the N-terminus on the side of the chloroplast stroma and six on the lumenal side of the TM (Figure 2.9). The Chls are closely spaced together and there are several pigment groups with mutual distances of 9–12 Å – Chls *a* 602/603, *a* 610/611/612, *b* 601′/608/609 on the stromal side and Chls *a* 613/614, *b*606/607 on the lumenal side. These tightly packed pigments strongly interact forming exciton domains. In addition, the Cars, especially the two central luteins and neoxanthin strongly interact with various Chls.

Energy transfer dynamics in LHCII

The dynamics of EET between pigments in LHCII has been studied with the help of various time-resolved spectroscopic techniques and theoretical approaches (van Amerongen and Croce, 2007). Although the pigments in LHCII do not strictly constitute an energy funnel, differences in their transition energies to a certain extent guide the absorbed energy from Cars or Chl *b* to Chl *a* until excitations are finally localized primarily on a small number of Chl *a* molecules constituting the so-called terminal emitters from where energy can be transferred toward the RC.

EET from Car and Chl *b* to Chl *a* occurs on multiple timescales ranging from fs to ps at room temperature (RT). The EET from Chl *b* to Chl *a* takes place with sub-ps characteristic times in the range of 0.15–0.6 ps at RT and 0.3–0.6 ps at low temperatures (Bittner et al., 1994; Pålsson et al., 1994; Bittner et al., 1995; Visser et al., 1996; Connelly et al., 1997; Kleima et al., 1997; Gradinaru et al., 1998) but slower, ps transfers are also detected, suggesting the presence of weakly coupled Chl *b*. Three-pulse photon-echo peak shift (3PEPS), a technique closely related to 2DES, determined two timescales of Chl *b* EET as 0.3 and 0.8 ps (Agarwal et al., 2000; Salverda et al., 2003). This fast phase is followed by a slower transfer from Chls absorbing in an intermediate region (660–670 nm) between the major Chl *b* and Chl *a* Q_y bands.

The blue-most Chl *a* transfer excitations to the bulk Chl *a* in 3–7 ps (Visser et al., 1996; Kleima et al., 1997; Gradinaru et al., 1998; Agarwal et al., 2000; Salverda et al., 2003; Palacios et al., 2006) and an even slower transfer has been detected at low temperature (Bittner et al., 1995; Visser et al., 1996; Kleima et al., 1997; Gradinaru et al., 1998). The equilibration among the lowest-energy Chl *a* states occurs on a timescale of up to tens of picoseconds and is assumed to involve transfer between the stromal and lumenal Chl layers as well as inter-monomer equilibration (van Amerongen and van Grondelle, 2001; Palacios et al., 2006; Novoderezhkin et al., 2011).

The efficiency of EET from Cars to Chls in LHCII is generally very high (Peterman et al., 1997; Caffarri et al., 2001) but varies depending on the specific Car site – luteins transfer energy (preferentially to Chl *a*) more efficiently than neoxanthin (to Chl *b*), whereas violaxanthin does not appear to contribute to any energy transfer to Chls (Caffarri et al., 2001; Croce et al., 2001; Gradinaru et al., 2001). The transfer primarily occurs via the Car

S_2 states despite their very short lifetimes, whereas S_1–Chl transfer is not significant, probably because of the low dipole strength of S_1.

Despite the wealth of data, there is no complete consensus on the dynamics and pathways of EET especially in the manifold of Chl *a* exciton states. The uncertainty in the time-scales in case of Chl *a* partly stems from the large spectral overlap between Chl *a* states, which makes it difficult to resolve EET by conventional time-resolved spectroscopy, and because of the comparable strengths of excitonic coupling between chromophores and coupling with protein vibrations (phonons).

Exciton models of LHCII

Several groups have used the published structures of LHCII to calculate the Chl exciton states using quantum-chemical theoretical methods and fitting to spectroscopy data (Novoderezhkin et al., 2005; Linnanto et al., 2006; Müh et al., 2010; Zucchelli et al., 2012). The general approach is to construct an exciton Hamiltonian with diagonal elements corresponding to the unperturbed transition energies (site energies) of all Chls, accounting for any shifts caused by the environment (protein, lipids, water, etc.), and off-diagonal elements corresponding to the Coulomb interaction energies (excitonic couplings) between Chls. The energy eigenstates (exciton states) of the complex are obtained by diagonalizing the Hamiltonian and can be used to calculate optical spectra, including CD. All published models are in good agreement with regard to the interaction energies (Zucchelli et al., 2012). The strongest couplings, between Chls *a*611 and *a*612, have magnitude around 100 cm^{-1}. However, because of uncertainties in the site energies, it is difficult to assign the dominant contributions of specific Chls to the exciton eigenstates, respectively absorption/CD bands. The model of Zucchelli *et al.* (2012) assigns the lowest eigenstate to Chl *a*612 on the stromal side of the protein, in agreement with earlier mutagenesis and spectroscopy data (Remelli et al., 1999), whereas other models point to *a*610 (Müh et al., 2010; Novoderezhkin et al., 2011) and the possibility of a temperature-dependent swap has been put forward (Müh et al., 2010; Vrandecic et al., 2015). Even less agreement exits regarding the low-energy states on the lumenal side and the identities of upper energy levels are also debatable. This poses difficulties in modelling and interpreting the spectroscopic data. Another challenge is to include vibronic and higher-energy transitions in the Hamiltonian for a realistic depiction of the optical spectra (Lindorfer et al., 2017).

2.3.3. Photosystem I

PSI is a large multisubunit transmembrane pigment–protein complex which catalyses the second part of the light induced electron transfer reactions in oxygenic photosynthesis- the oxidation of plastocyanin and the reduction of ferredoxin. Apart from its nearly 100% quantum efficiency (Nelson and Junge, 2015), PSI generates one of the most negative reduction potentials (–1.2 V) in nature. Such a negative reduction potential is necessary to deliver the electrons to the relatively poor electron acceptor NADP.

Structural organization

Both structurally and functionally, plant PSI can be viewed as composed of two parts: (1) the core complex and (2) and the peripheral antenna system. The structure and composition of core complex is highly conserved among all oxygen-evolving photosynthetic organisms (Fromme et al., 2001; Hohmann-Marriott and Blankenship, 2011; Nelson and Junge, 2015) even though cyanobacteria and plants diverged in evolution one billion years ago. However, the peripheral antenna, varies in the different organisms not just compared with cyanobacteria but also between different eukaryotic organisms (Hohmann-Marriott and Blankenship, 2011) as it is optimized for the absorption in their light-growth conditions (Blankenship, 2014).

The core complex harbors ~98 Chl *a* and ~22 Cars and all carriers of the electron-transport chain between the external electron donor and acceptor, plastocyanin (or cytochrome) and ferredoxin. Most of the Chls in the core complex form an internal antenna system – core antenna, which is directly coupled to the RC (Mazor et al., 2015; Qin et al., 2015). The RC consists of six Chl *a*, two phylloqiunones, and three iron-sulfur clusters, arranged in a configuration reminiscent of the bacterial RC and PSII (*Figure 2.10*).

The RC cofactors and core antenna are then coordinated by two largest protein subunits PsaA and PsaB (similar to the PsbA-D (D1-CP47, D2-CP43 subunits of PSII), forming pseudosymmetric heterodimer, both of which are involved in the electron transfer process, merging at the first iron-sulphur cluster. Each branch of the RC operates independently of the other in carrying out light-induced charge separation (Badshah et al., 2018).

In green algae and higher plants, the light harvesting capacity of PSI is increased by the attachment of several outer light-harvesting complexes. In higher plants the peripheral

antenna consists of four proteins Lhca1–Lhca4, called light-harvesting complex I (LHCI) and increase the absorption cross section of the PSI core by ~60%. Structures of the Lhcas are highly conserved but their spectroscopic properties differ substantially (Croce, 2015). The LHCI complexes are present in single copies per PSI and organized as two heterodimers, Lhca1/4 and Lhca2/3 (Nelson and Ben-Shem, 2004), located on one side of the core complex in a half-moon shape (Figure 2.10) .

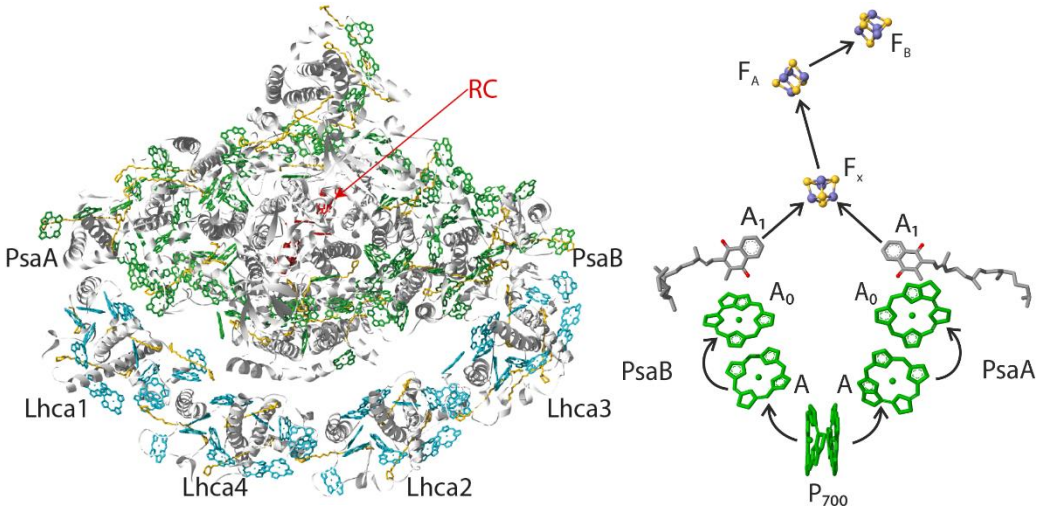

Figure 2.10. Structure of plant PSI–LHCI supercomplex. Left: the stromal side view, highlighting the two main moieties of PSI–LHCI complex — the core complex containing the RC and the attached peripheral antenna complexes, LHCI. The Chls (without the phytol chain for clarity) are coloured green in the core antenna, blue in the LHCI and red in the RC and Cars in yellow; Right: Structural arrangement of the electron transfer chain cofactors and electron transfer pathways in the RC. The figure was created based on PDB entry 5L8R (Mazor et al., 2015).

LHCI proteins share sequence and structural homology with the LHCII complexes of PSII. Each Lhca monomer is composed of three major transmembrane helices and binds ~14 Chl *a* and *b* molecules and three Cars: one β-carotene, one lutein, one violaxanthin (Qin et al., 2015). Another lutein is bound between Lhca1 and Lhca4, giving rise to a total of 13 Cars in the four Lhcas. The Chls in LHCI are arranged into two layers, the one close to the stromal side contains 36 Chls (29 Chls *a* and 7 Chls *b*) and the other layer on the luminal-side has a less dense packing composed of 16 Chls *a* and five Chls *b*. LHCI has some unique Chls compared to LHCII, located at the gap region between LHCI and the PSI core, or in connecting regions between adjacent LHCI subunits (Qin et al., 2015). Large differences have been observed between the antenna of green algae and plants: The PSI peripheral antenna of *C. reinhardtii* is more than twice larger than the PSI of higher plant.

Red chlorophylls in PSI

PSI of almost all organisms contains long-wavelength Chl forms, dubbed "red" Chls, absorbing photons of energy lower than the primary electron donor P_{700} (Karapetyan et al., 2006), broadening the absorption spectral range. The red forms are characterized by long-wavelength emission, large Stokes shift, large homogeneous and inhomogeneous broadening and unusually high electron-phonon coupling – properties attributed to the mixing of excitonic and CT states (Frese et al., 2002; Ihalainen et al., 2003; Vaitekonis et al., 2005; Romero et al., 2009; Novoderezhkin et al., 2016)

The number of the red Chl forms is species-dependent and their emission maxima vary between different organisms in the range of 700 to 760 nm (Karapetyan et al., 1997; Gobets and van Grondelle, 2001). The PSI–LHCI complexes of the green alga *C. reinhardtii* contain five-six "red" Chl forms with absorption maximum around 700 nm (Gibasiewicz et al., 2005). These red Chls are significantly blue shifted compared to cyanobacteria and plants and are isoenergetic with primary electron donor but still are distinguishable from it by their spectral features. The majority of the low-energy Chl forms in plants have been shown to reside on LHCI (Croce et al., 1996; Schmid et al., 1997; Croce et al., 1998; Castelletti et al., 2003; Croce et al., 2007). However, several authors have reported a range of values regarding the number of red Chls, their energies and distribution in the core complex and LHCI (Croce et al., 1998; Gobets and van Grondelle, 2001; Ihalainen et al., 2003). Some have hypothesized that red states at the interface between the core and LHCI maybe lost during their biochemical separation (Mazor et al., 2015).

Although red absorbing Chls account only for a small fraction (3–10%) of the total absorption cross-section (Croce and van Amerongen, 2013), they have sizeable impact on EET and trapping, as the excitations must be transferred energetically uphill to the RC (Jennings et al., 2003). Despite of the complexity of the PSI organization and slow-down of overall trapping by that uphill transfer, PSI is one of the most efficient solar converters with a quantum efficiency close to one (Nelson and Junge, 2015).

Energy transfer dynamics in PSI

The excitation dynamics and trapping in PSI of plants, photosynthetic bacteria and algae are widely investigated using several time-resolved spectroscopy techniques by many workers. Pioneering picosecond fluorescence studies in the 1970s revealed that PSI

fluorescence decays in 80 ps or less at RT (Beddard et al., 1975; Paschenko et al., 1975) but the lifetimes are drastically slower at cryogenic temperatures because of trapping of excitations on long-wavelength Chls (Searle et al., 1977; Butler et al., 1979).

Briefly, spectral equilibration in the core antenna has been found to occur on a timescale from 100–150 fs to several ps. A fast process of energy equilibration, typically on a timescale of 2–4 ps at RT (Hastings et al., 1995; Savikhin et al., 1999; Melkozernov et al., 2000; Savikhin et al., 2000; Gibasiewicz et al., 2001; Gobets and van Grondelle, 2001; Andrizhiyevskaya et al., 2004; Melkozernov et al., 2004; Gibasiewicz et al., 2007) and 4–6 ps at cryogenic temperature (Melkozernov et al., 2000; Gibasiewicz et al., 2002; Melkozernov et al., 2005), has been assigned to EET from the bulk antenna Chls to the red forms. The spectral changes on this timescale could also be interpreted as arising from excitation of the RC pigments followed by charge separation (Müller et al., 2003; Holzwarth et al., 2005; Slavov et al., 2008; Müller et al., 2010). In recent investigations of PSI from higher plants, the bleaching of states absorbing around 700 nm observed on a 2–4 ps timescale, was attributed to the RC pigments (Akhtar et al., 2018; Russo et al., 2020). One of the reasons for such assignment was that the majority of red Chls in plant PSI are located in the peripheral antenna, whereas the species in question was observed in the core. The intrasubunit equilibration time in all Lhcas is very fast (<10 ps), whereas the intersubunit time of EET within the Lhca dimers is somewhat slower (Wientjes et al., 2011). When connected to PSI supercomplex, these Lhcs mainly transfer directly to the core. The transfer is very fast for Lhca1 and Lhca2, whereas from Lhca3 and Lhca4, is slower, mainly because of their red Chls.

Despite the abundance of time-resolved spectroscopy data, the EET and trapping kinetics are still under debate (Croce and van Amerongen, 2013; Nelson and Junge, 2015). In most organisms, the effective photochemical trapping of excitations in the bulk antenna occurs by one major phase around 20 ps (Gobets and van Grondelle, 2001; Engelmann et al., 2006; Slavov et al., 2008; Wientjes et al., 2011; Akhtar et al., 2018) but the lifetime depends on the amount and energies of the “red” Chls (Gobets and van Grondelle, 2001). In the PSI–LHCI complex of green plants, trapping shows an additional phase between 50 and 130 ps

The excited-state kinetics results are generally described by two alternative models, differing from each other by the assignment of the rate-limiting step. According to the trap-

limited model, excitations are rapidly equilibrated between the antenna and the RC and the kinetics is limited by charge separation (Müller et al., 2003; Slavov et al., 2008; Müller et al., 2010). In this case, the probability that the excitation will escape from the RC before it is consumed is very high. In the alternative transfer-to-trap-limited model, the charge separation is very fast and the kinetic is limited by EET from the antenna to the RC which is slow, because of the large distance between the core antenna and the RC Chls (Valkunas et al., 1995; Savikhin et al., 2000; Gobets and van Grondelle, 2001; Savikhin et al., 2001; Ihalainen et al., 2005; Cherepanov et al., 2017; Cherepanov et al., 2020). In this case excitations, once captured by the RC, do not return to the antenna.

The complexity of the PSI antenna, the large number of pigments and spectral overlap makes it difficult to unambiguously interpret the spectroscopy data and distinguish between different kinetic models. The high-resolution crystal structures of PSI (Mazor et al., 2015; Qin et al., 2015) reveal new structural information about the green plant PSI supercomplex, including specific interactions between the core complex and LHCI. These, in combination with detailed ultrafast kinetics data, might improve understanding of the processes of EET, and draw a physical link between the EET function and the available structure. On the other hand, the red Chls can significantly affect the PSI kinetics, their stoichiometry, energetic properties, and subunit distribution must be taken into account in any informed model.

2.4. Macroorganization and flexibility of the thylakoid membrane

2.4.1. Architecture of the thylakoid membrane

The two photosystems, together with the other two major protein complexes of the photosynthetic electron-transport chain – the cytochrome b_6f complex and the chloroplast ATP-synthase – are exclusively located in the chloroplast TM. Higher-plant TM have a complex three-dimensional architecture generally consisting of stacked thylakoids forming grana that are interconnected by stroma lamellae. The duality makes for discrete membrane regions – the non-appressed stromal regions, the appressed membranes in the granum core and the grana margins, each with its distinct protein composition (Andersson and Anderson, 1980). Thylakoids are not isolated vesicles, as might be implied by their name (sac-like), but form a continuous network enclosing a single aqueous

volume, the thylakoid lumen (Weier et al., 1963; Austin and Staehelin, 2011; Daum and Kühlbrandt, 2011).

The three-dimensional structure of the granum has been a debatable subject for decades and several models have been put forward and used in the scientific and educational literature (for reviews see Nevo et al., 2012; Kowalewska et al., 2019). One of the earliest, the "helical model", proposed first by Paolillo (1970) and slightly refined by Mustárdy and co-workers (1979; 2003) is supported by most high-resolution electron tomography data available (Mustárdy et al., 2008; Daum et al., 2010; Austin and Staehelin, 2011; Daum and Kühlbrandt, 2011). According to the helical model, the granum has roughly cylindrical shape comprising a variable number of stacked granal thylakoids with a flat discoid shape and typical diameters in the range of 400–600 nm. The grana are connected by a fretwork of parallel stromal thylakoids spiralling around them and connecting with the grana margins via narrow junctions in a right-handed helical arrangement (Figure 2.11).

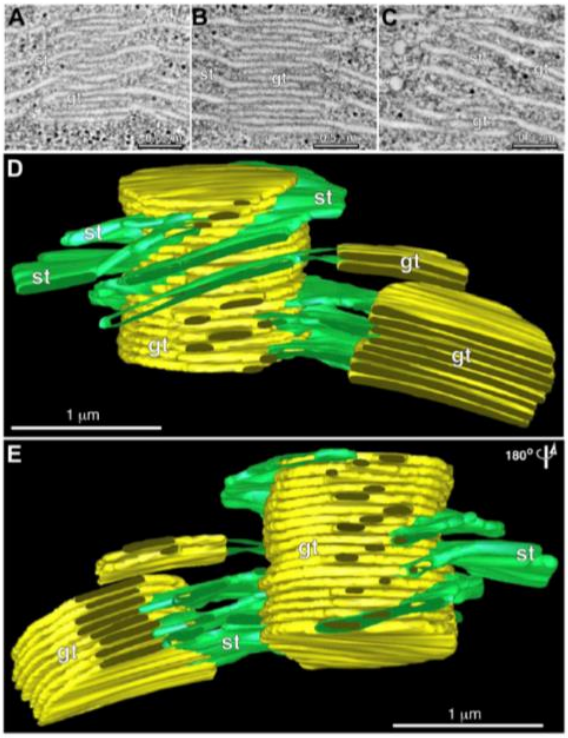

Figure 2.11. Organization of the granal TM revealed by cryo-EM. A–C: are three composite tomographic slice images. D–E tomographic reconstructed models of the grana stack with grana thylakoids in yellow and stroma thylakoids green. Reproduced from Austin and Staehelin (2011).

2.4.2. Composition and heterogeneity

Like other biological membranes, the thylakoids contain glycerolipids organised in ion-impermeable bilayers sustaining the proton-motive force (Williams, 1998). The lipid composition of the TM is, however, rather different from other cell membranes. In most plants, algae and cyanobacteria, TM predominantly consist of four lipid classes: two neutral galactolipids – monogalactosyldiacylglycerol (MGDG) and digalactosyl diacylglycerol (DGDG), and two anionic lipids – the glycolipid sulfoquinovosyl diacylglycerol (SQDG) and the phospholipid phosphatidylglycerol (PG) (Douce and Joyard, 1996; Kobayashi and Wada, 2016).

MGDG and DGDG are the major constituents – around 50% and 25%, respectively (Dorne et al., 1990) and are almost exclusively found in the TM and the inner chloroplast envelope under normal growth conditions. In lipid mixtures resembling the native thylakoid lipid composition, the coexistence and reversible transformation of H_{II} and lamellar phase has been observed depending on the hydration (Demé et al., 2014). The different lipids are asymmetrically distributed in the stroma- and lumen-exposed layers of the membrane (Douce and Joyard, 1996). Up to 40% of the thylakoid lipids are bound to proteins (Jost et al., 1973; Páli et al., 2003); lipids are found as structural components of the major photosynthetic protein complexes – PSI (Guskov et al., 2009; Qin et al., 2015), PSII (Umena et al., 2011; Su et al., 2017) and LHCII (Liu et al., 2004) – and are involved in the photosynthetic reactions (Mizusawa and Wada, 2011).

The TM are densely packed with proteins – the total integral proteins and pigment–protein complexes can take 70–80% of the area in appressed granal membranes (Kirchhoff et al., 2002; Haferkamp et al., 2010). Perhaps the most characteristic feature of the granal TM is the lateral heterogeneity or sorting of the membrane proteins in different domains – PSII and LHCII are found predominantly in the appressed regions in the granum core, PSI and ATP-ase are located exclusively in the stromal thylakoids and grana margins (Andersson and Anderson, 1980; Albertsson, 2001), and the cyt b_6f complex is evenly distributed throughout the TM (Dekker and Boekema, 2005; Nevo et al., 2012). The lateral separation of PSII and LHCII optimizes the packing density of the membrane system. Sorting of the stroma-side flat and protruding particles, followed by stacking of the flat regions, has been proposed to stabilise the granal membrane ultrastructure (Mustárdy and Garab, 2003; Garab, 2016).

2.4.3. Functional roles of grana

It is now accepted that the evolutionary pressure to develop grana was probably not a single critical advantage but a combination of factors (Chow et al., 2005; Anderson et al., 2008). One obvious advantage of thylakoid stacking is that it tremendously increases the number of photosynthetic complexes and the absorption cross section per unit volume (Barber, 1980; Horton, 1999; Mustárdy and Garab, 2003; Dekker and Boekema, 2005). The other principal role of grana is to provide a dynamic and flexible platform that can adjust various subcomponents of the photosynthetic apparatus in response to the environmental conditions – regulating thermal dissipation of excess energy or non-photochemical quenching (NPQ) (Ruban et al., 2012; Ruban, 2016), facilitating state transitions (Rochaix, 2011; Tikkanen et al., 2011; Johnson and Wientjes, 2019) and the repair and reassembly of damaged PSII (Tikkanen and Aro, 2012; Kirchhoff, 2018), balancing linear and cyclic electron transport (Albertsson, 2001; Johnson, 2018) and ATP synthesis (Chow et al., 2005; Anderson et al., 2008; Pribil et al., 2014). These regulatory roles require structural and functional plasticity, or flexibility, of the TM as a whole and involve concerted, cooperative or cascade rearrangements of the membrane macroorganization. The price to pay for the ability to densely pack large numbers of LHCII–PSII units in the granal TM, and especially in ordered semi-crystalline domains, is the restricted movement of molecules through it – from the mobile electron carriers plastoquinone and plastocyanine to the movement of lipids, proteins and protein-complexes for the maintenance and repair of the photosynthetic machinery (Kirchhoff, 2013; Kirchhoff, 2018).

2.4.4. Dynamic flexibility of thylakoid membranes

Granal TM are highly flexible adjusting their structure, composition and supramolecular organization at different hierarchical levels – on microscopic as well as mesoscopic scale – and on timescales spanning seconds to days. In the short term, exposure to high light reduces the grana diameter along with increased mobility of grana-hosted protein complexes (Herbstová et al., 2012) and partial unstacking of grana discs in the leaves of Arabidopsis (Fristedt et al., 2009) and isolated TM of spinach (Khatoon et al., 2009). The thylakoid lumen increases its size in the presence of light and shrinks in the dark (Kirchhoff et al., 2011). This swelling and shrinkage is controlled by regulated ion fluxes across TM through ion channels (for review see ref. Kirchhoff, 2013). Small-angle neutron scattering measurements on isolated spinach TM showed fast reversible light-

induced changes in the repeat distances on timescales of seconds. The light-induced changes are driven by the photoinduced proton and electron transport. Rapid small but clear light-induced changes in the membrane organization and repeat distances were observed in cyanobacteria (Nagy et al., 2011; Stingaciu et al., 2016) green algae (Nagy et al., 2014), diatom cells (Nagy et al., 2011; Nagy et al., 2012; Nagy et al., 2013) as well as intact leaves of various species (Ünnep et al., 2014) – (for a more extensive treatment see Ünnep et al., 2014; Garab, 2016). Dynamic reversible changes in the membrane macroorganization of isolated TM upon illumination can be followed by changes in the psi-type CD (Garab et al., 1988). Light-induced reversible changes were also detected in the psi-type CD of lamellar LHCII aggregates, associated with changes in their chiral macroorganization (Simidjiev et al., 1998). The observations were explained in terms of a so-called thermo-optic mechanism – according to it, the trigger for the structural transition is a local thermal jump caused by the dissipation of photon energy (Cseh et al., 2000; Garab et al., 2002; Cseh et al., 2005; Holm et al., 2005). These are only a few examples of dynamic structural rearrangements accompanying the acclimation of photosynthesis to the changing external conditions.

2.5. Regulation of excitation energy flow in the thylakoid membranes

2.5.1. State transitions

The linear photosynthetic electron transport from water to $NADP^+$ requires synchronized tandem operation of the two photosystems. One mechanism for adjustment of the excitation energy input between them in response to the spectral quality of light is the so-called state transitions. According to the canonical view, light absorbed predominantly by PSII (light 2) induces an acclimatory response in which the absorption cross section of PSI is enhanced at the expense of PSII (state 2) and vice versa. During the state 1–state 2 transition, the STN7 kinase (Bellafiore et al., 2005) activated by the reduced plastoquinone pool phosphorylates a subpopulation of the LHCII proteins, normally associated with PSII (in state 1); the phosphorylated LHCII migrates from the PSII-enriched stacked region to the PSI-containing unstacked stromal region – interacting with PSI and forming PSI–LHCII supercomplexes (in state 2) (Allen and Forsberg, 2001; Wollman, 2001; Tikkanen et al., 2011; Rochaix, 2014; Goldschmidt-Clermont and Bassi,

2015). State transitions as such are dynamic changes in TM macroorganization and presumably require remodelling of the photosystem supercomplexes. EM studies have revealed PSI–LHCI–LHCII supercomplexes in plant TM in state 2 (Zhang and Scheller, 2004; Kouřil et al., 2005; Galka et al., 2012) and a high-resolution cryo-EM structure has been recently presented (Pan et al., 2018), showing the specific interaction of the phosphorylated Thr in Lhcb2 with the PsaL subunit of PSI and the involvement of other PSI subunits (PsaO in PsaH) known to be essential for LHCII docking. Interestingly, no dissociation of PSII–LHCII supercomplexes was detected in state 2, indicating that the mobile fraction of LHCII belongs to the loosely bound L-trimer population (Galka et al., 2012; Wientjes et al., 2013). On the other hand, disassembly or destabilisation of PSII supercomplexes, by light treatment, promote state transitions (Dietzel et al., 2011). It is likely that LHCII in the stromal lamellae is energetically connected to PSI, but its physical interactions are very susceptible even to mild detergents and intact complexes cannot be isolated. LHCII could substitute LHCI as a PSI antenna in an LHCI-deficient Arabidopsis mutant (Bressan et al., 2016).

2.5.2. Non-photochemical quenching

Photosynthetic organisms thrive in constantly fluctuating light environment. The irradiance during a cloudy day or under the tree canopy can change over orders of magnitude in a matter of minutes. The capacity to utilize the available light energy can easily be exceeded, which can be extremely detrimental, as excess excitation energy can be a source of harmful reactive oxygen species that may ultimately kill the organism (Niyogi, 1999). The reduction of photosynthetic capacity caused by exposure to high irradiation is termed photoinhibition. All oxygenic photosynthetic organisms have evolved various redundant systems and mechanisms to avoid photoinhibition, among which is the so-called non-photochemical quenching of Chl fluorescence, NPQ (Muller et al., 2001; Li et al., 2009; Ruban, 2015). NPQ is a term combining several protective mechanisms of thermal dissipation of excess excitations. Although state transitions fall under the definition of NPQ, the main NPQ component is the so-called energy-dependent quenching that dissipates excess absorbed light energy safely into heat and is activated by the acidification of the thylakoid lumen and the consequent de-epoxidation of the LHCII-bound xanthophyll violaxanthin to zeaxanthin and protonation of the PSII-associated protein PsbS (Ruban et al., 2012; Demmig-Adams et al., 2014; Ruban, 2016).

The formation of quenching sites in the antenna effectively reduces the excitation diffusion length (the distance over which excitations can migrate before they are lost via radiative or nonradiative decay) and hence the fraction of excitations reaching the RCs (Bennett et al., 2018). The molecular mechanism behind NPQ has so far not been unequivocally established and there may in fact be several mechanisms acting in parallel, such as decay via the S_1 state of lutein (Pascal et al., 2005; Ruban et al., 2007) or to another dark electronic state (Mascoli et al., 2019), via a mixed Chl–Car exciton state (Bode et al., 2009), or a Chl–Chl CT state (Miloslavina et al., 2008; Holzwarth et al., 2009; Müller et al., 2010), or a Chl–Car CT state (Holt et al., 2005; Ahn et al., 2008). There is much debate over which of these mechanisms take place *in vivo* – some authors rule out the relevance of Chl–Chl CT states (Farooq et al., 2018; Gelzinis et al., 2018) while other studies point to the possibility of Chl–Car mechanisms to be an artefact of the laboratory measurements (van Oort et al., 2018).

Aggregation of LHCII in the TM was postulated by Horton and co-workers as the trigger for NPQ (Horton et al., 1991; Horton et al., 2005). The aggregation model was based primarily on the spectroscopic similarities of NPQ in vivo and in isolated LHCII aggregates (for review see Ruban et al., 2012; Ruban, 2016). Aggregation was thought to be promoted by either zeaxanthin (Ruban and Horton, 1994) or protonated PsbS (Holzwarth et al., 2009; Brooks et al., 2014). There is a general consensus that the activation of NPQ is associated with membrane macroorganization changes (Ruban et al., 2012). Biochemical evidence has been obtained for PsbS-dependent detachment of LHCII subunits from the PSII supercomplex (Betterle et al., 2009). Freeze-fracture EM (Johnson et al., 2011) revealed shorter distances between PSII in the TM under NPQ conditions and clustering of LHCII on the periphery of the grana (Figure 2.12). The PSII–LHCII rearrangements were found to be dependent on PsbS, which suppressed the formation of ordered semi-crystalline arrays and increased the mobility of the pigment–protein complexes in the grana (Damkjær et al., 2009; Goral et al., 2012).

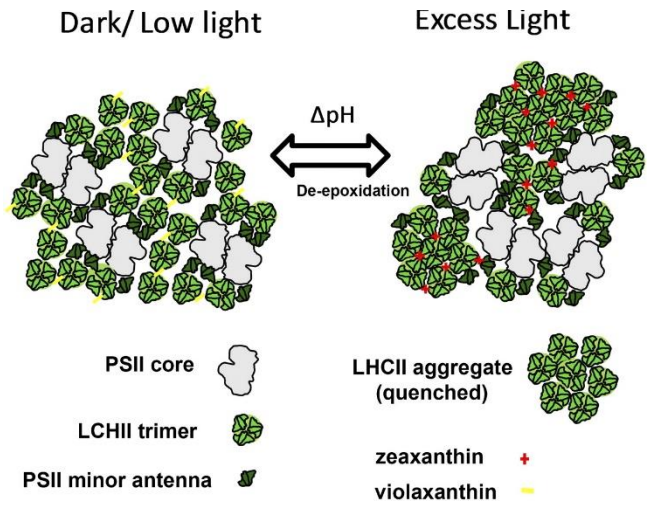

Figure 2.12. Structural Model of NPQ-Related Reorganization of Thylakoid Grana Membranes. In the dark and low light, LHCII is evenly distributed in the grana, forming large C2S2M2 supercomplexes with PSII and minor antenna proteins. In excess light, ΔpH triggers a conformational change within LHC complexes that causes the partial dissociation of the PSII–LHCII supercomplex and leads to LHCII aggregation. De-epoxidation of violaxanthin to zeaxanthin promotes LHCII aggregation and, thus, NPQ. Reproduced from Johnson et al. (2011). © American Society of Plant Biologists.

Holzwarth and co-workers (2009; 2014) proposed a four-state, two-site model for NPQ, separating the site of action of zeaxanthin and PsbS as Q1 and Q2, respectively (Figure 2.13). The PsbS-dependent mechanism involves detachment of LHCII from the PSII core complex and aggregation leading to the formation of quenching Chl-Chl CT states. In time-resolved fluorescence spectroscopy data of leaves, this type of quenching is identified by the reduced antenna cross-section of PSII and the appearance of far-red fluorescence ascribed to LHCII aggregates. The zeaxanthin-dependent mechanism, in contrast, is characterized by faster fluorescence decay in PSII and is interpreted as quenching of the antenna complexes still attached to the supercomplex (Jahns and Holzwarth, 2012).

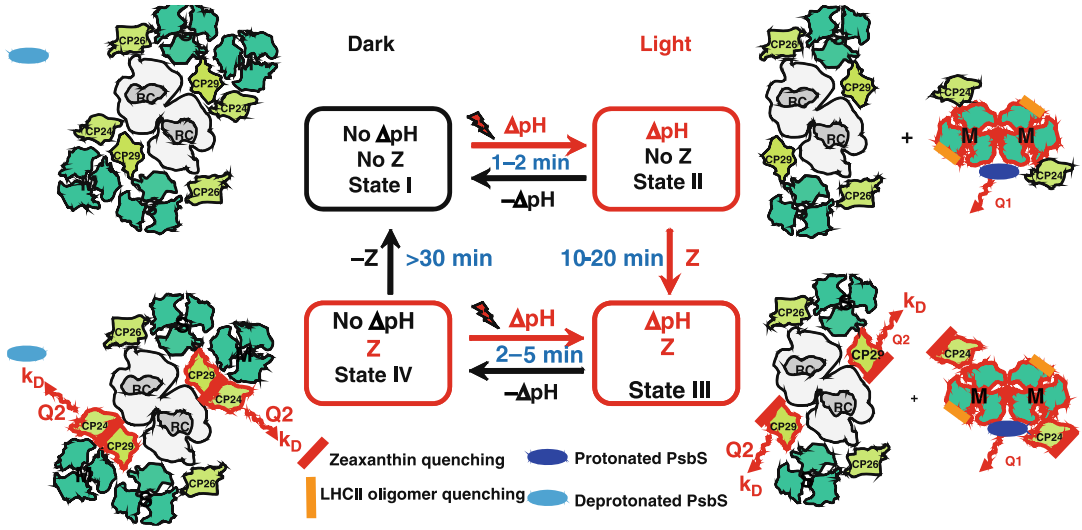

Figure 2.13. The 4-state 2-site quenching model for NPQ in plants. Left part : dark-adapted state (top) and slowly relaxing state (bottom). Right part : states appearing upon actinic light adaptation or NPQ induction. Four states are indicated in boxes. Right-hand side : The blue oval represents protonated PsbS. The model shown indicates that protonated PsbS may be associated with the detached and quenched LHCII aggregate. S and M denote the strongly and moderately, respectively, coupled LHCII trimers in the PSII–LHCII supercomplex. Reproduced from Holzwarth and Jahns (2014). © Springer

A recent study of an Arabidopsis mutant devoid of minor antenna complexes (NoM) confirmed the formation of far-red states under NPQ in the trimeric LHCII and showed the dependence of quenching on lutein in the minor but not in major LHCII (Dall'Osto et al., 2017). However, the NoM mutant also showed that quenching in the major LHCII strongly depends on zeaxanthin.

3. AIMS

The work summarized in the present dissertation aimed at elucidating the structure-function relationships in LHCII that endow it with a functional flexibility and the ability to regulate the energy flow to PSII and PSI. The main objectives of the research were:

1. To uncover the effects of the molecular environment and intermolecular interactions of LHCII on the Chl excited-state properties and excited-state dynamics of the complex.

It is known that the primary light-harvesting function of LHCII can be tuned by intermolecular interactions and it is proposed that the activation of NPQ involves some kind of conformational switch in the complex (Ruban et al., 2007). By systematically altering the molecular environment of isolated LHCII and observing spectroscopic parameters indicative of conformational and functional changes, we aimed to find clues on the mechanisms of control of the LHCII function.

2. To reveal molecular and physical mechanisms governing excitation quenching in LHCII in relation with NPQ in vivo.

The physical mechanism of NPQ is not known (see 2.5.2), although there is no lack of different proposed mechanisms and experimental evidence supporting them. One of the candidate mechanisms involves the formation of Chl-Chl CT states in LHCII. We aimed to find conditions where these states can be detected in vivo and in vitro and elucidate their connection with NPQ.

3. To gain insight into the excitonic structure of LHCII, connecting molecular structure with photophysical function.

Presently there are several different models regarding the Chl excited-state energies of LHCII (2.3.2), which determine energy transfer cascade in the complex. Optical spectroscopy experiments using new approaches such as ACD spectroscopy, combined with theoretical modelling, aimed to better characterize the Chl excited states in LHCII, their dynamics, and identify specific contributing Chls.

4. To gather detailed knowledge on the dynamics of EET within LHCII and between different complexes in the thylakoid membrane, that can further our understanding of the kinetic limitations of light harvesting.

Native photosynthetic membranes are densely packed with pigment–protein complexes that enables long-range energy transport. We used native and reconstituted LHCII-containing membranes and aggregates to determine the limitations of energy transfer, the so-called functional domain size, and the efficiency of energetic coupling between LHCII and PSI.

4. MATERIAL AND METHODS

4.1. Sample preparation

Plant material

Arabidopsis (*Arabidopsis thaliana* ecotype Columbia 0) wild-type and mutant plants were grown for 5–6 weeks on soil at a light intensity of 100–150 µmol photons m^{-2} s^{-1} and temperature of 20°C under long-day conditions (14 h of light/10 h of dark). The following mutants were used: *npq1*, defective in the violaxanthin deepoxidase; *npq2*, defective in the Zx epoxidase (Niyogi et al., 1998) ; *npq4*, PsbS deficient (Li et al., 2000); *L17*, PsbS overexpressing (Li et al., 2002); and *stn7*, defective in the LHCII kinase (Bonardi et al., 2005).

Pea (*Pisum sativum*) plants were grown for 2 weeks in the greenhouse on soil.

Fresh spinach was obtained from the local market.

Thylakoid membranes

TM were isolated from pea or spinach leaves, as indicated. Leaves were homogenized in ice-cold homogenization (20 mM Tricine (pH 7.5), 400 mM sorbitol, 5 mM $MgCl_2$, 5 mM KCl) and filtered through four layer of cheesecloth and centrifuged at 200×g for 2 min to remove the remaining debris. The supernatant was then centrifuged at 4000×g for 5 min. The pellet was resuspended in osmotic-shock buffer (20 mM Tricine, 5 mM $MgCl_2$, 5 mM KCl, pH 7.5), mixed and centrifuged at 7000×g for 5 min. The final pellet was resuspended in homogenization buffer to a Chl concentration of 5–7 mg/ml. Un-stacked (washed) TM were prepared by repeatedly resolubilizing in washing buffer (20 mM Tricine, pH 7.5) and centrifuging at 7000×g for 5 min.

LHC-enriched membranes

Lincomycin was used to block the synthesis of photosystem core proteins and stimulate the formation of TM enriched with LHCII and LHCI. Etiolated pea seedlings were grown hydroponically in ¼ strength Knop's solution (6.1 mM $Ca(NO_3)_2$, 1.8 mM KH_2PO_4, 2.1 mM $MgSO_4$, 1.7 mM KCl, $FeCl_3$, pH 6.5) in darkness. Lincomycin (250 mg/l) was added to the growth medium on the 7th day and after 8 h incubation the plants were exposed to

low light for three days. The greened leaves had Chl *a*/*b* ratio of 2.0 (sd < 0.1). TM were isolated according to the protocol described above.

Isolation of PSII-enriched membranes

PSII-enriched membrane fragments (BBYs) were isolated from pea seedlings or market spinach, as indicated, following the protocol of Dunahay et al. (1984).

Isolation of LHCII

LHCII was isolated by using PSII-enriched membrane fragments as a starting material following the protocol of Caffarri et al. (2001) with small modifications. The BBYs were resuspended in washing buffer (20 mM Tricine, pH 7.8) at concentration of 0.5 mg/ml Chl and solubilized by incubating with 0.7% of *n*-dodecyl-α-maltoside (α-DDM) or *n*-dodecyl-β-maltoside (β-DDM) in darkness for 15 min on ice with continuous stirring. The suspension was then centrifuged at 10000×g for 15 min and the supernatant was loaded on the gradients, prepared by freezing and slowly thawing a solution of 0.4 M sucrose in 5 mM Tricine buffer with 0.06% detergent. The samples were centrifuged in a swing-out rotor at 200,000×g for 18 h. Gradient bands containing the LHCII trimers were collected, concentrated with 30 kDa cutoff filters (Amicon, Millipore) and stored at −80 °C until use.

LHCII aggregates

LHCII aggregates were prepared by removing the detergent from solubilized LHCII using absorbing beads (Bio-beads SM4, Bio-Rad). The LHCII solution was diluted in washing buffer to concentration of 10–20 μg/ml Chl and incubated with 80–100 mg/ml Bio-Beads in dark for 2 h at RT with continuous stirring and decanted after sedimenting the beads. Lamellar macroaggregates were prepared from spinach leaves according to Simidjiev et al. (2011).

Detergent washing

To remove the detergent from LHCII without allowing any protein aggregation, LHCII trimers were trapped in polyacrylamide gel according to Ilioaia et al. (2008). Strips of 1.5 mm thickness, containing the detergent–LHCII solution and 6% acrylamide:bis-acrylamide (30:1), were polymerized with 0.1% ammonium persulfate and 0.1% N,N,N′,N′-tetramethylethylenediamine (TEMED). To remove the detergent, the gel strips were

incubated in 1000 volumes of washing buffer for 2 h under vigorous shaking. For control experiments, washed gels were incubated in washing buffer with 0.03% β-DDM.

Isolation of PSI

PSI-enriched stromal membrane vesicles were isolated from pea leaves by digitonin digestion of TM followed by differential centrifugation as in Peters et al. (1983). The preparations, with Chl *a*/*b* ratio of 9–10, were resuspended at concentration of 1 mg/ml Chl and solubilized by incubating with 1% β-DDM for 20–30 min. The unsolubilized material was removed by centrifugation at 10000×g for 15 min. The supernatant was then loaded on a 0.1–1 M sucrose density gradient and centrifuged in a swing-out rotor at 200,000×g for 18 h. The green bands containing PSI–LHCI complexes were collected, concentrated with Amicon filters (Millipore), frozen in liquid N_2, and stored at −80 °C until use. The purity of the samples was confirmed by SDS-PAGE / immunoblotting.

Preparation of proteoliposomes

Reconstitution of LHCII membranes was carried out by following standard protocols (Moya et al., 2001; Yang et al., 2006). Large unilamellar lipid vesicles (liposomes) were prepared from egg phosphatidylcholine (PC), or mixtures of plant thylakoid lipids: 50.0% (w/v) MGDG, 31% DGDG, 10.7% PG and 8.3% SQDG. The solvent from the lipid mixture was slowly dried in a vacuum rotary evaporator to form a thin film of lipids on the wall of a round-bottom glass vial. After completely drying the solvent, the lipid film was hydrated with reconstitution buffer (10 mM NaCl, 10 mM Tris/HCl, pH 7.8) to a total lipid concentration of 5 mg/ml. The suspension was vortexed for approximately 40–50 min and subsequently subjected to ten freeze-thaw cycles. Large unilamellar vesicles were formed by extruding the suspension through a 100-nm-pore membrane (Avanti Polar Lipids, USA). The preformed liposomes were then destabilized by adding 0.05% β-DDM. LHCII-detergent solution was added dropwise to the liposome suspension to the desired lipid/protein (L/P) ratio. For LHCII liposomes, the L/P ratio was estimated taking into account that LHCII contains 14 Chls per monomer. For preparing PSI–LHCII membranes, purified solubilized LHCII and PSI–LHCI were mixed at molar Chl ratios of LHCII:PSI equal to 0.26, 0.52 and 0.78 — equivalent to approximately one, two and three LHCII trimers per PSI, respectively. In this case, the L/P ratio was calculated (450:1) taking into consideration only PSI–LHCI Chls. The lipid–protein mixture was then

incubated at RT for 30 min in dark. The detergent was then removed by repeated incubation with absorbent beads (Bio-Beads SM2, Bio-Rad).

To determine the L/P ratios of the reconstituted proteoliposomes, the lipophilic fluorescent dye DiI (DiIC18(3) or 1,1′-dioctadecyl-3,3,3′,3′-tetramethylindocarbocyanine perchlorate, Invitrogen, USA) was added at a lipid:DiI ratio of 125:1 to the lipid mixture. Proteoliposome fractions of different density and L/P ratios were separated by density gradient ultracentrifugation. Discontinuous (step) gradients were prepared by adding 2 ml layers of 7, 14, 21, and 28% Ficoll PM-400 (GE Healthcare, USA) dissolved in reconstitution buffer. The proteoliposome sample was loaded on the gradient and centrifuged for 18 hours at 200,000×g, 4°C. Four to five coloured band fractions of different densities were collected.

The molar concentration of Chl (*a*+*b*) and DiI in the LHCII proteoliposome fractions was estimated from the measured absorbance at 553 nm (DiI absorption maximum) and 674 nm (Chl absorption maximum). Absorption spectra of DiI-liposomes and LHCII-liposomes (without DiI) of known concentration were used as reference. The L/P ratio was then calculated assuming a fixed lipid/DiI and Chl/LHCII ratios (125 and 14, respectively).

4.2. Steady-state spectroscopy

Absorption and circular dichroism spectra

Absorption and CD spectra in the range of 350–750 nm were recorded at RT with a Thermo Evolution 500 dual-beam spectrophotometer and a J-815 (Jasco, Japan) or a Chirascan (Applied Photophysics, UK) spectropolarimeter. The measurements were performed in a standard glass cell of 1-cm optical path length with 1 nm (absorption) or 2 nm (CD) spectral bandwidth. Samples were diluted to an absorbance of one at the red maximum

Anisotropic circular dichroism spectra

Anisotropic circular dichroism (ACD) spectra were recorded from macroscopically aligned samples. Different methods for achieving sample orientation were used, depending on the type of material — magnetic alignment, polyacrylamide gel compression or surface supported drying. TM were oriented by placing the sample in a magnetic field

(1.5 T) parallel to the measuring light. Lamellar LHCII macroaggregates and LHCII membranes were aligned by polyacrylamide gel compression as in ref (Miloslavina et al., 2012) or by drying the vesicles on a quartz surface under N_2 gas (Akhtar et al., 2019). The gel containing 5% acryla-mide:bis-acrylamide (30:1) was polymerized with 0.2% ammonium persulfate and 0.2% TEMED on ice. The polymerization time was about 15–20 min. The orientation was then done by compressing the gel along one dimension while allowing it to expand along the other two dimensions. The compression factor was 1.6, causing the vesicles' diameter to squeeze to half of the original size. The latter method promotes vesicle fusion into planar bilayer membrane patches. ACD was measured in face-aligned direction, with incident light parallel to the axis normal to the membrane plane.

Synchrotron-radiation CD spectra

UV CD/ACD measurements were performed at the Diamond Light Source B23 Beamline for synchrotron radiation circular dichroism (SRCD). SRCD spectra were measured under N_2 atmosphere at RT in the range 180–260 nm. Liquid suspension samples were placed in quartz cells with optical path length of 0.2 mm. For the UV ACD measurements, the quartz plates with membrane patches were mounted on a motorized translating stage (Lincam). The vertical probe beam was focused onto the plate with a microscope objective. In this way, an area of up to 25 mm^2 was scanned, sampling the CD spectra from different spots spaced 1 mm apart.

Low-temperature fluorescence spectra

For measurements at low temperature, diluted samples were deposited on Whatman glass fibre discs to ca. 0.5 µg Chl cm^{-1}. The filters were then immersed in liquid nitrogen and transferred to a Dewar vessel filled with liquid nitrogen that was placed into the measurement chamber of a Fluorolog spectrofluorimeter (Jobin Yvon Horiba). Fluorescence emission spectra from 600 to 800 nm were recorded with excitation wavelength of 436 nm and 3 nm detection bandwidth. Measurements were taken with 1 nm increment and 1 s integration time.

Chl a fluorescence induction kinetics

For measuring spectral changes associated with the activation of NPQ, a special dual LED spectrofluorometer was devised (Lambrev et al., 2010). Briefly, two LEDs are

focused onto a detached leaf – one (red-emitting) is used as continuous actinic light for the induction of NPQ and the other (blue-emitting) provided periodic short pulses used at the same time to close the RCs and as excitation source. The fluorescence excited by the blue LED is passed through a long-pass filter and detected by a CCD spectrometer (USB2000, Ocean Insight, USA), synchronized with the LED pulses. After switching off the actinic light, the relaxation of NPQ is monitored intermittently applying blue pulses only.

4.3. Time-resolved spectroscopy

Time-resolved fluorescence spectroscopy

Fluorescence decays were recorded at RT by time-correlated single-photon counting (TCSPC) using a FluoTime 200 instrument (PicoQuant, Germany) equipped with a microchannel plate detector (Hamamatsu, Japan) and a PicoHarp 300 TCSPC system (PicoQuant). The source of excitation is a Fianium WhiteLase Micro (NKT Photonics, UK) supercontinuum laser which provides white-light pulses with 6 ps temporal width at a repetition rate of 20 MHz. The excitation wavelength is 632 nm for all experiments which is selected by bandpass filter. Fluorescence emission was detected through a computer-controlled monochromator at wavelengths between 670 and 750 nm and binned in a 4 ps time channels. The sample was continuously circulated through a flow cell with 1.5 mm path length. The optical density at the excitation wavelength was 0.03. The instrument response function (IRF) was measured under the same optical conditions as the investigated fluorescent sample using 1% Ludox (colloidal silica) as scattering medium. The total width of IRF was 40–50 ps at the excitation wavelength.

For estimating the functional domain size of LHCII aggregates the fluorescence decays were recorded by using a TCSPC setup with 16 wavelength channels (PML 16-C and SPC-530, Becker & Hickl, Germany). The fluorescence was excited by ps pulses from a 632 nm diode-laser (BHL-635, 1 pJ pulse energy, 20 MHz repetition rate, ~65 ps FWHM) or 405 nm excitation laser pulses (BHL-405, PicoQuant, Berlin, 8 MHz repetition rate, ~60 ps FWHM). The fluorescence was detected at multiple wavelengths in the range of 600–800 nm simultaneously. The decays for each wavelength channel were stored in 10 ns time window. The optical density was 0.2 at excitation wavelength. The measurements were performed at 20 °C in a glass cuvette of 1 cm optical pathlength in a thermostated

cuvette-holder. The IRF was measured using distilled water containing 0.2% milk as scattering medium.

Fluorescence decays collected at different detection wavelengths were analysed by a global lifetime fitting routine using a kinetic model and convolution with the measured IRF. Kinetic models were either sums of exponential decays (global analysis) or compartment models (target analysis). The fitting algorithm, written in MATLAB, minimized the squared sum of residuals weighted by the Poisson distribution. The method of variable projection was employed, wherein rate constants (lifetimes) were global nonlinear fit parameters and amplitudes (spectra) were wavelength-dependent linear least-squares fit parameters (van Stokkum et al., 2004).

Two-dimensional electronic spectroscopy

The 2DES measurements were performed at RT and 77 K using a femtosecond laser system in a partially collinear pump–probe beam geometry setup producing absorptive 2D spectra. Excitation pulses of 30–55 fs (as indicated) were obtained by passing the output of an amplified Ti:sapphire laser system (Legend, Coherent) through a lab-built optical parametric amplifier or a non-collinear optical parametric amplifier (TOPAS, Light Conversion). Pulse pairs with controllable inter-pulse delay time and phase difference were generated with an acousto-optic programmable dispersive filter (AOPDF) pulse shaper (Dazzler, Fastlite) that was also used as a secondary compressor to pre-compensate for dispersion. The compressed shaped pump pulses were attenuated to the required energy per pulse and excitation wavelength. White-light supercontinuum pulses generated in a 2-mm sapphire window were used as the third interaction pulse (probe/detection). When using the TOPAS output (producing pulses of shorter duration), the dispersion of the probe pulses was compensated using chirp mirrors. The probe polarization was 54.7° with respect to the pump. Scattered light from the pump pulses was detected, and corrected for, by placing an optomechanical chopper on the probe path. The probe beam was further split into signal (overlapped with the pump) and reference and measured with a spectrometer resolving the signal in detection wavelength (λ_t). The cross-correlation width of the excitation and probe pulses was 40–70 fs FWHM, determined by measuring the optical Kerr effect.

The time delay τ between the two excitation pulses was scanned between 0 and 150 fs with 3-fs steps for RT measurements and between 0 and 300 fs with 5-fs steps for 77 K measurements applying a 2-phase cycling scheme ($\varphi = 0; \pi$) in a partially rotating frame of reference (Zhang et al., 2012). The signals (2D interferograms) were Fourier-transformed along τ to obtain 2D electronic spectra in the frequency/wavelength domain (with excitation/detection wavelengths λ_τ/λ_t). The waiting time (T_w) between the excitation and probe pulses was scanned from –100 fs up to 800 ps in a quasilogarithmic progression. For every $\tau/\varphi/T_w$ combination, 4000–10000 laser shots were recorded and averaged to achieve signal-to-noise ratio higher than 100 (>20 dB). Data processing and analysis was done in MATLAB.

5. STRUCTURAL AND FUNCTIONAL PLASTICITY OF LHCII

5.1. Exciton state changes in LHCII in different molecular environments

5.1.1. CD spectral changes induced by detergents and protein interactions

Differences in the CD spectra of aggregated and solubilized LHCII

The function of LHCII is regulated by interactions with its molecular surroundings – for example NPQ is controlled by lumenal pH, zeaxanthin and the PsbS protein and possibly involves a change in LHCII-LHCII interactions (Holzwarth et al., 2009). There is an ongoing debate whether, and to what extent and what nature of conformational changes are involved in these processes (Ruban et al., 2007). In vitro, LHCII has a strong propensity to aggregate in the absence of surfactants, whereupon the fluorescence yield is substantially reduced (Ruban and Horton, 1992; Ruban et al., 2007; Miloslavina et al., 2008), in contrast to the high yield when it is solubilized in detergent micelles. The quenching in LHCII aggregates has been studied as a model of NPQ and has inspired the hypothesis that NPQ in vivo involves aggregation of LHCII in the TM (Horton 1991, 2005).

The aggregated and solubilized state of LHCII *in vitro* show clear differences in resonance Raman spectra (Ruban and Horton, 1995; Ruban et al., 1995; Ruban et al., 2007) signifying alterations in protein conformation. Aggregates are also readily distinguished by the excitonic CD spectra (Ruban et al., 1997; Lambrev et al., 2007). When comparing the CD spectra of LHCII aggregates, solubilized trimers and TM, we observed that aggregates appear more similar to the native state despite their low fluorescence yield, whereas detergent solubilization of either LHCII or native TM induced specific spectral changes (Lambrev et al., 2007). We thus proposed that the fine structure and pigment excitonic interactions are perturbed by the detergent. There could be several reasons for the witnessed CD changes – disrupted pigment–pigment interactions between complexes, changes in the conformation of the complexes due to the disrupted protein–protein or lipid–protein interactions, or changes directly induced by the detergent molecules. We then carefully investigated the exact CD changes occurring when LHCII is transferred from one molecular environment to another aiming to separate the changes appearing

due to LHCII-LHCII interactions from those brought about by the artificial surfactants or lipids (Akhtar et al., 2015).

The CD spectra of LHCII solubilized with α-DDM or β-DDM and of aggregates, obtained by removing the detergent from the medium, are shown in Figure 5.1. The CD spectrum of LHCII has a characteristic negative-positive-negative band sequence in the red region, associated with the Q_y exciton states of Chl *b* and *a*. In the blue region, the spectra have a more complex structure, owing to the multitude of Chl and Car transitions.

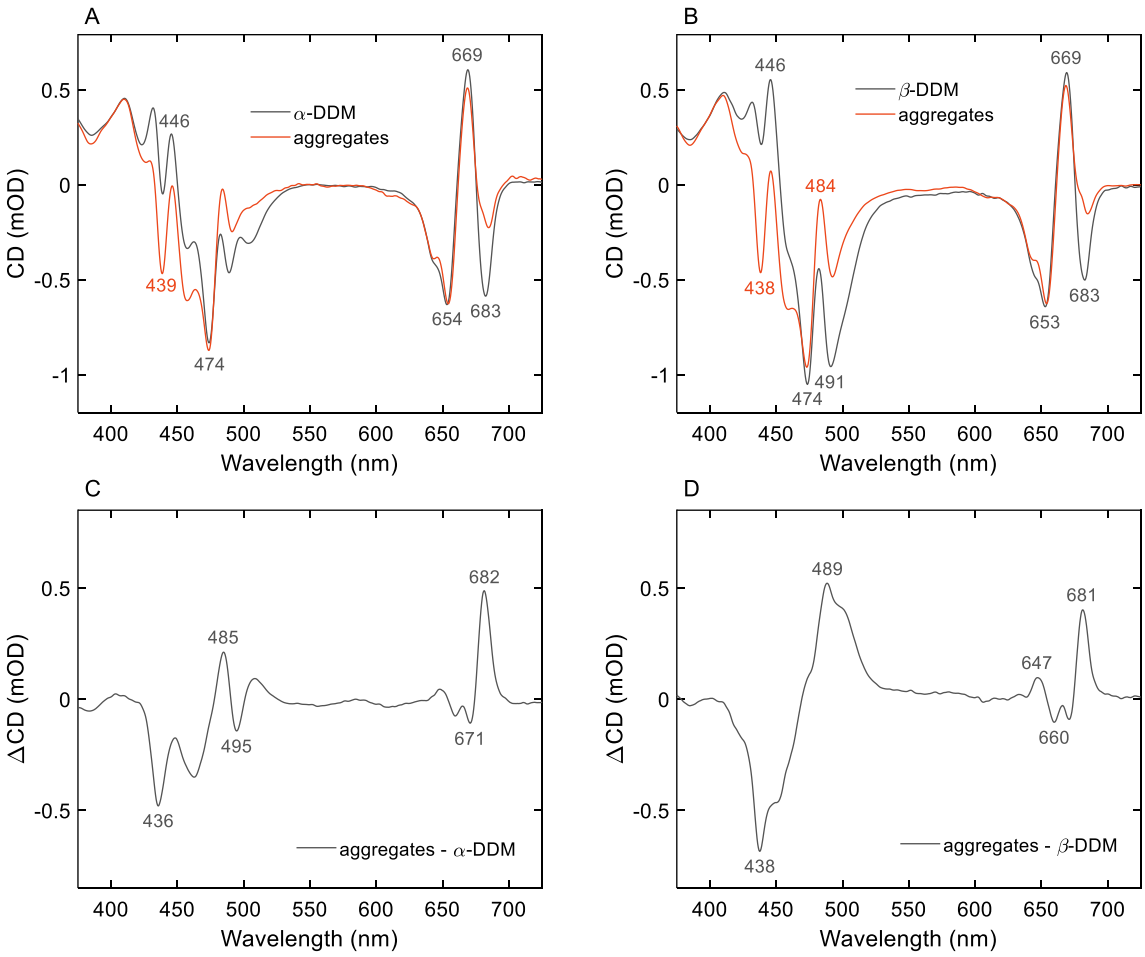

Figure 5.1. Comparison of the CD spectra of LHCII trimers and aggregates. A. CD spectra of LHCII trimers solubilized in α-DDM and of aggregates; B. CD spectra of LHCII trimers solubilized in β-DDM and of aggregates; C-D. CD difference spectra (aggregates minus trimers). Adapted from Akhtar et al. (2015).

The spectrum of LHCII in β-DDM micelles additionally has a strong negative peak at 492 nm, which is the most prominent difference between the two DM isomers. Removal of the detergent, regardless of the isomer used, led to distinctive changes in the CD

spectra – most notably, an increase of the (–) 438 and (+) 484 nm bands and a decrease of the (–) 683 nm band.

Separating detergent and protein interactions

By comparing aggregated and detergent-solubilized LHCII, it cannot be distinguished whether the spectral changes are due to the loss of protein–protein interactions or brought about by the detergent environment. To separate these two effects, we fixed LHCII in polyacrylamide gel slabs, allowing us to wash the detergent while keeping the proteins from aggregating (Ilioaia et al., 2008). By comparing the CD spectra of the LHCII in gels soaked in detergent and in washed detergent-free gels (Figure 5.2A), the effects of the detergent alone can be identified. It is evident that β-DDM is responsible for the (–) 492 nm band but it has no effect on the (–) 436–438 and (+) 482–484 nm bands. Enhancement of the latter two bands is clearly a signature of aggregation, or "protein interactions", as can be seen in the comparison of aggregates in solution and trimers in detergent-free gel (Figure 5.2A).

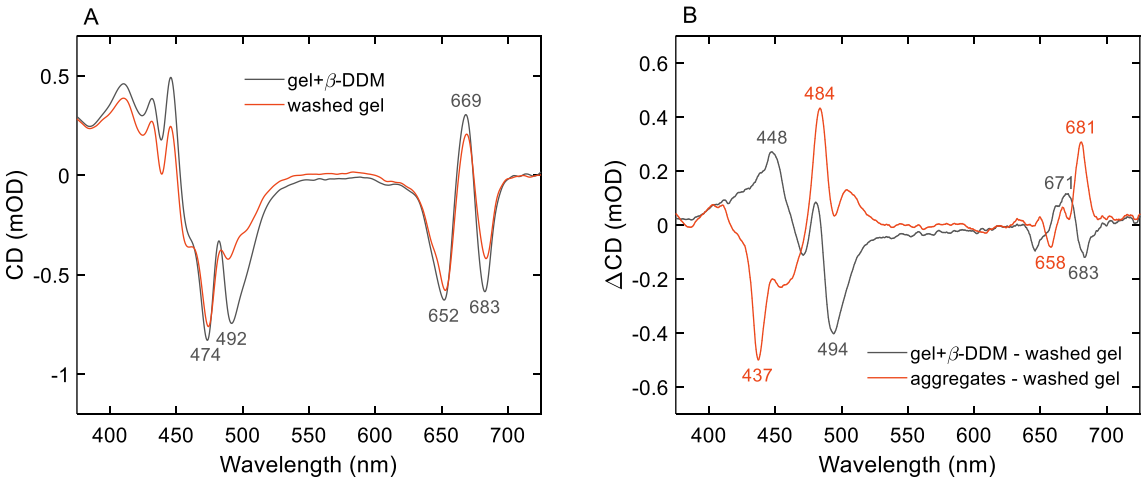

Figure 5.2. Separation of the effects of detergent and protein interactions on the CD of LHCII. A. CD spectra of LHCII trimers in polyacrylamide gel soaked in 0.03% β-DDM and washed without detergent. B. CD difference spectra of gel with and without β-DDM and of aggregates and washed gel.

Thus, the two difference spectra show separately the effects of aggregation and of the detergent (β-DDM. It is possible that the aggregation-specific bands originate from excitonic couplings between pigments bound to different interacting protein subunits. On the other hand, the detergent-specific spectral changes must reflect protein conformational changes brought by the detergent environment. In that case, however, LHCII-detergent micelles are indeed a flawed representation of the native state of the complex,

with detectable differences in the exciton landscape and likely the functionality. It is worth mentioning that the 492 nm spectral change induced by β-DDM is most likely associated with an altered conformation of the Car neoxanthin, since this CD band is suppressed when neoxanthin is absent (Akhtar et al., 2015).

5.1.2. Excitonic CD of LHCII in native and reconstituted membranes

Native LHCII-enriched thylakoid membranes

Earlier we observed that the excitonic CD spectra of lamellar LHCII aggregates bear strong resemblance to those of chloroplast TM and hypothesized that the protein conformation and pigment interactions are retained while differences were attributed mainly to the presence of PSI and PSII core complexes (Lambrev et al., 2007). To test this hypothesis further, we isolated LHCII-enriched TM from pea seedlings treated with lincomycin, which blocks the synthesis of the chloroplast-encoded core complex proteins. The CD spectra of the membranes (Figure 5.3) were very similar to the spectra of LHCII lamellar aggregates. Moreover, solubilization with β-DDM introduced identical spectral changes as in the LHCII aggregates (cf. Figure 5.3B and Figure 5.1B). This finding reveals that whatever structural, protein interactions or inter-complex excitonic couplings are responsible for the aggregation-specific CD features, the same are also present in the native membranes.

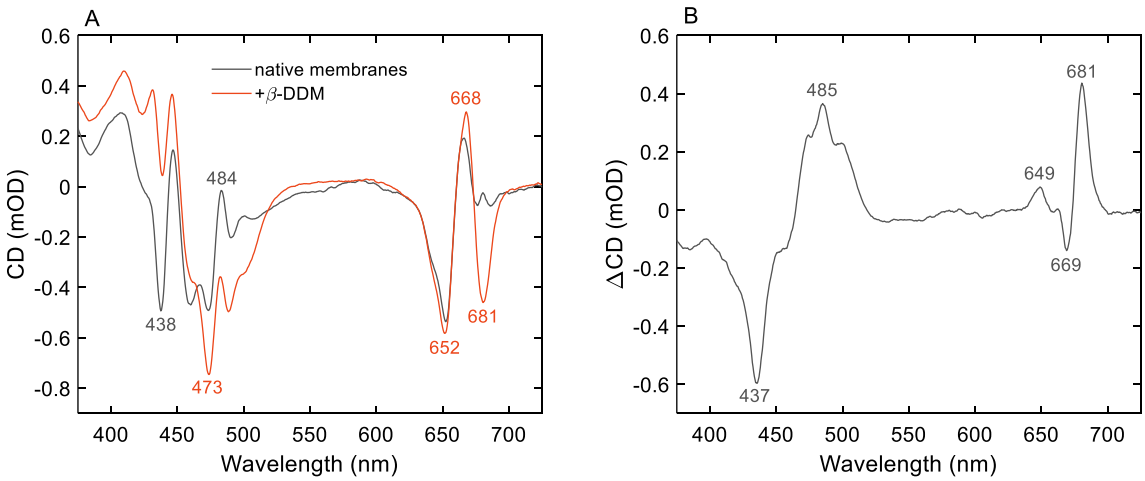

Figure 5.3. CD spectra of thylakoid membranes (native LHCII-enriched membranes) isolated from lincomycin-grown pea leaves. A. Membranes resuspended in 20 mM Tricine buffer and solubilized with 0.1% β-DDM; B. CD difference spectrum, unsolubilized minus solubilized.

Reconstituted LHCII-lipid membranes

To test the effects of lipids and to separate CD spectral changes due to specific protein–protein interactions in the membrane, we recorded CD spectra of LHCII reconstituted into artificial lipid membranes. Reconstituted LHCII membranes (proteoliposomes) and protein–lipid aggregates have been investigated to determine interprotein connectivity and protein–lipid interactions under various conditions (Zhou et al., 2009; Schaller et al., 2011; Wilk et al., 2013). The advantage of using liposomes is their flexibility; they permit the analysis of the characteristic of the antennas by varying lipid and protein composition (Yang et al., 2006) and L/P ratio (Zhou et al., 2009; Crisafi and Pandit, 2017).

We used either natural or synthetic PC or a mixture of native thylakoid lipids (MGDG, DGDG, SQDG and PG), and LHCII membranes were made at different L/P ratios. The morphology of the reconstituted LHCII:PC membranes is revealed by freeze-fracture electron microscopy. Spherical vesicles are typically observed with typical sizes of several hundred nm (Figure 5.4). The fractured membrane surface is patchy; the closely packed small entities — with a characteristic size of ca. 20 nm — evidently represent the embedded protein complexes.

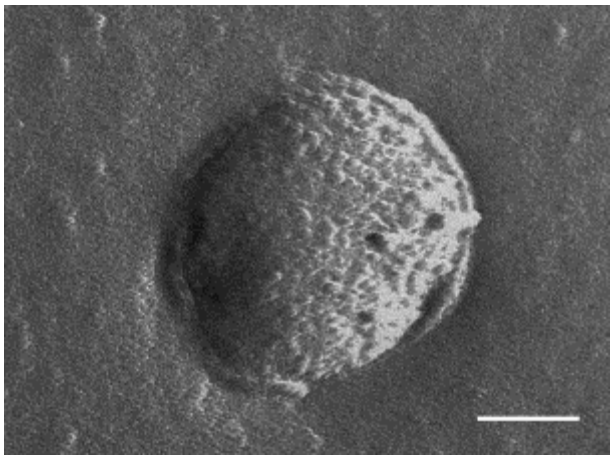

Figure 5.4. Representative freeze-fracture transmission electron microscopy image of LHCII:PC membranes reconstituted at L/P ratio of 300:1 and purified by sucrose density gradient ultracentrifugation. The scale bar corresponds to 200 nm.

The CD spectra of reconstituted LHCII membranes (Figure 5.5) were very similar to those published by other groups (Moya et al., 2001; Yang et al., 2006). A comparison of the membranes with LHCII in detergent-free gel (cf. Figure 5.2) induced spectral changes at 476–478 nm and 492–494 nm. Interestingly, the strong (–)492 nm band characteristic for β-DDM-solubilised trimers is also present in all lipid membranes. This

indicates that lipids and β-DDM create similar kind of environment for the excitonic interaction contributing to this band. It is also of note that the specific aggregation signatures at (+)484 nm and (−)437 nm were not observed in the membranes. The largest-amplitude difference in the CD of membranes compared to trimers — at 475–478 nm (Figure 5.5b) — is of a different origin than the aggregate-specific band at 484 nm. The likely reason for the decrease of 474 nm band is the monomerization of trimers upon incorporation into liposomes. Natali *et al.* (2016) have recently found similar changes in the CD spectra of LHCII reconstituted into liposomes. This effect is unexpected as LHCII trimers are very stable even in detergent environment (Croce et al., 1999), and it has been shown that trimerization is favoured by the presence of lipids (Hobe et al., 1994). Reconstitution with different lipids, including native thylakoid lipids, and with different intermediate detergents, resulted in essentially the same CD spectra.

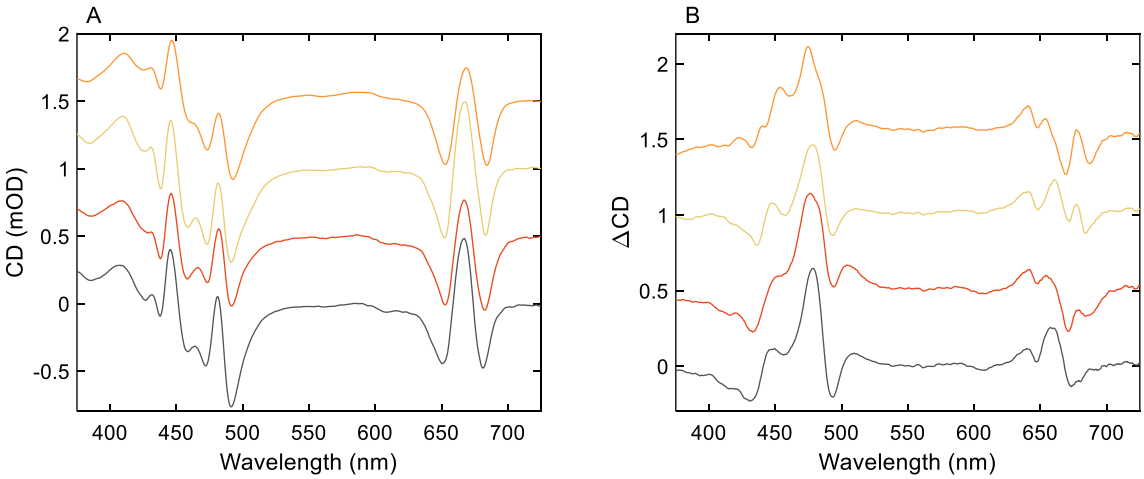

Figure 5.5. Comparison of CD spectra of LHCII reconstituted into lipid membranes. A. LHCII:DMPC membranes (gray curve), LHCII:PC membranes (red curve), LHCII:native thylakoid lipids membranes (golden and orange curves). The CD spectra are normalized to the absorbance at 675 nm. B. CD difference spectra (spectra in (a) minus "washed gel" in Figure 5.2).

Interestingly, the same CD differences at (+)448 nm, (−)494 nm attributed to the interaction of LHCII with detergent were also observed in reconstituted lipid membranes, even with native thylakoid lipids. This is somewhat surprising since the negative band was not observed in native LHCII-enriched membranes (Figure 5.3). It can be hypothesized that the protein density (number of LHCII per membrane area) and consequently interactions between complexes are different in the native and artificial membranes — this point is examined in the following section.

5.1.3. Heterogeneity of reconstituted membranes

Reconstituted LHCII-lipid membranes displayed significant variability in their CD spectra irrespective of the type of lipids used. The likely reason is that the reconstituted membranes are heterogeneous having domains or subpopulations with different structure and composition, e.g. vesicles with different sizes and L/P ratios. To test this, we fractionated the reconstituted LHCII membranes by density gradient ultracentrifugation and used a lipid marker to estimate the L/P ratios of each fraction (Tutkus et al., 2018).

Density gradients were prepared with Ficoll 400 – a high molecular weight polymer of sucrose having low osmotic pressure to keep the vesicles intact. After centrifugation, the samples separated into several bands of different color. The protein and lipid content of each separated fraction was estimated from the absorption of Chl and the lipid marker DiI, respectively, as described in Tutkus et al. (2018). The density gradients revealed a very high degree of heterogeneity in all reconstitution experiments. The distribution of LHCII among fractions of different L/P ratios is plotted in Figure 5.6 for two selected preparations. In the first preparation, containing a native-like mix of thylakoid lipids at a bulk L/P of 400:1, the majority of LHCII was found in fractions with L/P ratio of 200–300:1. In the second example, the reconstitution mixture contained in addition a very small amount (0.4 mole per cent) of biotinylated lipid (Biotin-PEG2000-PE), added to facilitate surface immobilization of vesicles for microscopy. In this case, the most abundant fraction was found with a L/P ratio of 96:1 – significantly lower than the predefined L/P ratio of 330:1.

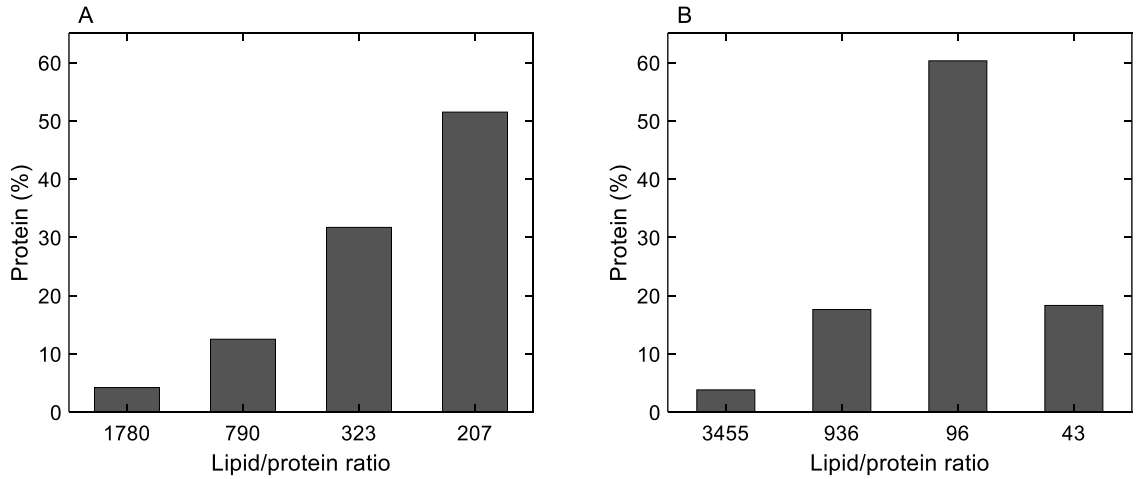

Figure 5.6. Distribution of LHCII in proteoliposome fractions of different L/P ratios. a) reconstitution mixture of thylakoid lipids with 0.8% (molar) DiI, L/P 400:1; b) reconstitution mixture of thylakoid lipids with 0.8% DiI and 0.4% Bt-PEG-PE, L/P 330. Reproduced from Akhtar et al. (2019).

The results highlight the structural heterogeneity and complexity reconstituted proteoliposomes. In such complex systems the enthalpy gains from the interactions of constituents with high affinity to each other can overcome the entropy forces that randomize and distribute them evenly. The same mechanisms of self-assembly play role in the self-organization of the native biological systems of high negative entropy. It is plausible that given the conditions and exact composition of the multicomponent system, certain structures will be thermodynamically favored, for example the formation of proteoliposomes of certain size and protein density (L/P ratios).

Our initial hypothesis was that fractions of high protein density (low L/P ratio) would exhibit aggregation-specific CD signatures. The CD spectra of separated proteoliposome fractions with different L/P ratios are shown in Figure 5.7. The CD spectra of low-density fractions with higher L/P ratios hinted at the presence of LHCII monomers, which lack the trimeric signature bands at (–)473 nm and (–)644 nm. More importantly, the aggregation-specific CD bands (e.g. at 437 nm) were not pronounced in any fraction. If present, their magnitude was definitely smaller than in lipid-free LHCII aggregates (cf. Figure 5.1) or in native LHCII-enriched membranes (cf. Figure 5.3).

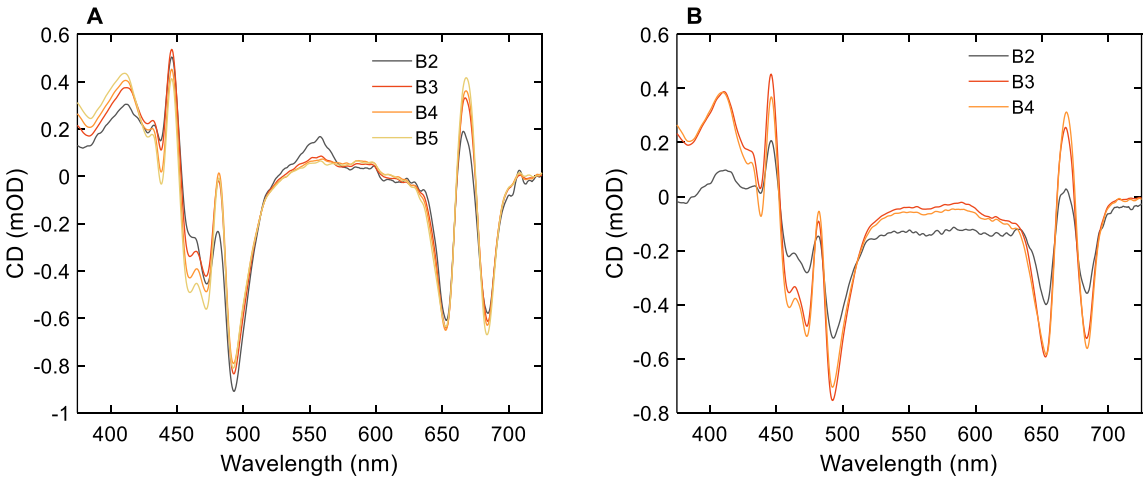

Figure 5.7. CD spectra of LHCII in proteoliposomes fractions of different density from two proteoliposome preparations. A: at initial L/P ratio of 500:1; B: at initial L/P ratio of 1000:1. The CD spectra are normalized to the absorbance at 675 nm.

The absence of the aggregation signature in the CD spectra of reconstituted membranes shows that even embedded in native lipids, LHCII can adopt different structural or macrostructural states where protein interactions cause the formation of different exciton states altering the energy landscape and the EET pathways in the complex.

5.2. Far-red-emitting states and fluorescence quenching

5.2.1. The excitation lifetime of LHCII depends on the environment

The molecular environment has a profound effect on the functionality of LHCII by modulating the excitation lifetime. The excitation lifetime is a defining characteristic of a light-harvesting antenna – the longer it is, the more likely it is that energy can migrate onward to be used for photochemistry and vice versa – short excitation lifetimes mean that energy is lost via nonphotochemical decay pathways. The fluorescence lifetime of detergent-solubilized LHCII is about 4 ns, whereas in membrane environment it can be significantly shorter (Figure 5.8). Complete removal of the detergent from the suspension and aggregation shortens the lifetime by up to 20-fold (Horton et al., 1991; Miloslavina et al., 2008).

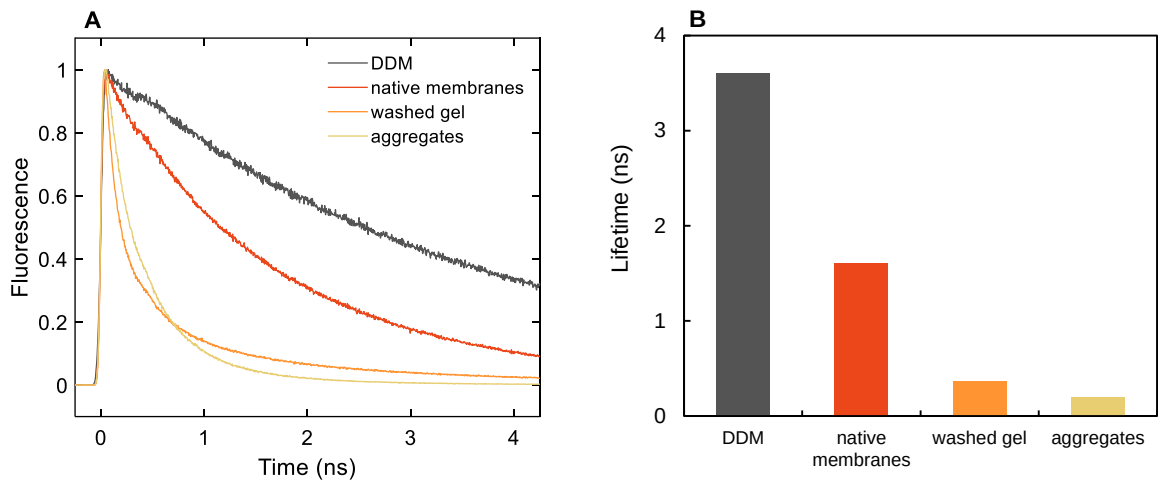

Figure 5.8. Fluorescence decays and lifetimes of LHCII in different environments. A. Picosecond fluorescence decay kinetics recorded at emission wavelength 680 nm; B. Average fluorescence lifetimes calculated from multiexponential fits of the decays

The ability of LHCII to adjust its excitation lifetime is thought to be essential for the short-term adjustments of the excitation energy flow in response to the fluctuating light conditions (Muller et al., 2001; Horton, 2012). It was initially believed that the mechanism of quenching is similar to concentration quenching of dense Chl solutions (Beddard and Porter, 1976). However, quenching is induced to a comparable magnitude even in washed gels where aggregation is averted (Ilioaia et al., 2008). Another postulation with ample experimental evidence is that conformational changes induced by aggregation, among other possible factors, switch from the functional to the quenched state (Horton et al., 2005; Pascal et al., 2005; Ruban et al., 2007). Indeed, in the previous section it was shown

that aggregation is accompanied by changes in the pigment exciton interactions that are consistent with protein conformational changes. It would be informative to link the excitonic changes detected by CD with fluorescence quenching. However, no such relationship was observed. Fluorescence quenching could be triggered effectively without aggregation in washed gels (Figure 5.8), which do not exhibit the specific CD signatures of aggregates (Figure 5.2). Conversely, native LHCII-enriched membranes showed pronounced aggregation-related CD bands (Figure 5.3) but relatively long fluorescence lifetimes. We can conclude that any structural changes affecting the CD signals in the spectral region of Cars are not the ones responsible for fluorescence quenching. Therefore, different spectroscopic tell-tale signs of the quenching mechanism must be sought.

5.2.2. Far-red-emitting states associated with quenching

A characteristic feature of the quenched LHCII aggregates is the appearance of a fluorescence band detectable in the far-red region (700 nm and above) at 77 K reported first by Horton and Ruban (1992; 1994). A more detailed time-resolved fluorescence study revealed similarities in the far-red emission from LHCII aggregates and from plant leaves pre-exposed to strong irradiance to induce NPQ (Miloslavina et al., 2008). This suggested that the same mechanism of quenching occurs in vitro and in vivo and that the far-red emission is closely associated with it. The far-red emission was ascribed to a Chl-Chl CT state mixed with an exciton state (Kell et al., 2014; Wahadoszamen et al., 2014).

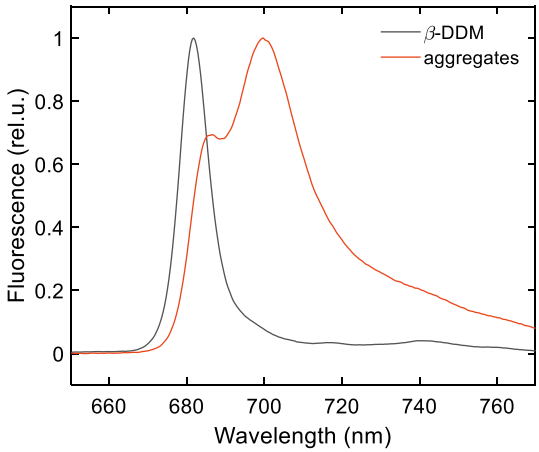

Figure 5.9. Fluorescence emission spectra of Arabidopsis LHCII solubilized in β-DDM and LHCII aggregates, recorded at 77 K. The spectra are normalized to the maximum. A very broad peak at 700 nm ascribed to a Chl-Chl CT state dominates the emission of aggregates. (Miloslavina et al., 2008)

Recently, the fluorescence decay kinetics of LHCII aggregates as well as quenched crystals recorded at temperatures as low as 4 K have revealed the existence of multiple far-red-emitting states with different emission maxima in the range 690–740 nm in both types of samples but no such low-lying states have been found in unquenched LHCII (Ostroumov et al., 2020). The low-temperature fluorescence kinetics could be described by a sequential kinetic model (Figure 5.10) whereby the initial Chl excited states are trapped by low-energy CT states before decaying to the ground state. Previously it had been shown that the far-red-emitting states have a long fluorescence lifetime and had been postulated that they are irrelevant to the quenching mechanism (Chmeliov et al., 2016; Gelzinis et al., 2018). In contrast, the sequential model of the low-temperature fluorescence kinetics explicitly defines the CT states as directly responsible for the quenching.

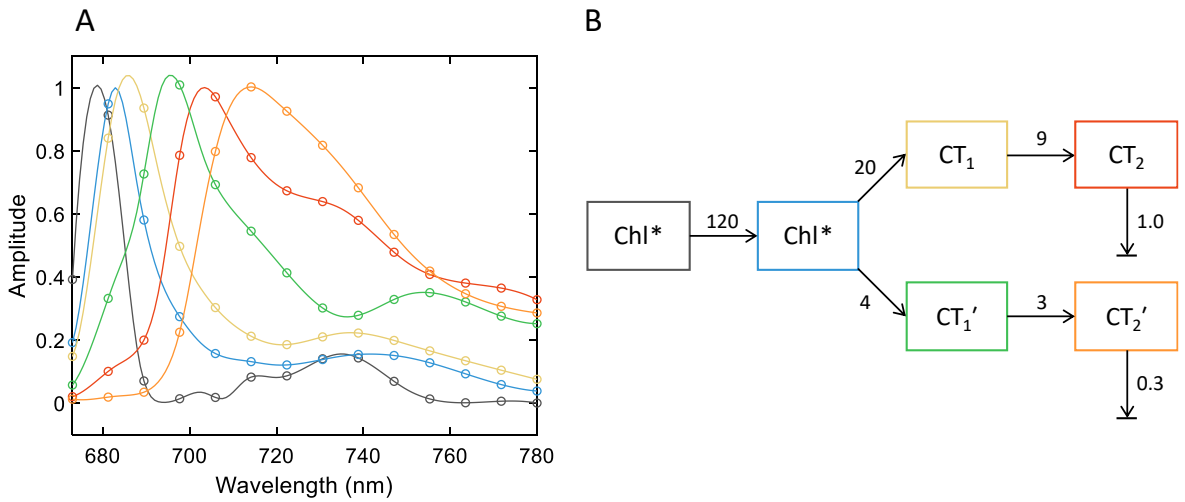

Figure 5.10. Time-resolved fluorescence of LHCII aggregates at 77 K. A. Species-associated emission spectra obtained from target analysis of the fluorescence kinetics. B. Kinetic model scheme. The numbers indicate rate constants (ns^{-1}). Adapted from Ostroumov et al. (2020).

5.2.3. Far-red signature of NPQ in vivo

While the far-red emission of LHCII in vitro is well established, there has been considerable doubt whether it occurs also in vivo. The evidence put forward by Holzwarth and co-workers (2009), that led to the proposal of two independent sites of quenching, was based on kinetic modelling of the time-resolved fluorescence data. More direct spectroscopic data revealing the far-red emission in intact plants was needed. Here I will briefly summarize the results obtained at the Max-Planck Institute of Bio-Inorganic Chemistry aiming to address this problem.

Fluorescence emission spectra of leaves at 77 K

We first carefully compared the low-temperature (77 K) fluorescence emission spectra of dark-adapted Arabidopsis leaves with those of leaves illuminated for different lengths of time and then immediately frozen. Preillumination led to changes in the shape of the leaf fluorescence emission spectrum, revealed in the spectra normalized at 760 nm Figure 5.11. We found a decrease of the bands at 683 and 695 nm that originate from the core antenna of PSII and enhanced emission at 730 nm (Figure 5.11). The far-red emission band in leaves is associated primarily with PSI and the change might also simply reflect the relative decrease of PSII fluorescence; however, this requires that the emission at 760 nm is predominantly from PSII as well.

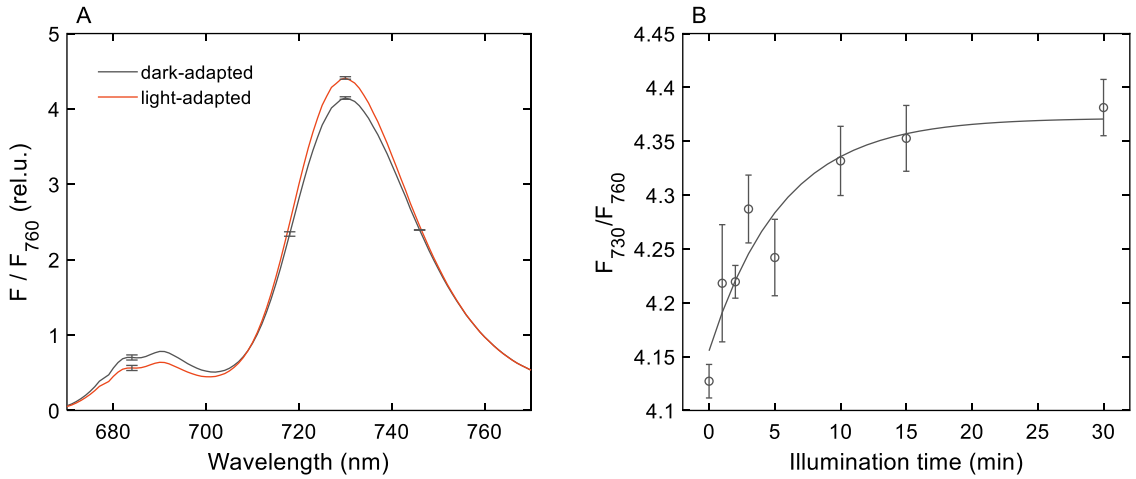

Figure 5.11. Fluorescence emission spectra at 77 K, normalized at 760 nm, of dark-adapted and preilluminated (30 min, 600 μmol photons m^{-2} s^{-1}) Arabidopsis leaves. The spectra are averages from four to six measurements on different leaves. B. Dependence of the fluorescence ratio F_{730}/F_{760} on the duration of preillumination.

Spectral and kinetic components of NPQ

To investigate further, we designed and constructed a spectrofluorometer capable of measuring the induction and relaxation kinetics of NPQ (Lambrev et al., 2010). Traditional instruments such as the Walz PAM fluorometer use a combination of actinic and modulated measuring light to detect the fluorescence yield changes in time but provide no spectral information. With the help of the novel method of Chl fluorescence induction spectroscopy, i.e. by measuring the fluorescence yield kinetics at different wavelengths, we could gain deeper insight into the time dependence of the spectral changes associated with NPQ and underlying quenching mechanisms. Figure 5.12 shows the time

and wavelength dependence of the NPQ parameter, calculated as NPQ = $F_m/F_m' - 1$, where F_m and F_m' stand for the maximal fluorescence of dark-adapted and light-adapted leaves, respectively (Baker, 2008).

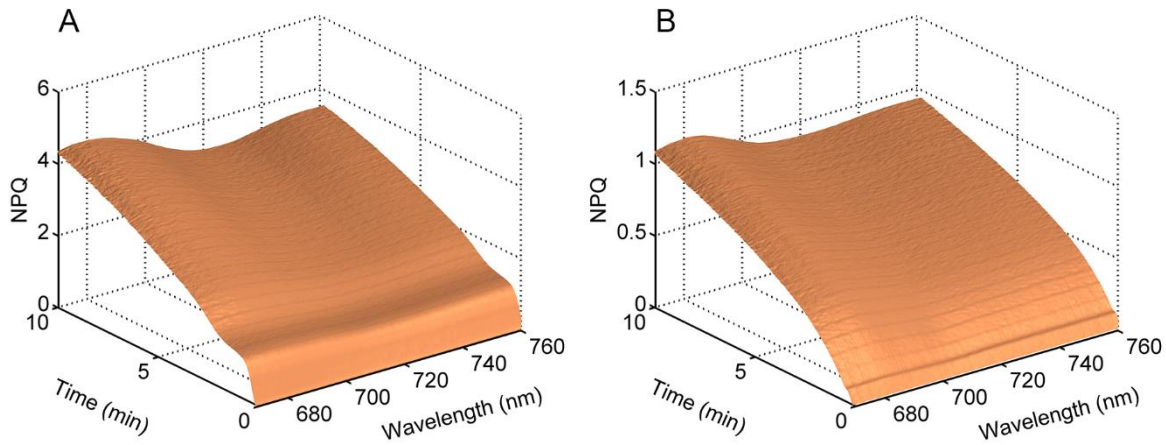

Figure 5.12. Wavelength-resolved induction kinetics of the NPQ parameter (NPQ = $F_m/F-1$) in leaves of Arabidopsis wild type (A) and PsbS-deficient mutant *npq4* (B). NPQ was induced by illuminating dark-adapted leaves with red light (1000 μmol photons m^{-2} s^{-1}). Reproduced from Lambrev et al. (2010).

In wild-type Arabidopsis leaves, NPQ has several kinetic components – a fast phase is ascribed to the energy-dependent quenching qE and a slower phase, originally denoted qI (Krause and Weis, 1991). The fast phase is strictly dependent on the PsbS protein and is absent in the PsbS-deficient mutant *npq4* (Brooks et al., 2014). The slow phase depends on the de-epoxidation of violaxanthin and accumulation of zeaxanthin in the TM (Nilkens et al., 2010). Inspection of the results along the wavelength axis shows a pronounced trough in the NPQ around 720 nm in wild type Arabidopsis but no such feature is observed in PsbS knockout mutant. The drop in NPQ could be caused by enhanced fluorescence emission at this wavelength. Figure 5.13 shows the light-induced spectral changes relative to the emission at 750 nm – predictably a negative maximum at PSII nm, which shows the quenching of PSII fluorescence, and a small but significant increase around 720 nm. The time dependence of the relative change at 720, ΔF_{720} is especially interesting (Figure 5.13B). In wild type, the spectral change appears in the first 5 min of illumination and then plateaus while overall NPQ continues to rise (cf. Figure 5.12). After turning of the actinic light, the spectral change quickly vanishes, whereas NPQ has a significant non-relaxing component, qI (not shown). This shows unequivocally that there are at least two separate quenching mechanisms – the rapidly forming and relaxing

quenching, termed qE, is associated with the appearance of far-red fluorescence, while the slowly-induced component is not. Moreover, as qE is known to depend on PsbS, so does the amplitude of the spectral change ΔF_{720} (Figure 5.13B). The far-red emission is enhanced in the PsbS-overexpressing mutant *L17*, whereas it is not observed at all in PsbS-deficient plants. On the other hand, the amplitude of the spectral change was independent of zeaxanthin, in contrast to the slowly-induced NPQ component (not shown).

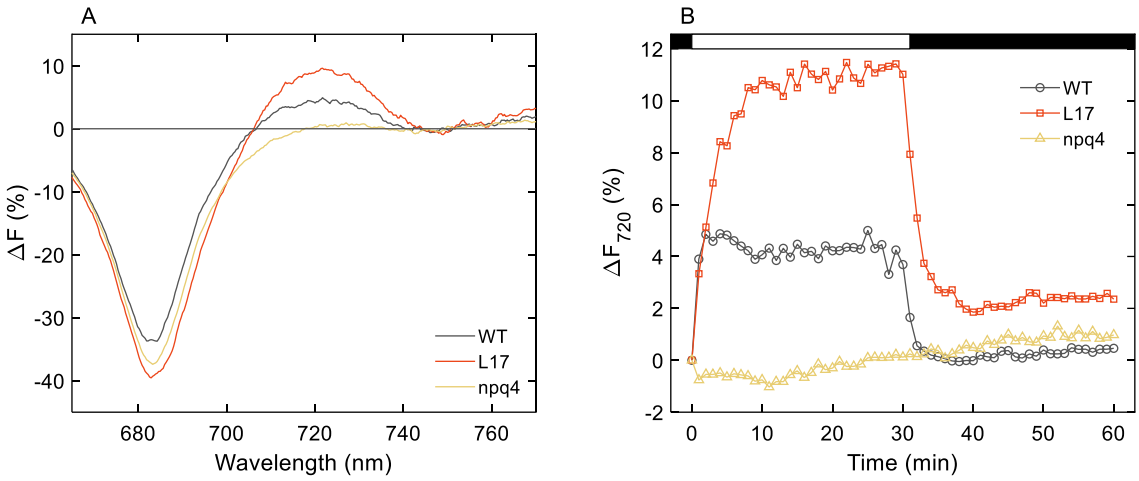

Figure 5.13. PsbS-dependent far-red emission in leaves under NPQ conditions. A. Light-minus-dark relative difference emission spectra of Arabidopsis leaves (wild type, PsbS overexpressing mutant *L17*, PsbS-deficient mutant *npq4*) after 30 min irradiation (600 μmol photons m^{-2} s^{-1} red light). Calculated by subtracting spectra normalized at 750 nm. B. Time dependence of the relative light-induced differences at 720 nm during 30 min irradiation and subsequent dark recovery.

The results confirm beyond doubt that the fast and slow kinetic components of NPQ are associated with different mechanisms of quenching and are in line with the two-site quenching model of Holzwarth (2009; 2014). According to the model, the rapidly-induced quenching qE is formed upon protonation of PsbS in the TM and interaction with LHCII, which brings about the detachment of LHCII trimers from the PSII–LHCII supercomplex and their subsequent clustering or aggregation. Aggregation of LHCII is associated with the formation of Chl-Chl CT states responsible for fluorescence quenching, i.e. thermal dissipation of Chl excited states, and for the far-red emission at 720–730 nm. Thanks to this far-red signature, spectral resolution of the NPQ kinetics provides a novel method to separate and quantify qE independently from other NPQ mechanisms.

5.2.4. Relationship between NPQ and photoprotection

Plants and algae employ various elaborate regulation and defence mechanisms to avoid photodamage (Li et al., 2009). Despite that, prolonged excess light conditions or combined with other stress factors can lead to photoinhibition (Aro et al., 1993; Li et al., 2018). NPQ is recognized as an important photoprotective mechanism (Ruban, 2016), especially under fluctuating light.

The main sites of photodamage are the photosynthetic RCs, primarily of PSII, the antenna of PSII and likely also PSI. Photodamage steps are mediated by ROS, the most important of them being singlet oxygen (Triantaphylides and Havaux, 2009; Keren and Krieger-Liszkay, 2011). Singlet oxygen is produced mainly by a photosensitization reaction between triplet excited Chl (^{3}Chl) and molecular oxygen in the TM. ^{3}Chl is produced by intersystem crossing from singlet excited Chl in the light-harvesting antenna complexes (Figure 2.2) but a more efficient process is by charge recombination in the PSII RC (Vass, 2011; Vass, 2012). The RC triplets live long enough to interact efficiently with ground state O_2 making this the primary route for photodamage in PSII (Telfer, 2005). Photoprotection of PSII then can be generalized as any process that lowers the probability for generation of ^{3}Chl* in PSII. In this framework, the photoprotective role of NPQ – which removes singlet Chl excitations – is easily understood.

The relationship between NPQ and the actual photoprotection of PSII has not been derived quantitatively because the latter is not easily measurable. Moreover, this question becomes more complicated if NPQ is not a single process but entailing different mechanisms and sites. Here I will summarize theoretical considerations (Lambrev et al., 2012) using a simplified model of the kinetics of charge separation in PSII based on the so-called exciton-radical pair equilibrium (ERPE) model (Schatz et al., 1988). The kinetic scheme is shown in Figure 5.14. It consists of three kinetic compartments: Ant*, RP_1 and RP_2 and a "dump" ^{3}Chl compartment. Ant* represents singlet excited states in PSII and RP stand for radical pairs in the RC. Excited states can either deactivate with a rate constant k_d or induce charge separation with k_{cs} forming RP_1. The primary radical pair in turn transform to RP_2 with a rate constant k_1 or can recombine regenerating the excited state with a rate constant k_{rec}. Radical pairs can also recombine nonradiatively to the ground state (k_{np}) or can form a triplet state (k_T).

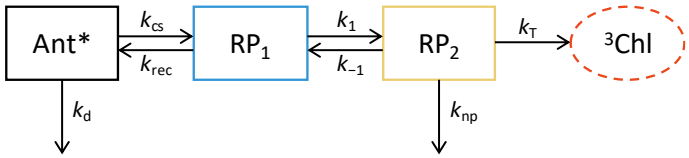

Figure 5.14. ERPE model of PSII kinetics used for calculation of NPQ and photoprotection. See text for explanation of the rate constants.

With an appropriate choice of rate constants, the kinetic model can be used to numerically calculate the fluorescence yield (or the average lifetime of the excited states Ant*) and the triplet yield (the final population of ^{3}Chl). As a reference point, we evaluate the model with the kinetic parameters in Table 5.1, obtained from global fitting of the fluorescence kinetics of dark-adapted Arabidopsis leaves with closed PSII RCs (Holzwarth et al., 2009).

Table 5.1. Rate constants (ns^{-1}) of the ERPE model for F_m conditions (Holzwarth et al., 2009)

k_d	0.4
k_{CS}	3.0
k_{rec}	8.5
k_1	2.0
k_{-1}	0.5
k_{np}	0.54
k_T	0.36

By changing model parameters, we can simulate NPQ mechanisms and estimate the resulting fluorescence quenching (NPQ = $F_m/F_m' - 1$) or *photoprotective effect* (PPE = $\varphi_T/\varphi_T' - 1$). More specifically, we examined the photoprotective effect of the two quenching mechanisms described in the previous section, namely antenna quenching and antenna detachment (Lambrev et al., 2012). The former is simulated in a straightforward way by increasing the dissipation rate constant k_d. Consequently, the lifetime of the excited states Ant* is shorter and a smaller proportion of excitations is converted to triplet states. In the case of antenna quenching, the relative decrease of the fluorescence and triplet yield is always the same, i.e. PPE = NPQ – non-photochemical quenching is an exact measure of the degree of photoprotection. This fundamental relationship holds regardless of the specific choice of model parameters.

In the second case – antenna detachment – the intrinsic rate constants are unchanged but the antenna cross-section is smaller – which also lowers the number of excitations

that can produce triplets and photodamage. At the same time, the effective charge separation rate constant k_{CS} is increased because the probability that antenna excitations are located at the RC is higher. As a result, there is a nonlinear relationship between the number of detached antenna units and NPQ or the photoprotective effect (Figure 5.15) and the measurable NPQ parameter tends to overestimate the potential for photoprotection. Overall, this mechanism appears to be significantly less effective than antenna quenching although it contributes to the NPQ response.

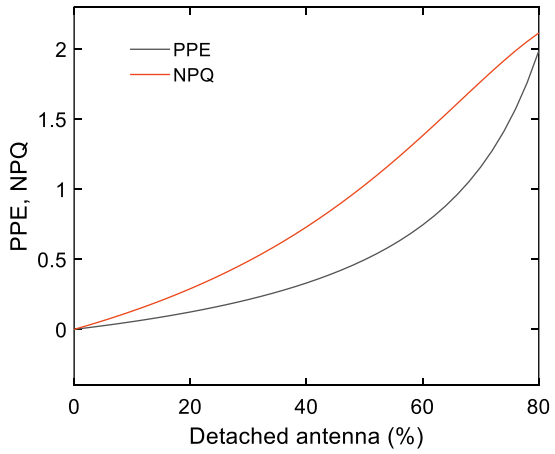

Figure 5.15. Dependence of the photoprotective effect (PPE) and non-photochemical quenching (NPQ) on the fraction of detached antenna Chls. The parameters are calculated as PPE = $\varphi_T/\varphi_T' - 1$ and NPQ = $\tau/[\tau'(1-A) + 0.4A]$, where φ_T = 0.2 and τ = 1.26 ns are the triplet yield and fluorescence lifetime of the unquenched F_m state, φ_T' and τ' are the simulated triplet yield and fluorescence lifetime, A is the fraction of detached antenna Chls, and 0.4 ns is the fluorescence lifetime of the detached antenna Chls.

To summarize, the theoretical simulations demonstrate that the fluorescence intensity is not always a good measure for the actual photoprotective capacity that may be reached. We also conclude that detachment of PSII antenna is not the most efficient strategy, judged in terms of the gained photoprotective capacity. On the other hand, as the PsbS-dependent LHCII detachment is a very rapid mechanism, it may have an important physiological role in providing some protection against rapid light fluctuations, while more efficient zeaxanthin-dependent quenching requires more time to activate. This result is well in accord with the findings that *npq4* plants were not prone to photodamage even in high light as long as constant light conditions prevailed, but were only sensitive to reduction in photosynthetic yield and photodamage under largely and rapidly varying light intensities (Külheim and Jansson, 2005).

5.2.5. Quenching in reconstituted LHCII membranes

The notion that photoprotective NPQ in vivo and fluorescence quenching in LHCII aggregates in vitro are one and the same process is still debated. Barros et al. (2009) argue that quenching in aggregates is a random unspecific process that should not be mistaken as the controlled and specific quenching mechanism in vivo. Random contacts between different peripheral Chls are possible in three-dimensional LHCII aggregates, but not in the membrane where LHCII are specifically oriented and interactions are constrained within the membrane plane.

Proteoliposomes are an attractive system to investigate in detail the mechanism of NPQ in a lipid bilayer environment. Liposomes containing zeaxanthin and PsbS, which are two essential factors in NPQ, in addition to LHCII were described (Wilk et al., 2013; Liu et al., 2016), opening way to study the molecular mechanism of NPQ in vitro. Moya et al. (2001) showed that the fluorescence yield of LHCII liposomes is lower than solubilized LHCII trimers. Schaller et al. (2011) reported that the fluorescence quenching depends on the types of lipids in the membrane. Two recent studies of LHCII reconstituted into liposomes and lipid nanodiscs have shown that LHCII fluorescence quenching is driven by LHCII protein–protein interactions and not from a specific thylakoid lipid microenvironment (Natali et al., 2016; Crisafi and Pandit, 2017). The fluorescence yield was lower at higher protein densities (lower L/P ratios) suggesting that clustering of LHCII in the membrane causes the quenching. However, there is a large mismatch between the magnitude of quenching and the reported L/P ratios (Moya et al., 2001; Crisafi and Pandit, 2017). There are also controversial reports regarding the necessity for Zx and PsbS for the induction of quenching and the actual quenching mechanism in these systems (Wilk et al., 2013; Liu et al., 2016).

Dependence of the fluorescence quenching on the L/P ratio

Section 5.1.3 showed that LHCII proteoliposomes are highly heterogeneous with respect to vesicle size and protein density and that the median L/P ratios of the vesicles can be very different from the L/P ratio of the reconstitution mixture. We also applied the same approach – separating the proteoliposome samples into fractions of different L/P ratios – to investigate the dependence of fluorescence quenching of LHCII on the protein density (Akhtar et al., 2019). The fluorescence decays of individual proteoliposome fractions with determined L/P ratios were recorded and the average fluorescence lifetimes were

estimated by global lifetime analysis. Representative decays and average lifetimes are shown in Figure 5.16. The decay of the LHCII membrane fraction with L/P ratio of 3000:1 is practically identical to the decay measured from LHCII solubilized in DDM with an average lifetime of 3.5 ns. With decreasing lipid content, however, progressively faster decay and shorter average lifetime is observed. The data establish beyond doubt that the fluorescence of LHCII in lipid membranes is strongly correlated with the L/P ratio.

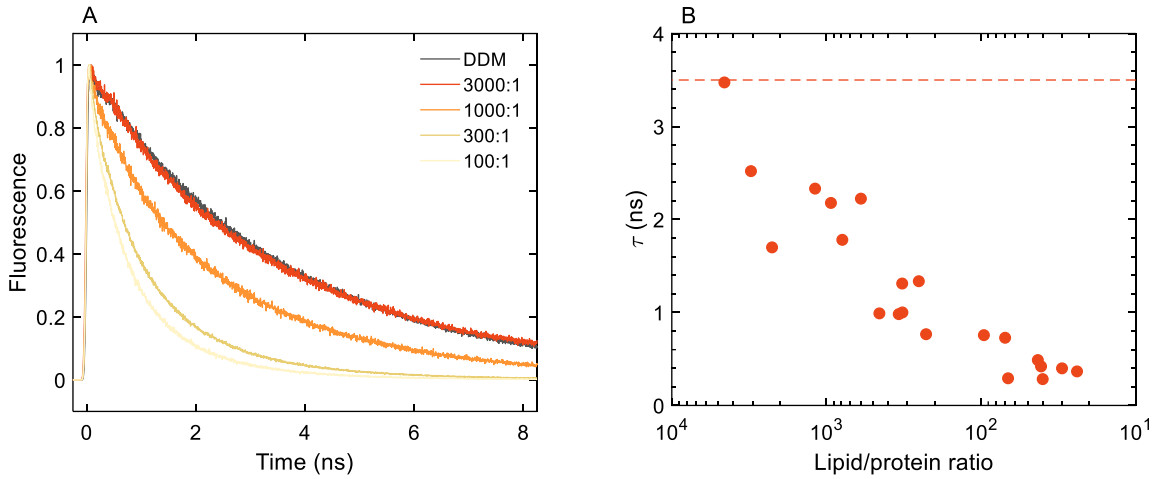

Figure 5.16. Time-resolved fluorescence of reconstituted LHCII membranes. A. Fluorescence decay kinetics recorded by TCSPC from LHCII solubilized in detergent (β-DDM) and selected fractions of reconstituted LHCII membranes having different L/P ratios, as indicated. The decays were recorded at 680 nm emission wavelength with excitation at 632 nm. B. Average fluorescence lifetimes plotted as function of L/P ratio. The dotted line indicates the average lifetime of detergent-solubilized LHCII. Reproduced from Akhtar et al. (2019).

The most protein-dense fractions with L/P ratios below 50:1 showed average fluorescence lifetimes comparable to those observed in LHCII aggregates (0.3–0.4 ns) – in contrast to previous studies, where relatively mild quenching was observed in a narrower range of L/P ratios. At the same time, no aggregation CD signature or any specific CD spectral change could be associated with the occurrence of quenching (cf. section 5.1.3). The present results prompt the conclusion that LHCII has the intrinsic capacity for fluorescence quenching to the extent observed in vivo under NPQ conditions and that this quenching can be triggered in the lipid membrane simply by clustering without the need for low pH, zeaxanthin or activated PsbS protein.

Mechanism of quenching in LHCII proteoliposomes

The question arises whether the same mechanisms are responsible for quenching in the lipid membrane as in aggregates. To answer this, we looked for far-red emission from the quenched proteoliposomes. As Figure 5.17 shows, the steady-state spectra of proteoliposome fractions with high protein density are practically indistinguishable from those of LHCII aggregates – displaying a prominent broad maximum at 700 nm (Figure 5.9). The band's intensity relative to the 680-nm band strongly correlated with the L/P ratio and hence with the fluorescence quenching. Thus, quenching in the reconstituted lipid membranes as well as in aggregates is associated with the formation of Chl-Chl CT states.

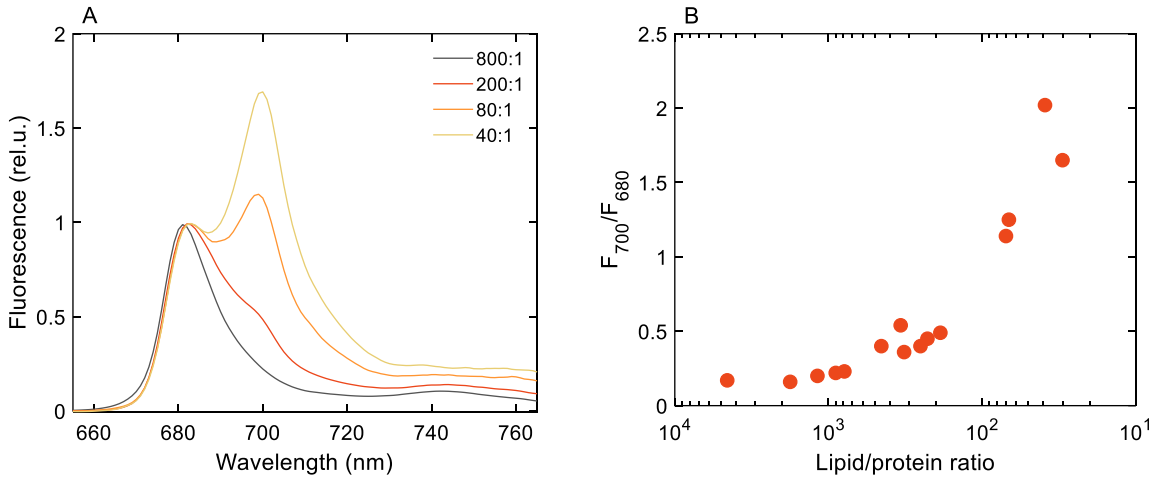

Figure 5.17. Steady-state 77 K fluorescence spectra of reconstituted LHCII membranes. A. Fluorescence emission spectra at different L/P ratios. The spectra are normalized to the maximum in the range of 675–685 nm. The samples with higher protein density show a strong emission band at 700 nm. B. Relationship between the 77 K fluorescence intensity at 700 nm relative to 680 nm and the L/P ratio. (Akhtar et al., 2019)

The finding of significant constitutive fluorescence quenching in all but the most lipid-rich proteoliposomes is puzzling. Native granal TM are extremely protein-dense, containing only 1.5 lipids per Chl (Duchêne and Siegenthaler, 2000). The lipid/Chl ratio is even less in isolated PSII-enriched membrane fragments (Haferkamp et al., 2010). Despite that, under normal conditions the fluorescence of LHCII in the native chloroplast membranes is not quenched. The reason why LHCII forms strongly quenched clusters in reconstituted membranes but not in native TM deserves further investigation.

5.3. Structural insights from anisotropic CD spectroscopy of LHCII

5.3.1. Anisotropic CD spectra of photosynthetic membranes

It has been documented that ACD spectroscopy provides additional, independent information about chiral and excitonic molecular systems which is not accessible from ordinary CD measurements (Kuball and Höfer, 2000; Kuball, 2002; Kuball et al., 2005). ACD measurements can, in principle, separate the exciton transitions and their corresponding CD bands by their orientation with respect to the axes of (macro)molecular symmetry (see section 2.2.1). Consequently, ACD can measure physical parameters, such as the orientation of the excitonic transition dipole moments and the exciton coupling strength. ACD spectra of photosynthetic pigment–protein complexes are essentially unknown and unexplored.

Orientation dependence of the psi-type CD

We performed ACD measurements on stacked and unstacked TM as well as lamellar macroaggregates of LHCII (Simidjiev et al., 2011) and PSII-enriched membranes (BBY particles) and showed that both the psi-type CD and the excitonic CD is dramatically affected by the sample orientation (Miloslavina et al., 2012). Stacked TM can be aligned in moderate magnetic field (0.5–1 T) due to their large diamagnetic susceptibility anisotropy, related to the long-range order of the protein complexes in the chiral macrodomains (Barzda et al., 1994). Optical spectra could be measured either in face-aligned or edge-aligned configuration (Figure 5.18).

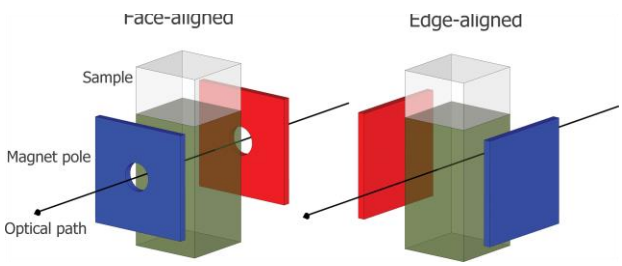

Figure 5.18. Macroscopic orientation of samples in magnetic field. The optical cuvette containing the sample is placed between the poles of a magnet providing field of 0.7–1.5 T. Spectroscopic measurements are performed with the measuring light propagating either along the field (face-aligned configuration) or perpendicular to it (edge-aligned). Reproduced from Miloslavina et al. (2012).

Intact TM exhibit large psi-type CD that is tightly correlated with the presence of grana (Faludi-Dániel et al., 1973; Faludi-Dániel and Mustárdy, 1983). It is attributed to the long-

range dipole-dipole interactions of Chls and Cars in PSII and LHCII embedded in the membrane in ordered three-dimensional arrays called chiral macrodomains (Garab, 1992; Garab and Mustárdy, 1999). The main spectral features of the psi-type CD of thylakoids are a positive band at 690 nm, a negative band with a maximum at 674 nm and a broad positive band peaking around 510 nm (Figure 5.19). It is established that these bands originate from distinct structural entities in the TM as they respond differently to various treatments and mutations (Garab et al., 1991; Kovács et al., 2006; Tóth et al., 2016) but their exact origin is unclear.

Comparison of the face- and edge-aligned ACD spectra of magnetically oriented TM revealed that they are remarkably unlike each other. The edge-aligned spectrum resembled closely the isotropic CD of the randomly oriented suspension – recall that the edge-aligned component has double contribution to the isotropic spectrum (Eq. (2.2.10) on page 20). The face-aligned spectrum showed a sign inversion of the main psi-type CD bands at 674 and 690 nm. A similar spectrum was recorded from oriented chloroplasts earlier (Garab et al., 1988). The sign inversion can at least partially be due to the angular dependence of differential scattering. We propose that the face-aligned ACD spectra reveal primarily in-plane structural order, whereas edge-aligned spectra are associated primarily with the inter-lamellar organization, i.e. features and interactions between membrane sheets.

Strong psi-type CD can be generated not only in the native grana but also in isolated LHCII, which also can form chirally ordered lamellar macroaggregates (Simidjiev et al., 1997). This demonstrates that the psi-type CD originates from ordered arrays of proteins. Interestingly, the psi-type CD of LHCII macroaggregates has similar features to that of TM but has opposite sign. In the same fashion as observed in TM, the main psi-type bands are inverted in the face-aligned ACD spectrum of oriented LHCII lamellae (Figure 5.19). The lack of a sufficiently developed theoretical model for psi-type CD allows only a qualitative description of these results, but we propose that ordered LHCII macroaggregates can be used as an experimental model system to develop such a theory.

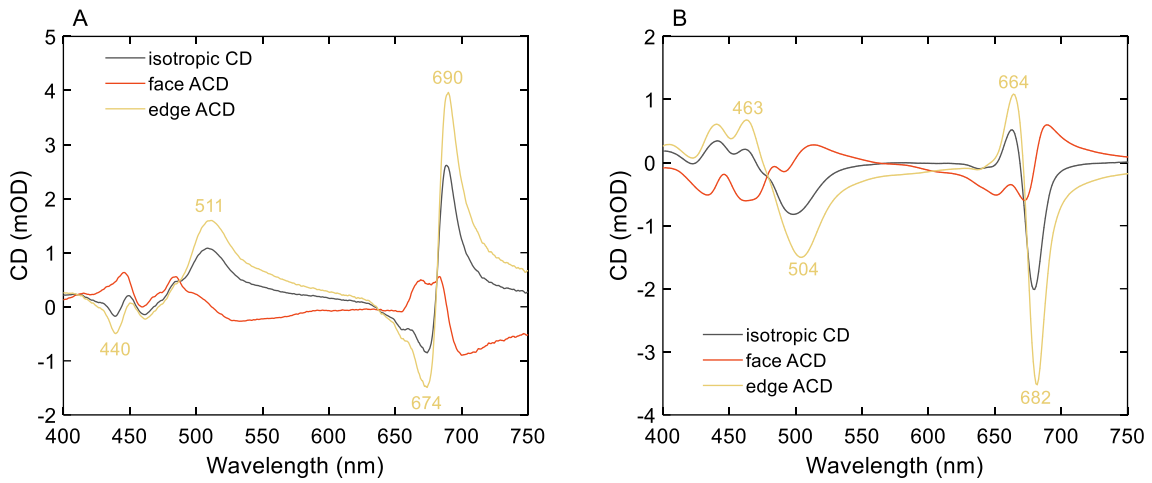

Figure 5.19. Psi-type CD and ACD of stacked thylakoid membranes (A) and lamellar LHCII macroaggregates (B). ACD spectra in face-aligned orientation are measured in magnetic field of 0.6 T and edge-aligned spectra are calculated using equation (2.2.10). (Miloslavina et al., 2012)

Excitonic ACD spectra

The excitonic ACD spectra of unstacked TM (washed in hypotonic law-salt buffer) and PSII-enriched membranes oriented by polyacrylamide gel compression also showed specific well reproducible differences with the isotropic CD (Figure 5.20). The ACD spectra of both types of samples were remarkably similar, especially in the Soret region, where two characteristic sharp and intense positive bands, at 447 nm and 484 nm, and two negative bands, at 435 and 460 nm, were observed. In the first approximation, the unique presence of certain bands in the face-aligned ACD spectrum, such as the 447 and 483 nm bands, indicates that the respective electronic transition dipole moments are oriented preferentially in the plane of the membrane. Conversely, CD bands missing from the face-aligned ACD are associated with transition dipoles with no component vector in the membrane plane. Such is, for example, the 475 nm CD band of TM and BBYs, which is also associated with trimerization of LHCII.

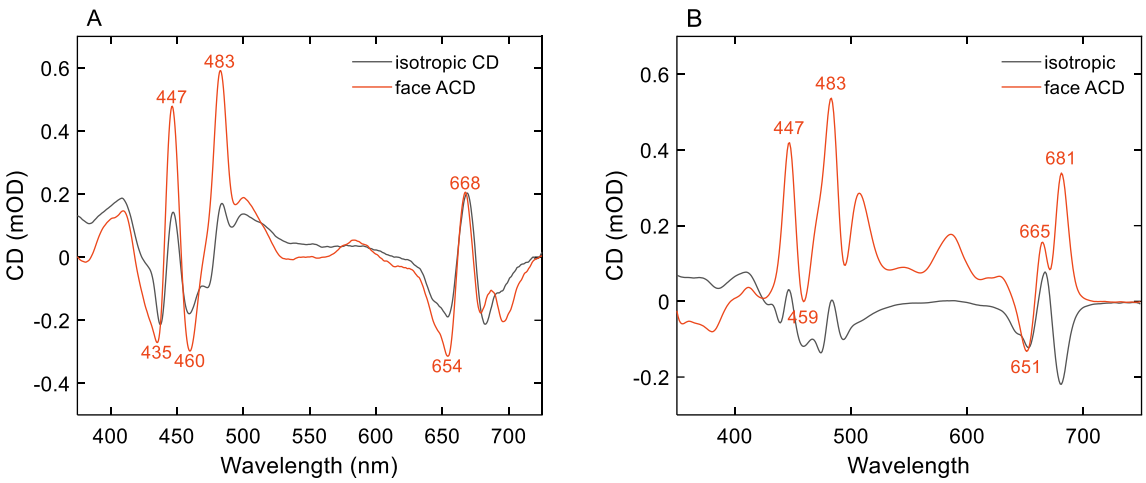

Figure 5.20. Excitonic CD and ACD spectra of unstacked thylakoid membranes (A) and PSII-enriched membranes (B). The ACD spectra are recorded in face-aligned configuration from samples oriented by uniaxial gel compression. (Miloslavina et al., 2012)

It is worth noting some bands associated with weak optical transitions in the region 500–600 nm are much more pronounced in the ACD spectra than in the isotropic CD or absorption spectra. In general, the ACD spectra showed several intense narrow bands resolved more clearly than in the isotropic spectra, demonstrating the potential of ACD to identify specific pigments and pigment interactions. These results serve as a "proof of principle" for the potential value of ACD spectroscopy in photosynthesis research and as reference data for future theoretical calculations and model validations. The marked similarity between the TM and BBYs shows that the features originate mainly from PSII and especially LHCII, which is the predominant Chl-binding protein. In the next section we focus specifically on the ACD spectra of LHCII.

5.3.2. Identifying energy sinks in LHCII by ACD spectroscopy

Experimental ACD spectra of isolated LHCII

Isolated LHCII is difficult to align macroscopically but can be oriented if incorporated into lipid membranes. The trimeric complexes are embedded in the planar lipid bilayer such that their axis of C_3 symmetry is parallel to the axis normal to the membrane plane $\boldsymbol{n}_\perp$. The reconstituted LHCII membranes were oriented by gel compression or as dehydrated films on fused silica plates and ACD spectra were measured in the face-aligned configuration, i.e. with the measuring beam parallel to $\boldsymbol{n}_\perp$ and hence the symmetry axis of the LHCII trimer (Akhtar et al., 2019). Figure 5.21 shows the isotropic CD, face-aligned ACD and the complementary (calculated) edge-aligned ACD spectrum. The spectra

were independent from the method of orientation. As could be expected, the ACD spectra were strikingly different in comparison to the isotropic CD spectra, featuring a larger number of well-resolved bands.

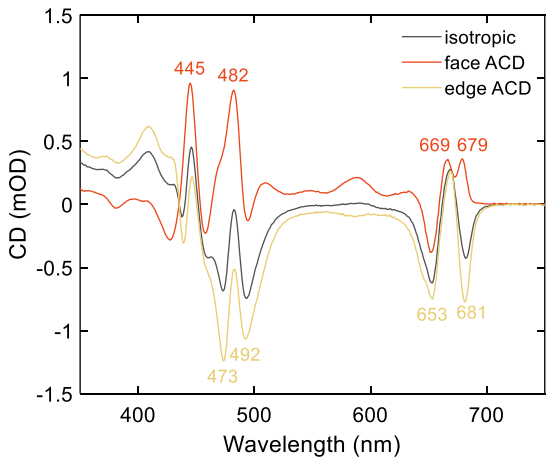

Figure 5.21. CD and ACD spectra of reconstituted LHCII membranes. Red curve – face-aligned ACD recorded from dehydrated membrane patches; grey curve – isotropic CD measured in buffer medium; yellow curve – edge-aligned ACD calculated as $(3CD_{iso} - ACD_{face})/2$ (Miloslavina et al., 2012; Lindorfer and Renger, 2018). The spectra are normalized to unity absorbance at 675 nm. Numbers indicate peak wavelengths. (Akhtar et al., 2019)

The most prominent features in the ACD spectra, e.g. the positive bands at 445 and 482 nm, are present in the isotropic spectra as well but better resolved and much more intense in ACD spectra. As discussed in the previous section, these features can be associated with transitions polarized preferentially in the membrane plane. Conversely, bands observed in the isotropic CD but not in the face-aligned ACD, can evidently be found in the complementary edge-aligned ACD spectrum and ascribed to out-of-plane transitions. To this group belong the negative 438, 473 and 493 nm bands, and the negative shoulder around 645 nm, that is characteristic for LHCII trimers as opposed to monomers (Nussberger et al., 1994). Other bands, especially in the wavelength region 500–650 nm, are only resolved in ACD, whereas the isotropic CD is flat and featureless. These bands seem to originate from excitonic coupling between optically weak transitions – Chl and Car transitions of intermediate energy between the Chl B and Q band, that have not been documented before. Especially striking is the sign inversion in the red-most part of the spectrum, i.e. the region of the lowest-energy Chl *a* sinks – the negative peak at 682 nm in the CD spectrum becomes a positive peak at 679 nm in the face-aligned ACD.

Theoretical calculation and modelling of the ACD spectra

The information potential of the ACD measurements was further analyzed by exciton calculations (Akhtar et al., 2019). The theory of optical spectra, based on the exciton Hamiltonian of the pigment–protein complex (section 2.1.2) is described by Müh et al. (2010). The parameters of the Hamiltonian that includes the ground and the lowest-lying singlet excited states of the Chls in the LHCII have been previously obtained (Müh and Renger, 2012) from a combination of quantum-chemical and electrostatic computations, and then refined by comparison with experimental absorption, CD and isotropic CD spectra. Using this theory and exciton Hamiltonian, the ACD spectra of LHCII in the Chl Q_y region were simulated according to the formalism developed recently (Lindorfer and Renger, 2018). The characteristic features of the ACD spectra, including the sign inversion of the long-wavelength band, were reproduced by the calculation without changing a single model parameter, further corroborating the exciton model (Figure 5.22).

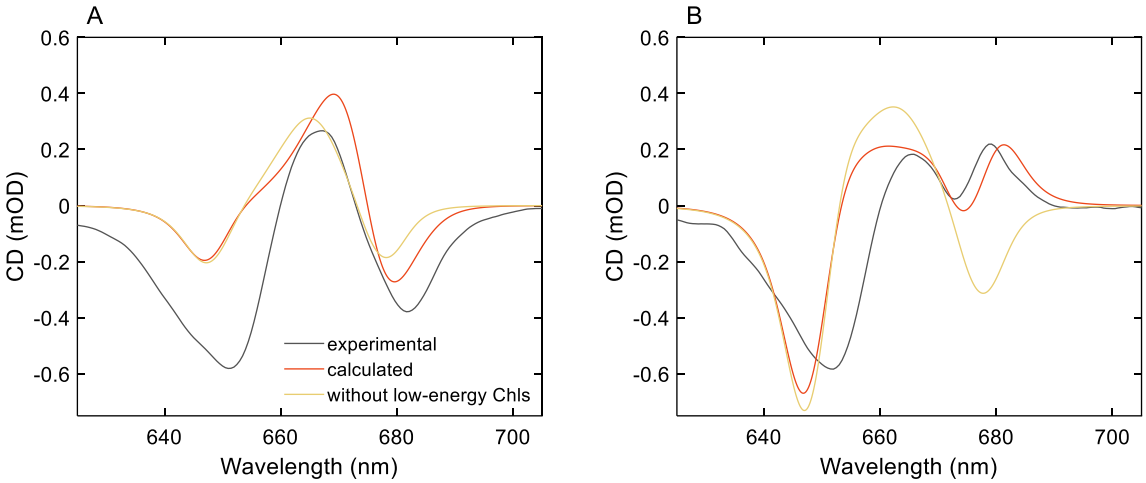

Figure 5.22. Comparison of the experimental and theoretically calculated Q_y-region CD (A) and face-aligned ACD (B) spectra of LHCII. Also shown are simulated spectra excluding the four lowest-energy Chls from the Hamiltonian (Akhtar et al., 2019).

The agreement between the simulations and experimental data in the red spectral edge give confidence in the assignment of the lowest-energy states – Chl *a*610 and Chl *a*603 on the stromal side and Chl *a*604 and *a*613 on the lumenal side. Removal of these Chls or using a different set of site energies resulted in worse fit. Because the ACD spectrum is extremely sensitive to the pigment geometry, this agreement between theory and experiment is a strong evidence that the pigments contributing to the low-energy exciton states are correctly assigned in the model. On the other hand, the deviations from the experimental spectra show that there is room for refinement of the model.

More open questions from the UV-ACD spectra

UV-ACD has been applied to study the membrane insertion of various small polypeptides, such as toxins and antibiotics (Wu et al., 1990) but its ability to monitor the structure and macroorganisation of photosynthetic proteins has not been explored until now (Akhtar et al., 2019). The UV-CD spectrum of TM shows (Figure 5.23) the characteristic shape for α-helical polypeptides: it has two negative bands, at 210 nm and 224 nm, crossing the zero at approximately 201 nm, and a strong positive band near 193 nm. This is not surprising considering that TM contain primarily intrinsic membrane proteins containing multiple transmembrane α-helices. The ACD spectra of oriented membranes showed enhanced positive band at 193 nm and a negative band at 224 nm, whereas the 210 nm band was largely missing, entirely consistent with the prevailing transmembrane orientation of the protein α-helices. Very similar spectra were recorded from PSII-enriched granal membranes. These results show that ACD in general can probe the embedding and orientation of photosynthetic complexes in the membrane. However, the ACD spectrum of isolated LHCII deviated from the predicted spectrum calculated by applying Moffitt's theory on the protein backbone of LHCII (Akhtar et al., 2019). The differences suggest that the UV-CD spectra of LHCII and of pigment–protein complexes in general reflect not only the protein secondary structure but might also include contributions from the pigment cofactors and pigment–protein couplings – an area that evidently needs further exploration.

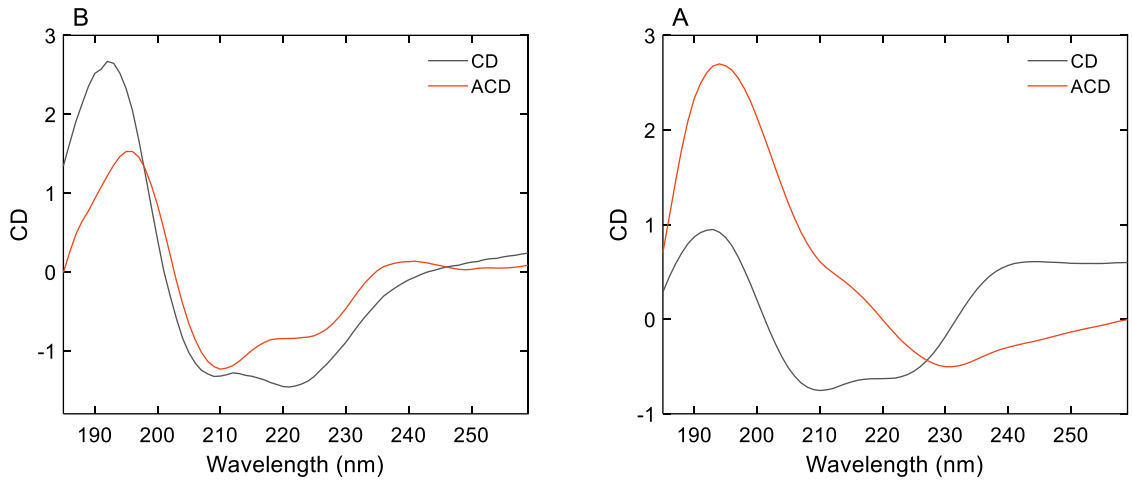

Figure 5.23. UV synchrotron-radiation CD (SRCD) and ACD spectra of thylakoid membranes (A) and reconstituted LHCII membranes (B). The SRCD spectra were recorded from liquid suspension in a quartz cell of 0.2 mm path length and ACD spectra were recorded from dry membranes patches. The data are obtained at the B23 synchrotron radiation CD beamline, Diamond Light Source, UK. (Akhtar et al., 2019)

6. DYNAMICS OF ENERGY TRANSFER

6.1. Probing energy transfer in LHCII by 2DES

The first 2DES investigation of the excitation dynamics in LHCII was reported a decade ago by Schlau-Cohen *et al.* (2009). They used broadband pulses (80 nm FWHM), covering the entire Chl Q_y region, in a fully non-collinear setup using diffractive optics to separately record rephasing and nonrephasing 2D spectra from trimeric LHCII from Arabidopsis at low temperature (77 K). These ground-setting 2DES experiments demonstrated the potential of the technique and generated great interest in the community. The 2D spectra revealed very fast dynamics of EET as well as quantum coherences, which had not been observed before. At the same time, however, the results exposed the technical challenges that needed to be overcome. The data were of limited time range – the signal decayed below the noise floor within 20 ps and the spectra were significantly distorted by imperfect phasing, hampering the interpretation and assignment of features. In collaboration with the group of Howe-Siang Tan at NTU, Singapore, we pursued a different approach, striving to record purely absorptive electronic spectra with high signal-to-noise ratio a "pump-probe" geometry setup, free from phasing and other artefacts, that could be analyzed in a straightforward manner and reconciled with the bulk of existing transient spectroscopy data. Admittedly, both approaches have their strengths and weaknesses and can be considered complementary to each other (for more details see Lambrev et al., 2020).

6.1.1. Energy transfer from Chl *b* to Chl *a*

The two types of Chl in LHCII – Chl *a* and *b* – differ in their light absorption characteristics, with Chl *b* absorbing predominantly in the wavelength range 640–660 nm and Chl *a* absorbing at 660–680 nm. Chl *b* thus acts as an energy donor and Chl *a* as an energy acceptor during the energetic equilibration of the complex. To follow the dynamics of EET from Chl *b* to Chl *a*, we performed 2DES experiments wherein the excitation (pump) pulses were spectrally tuned to cover Chl *b* absorption only having a central wavelength of 650 nm and bandwidth of ~15 nm. The probe pulses spanned the entire Q_y absorption band allowing us to monitor the relaxation of both Chl *b* and Chl *a* excited states.

2D electronic spectra upon Chl b excitation at RT

Selected 2D electronic spectra of LHCII trimers recorded at different waiting times T_w after excitation in the Chl *b* band are shown in Figure 6.1. The vertical axes represent the excitation wavelength λ_τ, which is related to the Fourier transform of the signal dynamics over the coherence time τ (as described in section 2.2.2). The horizontal axes represent the detection wavelength λ_t. The peak found along the diagonal line ($\lambda_\tau = \lambda_t \approx 650$ nm) corresponds to the Q_y band of Chl *b*, which is within the spectral range of the excitation pulses and reflects the population of the initially excited Chl *b* states at time T_w. As excitations are transferred to Chl *a* over time, the population of Chl *b* excited states decreases and so does the intensity of the diagonal peak. Simultaneously the population of acceptor Chl *a* states increases, as reflected in the off-diagonal peak centred around $\lambda_t = 680$ nm.

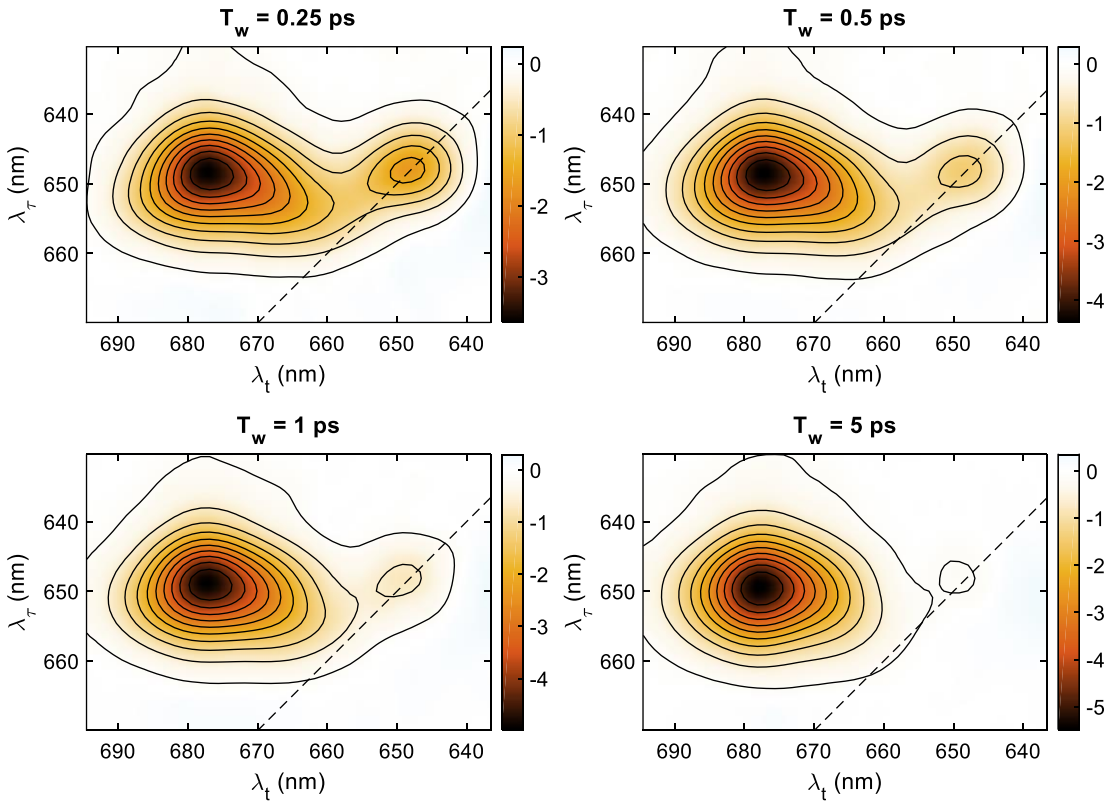

Figure 6.1. 2D electronic spectra of LHCII recorded at RT at different waiting times T_w with excitation pulses centred at 650 nm. The vertical axis represents excitation wavelength λ_τ and the horizontal axis – detection wavelength λ_t. Orange-red colour represents negative differential absorption (ground-state bleaching, stimulated emission). Contour lines are plotted at 10% intervals. Note that the axis directions are reversed to account for the inverse relationship between frequency and wavelength. Data from Wells et al. (2014).

The 2D electronic spectra are contributed by multiple excitonic states whose peakshapes largely overlap at RT and combined give the asymmetric time-dependent shapes of both the diagonal and off-diagonal peaks. The dynamics of excitonic states with different energies can partially be resolved by following the signal intensity at different points in 2D spectrum. Kinetic traces at selected excitation and detection wavelengths are plotted in Figure 6.2. The diagonal trace 650→650 nm representing the bulk Chl *b* states decays in two phases – rapidly, in the first 1 ps, followed by a slower decay phase over the next several ps. The multiphasic decay shows that not all Chl *b* molecules are equally coupled to Chl *a*. The 650→667 nm trace rises at first indicating EET from the bulk Chl *b* states to intermediate-energy states absorbing at 667 nm. The signal then decays as excitations are passed onward to lower-energy Chl *a* states – the rise in their population is reflected by the 650→680 nm trace.

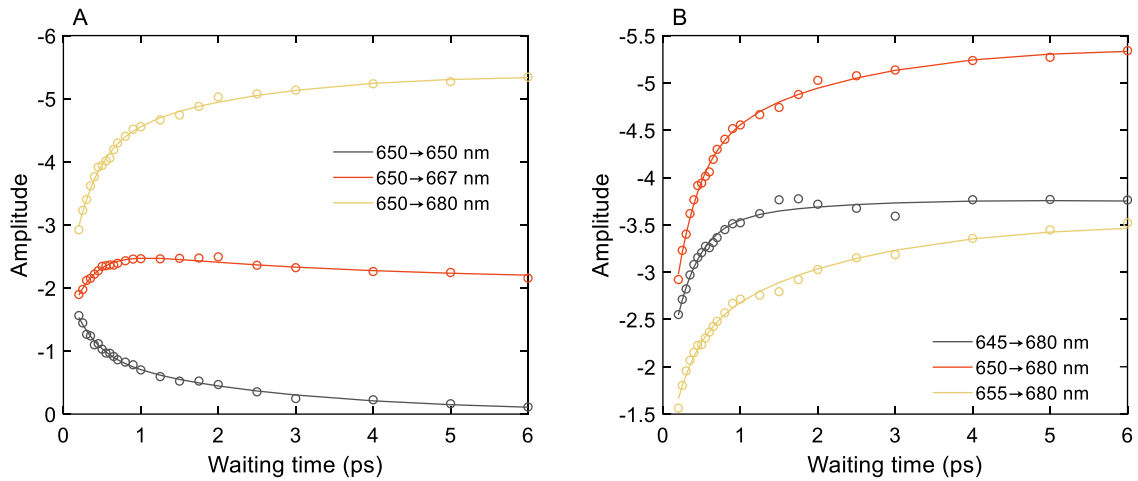

Figure 6.2. Kinetic traces of the absorptive 2D signal at different wavelengths indicated as $\lambda_\tau \rightarrow \lambda_t$. A. Selected traces at excitation wavelength λ_τ = 650 nm. B. Selected traces at detection wavelength λ_t = 680 nm. Note the reversed vertical axis.

Comparing the traces at the same detection wavelength (680 nm) and three excitation wavelengths (Figure 6.2B) reveals different dynamics of EET from different Chl *b* pools to the lowest-energy Chls. High-energy Chl *b* absorbing at 645 nm seem to transfer energy directly to the terminal emitters within 1 ps. In contrast, slow components of EET are observed from lower-energy Chl *b* (at 655 nm), which are evidently coupled to intermediate Chl *a* states.

Global lifetime analysis

Global lifetime analysis is a common approach to extract quantitative information about the system dynamics from time-resolved spectroscopy measurements (Holzwarth, 1996; Germano et al., 2004). The underlying assumption is that the time dependence of the signal at any given wavelength can be described as a sum of exponential functions – which will be the case if the signal is proportional to the population of reactants (excited states) in a first-order kinetic reaction. Following this, the time-dependent 2D absorptive signal at any given wavelength pair λ_τ, λ_t is described by the equation:

$$\Delta A(\lambda_\tau, \lambda_t; T_w) = \sum_{i=1}^{n} D_i(\lambda_\tau, \lambda_t) \cdot e^{-\frac{T_w}{\tau_i}} \tag{6.1.1}$$

where τ_i are lifetimes of the system, n is the total number of lifetime components, and $D_i(\lambda_\tau, \lambda_t)$ are 2D decay-associated spectra (2D DAS) for the respective lifetimes. Note that the lifetimes are wavelength independent and determined by simultaneous fitting of the kinetics at all wavelengths. The method of variable projection is applied (Germano et al., 2004) to obtain the 2D DAS amplitudes as linear parameters.

Three lifetimes were necessary to fit the 2DES data recorded from LHCII trimers with 650 nm excitation, for the given signal dynamic and time range. The first two – 0.3 ps, 2.4 ps are within the measurement window of 8 ps, when most of the EET takes place, while the third lifetime combines longer-lived components of excitation decay. The 2D DAS are plotted in Figure 6.5. The spectra have areas of negative amplitude, where the amplitude of the 2D spectra decays over time, and areas of positive amplitude, which indicate rise of signal amplitude with the respective lifetime. During EET, the population of donor states decreases, and the population of acceptor states simultaneously increases; therefore, we expect to see negative 2D DAS amplitudes at the donor wavelengths and positive amplitudes at the acceptor wavelengths of detection. Thus, the first 2D DAS shows predominantly EET from Chl *b* (negative diagonal peak at 650 nm) to Chl *a* (positive cross-peak around 680 nm) – occurring on a timescale of 0.3 ps. The second 2D DAS reflects slower EET from Chl *b* that are weakly coupled to Chl *a*. From the DAS amplitudes we can conclude that around 1/3rd of the initial excitations on Chl *b* are transferred on this slow timescale. Additionally, a negative cross-peak around 655→665 nm shows secondary EET from intermediate-energy Chls. An intermediate state around 667

nm has been observed in several studies and dubbed “bottleneck” state due to the slow EET from it. There is no consensus on which specific Chl molecule is responsible for the bottleneck state but one likely candidate is Chl *a*604 on the lumenal side of LHCII, as it is relatively isolated from other Chl *a* molecules.

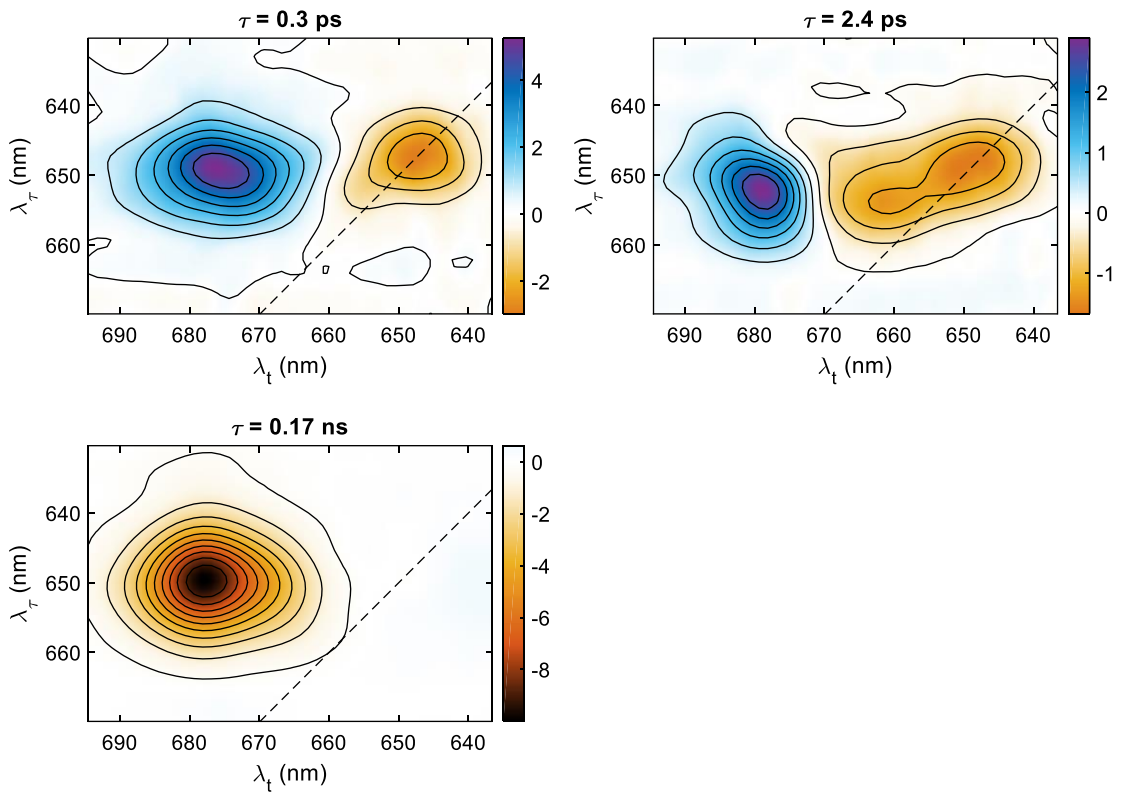

Figure 6.3. Lifetimes (τ) and 2D DAS obtained from global lifetime analysis of the 2D electronic spectra of LHCII trimers recorded with 650 nm excitation pulses. Negative amplitudes coloured in orange-red indicate decay of the negative (GSB/SE) signal and positive amplitudes (blue-purple) indicate rise. Contour lines are plotted at 10% intervals.

6.1.2. Exciton equilibration in the Chl *a* domain

2D electronic spectra upon Chl a excitation at RT

Tuning the excitation laser pulses to the wavelength region 660–680 nm, we can follow the dynamics of exciton equilibration upon direct excitation in the Chl *a* exciton domain. Representative 2D electronic spectra at characteristic waiting times are plotted in Figure 6.4, together with slices taken at different excitation wavelengths. The slices can be interpreted as analogous to pump-probe TA spectra recorded with the respective excitation pulse wavelengths. Due to the large spectral overlap, individual transitions (or cross-

peaks) are not resolved but contribute to the overall spectral shape. After initial excitation, the system tends to relax to progressively lower-energy states causing a shift of the 2D signal to longer detection wavelengths λ_t, i.e. to the left of the diagonal line.

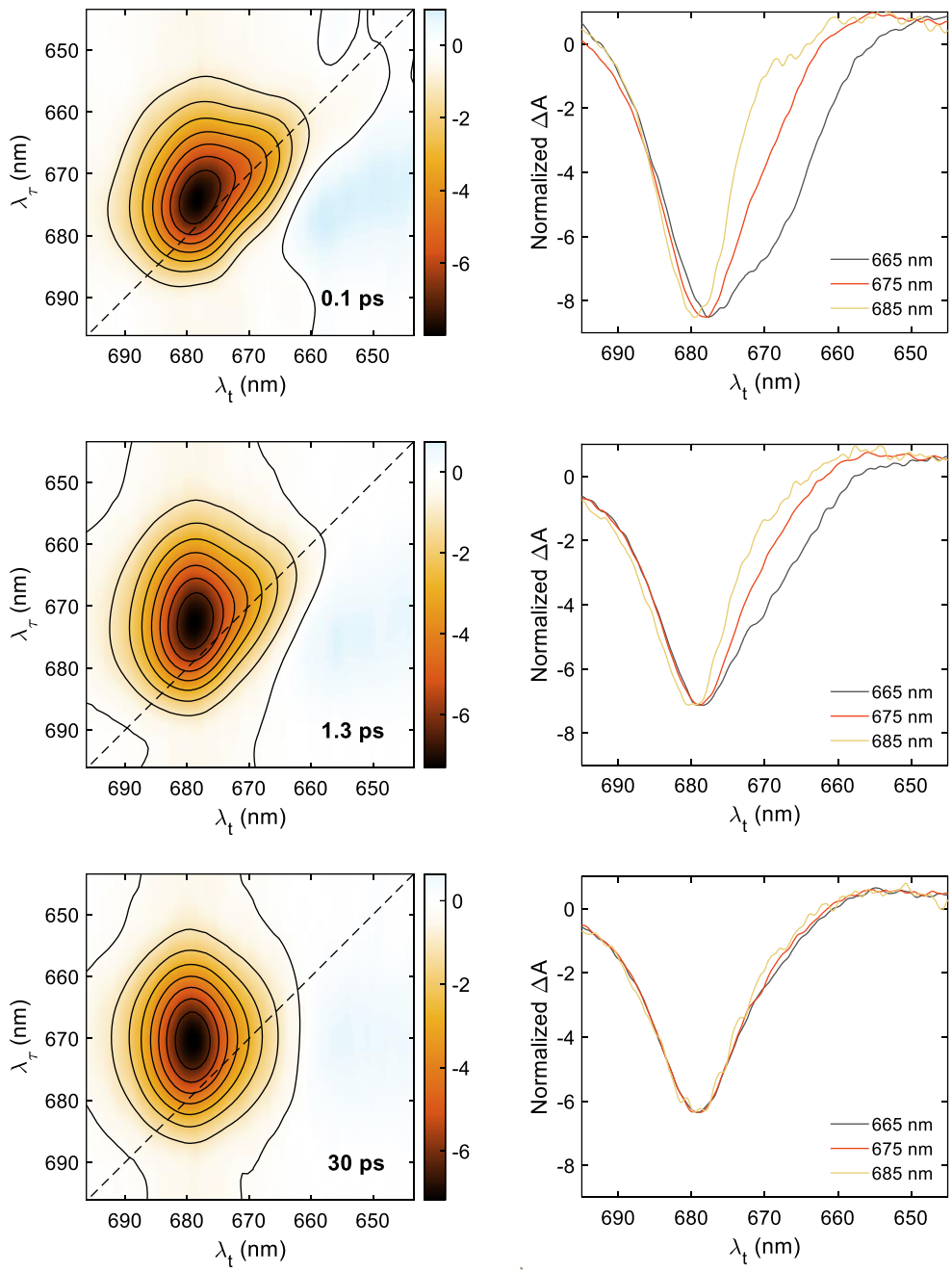

Figure 6.4. 2DES of LHCII with Chl *a* excitation. Left: purely absorptive 2D spectra of LHCII trimers recorded at waiting times (T_w) of 0.1, 1.3 and 30 ps with excitation pulses centred at 675 nm. Right: horizontal slices of the 2D spectra at excitation wavelengths of 665, 675 and 685 nm. The slices are normalized to the negative maximum at 680 nm.

Inspecting the 2D spectrum at T_w = 0.1 ps we can conclude that within this time part of the energy is already transferred from initially excited states absorbing at λ_τ = 660–670

nm to lower energy states at λ_t = 675–680 nm. At longer waiting times the population of higher-energy states diminishes and the spectra become narrower along λ_t. The 2D spectrum at T_w = 30 ps reveals that the complex has reached equilibrium by this time, as the spectrum is independent of the excitation wavelength. The uniformity of the 2D spectral shape is a testament that all absorbing chromophores in the system are coupled via EET. If uncoupled pigments were present, they would be identified as static diagonal peaks in the 2D spectra.

Downhill and uphill energy transfer pathways

Because the energy differences between Chl *a* states are comparatively small, at physiological temperatures there is a significant probability that energy is transferred also uphill, i.e. from lower-energy to higher-energy states. The terminal state is not the lowest-energy exciton state but a thermal quasiequilibrium, wherein different energy levels are populated according to the Boltzmann distribution. The k_BT term at 298 K corresponds to a wavelength difference of ~10 nm, spanning several exciton states. Uphill EET generates cross-peaks at $\lambda_\tau > \lambda_t$ – below the diagonal line. However, assessing uphill EET from snapshot 2D spectra is difficult because positive ESA may obscure any GSB/SE signal below the diagonal line.

Global analysis

The transient 2D data were subjected to global lifetime analysis as described in 6.1.1. Three lifetimes — 0.54 ps, 4.7 ps, and 3.2 ns — were necessary to obtain a good fit of the 2D signal in the time window from 0.15 ps to 60 ps. We stress that these lifetimes do not necessarily reflect exact intrinsic lifetimes in the system, the latter undoubtedly exhibiting a much more complex kinetic profile. Moreover, certain processes, like spectral diffusion, lead to a non-exponential evolution of the signal at a fixed wavelength. The lifetimes should be considered as mean values indicating the timescales that dominate the spectral evolution. The 2D DAS plotted in Figure 6.5 reveal the nature of spectral changes. As discussed before, a conservative positive/negative peak pair in the 2D DAS strongly suggests EET between two states or quasiequilibrated pools of strongly coupled states. As exciton equilibration at RT involves both downhill and uphill steps, positive/negative peak pairs are observed on both sides of the diagonal line. In any coupled group of pigments, the forward and backward transfers always occur on the same

characteristic timescale, therefore they appear as mirror-image peak pairs in the same 2D DAS. This makes 2DES especially useful to identify EET pathways, which would be difficult to resolve otherwise.

From the above it follows that exciton equilibration in the Chl *a* domain occurs with two characteristic timescales. The faster timescale of 0.5 ps involves multiple pathways from states across the Q_y band. The slower timescale, 4.7 ps, is characterised by a negative/positive peak pair signifying EET from around 670 to 680 nm, with its symmetric uphill counterpart 680→670 nm. Note that the spectra are not symmetric with respect to the peak intensity, which depends on the ratio of forward/backward EET as well as the dipole strength of the respective transitions. The final 2D DAS (3.2 ns) does not describe EET but decay of the completely equilibrated state. It is reasonable to assume, in accordance with other works, that the longer EET lifetime represents equilibration between Chls on the sides of the complex (stromal and lumenal) – Chl *a* 613/614 to 610/611/612. Faster EET processes on sub-ps timescale probably represent equilibration within the lumenal and stromal Chl *a* pools. It can be estimated from the DAS amplitudes that the slow equilibration time has up to 40% contribution to the kinetics, whereas ~25% of excitations on upper exciton states are transferred within 100 fs and ~35% are transferred on the timescale of 0.5 ps.

The results confirm previous knowledge that spectral equilibration in LHCII occurs on different timescales from under 100 fs (Calhoun et al., 2009; Schlau-Cohen et al., 2009) to several picoseconds. They also show unequivocally that the slowest major timescale is around 5 ps – we do not merely fail to resolve longer EET lifetimes but the final 2D DAS shows that the complex is completely equilibrated. This is contrary to previous studies assigning lifetimes in the range of tens of ps or even longer to exciton relaxation. We contend that lifetimes in the range of 10–20 ps observed previously (Kwa et al., 1992; Pålsson et al., 1994; Linnanto et al., 2006; Enriquez et al., 2015) are contributed by singlet–singlet annihilation, which is often evident because of the non-conservative shape of the DAS, indicating excitation decay rather than EET, and has been acknowledged in earlier works as discussed by Connelly et al. (1997). In fact we have confirmed this experimentally – under conditions where multiple excitations in the same complex and exciton annihilation are possible (using 10 nJ excitation pulses instead of 1 nJ), lifetimes in the 10–20 ps range appear in the kinetics (data not shown).

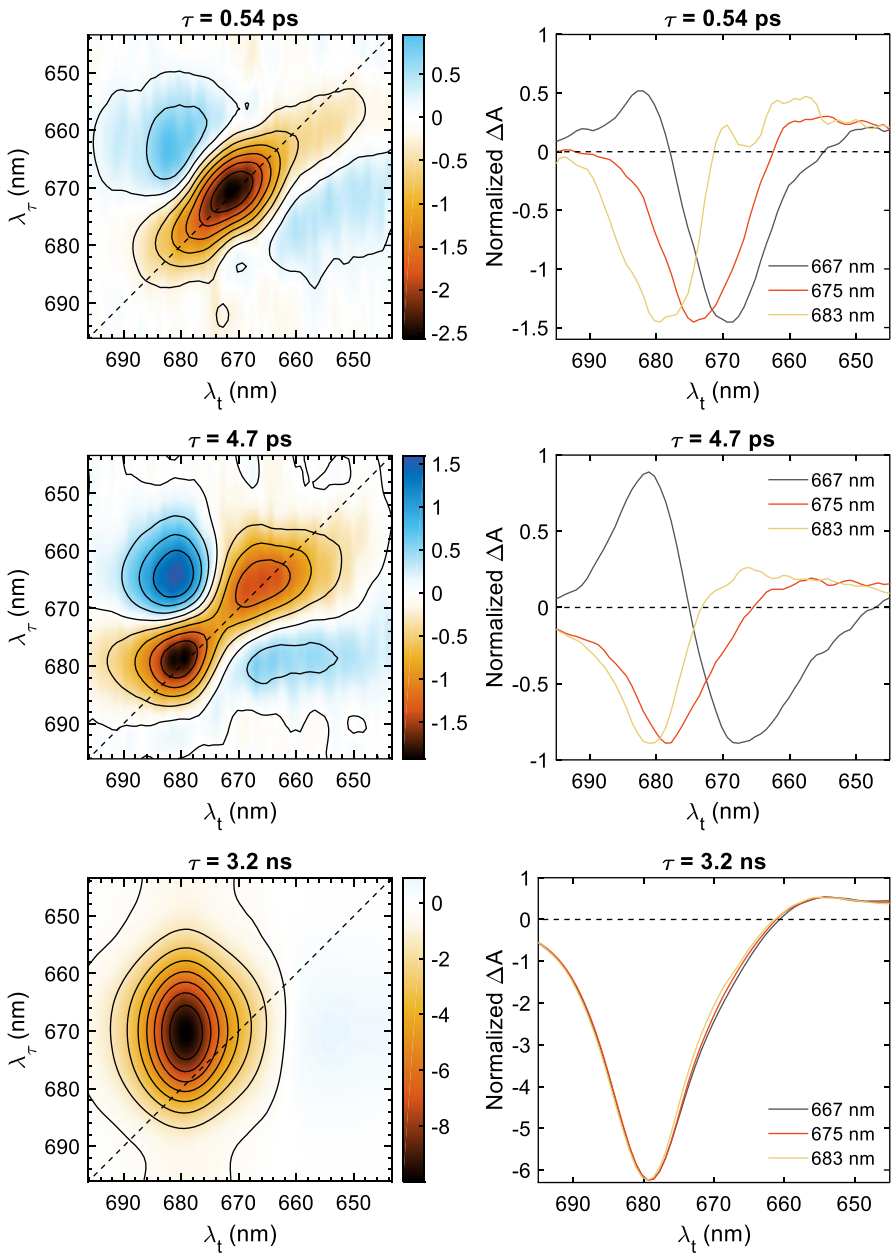

Figure 6.5. 2D decay-associated spectra of LHCII trimers, resulting from a three-exponential fit of the transient 2D signals from 150 fs to 64 ps with best-fit lifetimes of 0.54 ps, 4.7 ps, and 3.2 ns. Left: contour plots of the 2D DAS. Right: horizontal slices of the corresponding 2D DAS at three excitation wavelengths, normalized at their negative maxima.

Our results do not exclude longer processes of *spatial* equilibration of excited states in the trimeric complex that are not accompanied by detectable spectral changes but contribute to the dynamics of exciton annihilation. Equilibration between same-energy exciton states on different monomers may not have a spectral signature but contributes to the dynamics of exciton decay via annihilation (van Amerongen and van Grondelle, 2001; Palacios et al., 2006; Novoderezhkin and van Grondelle, 2010; Novoderezhkin et

al., 2011). Thus, the 2DES results presented here, while consistent with earlier data, separate the kinetics of spectral equilibration from inter-monomer transfer and combined with new structure-based modelling, enable a more accurate and detailed understanding of the light harvesting dynamics. We also demonstrated, for the first time, the bidirectional process of thermodynamic equilibration between excited states coupled by reversible EET and employed this capability of 2DES to identify EET pathways.

6.2. Dependence of energy transfer in LHCII on the molecular environment

6.2.1. Changes in EET induced by LHCII aggregation

2DES of LHCII aggregates with Chl b excitation

Aggregation of LHCII leads not only to strong excitation quenching but is associated with marked spectroscopic changes – as we learned in section 5.1. The CD spectra of LHCII aggregates point to changes in pigment excitonic interactions – especially in the region where Cars and Chl *b* absorb. It is then reasonable to expect that these changes may affect the dynamics of EET, particularly from Chl *b*. To test this hypothesis, we performed 2DES of LHCII aggregates upon Chl *b* excitation (as in section 6.1.1) and compared the results with those of solubilized LHCII trimers (Enriquez et al., 2015).

The 2D spectra of aggregates showed the same general features as solubilized LHCII (data not shown) with no immediately recognizable differences apart from a ~2-nm redshift and the comparatively faster loss of signal amplitude due to excitation quenching. Four lifetime components were necessary to fit the data – 0.23, 2.5, 14 and 160 ps. The 2D DAS show that the first two components represent EET, whereas excitation decay is the dominant process on longer timescales (Figure 6.6). Note that all experiments with Chl *b* excitation were performed with pulses of relatively high energy (10 nJ), which can create multiple excitations in the same complex that result in singlet-singlet exciton annihilation. Because the exciton diffusion length, or functional domain size, in aggregates is much greater (Lambrev et al., 2011), exciton annihilation is more probable and dominates the excitation decay kinetics.

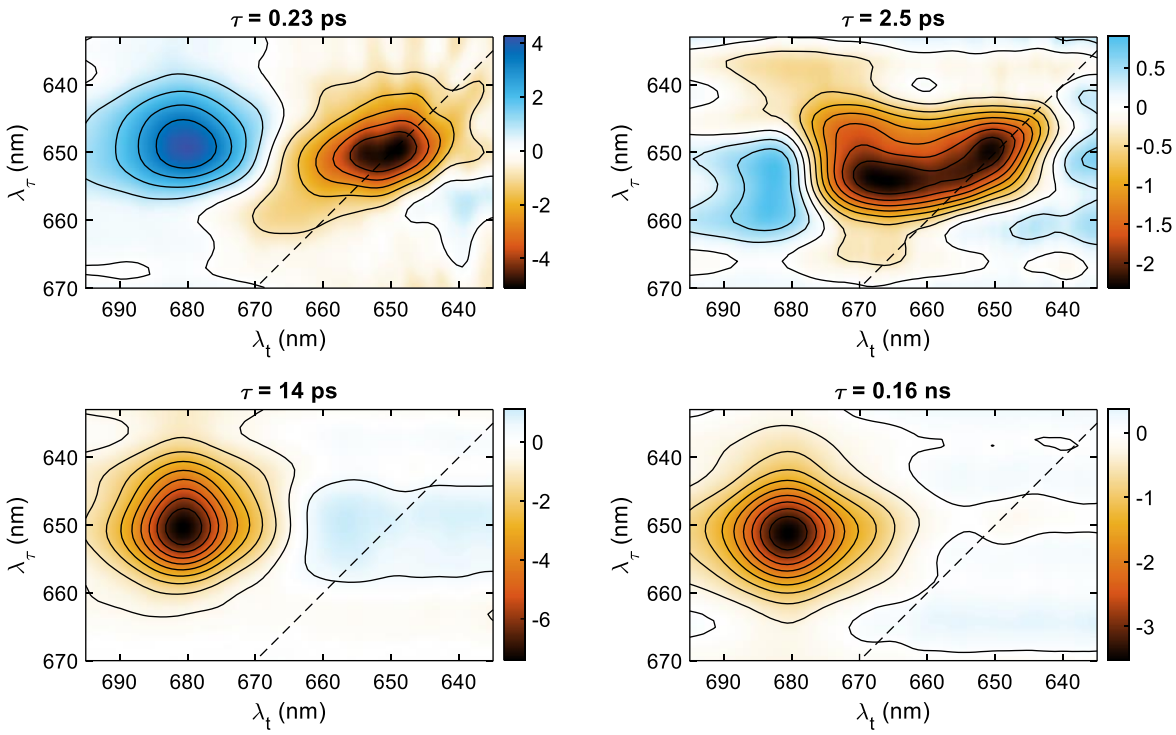

Figure 6.6. 2D DAS of LHCII aggregates, obtained from global lifetime analysis of a series of 2D spectra recorded with 650-nm excitation pulses at waiting times T_w = 150–800 ps. Negative amplitudes coloured in orange-red indicate decay of the negative (GSB/SE) signal and positive amplitudes (blue-purple) indicate rise. Contour lines are plotted at 10% intervals. The decay lifetimes are indicated as the title on each plot.

The main Chl *b* – Chl *a* EET lifetimes in aggregates appear to be similar to those found in solubilized LHCII. No specific differences can be identified in the first 2D DAS. However, the second 2D DAS (2.5 ps) appears qualitatively different in aggregates than the equivalent spectrum in trimers (Figure 6.3). In solubilized LHCII the 2.4 ps timescale was associated with EET from long-lived Chl *b* and from an intermediate state around 667 nm. The spectrum of aggregates shows additional decay in the Chl *a* region at wavelengths around 670 nm. We have ruled out the possibility that exciton annihilation is responsible for the decay on a 2 ps timescale (Enriquez et al., 2015), therefore it must represent a change in the EET dynamics. From measurements with Chl *a* excitation we know that in LHCII trimers equilibration between Chl *a* absorbing around 670 and 680 nm occurs on a 5 ps timescale. It appears that this equilibration process is about twice as fast in LHCII aggregates.

2DES of LHCII aggregates with Chl a excitation

The 2DES of LHCII aggregates with Chl *b* excitation showed that aggregation did not significantly alter the overall rate of EET from Chl *b* to Chl *a* but indicated a change in the equilibration among Chl *a*. To confirm this, we measured 2D electronic spectra of aggregates with excitation pulses centred at 670 nm and low pulse energy (1–2 nJ) to curtail exciton annihilation (unpublished data). Global analysis of the 2D data revealed two characteristic equilibration timescales with 2D DAS (Figure 6.7) that have similar features as in solubilized LHCII (Figure 6.5). However, the lifetimes are approximately half-long in aggregates (0.25 and 2.2 ps compared to 0.5 and 4.7 ps, respectively), confirming an overall acceleration of exciton equilibration.

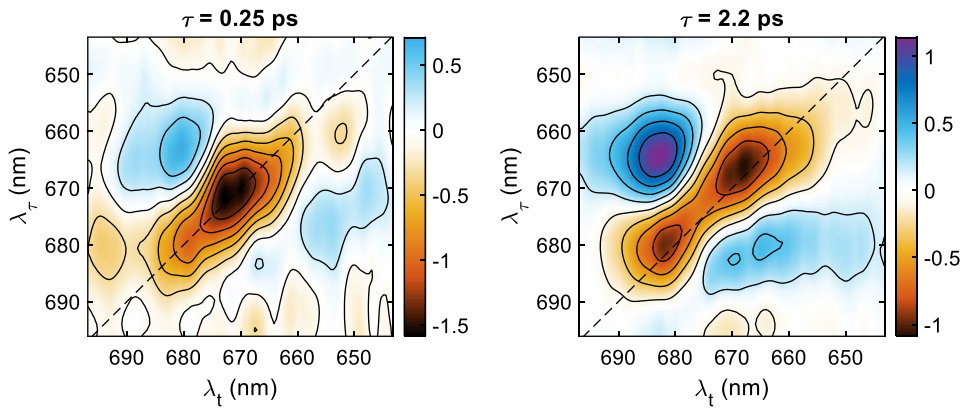

Figure 6.7. 2D DAS of LHCII aggregates, obtained from three-exponential lifetime analysis the 2DES data recorded with excitation pulses centred at 670 nm. The 2D DAS of the final component (excitation decay) is omitted.

There could be different possible reasons for the observed faster exciton equilibration in aggregates. One is that LHCII undergoes structural changes upon aggregation that alter the couplings between Chls in the complex. This has been previously proposed to explain the apparent acceleration of exciton annihilation decay in aggregates (Rutkauskas et al., 2012). Structure-based exciton calculations (Müh and Renger, 2012) predicted that upon aggregation the transition wavelengths of Chls *a*603 and *a*610 are red-shifted by 3 nm. A 1–2 nm red-shift was calculated for Chls *a*611, *a*612 and *a*613. The reorientations and changes in energy levels may be the reason for altered EET but are small enough so that 2D cross-peaks in trimers could be attributed to the same pigment groups. Accelerated equilibration could also be observed if there is rapid EET between subunits in the aggregate. The existence of inter-complex energy transfer was previously inferred from the large functional domain size of LHCII aggregates (Lambrev et al., 2011). We hypothesized

that the 5-ps equilibration time in trimers reflects transfer between the stromal and lumenal Chl *a* pools. In aggregates the equilibration time would be shortened if there is hopping from the peripherally positioned Chl 613/614 pair to Chls on the nearest neighbour complex. It must be said that regardless of the underlying mechanism, acceleration of exciton equilibration within and between LHCII in the aggregate coincidentally facilitates excitation quenching and, therefore, photoprotection.

6.2.2. Temperature dependence of EET in LHCII

In our earlier 2DES investigation of LHCII at RT (section 6.1.2), the slowest exciton relaxation timescale was found to be about 5 ps leading to complete thermal equilibration between all states. These data showed that overall exciton equilibration is faster than predicted by current models (Novoderezhkin et al., 2011; Renger et al., 2011). We also demonstrated that 2DES is well suited to simultaneously probe uphill and downhill EET processes which are difficult to resolve in transient absorption experiments. In this section, I will present the first reported 2DES study of a photosynthetic complex performed under conditions of very low excitation and hence negligible singlet-singlet annihilation, while at the same time with high signal-to-noise ratio to allow detailed kinetic modelling (Akhtar et al., 2019). We explore the kinetics of exciton relaxation in LHCII as a function of temperature in the range of 77 to 295 K using excitation pulses of very low energy (~0.5 nJ) centred at 670 nm and approximately covering the Chl Q_y absorption band from 650 to 700 nm.

2D electronic spectra at 77 K

Here I summarize the qualitative features of the 2D spectra of LHCII recorded at 77 K. A more detailed analysis of the kinetics of EET will be presented in section 6.2.3). Selected 2D electronic spectra at different waiting times T_w are plotted in Figure 6.8. Thanks to smaller homogeneous and inhomogeneous broadening at cryogenic temperatures, the spectra are more structured, and features are better resolved compared to RT. The spectrum at T_w = 0.1 ps has non-zero amplitude mostly along the diagonal line, indicating that very little population transfer has occurred in this time. In contrast, only long-wavelength states are populated at T_w > 10 ps and the spectrum resembles a vertical strip centred at λ_t = 678 nm. In-between, diagonal peaks give way to cross-peaks as energy is transferred downhill to longer-wavelength states.

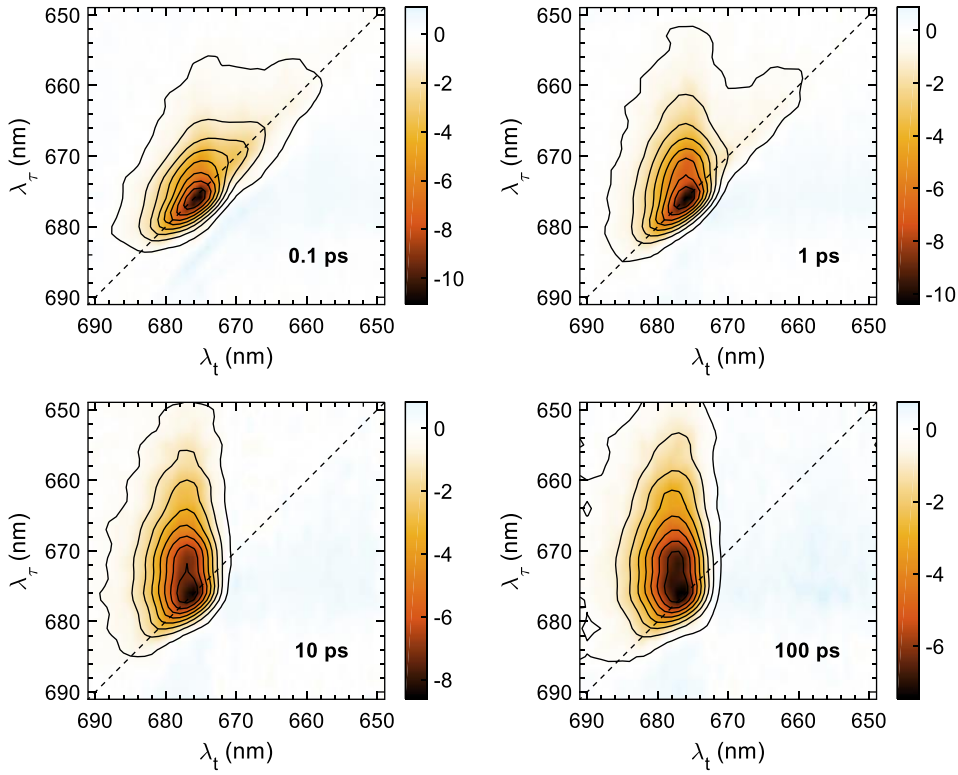

Figure 6.8. Representative purely absorptive 2D electronic spectra of detergent solubilized LHCII trimers recorded at 77 K with excitation pulses centred at 670 mm, at selected waiting times T_w as indicated. The symbols λ_τ and λ_t indicate excitation and detection wavelengths, respectively. (Akhtar et al., 2019)

In contrast to the results at RT, wherein the spectral evolution was all but completed by 10 ps, a gradual rise of the cross-peak amplitude is seen at 77 K indicating slower components of EET. Also in stark contrast to the RT data, the final spectrum retains pronounced dependence on the excitation wavelength, whereas at RT any such dependence is lost and the final state is thermally equilibrated within a few ps. The most probable reason for this is inhomogeneous broadening, or static disorder, of the final state. In other words, the lowest energy level varies among LHCII units, locked in slightly different protein conformations at low temperatures. At higher temperatures, thermal fluctuations diminish or completely lose the correlation between the excitation and detection wavelength (spectral diffusion). Another hypothesis, that will be tested in the next section, could be that there exist at least two distinct sink states in the same protein complex, which are not connected by EET. In favour of this possibility are the findings of Vrandecic et al. (2015) that the lowest-energy levels and fluorescent states are temperature-dependent – at RT and down to 150 K fluorescence is emitted mainly from Chl 612 but other

states also contribute to the emission below 150 K. This can be understood if at low temperatures there is effectively no EET between, e.g. the lumenal and stromal Chl *a* pools.

Global lifetime analysis of the 2DES data at 77 K revealed three characteristic EET timescales – 0.4, 2.7 and 15 ps – rising cross-peaks at various wavelengths in the respective 2D DAS (Figure 6.9). The fastest timescale comprises EET from Chl *a* states absorbing around 670 nm to lower states and from Chl *b* to states around 674 nm, EET from 660–668 nm to 675–678 nm occurs on a 2.7 ps timescale, and the slowest component reflects relaxation in the low-energy Chl *a* region 675–680 nm. The lifetimes as well as the spectral features are closely comparable to TA data reported by van Grondelle's group (Visser et al., 1996; Gradinaru et al., 1998; Palacios et al., 2006; Marin et al., 2012). Considering the different excitation wavelengths together as well as the 2D DAS, we can make a more confident analysis of the EET pathways at 77 K (in section 6.2.3).

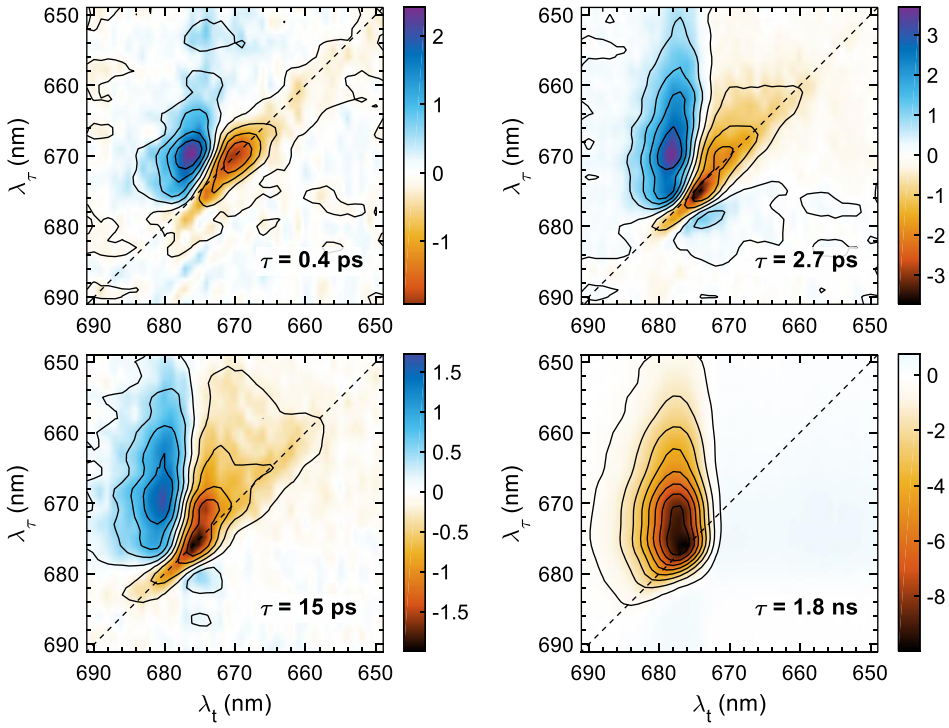

Figure 6.9. 2D DAS of LHCII at 77 K, obtained from four-component global lifetime analysis of the 2DES data. Red/blue colours represent negative/positive amplitudes (decay/rise of the GSB signal). (Akhtar et al., 2019)

Temperature dependence of uphill and downhill EET

It is evident that not only the absorptive spectral lineshape of the Chl Q_y transitions, but also the dynamics of EET recorded at 77 K considerably differ from those measured at RT. While cryogenic temperatures provide a great advantage in resolving spectral components and modelling the excitation dynamics, ultimately it is the goal to gain knowledge on the function of the light-harvesting antenna under natural physiological conditions. Figure 6.10 shows 2D electronic spectra recorded at temperatures 110, 150 and 230 K. With increasing temperature, the spectra gradually broaden and their maxima shift to longer detection wavelengths; at long waiting times the correlation between λ_t and λ_τ is gradually lost and the quasiequilibrated state is reached at shorter times (data not shown).

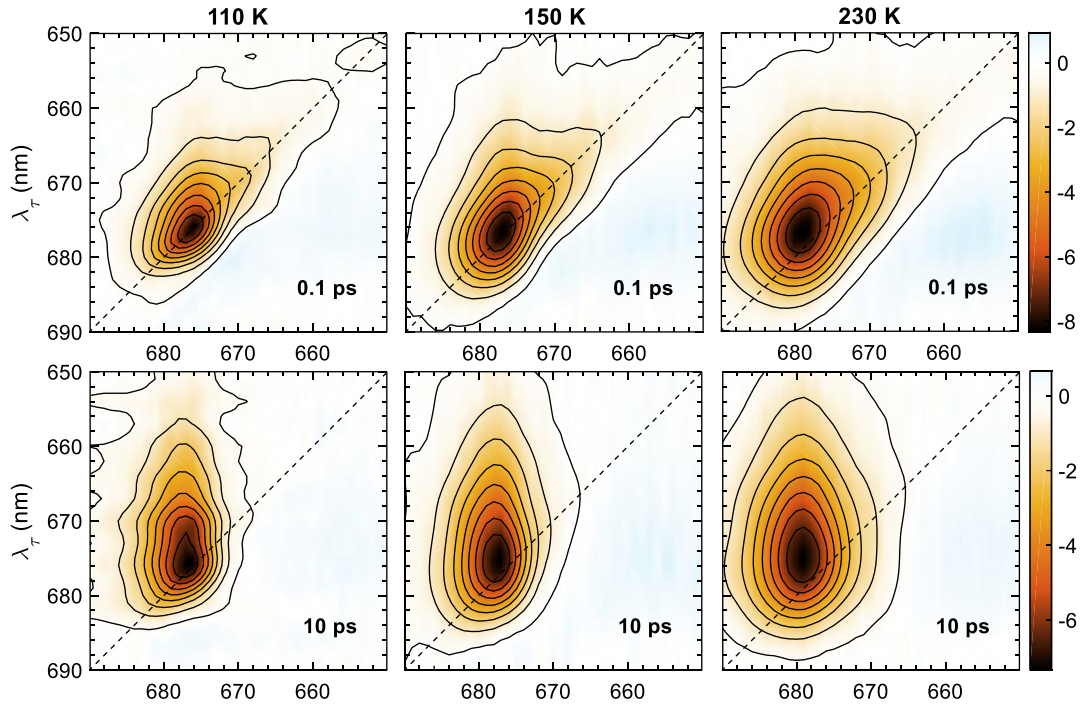

Figure 6.10. 2D electronic spectra of LHCII recorded at 110, 150 and 230 K. The top and bottom rows show 2D spectra at waiting times T_w = 0.1 and 10 ps, respectively.

The EET lifetimes determined by global analysis are gradually shortened as temperature is increased (Table 6.1). Also, the average lifetime of the rise of the cross-peaks, as an indicator of the overall EET time, sharply decreases with temperature. Undoubtedly, exciton equilibration occurs on faster timescales at higher temperatures.

Table 6.1. EET lifetimes at different temperatures

T (K)	τ_1 (ps)	τ_2 (ps)	τ_3 (ps)	τ_{avg}*
77	0.3	2.5	14.2	3.0
110	0.2	2.0	9.7	1.9
150	0.2	1.6	7.4	1.4
230	0.2	1.7	6.3	0.9
295	0.2	0.9	5.4	0.8

* average lifetime of the rise of the cross-peak 668→680 nm

It is well established that temperature affects the position and lineshape of the absorption/emission bands in LHCII (Hemelrijk et al., 1992). Changes in the transition energies and spectral lineshapes inevitably affect the EET rate constants as well, which is reflected in the kinetic lifetimes. The outcome is general acceleration of exciton relaxation with temperature, as the decay and rise lifetimes of the diagonal and cross-peak signals, respectively, as well as the lifetime amplitudes at different wavelengths show. A significant contribution to the acceleration of exciton relaxation with temperature is the strong temperature dependence of energetic uphill pathways. In an inhomogeneous energy landscape, excitations are dynamically trapped and detrapped via uphill transfer. As these routes become inaccessible at lower temperature, EET slows down.

As it was pointed out above, 2DES provides advantage over one-dimensional TA in its ability to simultaneously resolve uphill and downhill EET pathways. This is further corroborated by comparing downhill/uphill components resolved by 2DES as a function of temperature. The detailed-balance condition dictates that the ratio of forward/reverse (uphill/downhill) rate constants should follow the Boltzmann distribution function (Pollard and Friesner, 1994). Downhill/uphill EET is followed by the cross-peak intensity at λ_t greater/less than λ_τ (Duan et al., 2015). The overall redistribution of energy in downhill and uphill pathways is depicted by the sum of all EET 2D DAS, plotted in Figure 6.11 for different temperatures. The figure shows that as the temperature gets lower, the "uphill cross-peaks" amplitude is reduced, and the effect is more pronounced at detection wavelengths farther away from the diagonal (where the energy gap is larger).

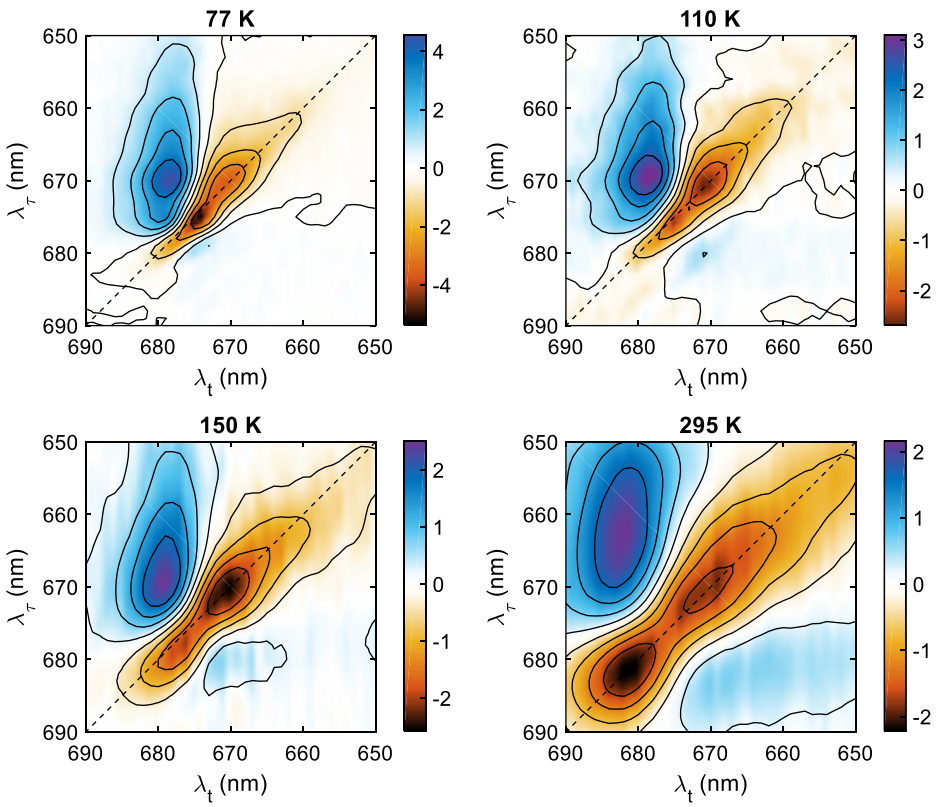

Figure 6.11. Total redistribution 2D difference spectra at different temperatures. For a given temperature, the redistribution difference spectrum is the sum of the 2D DAS for all components except the last decay (to the ground state). The total uphill EET signal decreases with lowering the temperature.

Figure 6.12 shows the ratio of the amplitudes of the final 2D DAS component (nanosecond decay) at selected "uphill" wavelengths relative to the "downhill" counterpart amplitude as a function of temperature. The uphill/downhill amplitude ratios increase with temperature, depending on the energy gap between the two wavelengths and approximately match the expected Boltzmann equilibrium population of the respective states. This is probably the first direct experimental proof that EET in LHCs follows the detailed balance condition.

The experimental data reported here encode a wealth of information regarding the energetic and dynamic properties of LHCII, including electronic dephasing times, inhomogeneous broadening, EET rates, etc., and their temperature dependence. While some of these parameters can be directly read from the data, others can be determined through modelling. Thus, these results will help in refining the current exciton model of LHCII and in better understanding the photophysics of LHCII and similar complexes.

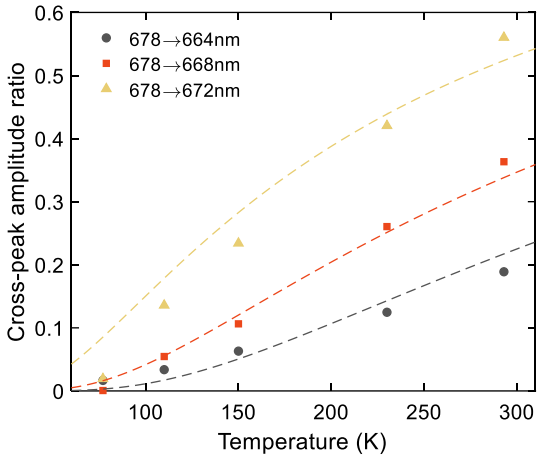

Figure 6.12. Temperature dependence of the uphill/downhill cross-peak amplitude ratios of the final 2D DAS representing the decay equilibrium in LHCII. Dashed lines – estimated equilibrated population of the respective states, from the Boltzmann distribution: $e^{(E_a-E_b)/k_BT}$.

6.2.3. Phenomenological model of EET at 77 K

Although valuable spectroscopic information has been unveiled with 2DES, a complete characterization of the EET network of LHCII with one to one mapping between the excitonic levels and pigment identities remains elusive. We applied phenomenological model fitting to the 2DES data of trimeric LHCII obtained at 77 K and proposed tentative EET schemes that compare well with the modified Redfield-generalized Förster models (Do et al., 2019).

Brief description of the theoretical model

The principles of the modelling method were proposed by Dostál et al. (2016) and were implemented to analyze the EET network of Fenna-Matthews-Olson (FMO) complex of green sulfur bacteria by Zigmantas's group (Thyrhaug et al., 2018). In contrast to FMO, which has only 7–8 pigments that are energetically separated, LHCII exhibits highly congested 2D electronic spectra necessitating modifications of the modelling approach to resolve the EET network.

The parameters of the model are excitonic energy levels **E**, transition dipole moments **μ**, spectral linewidths **σ**, the transfer-rate matrix **K** containing information about EET between excitons, and a matrix **X** containing information of the cross-peaks at zero waiting time.

The 2D electronic spectra are described by the equation

$$\mathbb{S}_{2\mathrm{D}}(\omega_t, T_w, \omega_\tau) = I_{exc}(\omega_\tau)\left[\sum_{i=1}^{N}\sum_{j=1}^{N} I_{ij}^{2\mathrm{D}}(T_w) S_{ij}(\omega_t, \omega_\tau) + \mathbf{S}^{\mathrm{A}}(\omega_t, \omega_\tau)\right] \tag{6.2.1}$$

where $I_{exc}(\omega_\tau)$ is the excitation pulse spectrum, the matrix $\mathbf{I}^{2\mathrm{D}}(T_w)$ describes the dynamic intensity (amplitude) of all exciton peaks, $\mathbf{S}(\omega_t, \omega_\tau)$ defines their peakshapes and $\mathbf{S}^{\mathrm{A}}(\omega_t, \omega_\tau)$ is a phenomenological ESA spectrum. The peakshapes are parametrized as 2D gaussians with σ as a width ρ as a correlation parameter related to the degree of inhomogeneous broadening. The time-dependent intensity matrix $\mathbf{I}^{2\mathrm{D}}$ is calculated by the equation

$$\mathbf{I}^{2\mathrm{D}}(T_w) = \mathrm{diag}(\boldsymbol{\mu}^2)\mathbf{F}e^{\mathbf{K}T_w}\mathrm{diag}(\boldsymbol{\mu}^2) \tag{6.2.2}$$

where $\mathbf{F} = \mathbb{I} + \mathbf{X}$ defines the species-associated spectra, with $\mathbb{I}$ the identity matrix corresponding to diagonal GSB/SE signals and $\mathbf{X}$ describing (time-independent) off-diagonal signals.

A non-linear least-square fitting routine is implemented to fit the modelled 2D electronic spectra to the experimental data. In this way, we can obtain valuable information about the excitons and EET network in LHCII. To determine the uniqueness of the best-fit solution and to ensure reaching a global χ^2 minimum, the optimization was repeated with random initial values of the model parameters.

Simulated 2D spectra and exciton parameters

Hereafter I will present the model fitting of the 77 K 2DES data with eight exciton states. Fewer states resulted in unsatisfactory fits while adding more than eight states in the model resulted in heavy interdependence of the model parameters. An eight-state model resulted in very good fit of the experimental spectra (Figure 6.13) and a low number of possible solutions (see below).

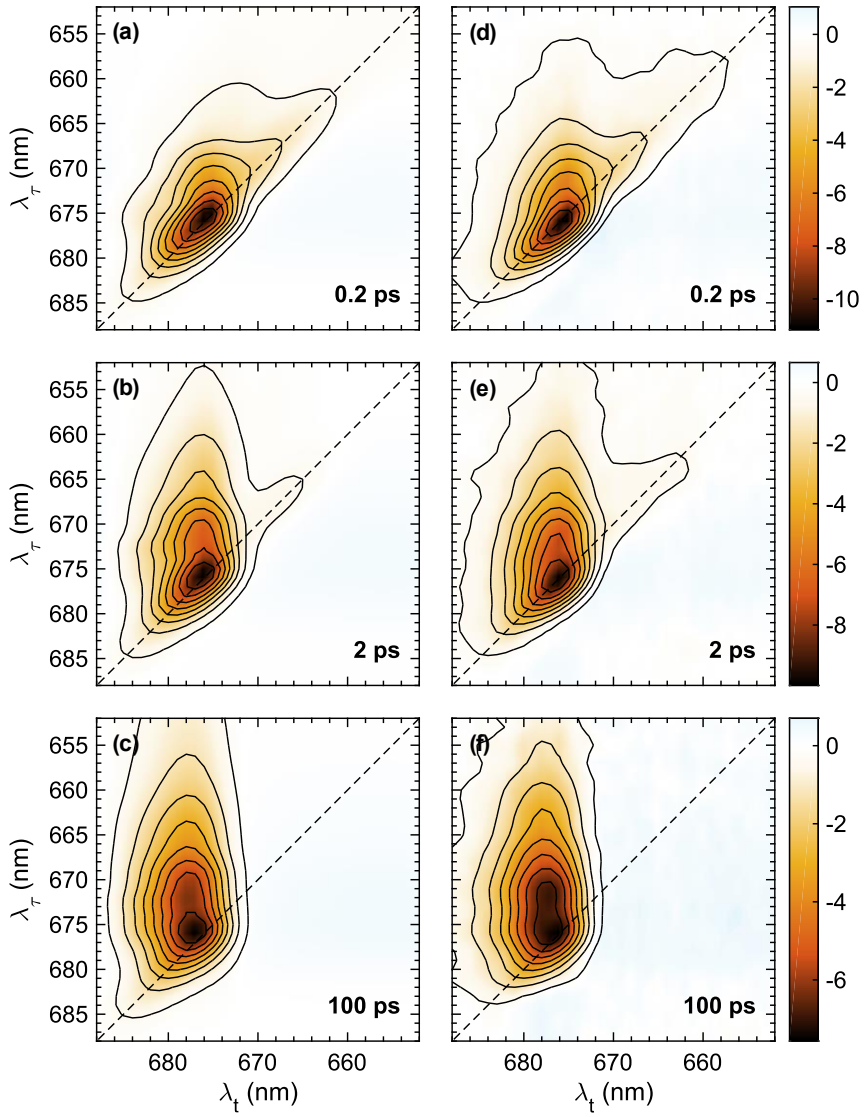

Figure 6.13. Comparison between the simulated 2D electronic spectra obtained from a representative fit with an eight- exciton model (left) vs. the corresponding experimental ones (right) at waiting times of T_w = 0.2, 2 and 100 ps. (Do et al., 2019)

The fitting results were sorted based on the residuals from the best fit (lowest residual) to the worst fit (highest residual) and the best 120 fits were selected to be further interpreted. The modal values of the wavelengths and widths (homogeneous and inhomogeneous half-width at half-maximum) are shown in Table 6.2. The top 120 fits showed variation in wavelengths of less than 1 nm for the four lower-energy states and within 2 nm for wavelengths <670 nm highlighting that the method is capable of resolving the exciton energies with great accuracy. The frequencies of the five lowest states coincide within 10 cm^{-1} with those determined by Calhoun et al. (2009) from the coherence beatings of the respective excitons. Exciton states in the short-wavelength region (<670 nm) are not fully resolved mainly because of the low excitation power, hence low signal-to-noise ratio in

the data. Thus, this region, is represented by three states with broad spectral widths, precluding a detailed mapping of the Chl *b* to Chl *a* EET pathways.

Table 6.2. Best-fit LHCII exciton parameters of the phenomenological model fit of 2DES data

Wavelength, nm	Frequency, cm^{-1}	Homogeneous width, cm^{-1}	Inh. width, cm^{-1}
655*	15265	75	200
664	15080	50	110
668	14990	32	140
670	14910	30	57
673	14860	20	25
675	14815	25	33
677	14760	27	52
680	14695	28	80

* fixed

Exciton dynamics

Exciton relaxation is described by the transfer-rate matrix **K**. In principle, the fitting does not result in a unique solution of **K** – different combinations of rate constants can yield similar goodness of fit. However, upon a closer look, we can identify recurring patterns in all 120 best fits. We applied machine-learning algorithms to group similar solutions into two clusters, denoted in red and blue colour in Figure 6.14. One cluster (blue) is highly homogeneous with virtually identical values among all solutions. The second cluster (red) also exhibits high degree of overall homogeneity except for some elements of the high-energy excitons, which display high variation. Further, we select representative solutions from the red and blue clusters and refer to them as Model A and Model B, respectively. The sets of rate constants of these two solutions are shown in Table 6.3 and Table 6.4 with red/gold shading indicating that the corresponding elements of the **X** matrix have high/intermediate values. The last column in the tables shows the decay lifetimes (inverse eigenvalues of the **K** matrix) rearranged to match the state dominating the decay. Because of the limited time resolution of the experiment, very fast EET pathways are unresolved and appear in the **X** matrix, somewhat complicating the model interpretation. Model A has more states decaying in 0.1–1 ps and provides better fit in this time window, whereas model B is better at $T_w > 1$ ps (data not shown).

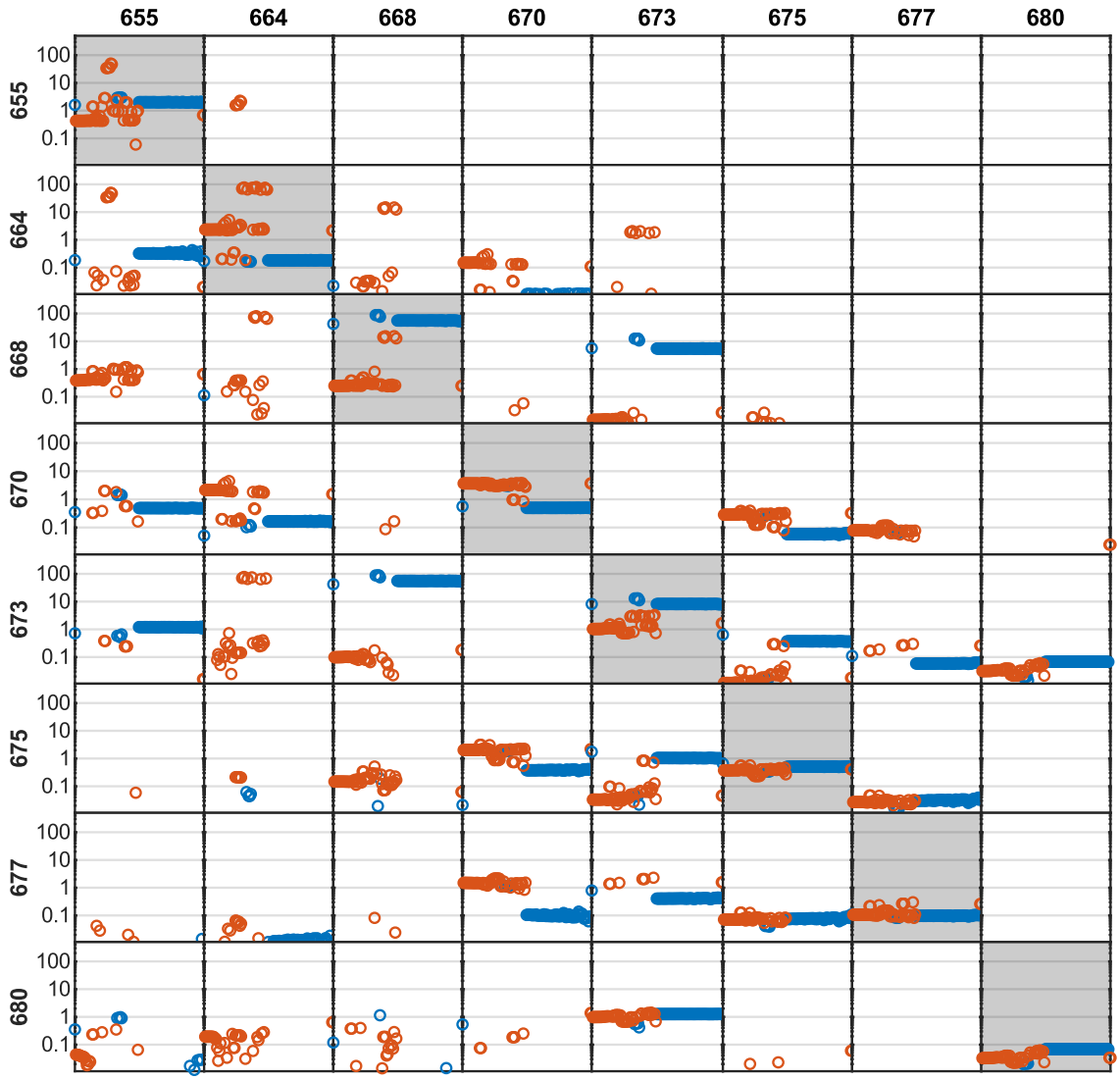

Figure 6.14. Best-fit values (ps^{-1}) of the EET rate constant matrix **K** for 120 fits, sorted by increasing mean squared error (left to right). Rows and columns represent donor and acceptor states, respectively and diagonal cells show the total decay rates of the corresponding excitons. (Do et al., 2019)

The two solutions share common traits especially in regard with the dynamics between the lowest three states (675–677–681 nm). Both models contain a long-lived intermediate state at 668 nm (A) or 664 nm (B) decaying with a rate of ~0.2 ps^{-1} (decay lifetime 4.4/5.7 ps). This clearly corresponds to the "bottleneck" state observed in other studies (Novoderezhkin et al., 2005; Calhoun et al., 2009; Schlau-Cohen et al., 2009; Schlau-Cohen et al., 2010; Renger et al., 2011; Marin et al., 2012). Both contain another state at 668–670 nm that rapidly relaxes (in 0.2 ps or less) to lower-energy states. In model A, the long-lived state is strongly coupled to lower states via the **X** matrix. This is not a physically realistic scenario as the bottleneck state is weakly coupled and, vice versa,

strongly coupled states are short-lived. Therefore, the result indicates the existence of degenerate states at this wavelength (not that there are more exciton states in this wavelength region, than are resolved by the model). Earlier experimental results suggested that the 664 nm state also contributes significantly to the 12–15 ps decay lifetime (Visser et al., 1996; Palacios et al., 2006). However, the present modelling clearly separates the decay of the 664 nm state occurring on a ~5 ps timescale from the 13 ps decay lifetime, which reflects equilibration among the lowest energy sinks (Table 6.4).

Table 6.3. Rate constants (ps^{-1}) of EET transfer in LHCII and strongly coupled states (model A)

	655	664	668	670	673	675	677	680	τ, ps
655	−0.43								2.3
664		−2.3		0.15					0.5
668	0.39		−0.25		0.01	0.01			4.4
670		2.1		−3.7		0.28	0.08		0.2
673			0.10		−1.0	0.01		0.03	0.9
675			0.15	2.0	0.03	−0.37	0.03		2.3
677				1.5		0.07	−0.11		170
680	0.04	0.19			0.98			−0.03	2000

Table 6.4. Rate constants (ps^{-1}) of EET transfer in LHCII and strongly coupled states (model B)

	655	664	668	670	673	675	677	680	τ, ps
655	−2.0	0.01							0.5
664	0.32	−0.18		0.01					5.7
668			−56		5.5				0.02
670	0.49	0.16		−0.49		0.06	0.01		1.7
673			56		−8.2	0.37	0.06	0.07	0.4
675				0.38	1.0	−0.50	0.03		3.3
677		0.01		0.10	0.40	0.07	−0.10		13
680					1.3			−0.07	2000

The three lowest-energy states 675–677–680 nm, which act as final energy sinks are populated from higher exciton levels mostly within 1 ps. A striking result is the lack of significant direct EET among these three sinks. The result is roughly in line with the calculations of Renger et al. (2011) who predict rather slow exchanges between the energy sinks. Nevertheless, the excitation energy is slowly equilibrated via higher-energy exciton levels acting as a bridge between the sinks. The 675-nm state equilibrates on a 3–6 ps timescale via 670–673 nm states. The slowest energy transfer (13 ps, Model B) is between

677 and 680 nm. In equilibrium all three sinks have non-zero population even at 77 K, in agreement with fluorescence studies (Pieper et al., 2001; Pieper et al., 2009; Vrandecic et al., 2015).

Mapping exciton states to Chls in LHCII

The model described above provides great detail about the dynamics in the frequency/wavelength domain but no information about EET in space, i.e. between Chls. Combining knowledge about the structure of LHCII (Figure 2.9) and structure-based exciton energy calculations (Novoderezhkin et al., 2011; Renger et al., 2011; Zucchelli et al., 2012), we can attempt to assign exciton states to specific Chl molecules or groups of Chls, thus creating a microscopic model of EET. There are several caveats – the energies of some Chls calculated by different authors vary widely (see section 2.3.2) and not all exciton states are resolved by the phenomenological model; therefore, the assignment is only tentative at this stage.

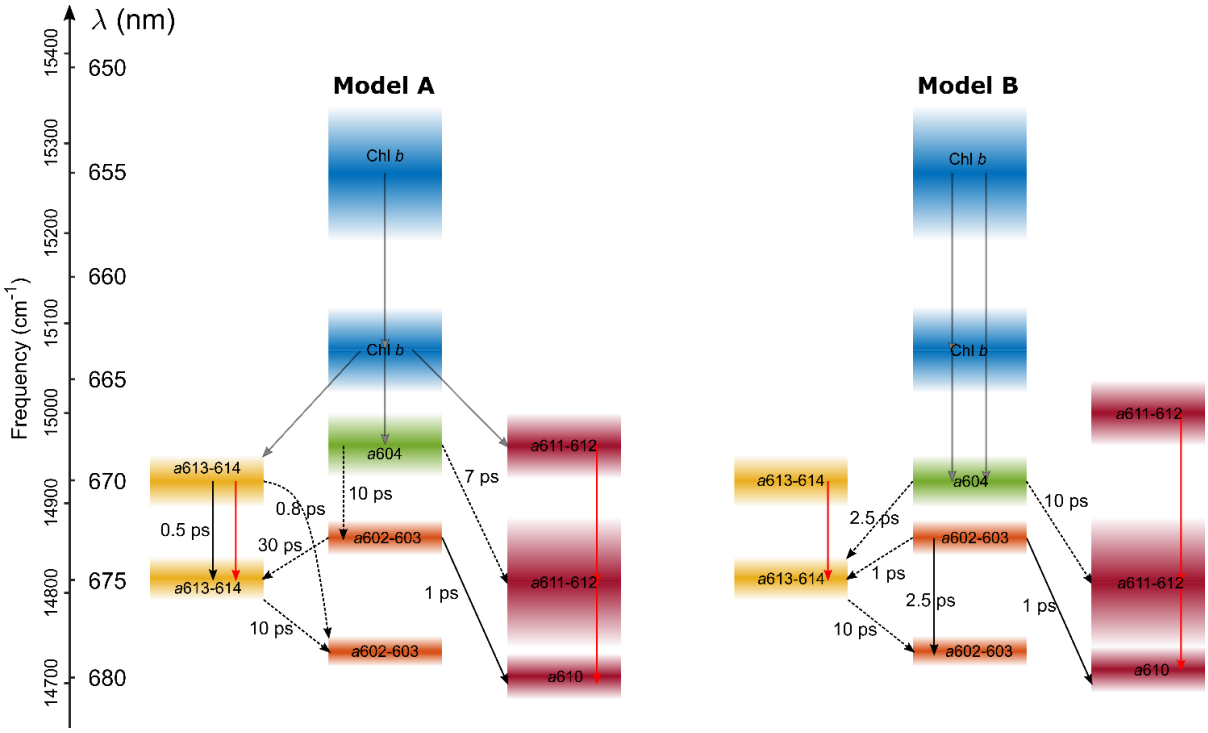

Figure 6.15. EET in trimeric LHCII at 77 K based on model A and model B. The colours of excitonic levels indicate strongly coupled domains, except the blue colour is used to represent the Chl *b* manifold. Only downhill transfers are presented by the arrows. Red arrows indicate fast relaxation within strongly coupled domains. (Do et al., 2019)

Several considerations are made in creating the scheme:

- Exciton states, which are simultaneously long-lived and coupled to other states via the **X** matrix are split into two degenerate states.
- Strongly coupled states are assigned to closely spaced Chls
- The three lowest exciton states are assigned to three excitonically coupled groups of Chls – *a*610/611/610, *a*602/603 and *a*613/614
- The lowest state is assigned to Chl *a*610 which is coupled to the pair *a*611-*a*612, on the stromal side of the complex
- The long-lived state around 667 nm can be assigned to Chl *a*604 according to Novoderezhkin et al. (2005; 2011), and another short-lived state in this region is interpreted as a higher-exciton level of the *a*611/612 pair.
- The 670–675 nm exciton level pair is weakly connected to the other groups and therefore assigned to Chls *a*613/614.

According to the model scheme (Figure 6.15), rapid relaxation occurs between levels belonging to each of the three groups of excitonically coupled Chl *a* but slow or no direct EET occurs between them. Overall, however, the exciton groups equilibrate via couplings between upper energy levels. This shows that thermally activated uphill EET components are crucial for the migration of excitons even at cryogenic temperatures and evidently more so under physiological conditions. The two stromal pools, *a*610/611/610 and *a*602/603 equilibrate on a timescale of 2–6 ps, on the same timescale as EET from the 'bottleneck' state (here is assumed that it belongs to *a*604 but this may not be the case). The slowest terms of the spectral dynamics of 10–15 ps represent equilibration between the stromal and the lumenal (*a*613/614) pools, in good agreement with the theoretical calculations (Novoderezhkin et al., 2011). The final state is a thermal equilibrium primarily among the three sinks, with Chl *a*610 having ~60% population. This equilibrium is independent from the initial excitation conditions, which is an important physiological characteristic of the light-harvesting antenna. Nevertheless, the 2D spectra at 77 K clearly show residual correlation between excitation and detection wavelength, which according to the present model is due to inhomogeneous broadening, or static disorder, of the lowest exciton state.

The phenomenological modelling of the 2DES data could not unambiguously resolve all individual exciton states, partly because of insufficient excitation pulse bandwidth and

consequently low signal-to-noise ratio in the Chl *b* region. Nevertheless, the approach clearly uncovered a wealth of information about the dynamics of EET in addition to conventional global analysis approaches – note that three EET timescales were resolved by global analysis. We were able to precisely determine the energies, homogeneous and inhomogeneous bandwidths of five exciton states – information that is not readily accessible by conventional transient absorption spectroscopy. Ultimately, structure based theoretical modelling combined parameter fitting of the 2DES data can reveal a more complete picture of EET but the phenomenological approach might be the best viable option for antenna complexes or experimental conditions of unknown protein structure.

6.2.4. Spectral tuning of LHCII in the green alga *Bryopsis corticulans*

Bryopsis corticulans (*B. corticulans*) is a siphonous green macroalga found in intertidal coastal areas where its single-cell thallus may get periodically partially or completely submerged. The ecological niche drives adaptive changes in the species to optimally utilize photosynthetic radiation under water and in a rapidly changing light environment (Kirk, 2011). Its light-harvesting system, including LHCII, is adapted for enhanced absorption of blue-green light. LHCII of *B. corticulans* has more than 70% sequence homology with plant LHCIIb (Chen et al., 2008; Wang et al., 2013) but has a different Car and Chl composition. Blue-green absorption is augmented by the keto-carotenoids siphonein and siphonaxanthin (Nakayama and Okada, 1990; Chen et al., 2008; Wang et al., 2013), that replace lutein and violaxanthin found in plant LHCII, and by a higher Chl *b*/*a* ratio. Pigment analysis suggested that instead of eight Chl *a* and six Chl *b*, LHCII of *B. corticulans* binds six Chl *a* and eight Chl *b* (Wang et al., 2013). The specific characteristics of *B. corticulans* LHCII make it a useful model to understand the design principles of light harvesting and photoprotection (Christa et al., 2017; Giovagnetti et al., 2018).

Previous investigations of EET in LHCII from a related species, *B. maxima*, suggested that a fraction of Chl *b* is energetically unconnected, raising the question whether spectral adaptation of the complex comes at a price of compromising its efficiency. We performed a comprehensive spectroscopic characterization of LHCII isolated from *B. corticulans* and analyzed the results in comparison with higher-plant LHCII (Akhtar et al., 2020).

Chl spectral forms and excitonic states

The 77K absorption and fluorescence emission spectra of LHCII trimers isolated from *B. corticulans* solubilized with β-DDM are compared with LHCII isolated from pea (*Pisum sativum*) in Figure 6.16. The absorption spectrum of higher-plant LHCII have two characteristic peaks, at 652 and 675 nm, corresponding to the Q_y transitions of Chl *b* and Chl *a*, respectively. LHCII from *B. corticulans* shows higher absorption from Chl *b* with two resolved peaks – at 650 and 658 nm – and lower absorption from Chl *a*. The difference spectrum with *P. sativum* shows negative peaks at 679 nm and 674 nm and positive peaks at 650 nm and 658 nm. Fluorescence emission spectra of LHCII from *B. corticulans* is shifted by 2 nm to shorter wavelength compared to *P. sativum* (Figure 6.16B). There is virtually no Chl *b* emission at 77 K, indicating that all the Chl *b* are energetically connected to Chl *a*. The very low Chl *b* emission (below 660 nm) is consistent with the results of Nakayama and Mimuro on *B. maxima* (Nakayama and Mimuro, 1994) and can be attributed to a small, substoichiometric fraction of uncoupled Chl *b* in the sample preparations.

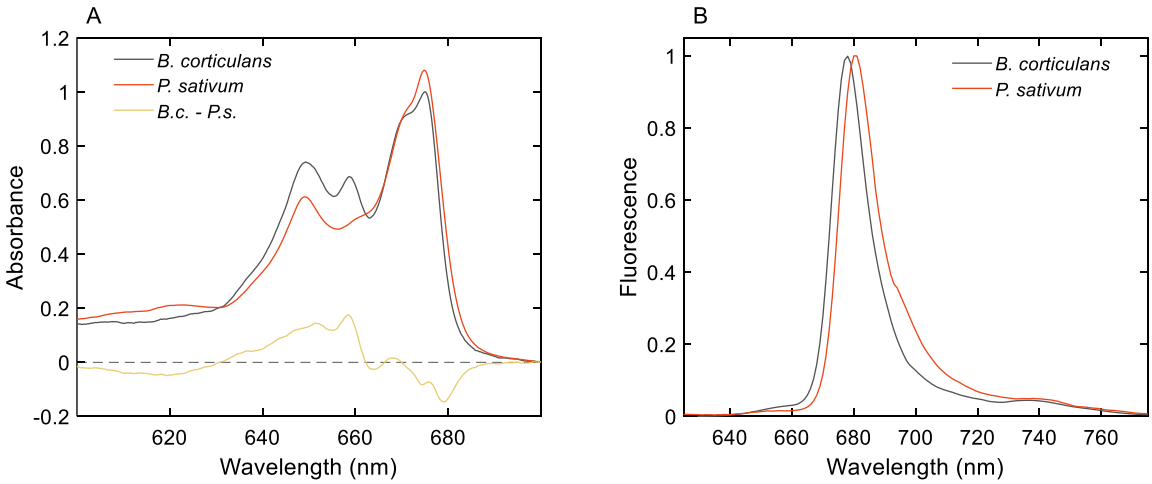

Figure 6.16. Absorption and fluorescence spectra of *B. corticulans* and *P. sativum* measured at 77 K. A. Absorption spectra in the Q_y region. B. Fluorescence emission spectra.

B. corticulans binds more Chl *b* at the expense of Chl *a* (compared to higher plants) to enhance the absorption of shorter-wavelength light – the absorption spectra indicate two extra Chl *b* molecules, giving rise to two positive peaks in the Chl *b* Q_y region of the absorption difference spectra. Because of the different binding sites, the two Chls differ in transition energy – one absorbs at 658 nm and the other around 650 nm. Similar 77 K absorption spectra were reported for *B. maxima*, where the 658-nm Chl form was

present and identified by gaussian decomposition analysis but ascribed to Chl *a* (Nakayama and Mimuro, 1994). Additional features in the absorption difference spectrum hint that the transition energies of other Chls are perturbed in *B. corticulans*. This is expected as the Chl *a*/*b* exchange will affect excitonic couplings with neighbouring Chls even if the overall pigment arrangement/conformation is retained. Furthermore, the transition energy of Chls may also be affected by the protein environment surrounding their binding sites (Remelli et al., 1999), since there are slight differences in the residues surrounding the binding sites (Wang et al., 2013) even though the direct ligands are conserved between the green alga and higher plants.

It is interesting to observe that the additional Chls *b* in *B. corticulans* LHCII are at the expense of apparently the lowest-energy form of Chl *a* (679–680 nm), according to the absorption difference spectrum (Figure 6.16A). This results in the blue-shifted maximum of the fluorescence emission spectrum.

Without a high-resolution structural model, we can only speculate about the binding sites of the extra Chl *b* molecules; however, the spectroscopic data presented here reveal that at least one of them is associated with the so-called terminal emitter or the lowest-energy exciton in plant LHCII. Earlier mutagenesis and spectroscopy studies on plant LHCII (Remelli et al., 1999) and the most recent model calculations (Zucchelli et al., 2012) have assigned the lowest exciton state to Chl *a*612, whereas other models point to *a*610 (Müh et al., 2010; Novoderezhkin et al., 2011). It is also possible that the latter two Chls change their role as the lowest-energy sink depending on temperature (Rogl et al., 2002; Vrandecic et al., 2015). Müh et al. (2010) suggested a possible conformational change of the Chl *a*604 site (with respect to the crystal structure) resulting in a red shift. Accordingly, Chls *a*604 and *a*610 may be the lowest-energy sinks in plant LHCII.

CD and ACD spectra

The CD and ACD spectra of LHCII from *B. corticulans* measured in the visible wavelength region are shown in Figure 6.17. Note that for the measurement of ACD and LD spectra, the complex was embedded in reconstituted membranes. The CD spectrum of reconstituted LHCII membranes is not significantly different from that of LHCII solubilized in β-DDM. In the red region, the CD spectrum is characterized by two negative (651 and 681 nm) and one positive band (665 nm) associated with the Q_y exciton states

of Chl *b* and *a*. *B. corticulans* shows stronger CD in the Q_y band of Chl *b*, 651 nm. The CD bands associated with Q_y transitions of Chl *a* (663 nm and 677 nm) are blue-shifted compared to higher-plant LHCII.

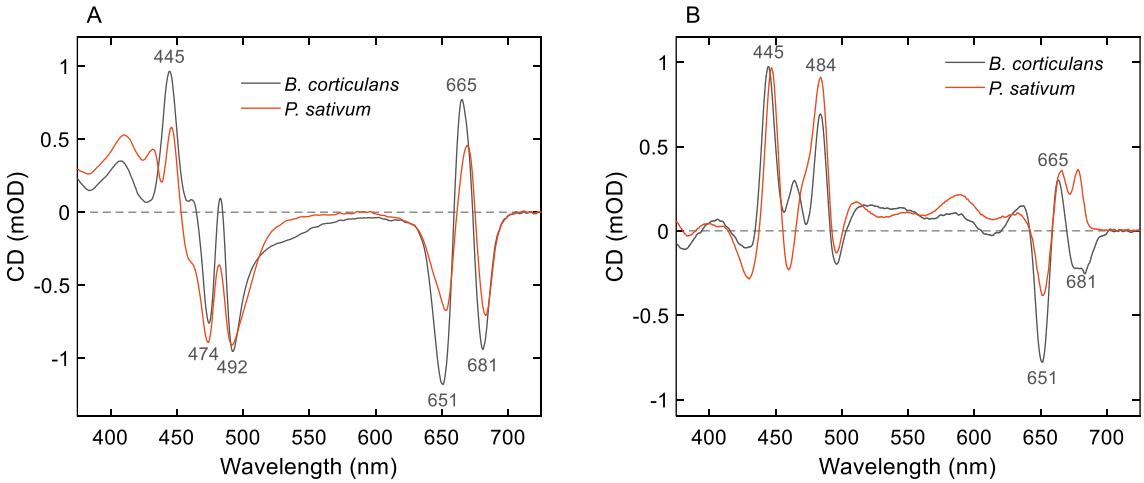

Figure 6.17. CD and ACD spectra of LHCII from *B. corticulans* and *P. sativum*. A. CD spectra of LHCII solubilized in 0.03% β-DDM normalized to unity absorption at 675 nm. B. ACD spectra of membranes oriented in dehydrated films. The spectra are plotted in units of $\Delta A \times 10^{-3}$ (mOD) and normalized to unity isotropic absorbance at 675 nm.

ACD spectroscopy can help identify the pigments contributing to spectral features by virtue of generally less crowded spectra (Miloslavina et al., 2012; Nielsen et al., 2016; Akhtar et al., 2019) and by linking excitonic bands and the orientation of the underlying transition dipole moments (Kuball et al., 2005). The face-aligned ACD spectrum enhances excitonic CD bands wherein the electronic transition dipole moment is predominantly parallel to the membrane plane. A notable difference between the ACD spectra of the algal and the higher-plant LHCII is that the positive band at 680 nm in the latter is not observed in *B. corticulans* – the red-most ACD band is negative in the algal spectrum. This is further evidence that the Chls forming the lowest-energy state in higher-plant LHCII are missing (substituted) in *B. corticulans* – as discussed in section 5.3.2, they are responsible for the positive red band in the ACD spectrum. If we rely on the assignments of Müh et al. (2010), we must conclude that one of the Chls *a*604, *a*610 or *a*613 must be substituted by Chl *b*.

Time-resolved fluorescence

The fluorescence decay kinetics of LHCII of *B. corticulans* was recorded at different emission wavelengths by time-correlated single photon counting. The time-resolved emission spectra (TRES) at all times are nearly identical (Figure 6.18A), indicating that no spectral changes happen after 20 ps. Global multiexponential analysis of the decays at emission wavelengths 664–744 nm required three decay lifetimes to fit the data – a major lifetime of 4.5 ns, having 90% contribution, and two shorter lifetimes (120 ps and 1.2 ns). Interestingly, this results in an average fluorescence lifetime of 4.0 ns – longer than higher-plant LHCII, which was found to be 3.5–3.6 ns, consistent with previous reports (Bassi et al., 1991; Lambrev et al., 2007). Similar to TRES, the decay-associated fluorescence emission spectra (DAES) are also identical for all three components (Figure 6.18B). Thus, it can be concluded that upon excitation at 632 nm (exciting both Chl *a* and *b*), EET is faster than the time resolution of the instrument.

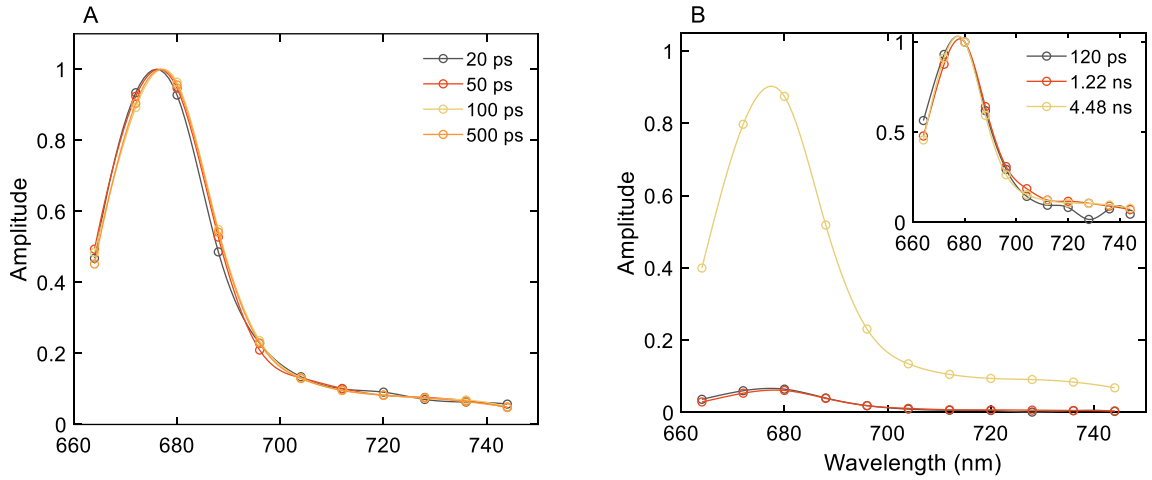

Figure 6.18. Time-resolved fluorescence spectroscopy of detergent solubilized LHCII of *B. corticulans.* A. Time-resolved emission spectra at selected time points. B. Decay-associated fluorescence emission spectra obtained from three-exponential global analysis of the decays at 664–744 nm. The inset shows normalized DAES.

Because excitation energy equilibration in the complex is generally very fast (< 0.1 ns), the fluorescence of the equilibrated system should decay monoexponentially. The minor contribution of short-lived fluorescence decay components (0.1–1.2 ns) might originate from small subpopulations (< 10% total) of aggregated or dynamically quenched complexes in the sample. Both the average lifetime (4 ns) and the major decay lifetime (4.5 ns) of LHCII from *B. corticulans* are slightly longer than the respective values in higher-plant LHCII but within the range of values observed previously, especially for

monomeric LHCII (unpublished data), and can be attributed to the slightly different local environment of the emitting Chls.

In an earlier work, Zhang *et al.* (2006) assumed that excitation equilibration in LHCII from *B. corticulans* occurs with time constants spanning up to 160 ps. While a decay component of comparable lifetime (120 ps) was resolved in the time-resolved fluorescence presented here, the multiwavelength global analysis results are definitive – no EET takes place on such a long timescale and EET is considerably shorter than 50 ps, as is the case with plant LHCII.

Dynamics of energy transfer at room temperature

The central question of the present investigation is how pigment composition changes in LHCII affect the dynamics and efficiency of EET. To this end we measured 2D electronic spectra of LHCII from *B. corticulans* using broadband excitation pulses overlapping with the Q_y absorption band and probe pulses at waiting times spanning the range 0.1–800 ps. Figure 6.19 shows selected RT 2D electronic spectra. At early waiting times (T_w = 100 fs), the negative GSB/SE signal is predominantly aligned along the diagonal, representing population of states directly excited by the pump pulse. Off-diagonal signals are also observed in the region λ_τ = 650–670 nm and λ_t = 660–680 nm, indicating very fast exciton relaxation among strongly coupled Chl domains. In the evolution of the 2D spectrum from 100 fs to 1 ps, the diagonal signal around 650 nm decays (by about 70%) while off-diagonal signals gain intensity.

The 2D spectra clearly show significant remaining population of states at around 665–670 nm up to 5 ps. On the other hand, almost no population of states absorbing below 660 nm is detected at this time (Figure 6.19c). The spectral evolution generally shows a multistep cascade with rapid EET (mostly within 1 ps) from Chl *b* to the intermediate wavelength region at 660–670, followed by slower dynamics to the low-energy Chl *a* states. The 2D spectra at T_w > 10 ps are centred at λ_t = 680 nm and exhibit no correlation between excitation and detection wavelengths (Figure 6.19d), which signifies that a thermal equilibrium among all states has been reached.

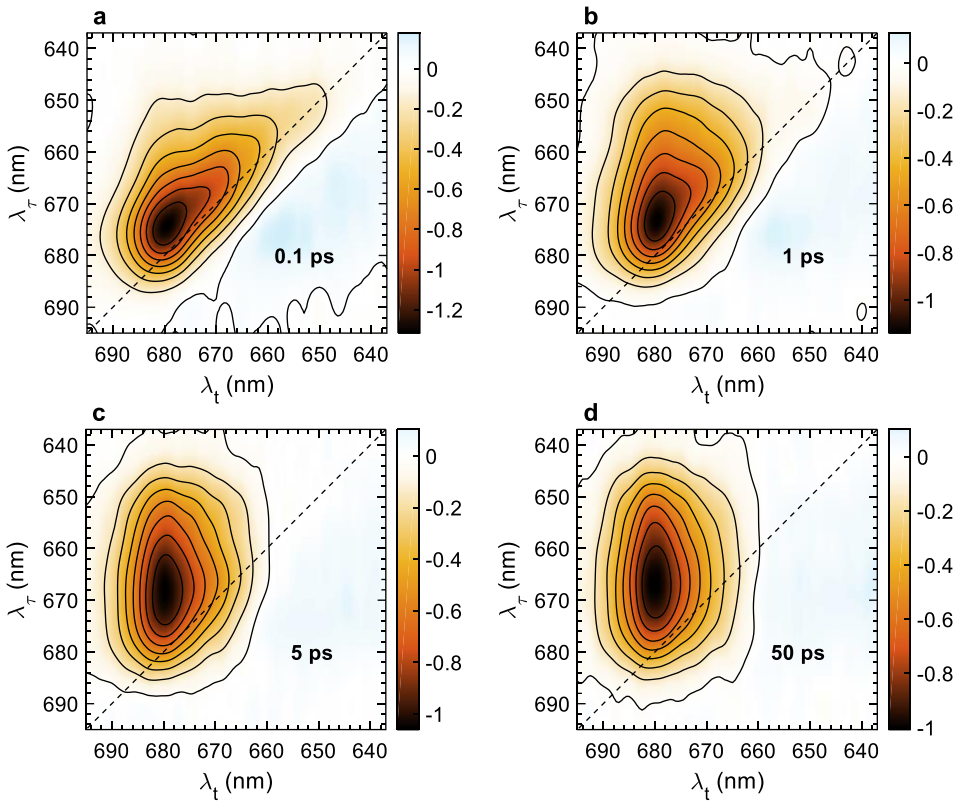

Figure 6.19. Representative purely absorptive 2D spectra of detergent solubilized LHCII (*B. corticulans*) recorded at RT with excitation pulses centred at 670 nm and selected waiting times (0.1, 1, 5 and 50 ps). The symbols λ_τ and λ_t indicate excitation and detection wavelengths, respectively. Yellow-red colours code the negative ground-state bleach/stimulated emission signal with contour lines at every 12.5% intensity.

Global analysis of the kinetics with four exponential components resulted in 2D DAS, shown in Figure 6.20. The shortest resolved lifetime (260 fs) is characterized by the decay of the diagonal signals along the entire probed region with local maxima at 652 and 660 nm, and the corresponding rise of off-diagonal signals at λ_t = 672–675 nm. The second 2D DAS with lifetime of 1.7 ps shows the decay of states at around 662–665 nm, which are either directly excited (on the diagonal) or populated via EET from upper-lying states (λ_τ = 650–660 nm) and the corresponding rise of low-energy Chl *a* excitons ($\lambda_t \approx$ 680 nm). The slowest EET timescale, 9.4 ps, shows decay of diagonal and cross-peak signals at $\lambda_t \approx$ 670 nm and further rise of the lowest-energy excitons. A diagonal peak at 650–655 nm is also resolved in the 2D DAS, revealing a small fraction of long-lived Chl *b* states.

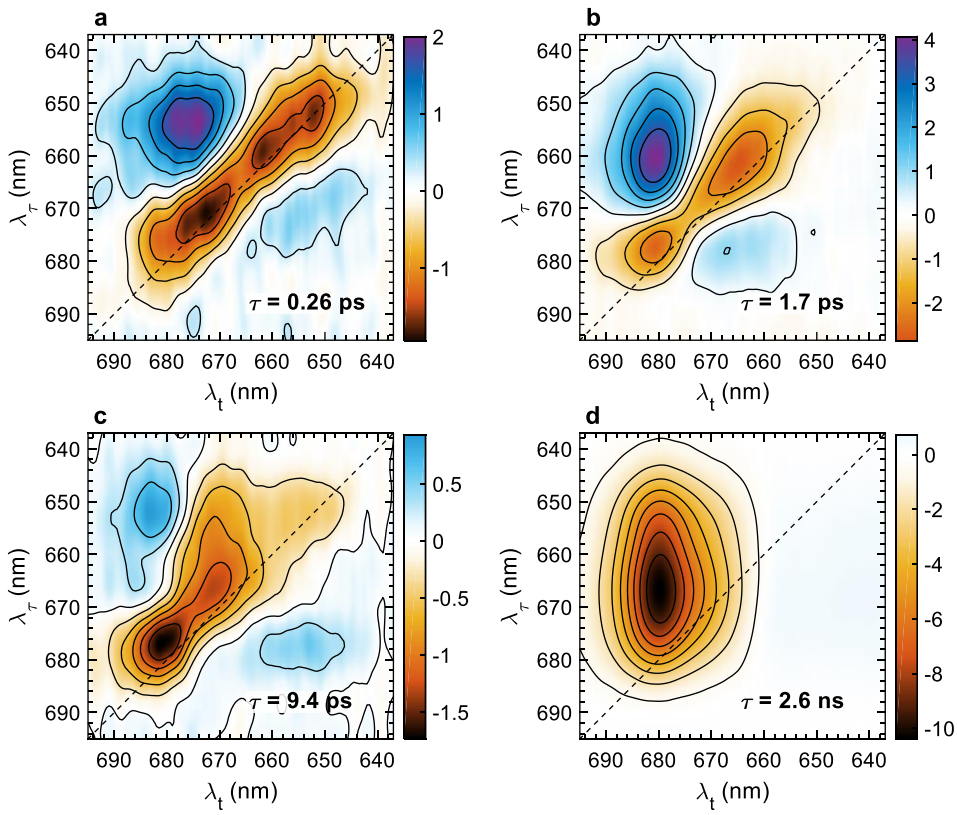

Figure 6.20. 2D decay-associated spectra of *B. corticulans* LHCII obtained from four-component global lifetime analysis of 2DES data collected at RT. Red/blue colours represent negative/positive amplitudes (decay/rise of the negative absorptive signal). Note the different colour coding of the signal amplitude.

All three EET components also show uphill pathways as cross-peaks below the diagonal ($\lambda_t < \lambda_\tau$). The final 2D DAS ($\tau \approx 3$ n) reflects the decay to the ground state. As described above, the shape of the spectrum shows almost no correlation between the excitation and detection wavelengths, indicating that EET is complete and a final, thermally equilibrated state population is reached independent of the initial excitation.

The RT 2D electronic spectra are generally similar to those of higher-plant LHCII obtained with the same experimental setup (section 6.1.2). They show spectral redistribution occurring on different timescales – from several hundred fs to several ps, ending up in a thermal equilibrium of excited states independently from the initially excited state. However, the pathways and dynamics of EET differ between plant LHCII and *B. corticulans*. An obvious change is that the longest resolved EET lifetime is around 5 ps in plant LHCII but 9.4 ps in *B. corticulans*. The EET process contributing mostly to the decay lifetime is from states around 669 nm – this spectral form can be related to the 'bottleneck' long-lived Chls in plant LHCII. The 9.4 ps 2D DAS also revealed a fraction of long-

lived Chl *b*, at 650–655 nm. Such long-lived Chl *b* states are not present in plant LHCII; therefore, the decay probably represents one of the extra Chl *b* molecules found in *B. corticulans*. As discussed above, a second additional Chl *b* in *B. corticulans* LHCII absorbs at 658–659 nm. This spectral form rapidly relaxes by EET to Chl *a*, as revealed by the well resolved diagonal peak in the 260-fs 2D DAS.

Dynamics of energy transfer at 77K

Cooling down to 77 K brings about more spectral details in the 2D electronic spectra (Figure 6.21) – the lineshapes are significantly narrower and individual peaks become resolved– around 650, 658, 669 and 677 nm. At early waiting times (T_w = 100 fs), all four peaks are along the diagonal line. A cross-peak is also observed around λ_τ = 670 nm and λ_t = 675–678 nm, which is separated from the diagonal peak at 669 nm and probably originates from excitonic coupling between Chl *a* molecules. In the time between 100 fs and 1 ps, the 650 and 658-nm peaks practically vanish and corresponding cross-peaks at $\lambda_t \approx$ 675 nm are visible. This indicates that EET from the high-energy Chl *b* band to Chl *a* occurs at a rate comparable to that observed at RT.

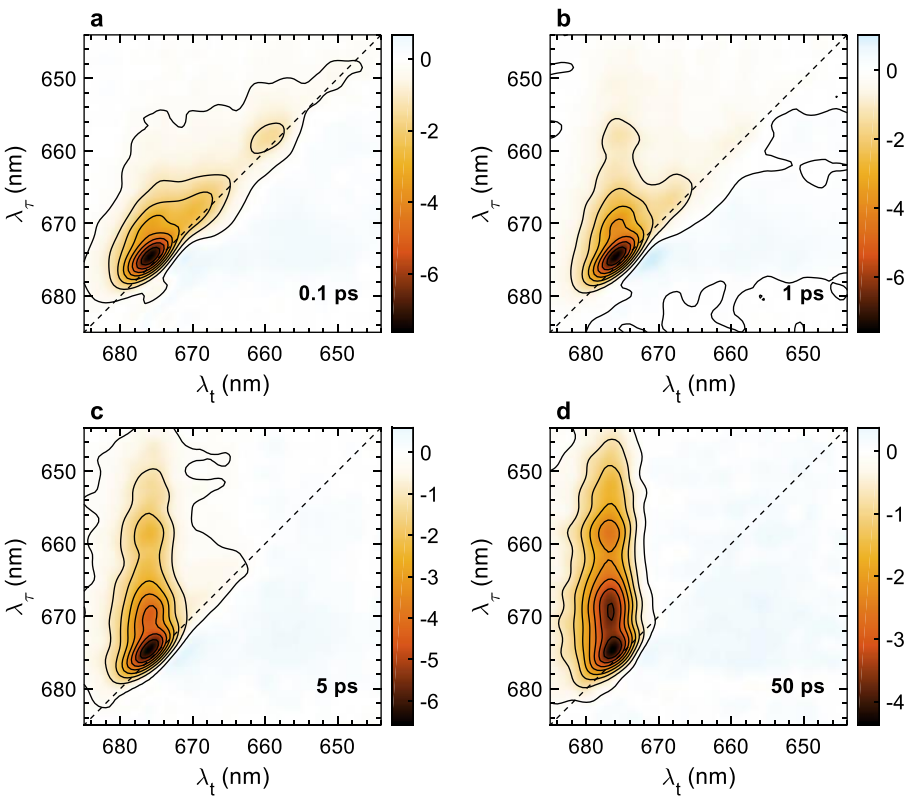

Figure 6.21. Representative purely absorptive 2D electronic spectra of *B. corticulans* LHCII trimers from recorded at 77 K with excitation pulses centred at 670 mm, at selected waiting times T_w as indicated. The symbols λ_τ and λ_t indicate excitation and detection wavelengths, respectively.

By 50 ps, all peaks are centred around λ_t = 677 nm, which is the terminal excited state. In contrast to the RT measurements, there is still a pronounced correlation between excitation and detection wavelengths at long waiting times. This is visualized by the horizontal cuts of the spectra at λ_τ in the range 676–680 nm (Figure 6.22). In other words, the final exciton state at 77 K, depicted by the diagonal peak at 677 nm, is inhomogeneously broadened.

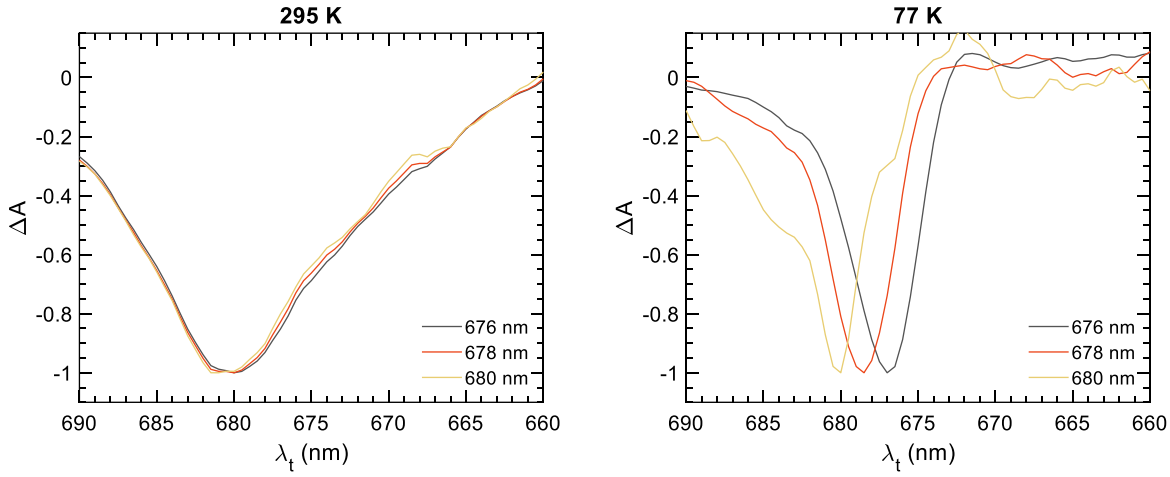

Figure 6.22. Horizontal slices of the 2D electronic spectra at wating time T_w = 50 ps at selected excitation wavelengths for RT (left) and 77 K (right). The curves are normalized to their negative maxima for easier comparison. A clear dependence of the final spectrum on excitation wavelength is observed at 77 K

The 2D DAS resulting from global analysis are plotted in Figure 6.23. The first three 2D DAS with lifetimes of 0.5, 2.7 and 15 ps are associated with EET as seen by the decaying diagonal states and corresponding rise of cross-peaks, mainly at longer detection wavelengths. The final lifetime in the nanoseconds range represents decay to the ground state. The shortest resolved lifetime of 0.5 ps is associated with decay of diagonal peaks at 650, 658 and 669 nm – giving rise to states at 665 and 675 nm. Also visible is the decay of a 652→658-nm cross-peak signal, i.e. relaxation of the 658-nm states, which have been populated from states absorbing around 652 nm by very fast EET.

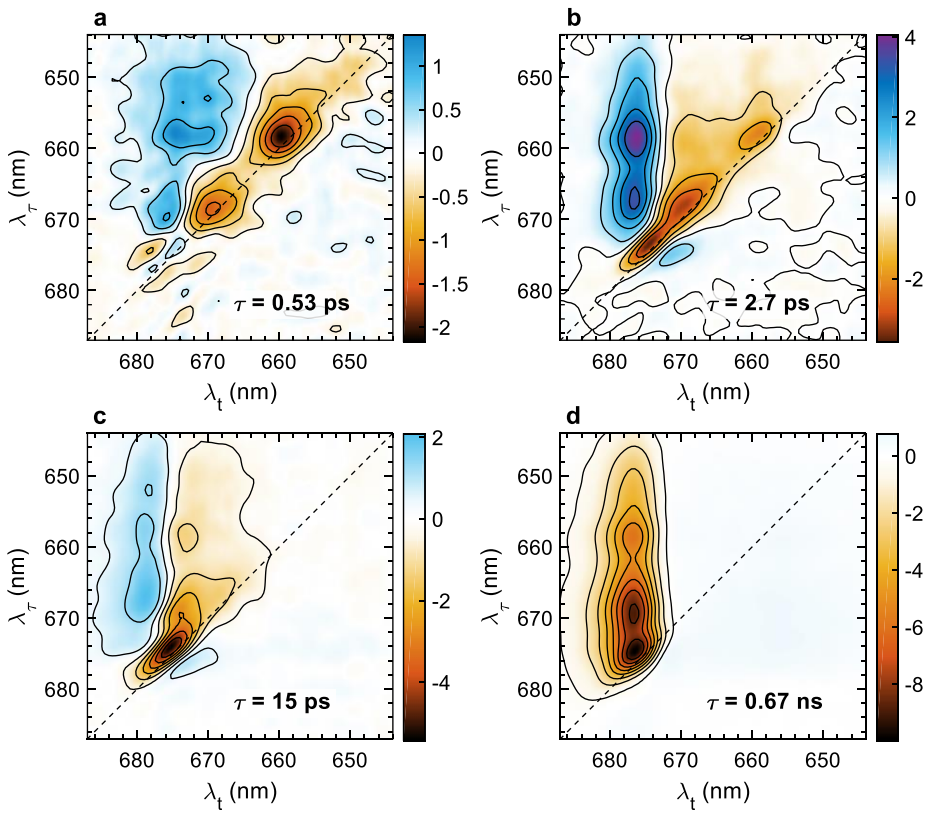

Figure 6.23. 2D decay-associated spectra of *B. corticulans* LHCII at 77 K, obtained from four-component global lifetime analysis of the 2DES data. Red/blue colours represent negative/positive amplitudes (decay/rise of the negative absorptive signal).

The second 2D DAS (2.7 ps) reflects the subsequent relaxation of excitons at 658 and 669 nm. The negative-amplitude cross-peaks show that these intermediate states bridge the EET from the high-energy Chl *b* to Chl *a*. Exciton equilibration in the 670–675 nm region also occurs on this timescale, with well resolved downhill and uphill cross-peaks. The slowest EET lifetime of 15 ps is associated mainly with EET between the lowest Chl *a* states in the 674–678 nm region. However, diagonal peaks at 664–669 nm and at 650 nm are also visible, showing the existence of weakly coupled Chls, presumably Chl *a* and Chl *b*, respectively. The shape of the final 2D DAS (representing decay to the ground state) is practically identical to the 2D electronic spectrum at $T_w = 50$ ps.

The relative contribution of decay lifetimes to the diagonal peaks in the 2D electronic spectra at 77 K is shown in Table 6.5. Comparing these diagonal peak lifetimes with the values corresponding to LHCII from *P. sativum*, it is evident that EET can be up to two-fold slower in *B. corticulans*. The slowest EET dynamics is in the Chl *a* region – with average lifetimes of 8.4 and 10.7 ps for the diagonal signals at 672 and 674 nm, respectively. The slower EET in the Chl *a* wavelength region may be intuitively understood in

terms of comparatively lower Chl *a* concentration and lower density of excited states in energy domain. It can be said that adaptation of LHCII to shorter-wavelength light in the intertidal alga does come with a trade-off between the enhanced absorption cross-section and excitation migration time. Although exciton equilibration time is longer in *B. corticulans* – about 10 ps – it is still an order of magnitude shorter compared to the trapping time of PSII (Caffarri et al., 2011). Therefore, the adaptive change should have negligible effect on the overall quantum efficiency.

Table 6.5. Decay lifetimes and relative amplitudes of the diagonal peaks in the 2D spectra at 77 K.

Lifetime (ps)	650 nm	658 nm	669 nm	672 nm	674 nm
0.5	50%	51%	26%	8%	0%
2.7	22%	48%	50%	46%	40%
15.4	28%	1%	24%	46%	60%
Average lifetime (ps)	5.2	1.8	5.1	8.4	10.7
Average lifetime (*P. sativum*)*	2.5	4.2	3.5	4.5	5.7

* from section 6.2.2

Conclusions

The comprehensive spectroscopic characterization presented here reveals details on the adaptation of the siphonous alga *B. corticulans* to its intertidal habitat by spectrally tuning LHCII to shorter wavelengths. Compared to higher-plant LHCII, the complex contains two additional spectral forms of Chl *b* – absorbing at around 650 nm and 658 nm, at the expense of Chl *a* absorbing at around 674 nm and 679 nm – the lowest-energy Chl *a* form in LHCII. The specific Chl *a*/*b* exchange in *B. corticulans*, while retaining the general tertiary structure of the protein complex, presents a valuable opportunity to identify spectral forms and the associated Chl binding sites, which has been a highly challenging and contentious issue (Lambrev et al., 2020). It would be highly informative to analyse the present spectroscopic results in terms of the complex structure, whenever it becomes determined, e.g. by X-ray diffraction or cryo-electron microscopy.

The adaptive change in Chl composition in *B. corticulans* LHCII alters the pathways and dynamics of EET. The Chl *b* form at 650 nm is relatively long-lived, slowing down EET to Chl *a*. The lower density of Chl *a* also results in a markedly slower EET to the lowest-energy state (677 nm), which occurs on a timescale of about 10 ps at 77 K. Thus, there is

a trade-off between the increased absorption cross-section at shorter wavelengths and the excitation migration time. However, as the latter is much shorter than the overall excitation trapping time, the quantum efficiency of PSII should not be significantly affected. These results show that LHCII is a robust adaptable system whose spectral properties can be tuned to the environment while maintaining efficiency of EET.

6.3. Long-range energy transfer in native and reconstituted membranes

6.3.1. Functional domain size in LHCII membranes

In 1932 Emerson and Arnold proposed that a large number of Chls – as many as 2500 molecules – cooperate to carry out one photochemical reaction, leading to the concept of the photosynthetic unit (Blankenship, 2014). It is beyond doubt that excitation energy migrates at long distances hopping over multiple pigment–protein complexes before being trapped by the RC. In plant TM each photosystem is surrounded by several LHCs creating a physical domain of a few hundred Chls. It can be assumed that the *functional domain size*, i.e. the number of molecules that excitation can visit before being lost non-photochemically, is larger. Theories relating the excited-state lifetime with the domain size have been put forward (Paillotin et al., 1979). Measurements and models of the extent of singlet-triplet and singlet-singlet annihilation (den Hollander et al., 1983) in native TM and aggregates of isolated LHCII have estimated functional domain sizes from 200 to more than 1000 Chls (Kolubayev et al., 1985; Gillbro et al., 1988; Barzda et al., 1996; Barzda et al., 2001). However, quantitative analysis of annihilation results is limited by the model approximations (Schödel et al., 1996; Richter et al., 2007). We complemented the annihilation-based estimates of the functional domain size by measuring the Chl fluorescence lifetime in the presence of exogenous quenchers – phenyl-*p*-benzoquinone (PPQ) or dinitrobenzene (DNB) – assuming that the effective quenching rate constant increases with the domain size (Lambrev et al., 2011).

To estimate the effective quenching constant, the fluorescence decays were recorded for a range of quencher concentrations and the average fluorescence lifetimes were calculated after global lifetime analysis of the decay kinetics. The fluorescence lifetimes in the absence and presence of quencher, τ_0 and τ can be written as

$$\tau_0 = \frac{1}{k_f + k_d} \tag{6.3.1}$$

$$\tau_0 = \frac{1}{k_f + k_d + k_q[Q]} \tag{6.3.2}$$

where k_f and k_d are the radiative and nonradiative rate constants, k_q is the bimolecular quenching rate constant and $[Q]$ is the quencher concentration. Rearranging leads to the Stern-Volmer equation:

$$\frac{\tau_0}{\tau} = 1 + \frac{k_q[Q]}{k_f + k_d} = 1 + K_{SV}[Q] \tag{6.3.3}$$

with K_{SV} being the Stern-Volmer constant. K_{SV} can be experimentally determined from the slope of the ratio τ_0/τ, plotted against the quencher concentration (Figure 6.24) and the effective quenching rate constant is $k_q = K_{SV}/\tau_0$. As the figure shows, significantly lower concentrations of the quenchers PPQ and DNB are needed for the same amount of quenching in LHCII aggregates compared to solubilized trimers.

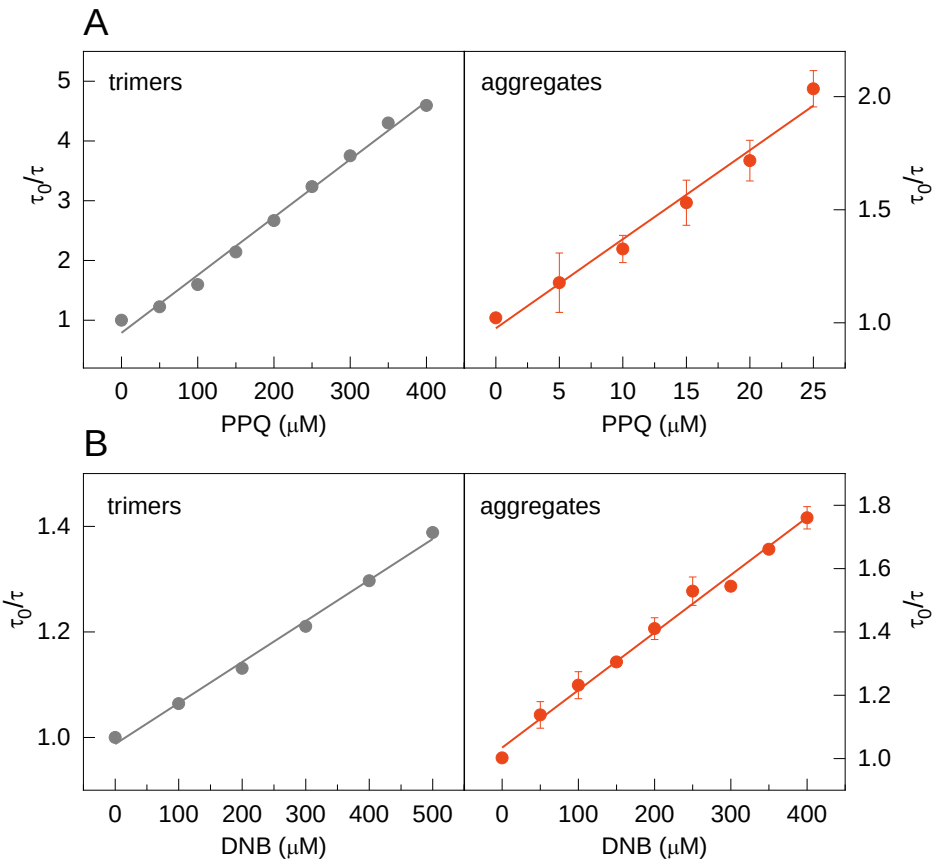

Figure 6.24. Stern-Volmer plots of the fluorescence quenching in solubilized LHCII trimers and lamellar macroaggregates by externally added quenchers: A. PPQ; B. DNB. The quenching is calculated

as τ_0/τ where τ and τ_0 are the average lifetimes of the Chl fluorescence with and without quencher, respectively.

In a domain formed by N units connected via efficient EET, the quencher molecules can be regarded as acting upon the entire domain. In the fast EET limit, the apparent quenching rate constant can be approximated by $k_q' = N \cdot k_q$, where k_q is the quenching rate constant for unconnected units (solubilized trimers).

The effective quenching rate constants and domain sizes N for LHCII in different molecular environments are shown in Table 6.6. Using this method and PPQ as a quencher, we estimated the average domain size of LHCII aggregates to be about 25 trimers (~1000 Chls). Similar values (15–25) were obtained using DNB as a quencher. The values were independent of the method of aggregate preparation and aggregate size (Lambrev et al., 2011) suggesting that the functional domain size is limited by EET and not by the physical size of the aggregate. Further we tested reconstituted LHCII membranes (Akhtar et al., 2015), for which it can be expected that LHCII also forms connected domains. For LHCII membranes reconstituted at L/P ratios of 300 and 100, the relative domain size values were 9 and 27, respectively. These results show that connectivity was dependent on the L/P ratio until the functional domain size becomes limited by the EET rate. Somewhat smaller domain sizes were found for native LHCII-enriched membranes – between 8 and 15 trimers.

Table 6.6. Average lifetimes and functional domain sizes of LHCII in different molecular environments

	τ_0 (ns)	K_{SV} (M^{-1})*	k_q ($M^{-1}s^{-1}$)	N (trimers)
LHCII trimers	3.5	1.4×10^4	3.6×10^{12}	1
LHCII aggregates	0.4	3.6×10^4	9.0×10^{13}	25
LHCII membranes L/P 100:1	1.1	1.2×10^5	1.1×10^{14}	27
LHCII membranes L/P 300:1	2.1	9.7×10^4	3.4×10^{13}	9
Thylakoid membranes	1.0	5.2×10^4	5.3×10^{13}	15
PSII-enriched membranes (BBY)	0.4	2.5×10^4	6.3×10^{13}	18
LHCII-enriched membranes	1.6	4.6×10^4	5.1×10^{13}	9

* quenching by PPQ

To gain insight into the possible functional domain sizes *in vivo*, measurements were done on TM isolated from spinach leaves, adding DCMU to close the PSII RCs, as well as PSII-enriched membranes (BBYs) and LHCII-enriched TM from lincomycin-treated

pea plants. The TM represent a much more complex system containing various pigment–protein complexes and the results can only be regarded as an approximate reflection of the *in vivo* situation. The estimated domain size in stacked TM varied between 12 and 16 (in units of LHCII trimers). Unstacking the membranes by resuspension in a hypotonic cation-free buffer did not led to a change in the apparent functional domain size. Therefore, it could be concluded that stacking of the membranes does not affect the connectivity of the antenna units, which also implies that EET between the membrane sheets does not occur. This finding is in agreement with the fact that the sigmoidicity of the fluorescence induction curves, does not change with unstacking (Kirchhoff et al., 2004) and has recently been corroborated in another study (Farooq et al., 2016).

Measurements on BBYs yielded domain size equivalent to 2–3 PSII–LHCII supercomplexes, on Chl basis. The numbers are in good agreement with the estimation of Trissl and Lavergne (1995) based on analysis of fluorescence induction curves.

The finding of a limited functional domain size of up to about 25 LHCII trimers in various types of aggregated domains that can have very large physical sizes (up to 20 μm) is most interesting because the number of functionally interconnected trimers is comparable to the maximum antenna size typically proposed for plant photosynthetic membranes. Our study predicts that excited states in larger hypothetical antenna systems will not be efficiently trapped by photochemistry and therefore the physiological structure would no longer be optimized. It seems most reasonable to assume that the light-harvesting antenna complexes in plants are adapted to the diffusive excited state domain size accessible by a single exciton after light absorption.

6.3.2. Energy transfer between LHCII and PSI in model membranes

Recent studies have put forward the notion that a significant amount of LHCII is associated with PSI under normal conditions (Wientjes et al., 2013; Bell et al., 2015; Grieco et al., 2015) in the absence of phosphorylation. For example, Bell et al. (2015) have isolated PSI–LHCII membrane fractions from stacked spinach thylakoids at estimated stoichiometry of three LHCII trimers per PSI, at least some of them being functionally coupled to the RC. We investigated the ability of LHCII to transfer absorbed light energy to PSI in reconstituted membranes (Akhtar et al., 2016). Isolated LHCII and PSI were incorporated into lipid membranes separately or in mixtures of known stoichiometry, to test the

effective antenna size of PSI under controlled conditions at varying known stoichiometries of LHCII:PSI.

Composition and structural organization of the reconstituted membranes

To verify that the reconstituted PSI–LHCII membranes have the correct composition and structural organization, absorption and CD spectra were recorded and compared with membranes containing only LHCII or PSI. Subtracting the PSI absorption spectrum from the spectra of the PSI–LHCII membranes (Figure 6.25A), resulted in absorption difference spectra closely matching the spectrum of LHCII-only membranes (Figure 6.25 B) – confirming that the absorption of both PSI and LHCII is unchanged in the mixed membranes.

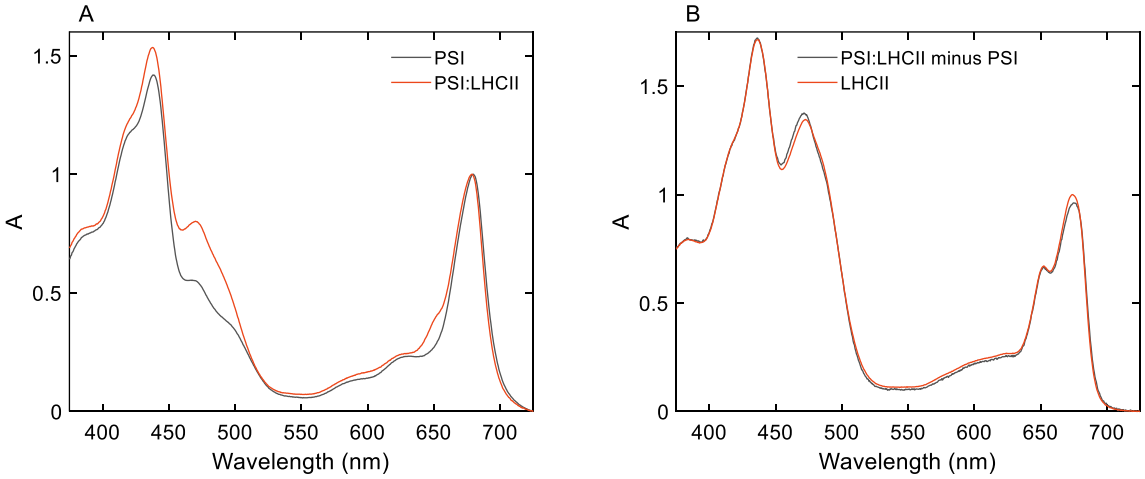

Figure 6.25. Absorption spectra of PSI–LHCII membranes. A. absorption spectra of reconstituted PSI-only or PSI–LHCII membranes (2 trimers per PSI); B. absorption difference spectra PSI–LHCII minus PSI-only membranes compared with the spectra of LHCII-only membranes.

Similarly, the excitonic CD spectra (Figure 6.26) of the mixed membranes could be fully reconstructed by linear combinations of the two individual component spectra PSI and LHCII, which testifies that neither LHCII nor PSI were structurally altered in the mixed reconstituted membranes. No indication of LHCII aggregation was found in the CD spectrum either.

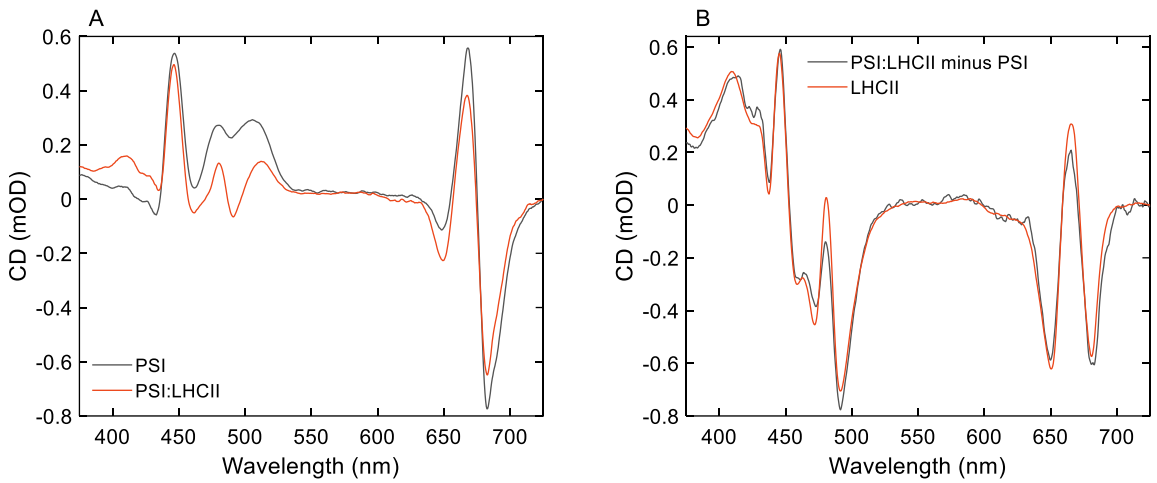

Figure 6.26. CD spectra of PSI–LHCII membranes. A. CD spectra of reconstituted PSI-only or PSI–LHCII membranes (2 LHCII trimers per PSI); B. CD difference spectra PSI–LHCII minus PSI-only membranes compared with the spectra of LHCII-only membranes.

Energetic connectivity of the complexes in the membranes

The emission spectra of PSI and LHCII (Figure 6.27) are readily distinguishable at 77 K – the fluorescence of PSI has a maximum at 730 nm, whereas LHCII emits maximally at 680 nm. The emission spectra of PSI–LHCII membranes showed features of both PSI and LHCII – peaks in the emission spectra at both 680 and 730 nm. The emission at 680 nm gradually increased with increasing the LHCII:PSI ratio in the membranes, which shows that at least part of the excitation energy in LHCII was not trapped by PSI.

In the absence of EET from one complex to the other, the spectra of PSI–LHCII membranes would be equal to the sum of PSI-only and LHCII-only membranes' fluorescence spectra. To test this hypothesis, the experimental data obtained were compared with theoretical spectra, calculated for PSI–LHCII mixtures at the same PSI:LHCII ratios but in the absence of EET (Figure 6.27C). The experimental spectra are markedly different — showing less LHCII emission compared to the calculated ones – indicating that part of excitation energy in LHCII was quenched by PSI.

If the fluorescence of LHCII was indeed quenched by interaction with PSI, then the emission should be recovered by disrupting the protein interactions in the membrane with a detergent. Upon solubilization of the reconstituted PSI–LHCII membranes with 0.03% β-DM, the emission intensity at 680 nm increased six-fold (Figure 6.27D) compared to a two-fold increase in the fluorescence intensity of LHCII-only membranes (data not shown).

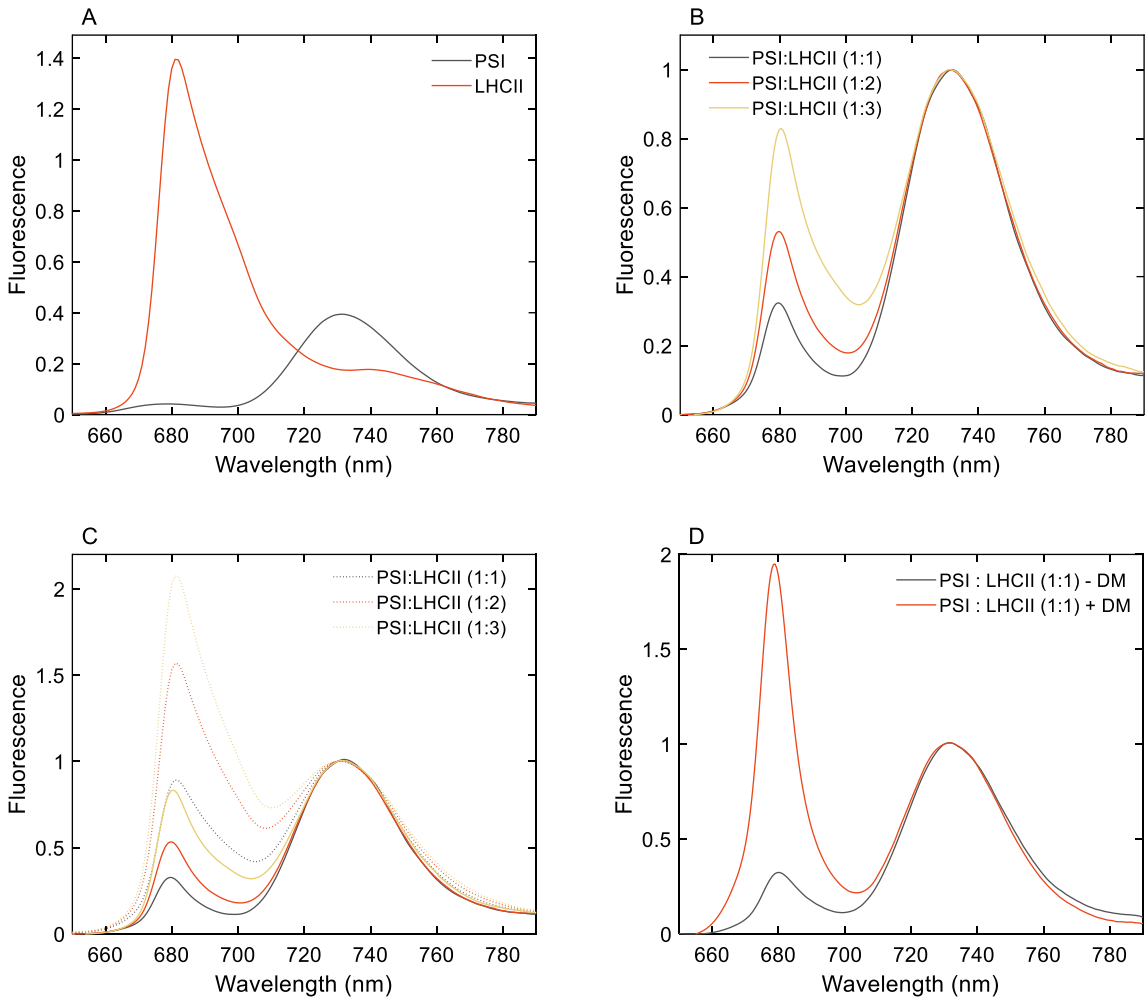

Figure 6.27. Fluorescence emission spectra of PSI–LHCII membranes at 77 K with 436 nm excitation light. A. PSI- and LHCII-only membranes; B. PSI–LHCII membranes (1, 2 and 3 trimers per PSI); calculated spectra of PSI–LHCII mixtures at PSI:LHCII ratios of 1:1, 1:2 and 1:3 (dotted lines); D. emission spectra of PSI–LHCII membranes (1 trimer per PSI) before and after solubilization with 0.03% β-DM

To determine the efficiency and dynamics of EET, we recorded the picosecond fluorescence decay kinetics of LHCII, PSI and the reconstituted PSI–LHCII membranes at RT under the same experimental conditions. Representative DAES of reconstituted PSI and LHCII membranes obtained by global analysis are shown in Figure 6.28. The fluorescence kinetics of PSI is characterized by two decays components – 15–20 ps, with an emission maximum at 685 nm, and 60–80 ps, with a broad peak around 720 nm. These components represent photochemical trapping and equilibration with the red Chls (Ihalainen et al., 2005; Engelmann et al., 2006; Slavov et al., 2008; Wientjes et al., 2011).. The fluorescence of LHCII in reconstituted membranes decays multiexponentially with

lifetimes depending on the L/P ratio (see 5.2.5). For L/P 100:1, the main lifetimes are in the range of 1 ns, i.e. significantly longer than in PSI (see also Figure 5.16).

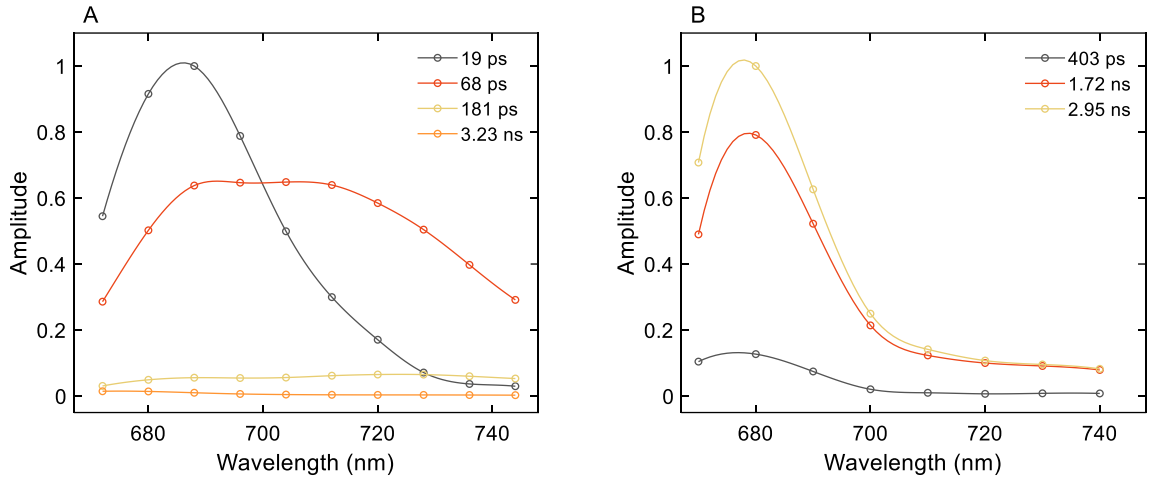

Figure 6.28. Decay-associated fluorescence emission spectra of PSI and LHCII reconstituted in membranes. A. PSI; B. LHCII.

The DAES of PSI–LHCII membranes (Figure 6.29) show the characteristic spectra for PSI and LHCII, however, with notable differences. The PSI lifetimes are longer (25 and 80–90 ps) and the 80 ps DAES shows increased emission at 680 nm. The changes are more pronounced in samples with higher LHCII content. On the other hand, the LHCII components have shorter lifetimes (Table 6.7) – the main decay lifetime is 210–260 ps. This is yet another evidence for EET from LHCII to PSI.

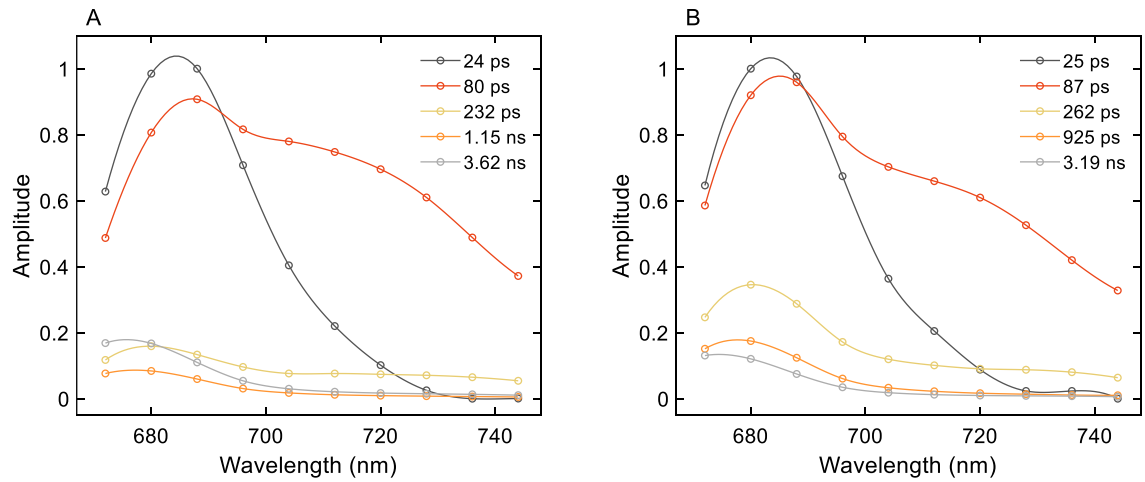

Figure 6.29. Decay-associated fluorescence emission spectra of reconstituted PSI–LHCII membranes. A. PSI–LHCII at stoichiometry ratio 1:2; B. PSI–LHCII at 1:3 ratio.

Table 6.7. Fluorescence lifetimes and relative amplitudes at 680 nm of reconstituted membranes

LHCII		PSI		PSI:LHCII (1:1)		PSI:LHCII (1:2)		PSI:LHCII (1:3)	
τ (ps)	a	τ (ps)	a	τ (ps)	a	τ (ps)	a	τ (ps)	a
-	-	19	62	21	51	24	45	25	39
-	-	68	34	74	34	80	37	87	36
403	7	181	3	214	5	232	7	262	13
1720	41	-	-	1478	3	1155	4	925	7
2950	52	3230	1	3904	8	3625	8	3193	5

Kinetic modelling

For a more detailed understanding of the kinetics of EET between LHCII and PSI, we used kinetic model fitting to the fluorescence data. The following analysis applies to reconstituted PSI–LHCII membranes at a 1:3 ratio. The kinetic model contains different compartments for PSI and LHCII (Figure 6.30). PSI is modelled with two compartments – "Bulk" representing bulk antenna Chls and the RC and "LHCI" representing red Chls in the peripheral antenna. The model is based on measurements of isolated PSI core and PSI–LHCII complexes (Akhtar et al., 2018). The kinetic scheme is similar to the one applied by Le Quiniou et al. (2015; 2015) to model the kinetics of PSI–LHCI and PSI–LHCI–LHCII supercomplexes from *Chlamydomonas*.

LHCII is modelled with three compartments representing different populations – a strongly connected (S), weakly connected (W) and free (F). The time constants of EET between the compartments, the DAES and the respective species-associated emission spectra (SAES) are also shown in Figure 6.30. The connected LHCII trimers transfer energy to PSI on timescales of < 20 ps and 300 ps, respectively. From the amplitudes of the SAES, we can estimate the sizes of each LHCII pool, relative to PSI: 27% (S), 19% (W), and 15% (F). The total estimated absorption cross-section of all LHCII pools is 61% compared to PSI, equivalent to about 2.4 LHCII trimers. It must be noted that, although the kinetic scheme depicts different LHCII pools directly coupled to PSI, this is not necessarily the actual case. The exact topology of the protein network cannot be uncovered by the fluorescence data alone. From the results in the previous section (6.3.1), we know that LHCII are well interconnected in the reconstituted membranes, therefore we must assume that energy can also be transferred from LHCII to PSI via multiple hops between

LHCII. Therefore, slower EET components (200–300 ps) should, at least partially, reflect multistep EET routes.

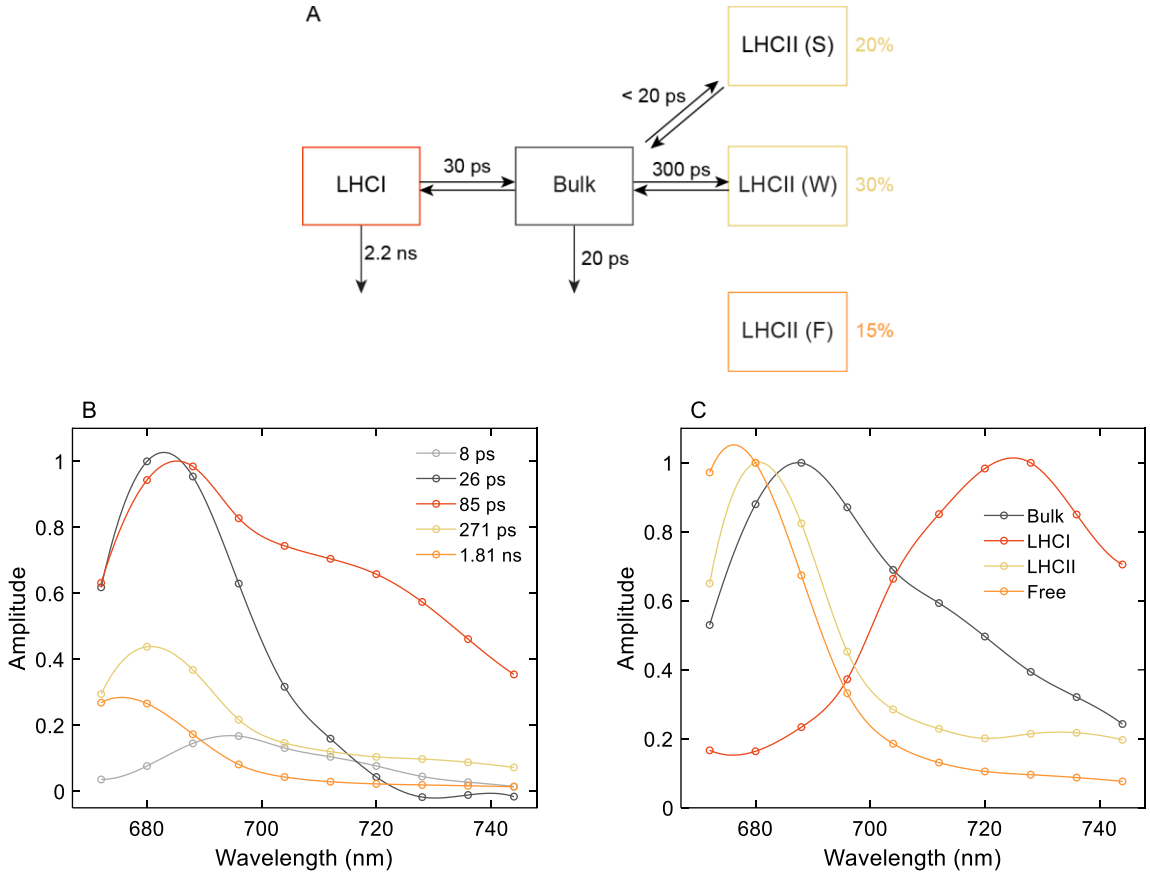

Figure 6.30. Target analysis of the fluorescence kinetics of PSI–LHCII (1:3) membranes. A. kinetic scheme with effective EET timescales; B. decay-associated emission spectra; C. normalized species-associated spectra.

Efficiency of energy transfer and photochemistry

The efficiencies of excitation energy trapping from each LHCII pool (number of photons trapped by PSI charge separation over the number of photons absorbed by LHCII) were estimated by solving the kinetic model with initial excitation on each LHCII compartment separately. The overall efficiency of energy transfer from all LHCII pools combined to PSI was 72%. Hence, the addition of LHCII increased the effective absorption cross-section of PSI by 47%. The size of the strongly coupled LHCII (S) pool is equivalent to one LHCII trimer. Interestingly, the estimated timescale and efficiency of transfer (96%) are about the same as in PSI–LHCII supercomplexes isolated by Wientjes *et al.* (2013). Hence, this pool could represent LHCII trimers forming similar PSI–LHCII supercomplexes in the artificial membrane.

How does the increased antenna size affect the quantum yield of photochemistry in PSI? The overall photochemical quantum yield φ can be estimated from the average fluorescence lifetime τ by the formula $\varphi = 1 - \tau/\tau_0$, where τ_0 is the excited-state lifetime without RC, which is about 2 ns. The calculated average fluorescence lifetimes of PSI and PSI–LHCII membranes, measured at 688 nm, and the calculated quantum yields of PSI photochemistry are shown in Table 6.8. The average lifetime of isolated PSI was 44 ps, hence the calculated yield is 0.98. In the presence of LHCII, the overall quantum yield of charge separation decreased to 0.87–0.89, i.e. by only about 10% even as the total Chl content was increased by 70%. The photochemical yield calculated for PSI–LHCII membranes (1:3) is 0.87.

Table 6.8 Average lifetimes and photochemical quantum efficiencies of PSI–LHCII membranes*

Type	**‹τ›, ps***	**Φ_p**
PSI	44	0.98
PSI:LHCII (1:1)	267	0.87
PSI:LHCII (1:2)	269	0.87
PSI:LHCII (1:3)	222	0.89

* ‹τ› — average lifetime at 688 nm; Φ_p — quantum yield of photochemistry: $\Phi_p = (1 — ‹\tau›) / 2000$.

Thus, we show that the absorption cross-section of PSI can be substantially increased by the addition of LHCII in reconstituted membranes and that, owing to the rapid EET, this occurs with a marginal loss in the overall photochemical quantum efficiency. The energetic coupling of LHCII to PSI and consequently the trapping efficiency of the artificial membranes seems lower compared to the recent reports on isolated PSI–LHCII supercomplexes (Galka et al., 2012; Wientjes et al., 2013; Bell et al., 2015; Le Quiniou et al., 2015). In our case, the numbers represent the bulk membrane system, which is evidently highly heterogeneous (cf. 5.2.5).

In conclusion, our results bring further support to other recent studies suggesting that LHCII can be a very efficient antenna for PSI even in the absence of phosphorylation (Wientjes et al., 2013; Grieco et al., 2015), given the opportunity that the two interact in the membrane. It can be indeed expected then that in the grana margins and in unstacked TM PSII and PSI would share a common pool of LHCII antenna and only the steric exclusion of PSI from the appressed granal regions prevents “spillover”.

7. SUMMARY

1. **The structure and excitation properties of LHCII are sensitive to the molecular surroundings of the complex.**
   a. Comparison of the CD spectra of isolated LHCII solubilized in detergent micelles, detergent-free aggregates, non-aggregated LHCII in washed gels, and LHCII embedded in reconstituted membranes revealed specific spectral changes ascribed to changes in the Chl and Car exciton states due to protein–protein, lipid–protein, or detergent-protein interactions. For instance, aggregation (LHCII-LHCII interactions interactions) and removal or replacement of the detergent invoked specific changes in the CD spectra indicating that these types of intermolecular interactions affect different excitonic states, respectively pigment molecules. These results show that the excitonic structure of LHCII is sensitive to the molecular environment and hint that the excitation properties of the complex in its native membrane environment and in a detergent-solubilized state may not be the same. Therefore, the structural and functional plasticity of the complex needs to be considered when inferring about physiological function from in vitro experiments.
   b. Reconstituted lipid–protein membranes represent a useful native-like model system; however, investigations remain challenging in part because of a high degree of heterogeneity with respect to the proteoliposome macrostructure. The combined application of lipid markers and physicochemical separation by density revealed that reconstituted LHCII proteoliposomes are remarkably heterogeneous in particle sizes and protein densities (L/P ratios). LHCII showed strong propensity to associate into protein-dense membrane domains and was rarely or not at all found as single complexes surrounded by lipids. Surprisingly, aggregation-specific CD signatures were not observed in reconstituted LHCII membranes but only in native LHCII-enriched membranes and lipid-free aggregates, indicating that even in membrane environment LHCII can adopt different structural and macrostructural states affecting the excitonic landscape.
2. **Chlorophyll charge-transfer states endow LHCII with the mechanism to self-regulate its light-harvesting function depending on the environment in vitro and in vivo.**
   a. The molecular environment has profound effects on the pigment excitation dynamics in LHCII. Self-segregation and clustering of LHCII in reconstituted membranes results in reduction of the Chl fluorescence yield and excitation lifetime. The extent

of quenching is inversely correlated with L/P ratio over a wide range of values. The Chl fluorescence lifetime of LHCII in proteoliposomes with L/P molar ratios over 1000:1 was found to be similar to that in detergent-solubilized LHCII (about 3.5 ns). At high protein densities the fluorescence lifetimes decreased more than 10-fold, showing fluorescence quenching of equal magnitude as in lipid-free LHCII aggregates. These results demonstrate an intrinsic capacity of LHCII to regulate the excitation lifetime.

b. The fluorescence quenching in LHCII aggregates as well as in lipid membranes is always accompanied by the appearance of far-red fluorescence emission (at wavelengths 700–720 nm). The emission originates from low-lying Chl exciton states with pronounced CT character, whose properties markedly depend on the molecular environment. The existence of multiple CT states was confirmed in LHCII aggregates as well as crystals by time-resolved fluorescence spectroscopy at cryogenic temperatures. In contrast, no low-lying far-red-emitting CT states were detected in unquenched detergent-solubilized LHCII. The CT states themselves have relatively long excitation lifetimes but are nonetheless capable of trapping excitation energy from the bulk of pigments and as such present a viable mechanism of non-photochemical quenching. The similarity of the far-red emission observed in reconstituted and native membranes and in intact leaves upon induction of fluorescence quenching is an indication that the CT mechanism is not only inherent to LHCII but that it is part of photoprotective non-photochemical quenching in plants.

c. With the help of the novel method of Chl fluorescence induction spectroscopy, we detected spectral signatures of the different kinetic components of non-photochemical quenching qE (rapidly reversible) and qZ or qI (sustained) in intact Arabidopsis leaves. The far-red fluorescence signature of CT-state quenching was found to coincide with the induction of qE and to be quantitatively correlated with the magnitude of qE but not with qI or qZ. These results strongly support the notion that 1) this physical mechanism is common to isolated LHCII as well as quenching in vivo and 2) that multiple quenching mechanisms act on different timescales in vivo.

3. **Anisotropic CD spectroscopy helps identify excitonic transitions and validate structure-based exciton models.**

a. The oriented CD or anisotropic CD (ACD) of macroscopically aligned pigment–protein complexes such as LHCII reveals additional information about their excited states that is lost in the CD of randomly oriented proteins in solution. ACD spectroscopy has the advantage of separating the optical transitions by the

orientation of the underlying transition dipole moment, in the case of oriented membrane proteins such as LHCII, it allows us to observe separately transitions oriented preferentially in and out of the membrane plane. The ACD spectra of LHCII featured more intense, shaper bands in the visible region that markedly improve the ability to resolve pigment excitonic states.

b. Structure-based exciton calculations, aided by comparing the predicted and experimental optical spectra, provide the most detailed understanding of the photophysical function of the pigment–protein complexes. The ACD spectra potentially raise the fidelity and confidence of structure-based exciton models by additionally restricting the orientation of the modelled excitonic transitions. Calculations of the ACD spectra of LHCII using an exciton Hamiltonian proposed earlier reproduced the qualitative features of the experimental spectra in the Chl Q_y region. Moreover, it was demonstrated that the red-most ACD band is contributed by Chls of a604, a610 and a613, which comprise the lowest-energy exciton states.

4. **Detailed knowledge of the dynamics of energy transfer between chlorophylls in LHCII has been obtained by two-dimensional electronic spectroscopy (2DES).**
   a. 2DES revealed different connected pools of Chl b and Chl a as well as simultaneous uphill and downhill energy transfer in the Chl a manifold. Exciton equilibration was found to occur on timescales up to about 5 ps at RT.
   b. Energy transfer in LHCII is strongly temperature-dependent. The rate of equilibration with the terminal states slowed down by a factor of three at 77 K compared to RT. Static energetic disorder sets in at temperatures below the glass transition of the protein (< 230 K). Freezing protein motions blocked uphill energy transfer pathways following predictions from the detailed balance, which has a high impact on the overall energy transfer rate.
   c. Phenomenological model fitting can extract sound physical parameters from the two-dimensional spectroscopy data, such as the excitonic state energies, homogeneous and inhomogenous widths and microscopic rates of energy transfer. The spectro-kinetic model of LHCII shows three terminal Chls states in LHCII weakly connected to each other and equilibration via bridging higher-energy excitonic states.
5. **LHCII is a spectrally tunable light-harvesting antenna.**
   a. The green syphonous alga Bryopsis corticulans has LHCII adapted for enhanced absorption of short-wavelength light by way of altered pigment composition. Two additional short-wavelength Chl states were identified at the expense of the longest-wavelength states. Thus, LHCII possesses spectral tunability. The broader

absorption spectrum comes at the expense of slower energy transfer in the complex, which, however, is not expected to result in meaningful loss of photosynthetic efficiency.

6. **The rate of energy transfer between LHCII complexes largely determines the functional antenna size of PSII in thylakoid membranes.**
   a. The functionally connected domains in LHCII aggregates, artificial and native membranes were determined to be limited to about 25 trimeric complexes. This number is in a good agreement with estimations of the size of the "photosynthetic unit" in terms of number of interconnected Chls.
   b. While it is possible to produce larger physical aggregates in vitro, the functional antenna size is limited mainly by the rate of energy transfer between LHCII complexes.
7. **LHCII is an efficient antenna for both photosystems.**
   a. In model membranes, LHCII can deliver absorbed energy to PSI thereby increasing the photosystem's absorption cross-section. The timescales of energy transfer indicate multiple binding sites. In this way the effective antenna size of the photosystem can be enhanced by 50% while the photochemical quantum yield remains near 90%. These results demonstrate the feasibility to construct efficient biohybrid systems with desired functional antenna sizes.

8. ACKNOWLEDGEMENTS

I am grateful to Dr. Győző Garab for having supplied a constant stream of support, resourcefulness and enthusiasm over the years. I wish to thank the director of the Institute of Plant Biology, Dr. Imre Vass, and the administration staff of the Institute of Plant Biology and the Biological Research Centre who have worked hard to leave only the scientific problems to me.

Much of the work in this dissertation was done with the help of terrific members, current and former, of the Photosynthetic Membranes Group – Drs. Parveen Akhtar, Márta Dorogi, Christos Kotakis, László Kóvács, Melinda Magyar, Yulia Miloslavina, Christian-Herman Lucas Patty, Gábor Sipka, Milan Szabó, Zsuzsanna Várkonyi, Bettina Ughy, Ottó Zsiros and the students Fanny Balog-Vig, Avratanu Biswas, Fanni Görföl, Mónika Lingvay, and Mira Sass – hearty thanks for their invaluable contribution. Thanks to all colleagues from the Biological Research Centre, whose through collaboration or pure collegiality have supported this work.

Special thanks to the partner institutions and collaborators who have participated in the research: Prof. Alfred Holzwarth and the colleagues from the Max Planck Institute for Bio-Inorganic Chemistry (Mülheim a.d. Ruhr, Germany), Dr. Howe-Siang Tan, the staff and students from Nanyang Technological University (Singapore), Dr. Giuliano Siligardi, the staff of the CD beamline at the Diamond Light Source (United Kingdom), Prof. Thomas Renger and Dr. Dominik Lindorfer, (Kepler University Linz (Austria), Prof. Jian-Ren Shen, Prof. Chunhong Yang, and colleagues from the Institute of Botany, Chinese Academy of Sciences, Prof. Leonas Valkunas and the colleagues from the Centre for Physical Sciences and Technology (Vilnius, Lithuania), Dr. Attila Bóta and the colleagues from the Research Centre for Natural Sciences (Budapest), Prof. Gernot Renger and colleagues from the former Max Volmer Laboratory, Technical University Berlin (Germany), Prof. Peter Jahns and Dr. Manuela Nilkens, University of Düsseldorf (Germany), Prof. Claudia Büchel and colleagues from the Goethe University Frankfurt (Germany), Prof. Rienk van Grondelle, Prof. Roberta Croce, Dr. Ivo van Stokkum, Prof. Marie-Louise Groot, Dr. Andreas Stahl, from the Free University of Amsterdam (The Netherlands), Prof. Sashka Krumova and colleagues from the Institute of Biophysics and Biomedical Engineering, Bulgarian Academy of Sciences).

Funding

The research was supported by the Hungarian National Research, Development and Innovation Fund (Grants K-80345, PD-104530, K-112688, NIH-A*STAR TET_10-1-2011-027, NN-124930, 2018-1.2.1-NKP-2018-00009), Hungarian Ministry of National Economy (grant GINOP-2.3.2-15-2016-00001), EU 6th Framework Program, (Marie Curie RTN "INTRO2", grant MCRTN-CT-2003-505069), EU 7th Framework Program (Marie Curie ITN "HARVEST", grant No. 238017), EU Framework Program HORIZON 2020 (grant 730872 "CALIPSOplus"), German Research Fund (grants SFB-429, SFB-663), Singapore National Research Foundation (NRF-CRP5-2009-04), Singapore Ministry of Education Academic Research Fund (grants MOE2015-T2-1-039, RG15/18, RG16/15), A*STAR (SERC Grant No. 102-149-0153), the National Key Research and Development Program of China (grant 2017YFA0503700), a CAS Key Research Program for Frontier Science (grant QYZDY-SSW-SMC003), and the National Natural Science Foundation of China (grant 31600191).

9. BIBLIOGRAPHY

Agarwal R, Krueger BP, Scholes GD, Yang M, Yom J, Mets L, Fleming GR (2000) Ultrafast energy transfer in LHC-II revealed by three-pulse photon echo peak shift measurements. J. Phys. Chem. B **104:** 2908–2918

Ahn TK, Avenson TJ, Ballottari M, Cheng Y-C, Niyogi KK, Bassi R, Fleming GR (2008) Architecture of a charge-transfer state regulating light harvesting in a plant antenna protein. Science **320:** 794–797

Akhtar P, Do TN, Nowakowski PJ, Huerta-Viga A, Khyasudeen MF, Lambrev PH, Tan H-S (2019) Temperature dependence of the energy transfer in LHCII revealed by two-dimensional electronic spectroscopy. J. Phys. Chem. B **123:** 6765–6775

Akhtar P, Dorogi M, Pawlak K, Kovács L, Bóta A, Kiss T, Garab G, Lambrev PH (2015) Pigment interactions in light-harvesting complex II in different molecular environments. J. Biol. Chem. **290:** 4877–4886

Akhtar P, Görföl F, Garab G, Lambrev PH (2019) Dependence of chlorophyll fluorescence quenching on the lipid-to-protein ratio in reconstituted light-harvesting complex II membranes containing lipid labels. Chem. Phys. **522:** 242–248

Akhtar P, Lindorfer D, Lingvay M, Pawlak K, Zsiros O, Siligardi G, Jávorfi T, Dorogi M, Ughy B, Garab G, Renger T, Lambrev PH (2019) Anisotropic circular dichroism of light-harvesting complex II in oriented lipid bilayers: Theory meets experiment. J. Phys. Chem. B **123:** 1090–1098

Akhtar P, Lingvay M, Kiss T, Deák R, Bóta A, Ughy B, Garab G, Lambrev PH (2016) Excitation energy transfer between light-harvesting complex II and photosystem I in reconstituted membranes. Biochim. Biophys. Acta Bioenerg. **1857:** 462–472

Akhtar P, Nowakowski PJ, Wang W, Do TN, Zhao S, Siligardi G, Garab G, Shen J-R, Tan H-S, Lambrev PH (2020) Spectral tuning of light-harvesting complex II in the siphonous alga Bryopsis corticulans and its effect on energy transfer dynamics. Biochim. Biophys. Acta **1861:** 148191

Akhtar P, Zhang C, Liu Z, Tan H-S, Lambrev PH (2018) Excitation transfer and trapping kinetics in plant photosystem I probed by two-dimensional electronic spectroscopy. Photosynth. Res. **135:** 239–250

Albertsson PÅ (2001) A quantitative model of the domain structure of the photosynthetic membrane. Trends Plant Sci. **6:** 349–354

Allen JF, Forsberg J (2001) Molecular recognition in thylakoid structure and function. Trends Plant Sci. **6:** 317–326

Anderson JM, Chow WS, De Las Rivas J (2008) Dynamic flexibility in the structure and function of photosystem II in higher plant thylakoid membranes: the grana enigma. Photosynth. Res. **98:** 575–587

Andersson B, Anderson JM (1980) Lateral heterogeneity in the distribution of chlorophyll-protein complexes of the thylakoid membranes of spinach chloroplasts. Biochim. Biophys. Acta **593:** 427–440

Andrizhiyevskaya EG, Frolov D, van Grondelle R, Dekker JP (2004) Energy transfer and trapping in the photosystem I complex of *Synechococcus* PCC 7942 and in its supercomplex with IsiA. Biochim. Biophys. Acta **1656:** 104–113

Aro E-M, Virgin I, Andersson B (1993) Photoinhibition of photosystem II. Inactivation, protein damage and turnover. Biochimica et Biophysica Acta (BBA)- Bioenergetics **1143:** 113–134

Austin JR, Staehelin LA (2011) Three-dimensional architecture of grana and stroma thylakoids of higher plants as determined by electron tomography. Plant Physiol. **155:** 1601–1611

Badshah SL, Sun J, Mula S, Gorka M, Baker P, Luthra R, Lin S, van der Est A, Golbeck JH, Redding KE (2018) Mutations in algal and cyanobacterial photosystem I that independently affect the yield of initial charge separation in the two electron transfer cofactor branches. Biochim. Biophys. Acta **1859:** 42–55

Baker NR (2008) Chlorophyll fluorescence: a probe of photosynthesis in vivo. Annu. Rev. Plant Biol. **59:** 89–113

Barber J (1980) Membrane surface charges and potentials in relation to photosynthesis. Biochimica et Biophysica Acta (BBA)-Reviews on Bioenergetics **594:** 253–308

Barber J (2006) The engine of life: Photosystem II. The Biochemist **28:** 7–11

Barros T, Royant A, Standfuss J, Dreuw A, Kühlbrandt W (2009) Crystal structure of plant light - harvesting complex shows the active, energy - transmitting state. EMBO J. **28:** 298–306

Barzda V, Garab G, Gulbinas V, Valkunas L (1996) Evidence for long-range excitation energy migration in macroaggregates of the chlorophyll *a/b* light-harvesting antenna complexes. Biochim. Biophys. Acta **1273:** 231–236

Barzda V, Gulbinas V, Kananavicius R, Cervinskas V, van Amerongen H, van Grondelle R, Valkunas L (2001) Singlet–singlet annihilation kinetics in aggregates and trimers of LHCII. Biophys. J. **80:** 2409–2421

Barzda V, Mustárdy L, Garab G (1994) Size dependency of circular dichroism in macroaggregates of photosynthetic pigment–protein complexes. Biochemistry **33:** 10837–10841

Bassi R, Silvestri M, Dainese P, Moya I, Giacometti GM (1991) Effects of a non-ionic detergent on the spectral properties and aggregation state of the light-harvesting chlorophyll a/b protein complex (LHCII). J. Photochem. Photobiol. B: Biol. **9:** 335–353

Beddard G, Porter G (1976) Concentration quenching in chlorophyll. Nature **260:** 366–367

Beddard G, Porter G, Tredwell C, Barber J (1975) Fluorescence lifetimes in the photosynthetic unit. Nature **258:** 166–168

Bell AJ, Frankel LK, Bricker TM (2015) High yield non-detergent isolation of photosystem I–light-harvesting chlorophyll II membranes from spinach thylakoids: implications for the organization of the PS I antennae in higher plants. J. Biol. Chem. **290:** 18429–18437

Bellafiore S, Barneche F, Peltier G, Rochaix J-D (2005) State transitions and light adaptation require chloroplast thylakoid protein kinase STN7. Nature **433:** 892–895

Bennett DIG, Fleming GR, Amarnath K (2018) Energy-dependent quenching adjusts the excitation diffusion length to regulate photosynthetic light harvesting. Proc. Natl. Acad. Sci. U.S.A. **115:** E9523–E9531

Betterle N, Ballottari M, Zorzan S, de Bianchi S, Cazzaniga S, Dall'Osto L, Morosinotto T, Bassi R (2009) Light-induced dissociation of an antenna hetero-oligomer is needed for non-photochemical quenching induction. J. Biol. Chem. **284:** 15255–15266

Bittner T, Irrgang KD, Renger G, Wasielewski MR (1994) Ultrafast excitation energy transfer and exciton–exciton annihilation processes in isolated light-harvesting complexes of photosystem II (LHC II) from spinach. J. Phys. Chem. **98:** 11821–11826

Bittner T, Wiederrecht GP, Irrgang K-D, Renger G, Wasielewski MR (1995) Femtosecond transient absorption spectroscopy on the light-harvesting Chl *a/b* protein complex of photosystem II at room temperature and 12 K. Chem. Phys. **194:** 311–322

Blankenship RE (2014) Molecular Mechanisms of Photosynthesis, Ed 2nd. John Wiley & Sons

Bode S, Quentmeier CC, Liao PN, Hafi N, Barros T, Wilk L, Bittner F, Walla PJ (2009) On the regulation of photosynthesis by excitonic interactions between carotenoids and chlorophylls. Proc. Natl. Acad. Sci. U.S.A. **106:** 12311–12316

Boekema EJ, van Roon H, Calkoen F, Bassi R, Dekker JP (1999) Multiple types of association of photosystem II and its light-harvesting antenna in partially solubilized photosystem II membranes. Biochemistry **38:** 2233–2239

Bonardi V, Pesaresi P, Becker T, Schleiff E, Wagner R, Pfannschmidt T, Jahns P, Leister D (2005) Photosystem II core phosphorylation and photosynthetic acclimation require two different protein kinases. Nature **437:** 1179–1182

Bressan M, Dall'Osto L, Bargigia I, Alcocer MJP, Viola D, Cerullo G, D'Andrea C, Bassi R, Ballottari M (2016) LHCII can substitute for LHCI as an antenna for photosystem I but with reduced light-harvesting capacity. Nat. Plants **2:** 16131

Brooks MD, Jansson S, Niyogi KK (2014) PsbS-dependent non-photochemical quenching. *In* B Demmig-Adams, G Garab, W Adams Iii, Govindjee, eds, Non-Photochemical Quenching and Energy Dissipation in Plants, Algae and Cyanobacteria, Vol 40. Springer Netherlands, pp 297–314

Butler W, Tredwell C, Malkin R, Barber J (1979) The relationship between the lifetime and yield of the 735 nm fluorescence of chloroplasts at low temperatures. Biochim. Biophys. Acta **545:** 309–315

Bürck J, Roth S, Wadhwani P, Afonin S, Kanithasen N, Strandberg E, Ulrich AS (2008) Conformation and membrane orientation of amphiphilic helical peptides by oriented circular dichroism. Biophys. J. **95:** 3872–3881

Bürck J, Wadhwani P, Fanghänel S, Ulrich AS (2016) Oriented circular dichroism: A method to characterize membrane-active peptides in oriented lipid bilayers. Acc. Chem. Res. **49:** 184–192

Caffarri S, Broess K, Croce R, van Amerongen H (2011) Excitation energy transfer and trapping in higher plant photosystem II complexes with different antenna sizes. Biophys. J. **100:** 2094–2103

Caffarri S, Croce R, Breton J, Bassi R (2001) The major antenna complex of photosystem II has a xanthophyll binding site not involved in light harvesting. J. Biol. Chem. **276:** 35924–35933

Caffarri S, Kouřil R, Kereïche S, Boekema EJ, Croce R (2009) Functional architecture of higher plant photosystem II supercomplexes. EMBO J. **28:** 3052–3063

Calhoun TR, Ginsberg NS, Schlau-Cohen GS, Cheng Y-C, Ballottari M, Bassi R, Fleming GR (2009) Quantum coherence enabled determination of the energy landscape in light-harvesting complex II. J. Phys. Chem. B **113:** 16291–16295

Cantor CR, Schimmel PR (1980) Biophysical chemistry: Part II: Techniques for the study of biological structure and function. W. H. Freeman and Company, Oxford

Cao P, Su X, Pan X, Liu Z, Chang W, Li M (2018) Structure, assembly and energy transfer of plant photosystem II supercomplex. Biochim. Biophys. Acta **1859:** 633–644

Castelletti S, Morosinotto T, Robert B, Caffarri S, Bassi R, Croce R (2003) Recombinant Lhca2 and Lhca3 subunits of the photosystem I antenna system. Biochemistry **42:** 4226–4234

Chen G, Niu X, Chen X, Li L, Kuang T, Li S (2008) Characterization of chlorophyll–protein complexes isolated from a Siphonous green alga, *Bryopsis corticulans*. Photosynth. Res. **96:** 75–81

Cherepanov DA, Shelaev IV, Gostev FE, Aybush AV, Mamedov MD, Shuvalov VA, Semenov AY, Nadtochenko VA (2020) Generation of ion-radical chlorophyll states in the light-harvesting antenna and the reaction center of cyanobacterial photosystem I. Photosynth. Res. **146:** 55–73

Cherepanov DA, Shelaev IV, Gostev FE, Mamedov MD, Petrova AA, Aybush AV, Shuvalov VA, Semenov AY, Nadtochenko VA (2017) Mechanism of adiabatic primary electron transfer in photosystem I: Femtosecond spectroscopy upon excitation of reaction center in the far-red edge of the Q_Y band. Biochim. Biophys. Acta **1858:** 895–905

Chmeliov J, Gelzinis A, Songaila E, Augulis R, Duffy CD, Ruban AV, Valkunas L (2016) The nature of self-regulation in photosynthetic light-harvesting antenna. Nat. Plants **2:** 16045

Chow WS, Kim EH, Horton P, Anderson JM (2005) Granal stacking of thylakoid membranes in higher plant chloroplasts: the physicochemical forces at work and the functional consequences that ensue. Photochem. Photobiol. Sci. **4:** 1081–1090

Christa G, Cruz S, Jahns P, de Vries J, Cartaxana P, Esteves AC, Serôdio J, Gould SB (2017) Photoprotection in a monophyletic branch of chlorophyte algae is independent of energy‐dependent quenching (qE). New Phytol. **214:** 1132‐1144

Connelly JP, Müller MG, Bassi R, Croce R, Holzwarth AR (1997) Femtosecond transient absorption study of carotenoid to chlorophyll energy transfer in the light-harvesting complex II of photosystem II. Biochemistry **36:** 281–287

Connelly JP, Müller MG, Hucke M, Gatzen G, Mullineaux CW, Ruban AV, Horton P, Holzwarth AR (1997) Ultrafast spectroscopy of trimeric light-harvesting complex II from higher plants. J. Phys. Chem. B **101:** 1902–1909

Crisafi E, Pandit A (2017) Disentangling protein and lipid interactions that control a molecular switch in photosynthetic light harvesting. Biochim. Biophys. Acta **1859:** 40–47

Croce R (2015) A close view of photosystem I. Science **348:** 970–971

Croce R, Chojnicka A, Morosinotto T, Ihalainen JA, Van Mourik F, Dekker JP, Bassi R, Van Grondelle R (2007) The low-energy forms of photosystem I light-harvesting complexes: spectroscopic properties and pigment-pigment interaction characteristics. Biophys. J. **93:** 2418–2428

Croce R, Müller MG, Bassi R, Holzwarth AR (2001) Carotenoid-to-chlorophyll energy transfer in recombinant major light-harvesting complex (LHCII) of higher plants. I. Femtosecond transient absorption measurements. Biophys. J. **80:** 901–915

Croce R, van Amerongen H (2013) Light-harvesting in photosystem I. Photosynth. Res. **116:** 1–14

Croce R, van Amerongen H (2020) Light harvesting in oxygenic photosynthesis: Structural biology meets spectroscopy. Science **369**

Croce R, Weiss S, Bassi R (1999) Carotenoid-binding sites of the major light-harvesting complex II of higher plants. J. Biol. Chem. **274:** 29613–29623

Croce R, Zucchelli G, Garlaschi FM, Bassi R, Jennings RC (1996) Excited state equilibration in the photosystem I–light-harvesting I complex: P700 is almost isoenergetic with its antenna. Biochemistry **35:** 8572–8579

Croce R, Zucchelli G, Garlaschi FM, Jennings RC (1998) A thermal broadening study of the antenna chlorophylls in PSI-200, LHCI, and PSI core. Biochemistry **37:** 17355–17360

Curutchet C, Mennucci B (2017) Quantum Chemical Studies of Light Harvesting. Chem. Rev. **117:** 294–343

Curutchet C, Mennucci B (2018) Chlorophylls in a protein environment: How to calculate their spectral and redox properties (from MO to DFT). *In* R Croce, R van Grondelle, H van Amerongen, I van Stokkum, eds, Light Harvesting in Photosynthesis. CRC Press, Boca Raton, FL, p 21

Cseh Z, Rajagopal S, Tsonev T, Busheva M, Papp E, Garab G (2000) Thermooptic effect in chloroplast thylakoid membranes. Thermal and light stability of pigment arrays with different levels of structural complexity. Biochemistry **39:** 15250–15257

Cseh Z, Vianelli A, Rajagopal S, Krumova S, Kovács L, Papp E, Barzda V, Jennings R, Garab G (2005) Thermo-optically induced reorganizations in the main light harvesting antenna of plants. I. Non-arrhenius type of temperature dependence and linear light-intensity dependencies. Photosynth. Res. **86:** 263–273

Dall'Osto L, Cazzaniga S, Bressan M, Paleček D, Židek K, Niyogi KK, Fleming GR, Zigmantas D, Bassi R (2017) Two mechanisms for dissipation of excess light in monomeric and trimeric light-harvesting complexes. Nat. Plants **3:** 17033

Damkjær JT, Kereïche S, Johnson MP, Kovacs L, Kiss AZ, Boekema EJ, Ruban AV, Horton P, Jansson S (2009) The photosystem II light-harvesting protein Lhcb3 affects the macrostructure of photosystem II and the rate of state transitions in Arabidopsis. Plant Cell **21:** 3245–3256

Daum B, Kühlbrandt W (2011) Electron tomography of plant thylakoid membranes. J. Exp. Bot. **62:** 2393–2402

Daum B, Nicastro D, Austin II J, McIntosh JR, Kühlbrandt W (2010) Arrangement of photosystem II and ATP synthase in chloroplast membranes of spinach and pea. Plant Cell **22:** 1299–1312

Dave PC, Billington E, Pan YL, Straus SK (2005) Interaction of alamethicin with ether-linked phospholipid bilayers: Oriented circular dichroism, ^{31}P solid-state NMR, and differential scanning calorimetry studies. Biophys. J. **89:** 2434–2442

Dekker JP, Boekema EJ (2005) Supramolecular organization of thylakoid membrane proteins in green plants. Biochim. Biophys. Acta **1706:** 12–39

Demé B, Cataye C, Block MA, Maréchal E, Jouhet J (2014) Contribution of galactoglycerolipids to the 3-dimensional architecture of thylakoids. FASEB J. **28:** 3373–3383

Demmig-Adams B, Garab G, Adams III W, Govindjee (2014) Non-photochemical quenching and energy dissipation in plants, algae and cyanobacteria. Springer, Dordrecht, The Netherlands

den Hollander WTF, Bakker JGC, van Grondelle R (1983) Trapping, loss and annihilation of excitations in a photosynthetic system. I. Theoretical aspects. Biochim. Biophys. Acta **725:** 492–507

Dexter DL (1953) A theory of sensitized luminescence in solids. J. Chem. Phys. **21:** 836–850

Dietzel L, Bräutigam K, Steiner S, Schüffler K, Lepetit B, Grimm B, Schöttler MA, Pfannschmidt T (2011) Photosystem II supercomplex remodeling serves as an entry mechanism for state transitions in Arabidopsis. Plant Cell **23:** 2964–2977

Dinh T-C, Renger T (2015) Towards an exact theory of linear absorbance and circular dichroism of pigment-protein complexes: Importance of non-secular contributions. J. Chem. Phys. **142:** 034104

Do TN, Huerta-Viga A, Akhtar P, Nguyen HL, Nowakowski PJ, Khyasudeen MF, Lambrev PH, Tan H-S (2019) Revealing the excitation energy transfer network of Light-Harvesting Complex II by a phenomenological analysis of two-dimensional electronic spectra at 77 K. J. Chem. Phys. **151:** 205101

Dockter C, Müller AH, Dietz C, Volkov A, Polyhach Y, Jeschke G, Paulsen H (2012) Rigid core and flexible terminus: structure of solubilized light-harvesting chlorophyll *a/b* complex (LHCII) measured by EPR. J. Biol. Chem. **287:** 2915–2925

Dogutan DK, Nocera DG (2019) Artificial Photosynthesis at Efficiencies Greatly Exceeding That of Natural Photosynthesis. Acc. Chem. Res. **52:** 3143–3148

Dorne A-J, Joyard J, Douce R (1990) Do thylakoids really contain phosphatidylcholine? Proc. Natl. Acad. Sci. U.S.A. **87:** 71–74

Dostál J, Pšenčík J, Zigmantas D (2016) In situ mapping of the energy flow through the entire photosynthetic apparatus. Nature Chemistry **8:** 705–710

Douce R, Joyard J (1996) Biosynthesis of thylakoid membrane lipids. *In* DR Ort, CF Yocum, eds, Oxygenic Photosynthesis: The Light Reactions. Kluwer Academic Publishers, Dordrecht, pp 69–101

Duan H-G, Stevens AL, Nalbach P, Thorwart M, Prokhorenko VI, Miller RJD (2015) Two-dimensional electronic spectroscopy of light-harvesting complex II at ambient temperature: a joint experimental and theoretical study. J. Phys. Chem. B **119:** 12017–12027

Duchêne S, Siegenthaler P-A (2000) Do glycerolipids display lateral heterogeneity in the thylakoid membrane? Lipids **35:** 739–744

Dunahay TG, Staehelin LA, Seibert M, Ogilvie PD, Berg SP (1984) Structural, biochemical and biophysical characterization of four oxygen-evolving photosystem II preparations from spinach. Biochim. Biophys. Acta **764:** 179–193

Engelmann E, Zucchelli G, Casazza AP, Brogioli D, Garlaschi FM, Jennings RC (2006) Influence of the photosystem I–light harvesting complex I antenna domains on fluorescence decay. Biochemistry **45:** 6947–6955

Enriquez MM, Akhtar P, Zhang C, Garab G, Lambrev PH, Tan HS (2015) Energy transfer dynamics in trimers and aggregates of light-harvesting complex II probed by 2D electronic spectroscopy. J. Chem. Phys. **142:** 212432

Faludi-Dániel Á, Demeter S, Garay A (1973) Circular dichroism spectra of granal and agranal chloroplasts of maize. Plant Physiol. **52:** 54–56

Faludi-Dániel Á, Mustárdy LA (1983) Organization of Chlorophyll a in the Light-Harvesting Chlorophyll a/b Protein Complex as Shown by Circular Dichroism: Liquid Crystal-Like Domains. Plant Physiol. **73:** 16–19

Farooq S, Chmeliov J, Trinkunas G, Valkunas L, van Amerongen H (2016) Is There Excitation Energy Transfer between Different Layers of Stacked Photosystem-II-Containing Thylakoid Membranes? J. Phys. Chem. Lett. **7:** 1406–1410

Farooq S, Chmeliov J, Wientjes E, Koehorst R, Bader A, Valkunas L, Trinkunas G, van Amerongen H (2018) Dynamic feedback of the photosystem II reaction centre on photoprotection in plants. Nat. Plants **4:** 225

Fassioli F, Dinshaw R, Arpin PC, Scholes GD (2014) Photosynthetic light harvesting: excitons and coherence. Journal of The Royal Society Interface **11:** 20130901

Fischer BB, Hideg E, Krieger-Liszkay A (2013) Production, detection, and signaling of singlet oxygen in photosynthetic organisms. Antioxidants & Redox Signaling **18:** 2145–2162

Förster T (1965) Delocalized excitation and excitation transfer. Florida State University, Tallahassee, Florida

Frese RN, Palacios MA, Azzizi A, Van Stokkum IH, Kruip J, Rögner M, Karapetyan NV, Schlodder E, van Grondelle R, Dekker JP (2002) Electric field effects on red chlorophylls, β-carotenes and P_{700} in cyanobacterial photosystem I complexes. Biochim. Biophys. Acta **1554:** 180–191

Fristedt R, Willig A, Granath P, Crevecoeur M, Rochaix JD, Vener AV (2009) Phosphorylation of Photosystem II Controls Functional Macroscopic Folding of Photosynthetic Membranes in Arabidopsis. Plant Cell **21:** 3950–3964

Fromme P, Jordan P, Krauß N (2001) Structure of photosystem I. Biochim. Biophys. Acta **1507:** 5–31

Fuller FD, Ogilvie JP (2015) Experimental implementations of two-dimensional Fourier transform electronic spectroscopy. Annu. Rev. Phys. Chem. **66:** 667–690

Galka P, Santabarbara S, Thi THK, Degand H, Morsomme P, Jennings RC, Boekema EJ, Caffarri S (2012) Functional analyses of the plant photosystem I–light-harvesting complex II supercomplex reveal that light-harvesting complex II loosely bound to photosystem II is a very efficient antenna for photosystem I in state II. Plant Cell **24:** 2963–2978

Gallagher Faeder SM, Jonas DM (1999) Two-Dimensional Electronic Correlation and Relaxation Spectra: Theory and Model Calculations. J. Phys. Chem. A **103:** 10489–10505

Garab G (1992) Macrodomain organization of complexes in the thylakoid membranes. *In* N Murata, ed, Research in Photosynthesis, Vol Vol. 1. Kluwer Academic Publishers, Dordrecht, The Netherlands, pp 171–178

Garab G (1996) Linear and circular dichroism. *In* J Amesz, AJ Hoff, eds, Biophysical Techniques in Photosynthesis. Springer, The Netherlands, pp 11–40

Garab G (2016) Self-assembly and structural–functional flexibility of oxygenic photosynthetic machineries: personal perspectives. Photosynth. Res. **127:** 131–150

Garab G, Cseh Z, Kovács L, Rajagopal S, Várkonyi Z, Wentworth M, Mustárdy L, Der A, Ruban AV, Papp E, Holzenburg A, Horton P (2002) Light-induced trimer to monomer transition in the main light-harvesting antenna complex of plants: Thermo-optic mechanism. Biochemistry **41:** 15121–15129

Garab G, Faludi-Daniel A, Sutherland JC, Hind G (1988) Macroorganization of chlorophyll *a*/*b* light-harvesting complex in thylakoids and aggregates: information from circular differential scattering. Biochemistry **27:** 2425–2430

Garab G, Kieleczawa J, Sutherland JC, Bustamante C, Hind G (1991) Organization of pigment protein complexes into macrodomains in the thylakoid membranes of wild-type and chlorophyll-b-less mutant of barley as revealed by circular-dichroism. Photochem. Photobiol. **54:** 273–281

Garab G, Leegood RC, Walker DA, Sutherland JC, Hind G (1988) Reversible changes in macroorganization of the light-harvesting chlorophyll *a*/*b* pigment-protein complex detected by circular dichroism. Biochemistry **27:** 2430–2434

Garab G, Mustárdy L (1999) Role of LHCII-containing macrodomains in the structure, function and dynamics of grana. Aust. J. Plant Physiol. **26:** 649–658

Garab G, van Amerongen H (2009) Linear dichroism and circular dichroism in photosynthesis research. Photosynth. Res. **101:** 135–146

Garab G, Wells S, Finzi L, Bustamante C (1988) Helically organized macroaggregates of pigment protein complexes in chloroplasts - evidence from circular intensity differential scattering. Biochemistry **27:** 5839–5843

Gelzinis A, Augulis R, Butkus V, Robert B, Valkunas L (2019) Two-dimensional spectroscopy for non-specialists. Biochim. Biophys. Acta **1860:** 271–285

Gelzinis A, Chmeliov J, Ruban AV, Valkunas L (2018) Can red-emitting state be responsible for fluorescence quenching in LHCII aggregates? Photosynth. Res. **135:** 275–284

Georgakopoulou S, van der Zwan G, Bassi R, van Grondelle R, van Amerongen H, Croce R (2007) Understanding the changes in the circular dichroism of light harvesting complex II upon varying its pigment composition and organization. Biochemistry **46:** 4745–4754

Germano M, Gradinaru CC, Shkuropatov AY, van Stokkum IHM, Shuvalov VA, Dekker JP, van Grondelle R, van Gorkom HJ (2004) Energy and electron transfer in photosystem II reaction centers with modified pheophytin composition. Biophys. J. **86:** 1664–1672

Gibasiewicz K, Ramesh V, Lin S, Redding K, Woodbury N, Webber A (2007) Two equilibration pools of chlorophylls in the photosystem I core antenna of *Chlamydomonas reinhardtii.* Photosynth. Res. **92:** 55–63

Gibasiewicz K, Ramesh VM, Lin S, Woodbury NW, Webber AN (2002) Excitation dynamics in eukaryotic PS I from *Chlamydomonas reinhardtii* CC 2696 at 10 K. Direct detection of the reaction center exciton states. J. Phys. Chem. B **106:** 6322–6330

Gibasiewicz K, Ramesh VM, Melkozernov AN, Lin S, Woodbury NW, Blankenship RE, Webber AN (2001) Excitation dynamics in the core antenna of PS I from *Chlamydomonas reinhardtii* CC 2696 at room temperature. J. Phys. Chem. B **105:** 11498–11506

Gibasiewicz K, Szrajner A, Ihalainen JA, Germano M, Dekker JP, van Grondelle R (2005) Characterization of low-energy chlorophylls in the PSI-LHCI supercomplex from *Chlamydomonas reinhardtii.* A site-selective fluorescence study. J. Phys. Chem. B **109:** 21180–21186

Gillbro T, Sandström A, Spangfort M, Sundström V, van Grondelle R (1988) Excitation energy annihilation in aggregates of chlorophyll *a*/*b* complexes. Biochim. Biophys. Acta **934:** 369–374

Giovagnetti V, Han G, Ware MA, Ungerer P, Qin X, Wang W-D, Kuang T, Shen J-R, Ruban AV (2018) A siphonous morphology affects light-harvesting modulation in the intertidal green macroalga *Bryopsis corticulans* (Ulvophyceae). Planta **247:** 1293–1306

Gobets B, van Grondelle R (2001) Energy transfer and trapping in photosystem I. Biochim. Biophys. Acta **1507:** 80–99

Goldschmidt-Clermont M, Bassi R (2015) Sharing light between two photosystems: mechanism of state transitions. Curr. Opin. Plant Biol. **25:** 71–78

Goral TK, Johnson MP, Duffy CDP, Brain APR, Ruban AV, Mullineaux CW (2012) Light-harvesting antenna composition controls the macrostructure and dynamics of thylakoid membranes in Arabidopsis. Plant J. **69:** 289–301

Gouterman M, Wagnière GH, Snyder LC (1963) Spectra of porphyrins: Part II. Four orbital model. J. Mol. Spectrosc. **11:** 108–127

Gradinaru CC, Kennis JTM, Papagiannakis E, van Stokkum IHM, Cogdell RJ, Fleming GR, Niederman RA, van Grondelle R (2001) An unusual pathway of excitation energy deactivation in carotenoids: Singlet-to-triplet conversion on an ultrafast timescale in a photosynthetic antenna. Proc. Natl. Acad. Sci. U.S.A. **98:** 2364–2369

Gradinaru CC, Özdemir S, Gülen D, van Stokkum IHM, van Grondelle R, van Amerongen H (1998) The flow of excitation energy in LHCII monomers: Implications for the structural model of the major plant antenna. Biophys. J. **75:** 3064–3077

Grieco M, Suorsa M, Jajoo A, Tikkanen M, Aro EM (2015) Light-harvesting II antenna trimers connect energetically the entire photosynthetic machinery – including both photosystems II and I. Biochim. Biophys. Acta **1847:** 607–619

Grimm B, Porra RJ, Rüdiger W, Scheer H (2007) Chlorophylls and bacteriochlorophylls: biochemistry, biophysics, functions and applications, Vol 25. Springer Science & Business Media

Guskov A, Kern J, Gabdulkhakov A, Broser M, Zouni A, Saenger W (2009) Cyanobacterial photosystem II at 2.9-A resolution and the role of quinones, lipids, channels and chloride. Nat. Struct. Mol. Biol. **16:** 334–342

Haferkamp S, Haase W, van Amerongen H, Kirchhoff H (2010) Efficient light harvesting by photosytem II requires an optimized protein packing density in grana thylakoids. J. Biol. Chem. **285:** 17020–17028

Hamm P, Zanni M (2011) Concepts and methods of 2D infrared spectroscopy. Cambridge University Press, Cambridge

Hankamer B, Morris E, Nield J, Carne A, Barber J (2001) Subunit positioning and transmembrane helix organisation in the core dimer of photosystem II. FEBS Lett. **504:** 142–151

Hansen AE (2005) Molecular exciton approach to anisotropic absorption and circular dichroism I. General formulation. Monatsh. Chem./Chem. Mon. **136:** 253–273

Hastings G, Reed LJ, Lin S, Blankenship RE (1995) Excited state dynamics in photosystem I: effects of detergent and excitation wavelength. Biophys. J. **69:** 2044

Hemelrijk PW, Kwa SLS, van Grondelle R, Dekker JP (1992) Spectroscopic properties of LHC-II, the main light-harvesting chlorophyll a/b protein complex from chloroplast membranes. Biochim. Biophys. Acta **1098:** 159-166

Herbstová M, Tietz S, Kinzel C, Turkina MV, Kirchhoff H (2012) Architectural switch in plant photosynthetic membranes induced by light stress. Proc. Natl. Acad. Sci. U.S.A. **109:** 20130–20135

Hobe S, Prytulla S, Kuhlbrandt W, Paulsen H (1994) Trimerization and crystallization of reconstituted light-harvesting chlorophyll *a*/*b* complex. EMBO J. **13:** 3423–3429

Hohmann-Marriott MF, Blankenship RE (2011) Evolution of photosynthesis. Annu. Rev. Plant Biol. **62:** 515–548

Holm JK, Várkonyi Z, Kovács L, Posselt D, Garab G (2005) Thermo-optically induced reorganizations in the main light harvesting antenna of plants. II. Indications for the role of LHCII-only macrodomains in thylakoids. Photosynth. Res. **86:** 275–282

Holt NE, Zigmantas D, Valkunas L, Li X-P, Niyogi KK, Fleming GR (2005) Carotenoid cation formation and the regulation of photosynthetic light harvesting. Science **307:** 433–436

Holzwarth A, Jahns P (2014) Non-photochemical quenching mechanisms in intact organisms as derived from ultrafast-fluorescence kinetic studies. *In* B Demmig-Adams, G Garab, W Adams III, Govindjee, eds, Non-Photochemical Quenching and Energy Dissipation in Plants, Algae and Cyanobacteria. Springer, Dordrecht, The Netherlands, pp 129–156

Holzwarth AR (1996) Data analysis of time-resolved measurements. *In* J Amesz, AJ Hoff, eds, Biophysical Techniques in Photosynthesis. Springer, Dordrecht, The Netherlands, pp 75–92

Holzwarth AR, Miloslavina Y, Nilkens M, Jahns P (2009) Identification of two quenching sites active in the regulation of photosynthetic light-harvesting studied by time-resolved fluorescence. Chem. Phys. Lett. **483:** 262–267

Holzwarth AR, Müller MG, Niklas J, Lubitz W (2005) Charge recombination fluorescence in photosystem I reaction centers from *Chlamydomonas reinhardtii.* J. Phys. Chem. B **109:** 5903–5911

Horton P (1999) Are grana necessary for regulation of light harvesting? Aust. J. Plant Physiol. **26:** 659–669

Horton P (2012) Optimization of light harvesting and photoprotection: molecular mechanisms and physiological consequences. Transactions of the Royal Society B **367:** 3455–3465

Horton P, Ruban AV (1992) Regulation of photosystem II. Photosynth. Res. **34:** 375–385

Horton P, Ruban AV, Rees D, Pascal AA, Noctor G, Young AJ (1991) Control of the light-harvesting function of chloroplast membranes by aggregation of the LHCII chlorophyll protein complex. FEBS Lett. **292:** 1–4

Horton P, Wentworth M, Ruban A (2005) Control of the light harvesting function of chloroplast membranes: The LHCII-aggregation model for non-photochemical quenching. FEBS Lett. **579:** 4201–4206

Ihalainen JA, Rätsep M, Jensen PE, Scheller HV, Croce R, Bassi R, Korppi-Tommola JE, Freiberg A (2003) Red spectral forms of chlorophylls in green plant PSI: a site-selective and high-pressure spectroscopy study. J. Phys. Chem. B **107:** 9086–9093

Ihalainen JA, van Stokkum IHM, Gibasiewicz K, Germano M, van Grondelle R, Dekker JP (2005) Kinetics of excitation trapping in intact photosystem I of *Chlamydomonas reinhardtii* and *Arabidopsis thaliana.* Biochim. Biophys. Acta **1706:** 267–275

Ilioaia C, Johnson MP, Horton P, Ruban AV (2008) Induction of efficient energy dissipation in the isolated light-harvesting complex of photosystem II in the absence of protein aggregation. J. Biol. Chem. **283:** 29505–29512

Jahns P, Holzwarth AR (2012) The role of the xanthophyll cycle and of lutein in photoprotection of photosystem II. Biochim. Biophys. Acta **1817:** 182–193

Jansson S (1999) A guide to the Lhc genes and their relatives in *Arabidopsis.* Trends Plant Sci. **4:** 236–240

Jennings RC, Zucchelli G, Croce R, Garlaschi FM (2003) The photochemical trapping rate from red spectral states in PSI–LHCI is determined by thermal activation of energy transfer to bulk chlorophylls. Biochim. Biophys. Acta **1557:** 91–98

Johnson MP (2018) Metabolic regulation of photosynthetic membrane structure tunes electron transfer function. Biochem. J. **475:** 1225–1233

Johnson MP, Goral TK, Duffy CD, Brain AP, Mullineaux CW, Ruban AV (2011) Photoprotective energy dissipation involves the reorganization of photosystem II light-harvesting complexes in the grana membranes of spinach chloroplasts. Plant Cell: tpc. 110.081646

Johnson MP, Wientjes E (2019) The relevance of dynamic thylakoid organisation to photosynthetic regulation. Biochim. Biophys. Acta **1861:** 148039

Jonas DM (2003) Two-dimensional femtosecond spectroscopy. Annu. Rev. Phys. Chem. **54:** 425–463

Jost PC, Griffith OH, Capaldi RA, Vanderkooi G (1973) Evidence for Boundary Lipid in Membranes. Proc. Natl. Acad. Sci. U.S.A. **70:** 480–484

Karapetyan NV, Dorra D, Schweitzer G, Bezsmertnaya IN, Holzwarth AR (1997) Fluorescence spectroscopy of the longwave chlorophylls in trimeric and monomeric photosystem I core complexes from the cyanobacterium *Spirulina platensis*. Biochemistry **36:** 13830–13837

Karapetyan NV, Schlodder E, van Grondelle R, Dekker JP (2006) The long-wavelength chlorophylls of photosystem I. *In* JH Golbeck, ed, Photosystem I: The Light-Driven, Plastocyanin:Ferredoxin Oxidoreductase. Springer, Dordrecht, The Netherlands, pp 177–192

Kell A, Feng X, Lin C, Yang Y, Li J, Reus M, Holzwarth AR, Jankowiak R (2014) Charge-Transfer Character of the Low-Energy Chl a Q y Absorption Band in Aggregated Light Harvesting Complexes II. J. Phys. Chem. B **118:** 6086–6091

Keller D, Bustamante C (1986) Theory of the interaction of light with large inhomogeneous molecular aggregates. II. Psi-type circular dichroism. J. Chem. Phys. **84:** 2972–2980

Keren N, Krieger-Liszkay A (2011) Photoinhibition: molecular mechanisms and physiological significance. Physiol. Plant. **142:** 1–5

Keusters D, Tan H-S, Warren WS (1999) Role of pulse phase and direction in two-dimensional optical spectroscopy. J. Phys. Chem. A **103:** 10369–10380

Khatoon M, Inagawa K, Pospisil P, Yamashita A, Yoshioka M, Lundin B, Horie J, Morita N, Jajoo A, Yamamoto Y, Yamamoto Y (2009) Quality control of photosystem II thylakoid unstacking is necessary to avoid further damage to the D1 protein and to facilitate D1 degradation under light stress in spinach thylakoids. J. Biol. Chem. **284:** 25343–25352

Kirchhoff H (2013) Architectural switches in plant thylakoid membranes. Photosynth. Res. **116:** 481–487

Kirchhoff H (2018) Structure-function relationships in photosynthetic membranes: challenges and emerging fields. Plant Sci. **266:** 76–82

Kirchhoff H (2019) Chloroplast ultrastructure in plants. New Phytol. **224:** 994–994

Kirchhoff H, Borinski M, Lenhert S, Chi L, Büchel C (2004) Transversal and lateral exciton energy transfer in grana thylakoids of spinach. Biochemistry **43:** 14508–14516

Kirchhoff H, Hall C, Wood M, Herbstová M, Tsabari O, Nevo R, Charuvi D, Shimoni E, Reich Z (2011) Dynamic control of protein diffusion within the granal thylakoid lumen. Proc. Natl. Acad. Sci. U.S.A. **108:** 20248–20253

Kirchhoff H, Mukherjee U, Galla H-J (2002) Molecular architecture of the thylakoid membrane: lipid diffusion space for plastoquinone. Biochemistry **41:** 4872–4882

Kirk JT (2011) Light and photosynthesis in aquatic ecosystems, Ed 3rd edn. Cambridge University Press, Cambridge

Kleima FJ, Gradinaru CC, Calkoen F, van Stokkum IHM, van Grondelle R, van Amerongen H (1997) Energy transfer in LHCII monomers at 77 K studied by sub-picosecond transient absorption spectroscopy. Biochemistry **36:** 15262–15268

Kobayashi K, Wada H (2016) Role of lipids in chloroplast biogenesis. *In* Lipids in Plant and Algae Development. Springer, pp 103–125

Kolubayev T, Geacintov NE, Paillotin G, Breton J (1985) Domain sizes in chloroplasts and chlorophyll-protein complexes probed by fluorescence yield quenching induced by singlet-triplet exciton annihilation. Biochim. Biophys. Acta **808:** 66–76

Kouřil R, Wientjes E, Bultema JB, Croce R, Boekema EJ (2013) High-light vs. low-light: Effect of light acclimation on photosystem II composition and organization in *Arabidopsis thaliana*. Biochim. Biophys. Acta **1827:** 411–419

Kouřil R, Zygadlo A, Arteni AA, de Wit CD, Dekker JP, Jensen PE, Scheller HV, Boekema EJ (2005) Structural characterization of a complex of photosystem I and light-harvesting complex II of *Arabidopsis thaliana*. Biochemistry **44:** 10935–10940

Kovács L, Damkjaer J, Kereïche S, Ilioaia C, Ruban AV, Boekema EJ, Jansson S, Horton P (2006) Lack of the light-harvesting complex CP24 affects the structure and function of the grana membranes of higher plant chloroplasts. Plant Cell **18:** 3106–3120

Kowalewska Ł, Bykowski M, Mostowska A (2019) Spatial organization of thylakoid network in higher plants. Bot. Lett. **118:** 1–18

König C, Neugebauer J (2012) Quantum Chemical Description of Absorption Properties and Excited-State Processes in Photosynthetic Systems. Chem. Phys. Chem. **13:** 386–425

Krause G, Weis E (1991) Chlorophyll fluorescence and photosynthesis: the basics. Annu. Rev. Plant Biol. **42:** 313–349

Kromdijk J, Głowacka K, Leonelli L, Gabilly ST, Iwai M, Niyogi KK, Long SP (2016) Improving photosynthesis and crop productivity by accelerating recovery from photoprotection. Science **354:** 857–861

Kuball H-G (2002) CD and ACD spectroscopy on anisotropic samples: Chirality of oriented molecules and anisotropic phases—a critical analysis. Enantiomer **7:** 197–205

Kuball H-G, Dorr E, Höfer T, Türk O (2005) Exciton chirality method. Oriented molecules – anisotropic phases. Monatsh. Chem./Chem. Mon. **136:** 289–324

Kuball H-G, Höfer T (2000) Chirality and circular dichroism of oriented molecules and anisotropic phases. Chirality **12:** 278–286

Külheim C, Jansson S (2005) What leads to reduced fitness in non-photochemical quenching mutants? Physiol. Plant. **125:** 202–211

Kwa SLS, Groeneveld FG, Dekker JP, van Grondelle R, van Amerongen H, Lin S, Struve WS (1992) Steady-state and time-resolved polarized-light spectroscopy of the green plant light-harvesting complex-II. Biochim. Biophys. Acta **1101:** 143–146

Lambrev P, Várkonyi Z, Krumova S, Kovács L, Miloslavina Y, Holzwarth AR, Garab G (2007) Importance of trimer–trimer interactions for the native state of the plant light-harvesting complex II. Biochim. Biophys. Acta **1767:** 847–853

Lambrev PH, Akhtar P (2019) Macroorganisation and flexibility of thylakoid membranes. Biochem. J. **476:** 2981–3018

Lambrev PH, Akhtar P, Tan H-S (2020) Insights into the mechanisms and dynamics of energy transfer in plant light-harvesting complexes from two-dimensional electronic spectroscopy. Biochim. Biophys. Acta Bioenerg. **1861:** 148050

Lambrev PH, Miloslavina Y, Jahns P, Holzwarth AR (2012) On the relationship between non-photochemical quenching and photoprotection of photosystem II. Biochim. Biophys. Acta **1817:** 760–769

Lambrev PH, Nilkens M, Miloslavina Y, Jahns P, Holzwarth AR (2010) Kinetic and spectral resolution of multiple nonphotochemical quenching components in *Arabidopsis* leaves. Plant Physiol. **152:** 1611–1624

Lambrev PH, Schmitt FJ, Kussin S, Schoengen M, Várkonyi Z, Eichler HJ, Garab G, Renger G (2011) Functional domain size in aggregates of light-harvesting complex II and thylakoid membranes. Biochim. Biophys. Acta **1807:** 1022–1031

Le Quiniou C, Tian L, Drop B, Wientjes E, van Stokkum IHM, van Oort B, Croce R (2015) PSI–LHCI of *Chlamydomonas reinhardtii*: Increasing the absorption cross section without losing efficiency. Biochim. Biophys. Acta **1847:** 458–467

Le Quiniou C, van Oort B, Drop B, van Stokkum IH, Croce R (2015) The high efficiency of photosystem I in the green alga *Chlamydomonas reinhardtii* is maintained after the antenna size is substantially increased by the association of light-harvesting complexes II. J. Biol. Chem. **290:** 30587–30595

Li L, Aro E-M, Millar AH (2018) Mechanisms of Photodamage and Protein Turnover in Photoinhibition. Trends Plant Sci. **23:** 667–676

Li X-P, Bjorkman O, Shih C, Grossman AR, Rosenquist M, Jansson S, Niyogi KK (2000) A pigment-binding protein essential for regulation of photosynthetic light harvesting. Nature **403:** 391–395

Li XP, Muller-Moule P, Gilmore AM, Niyogi KK (2002) PsbS-dependent enhancement of feedback de-excitation protects photosystem II from photoinhibition. Proc. Natl. Acad. Sci. U.S.A. **99:** 15222–15227

Li Z, Wakao S, Fischer BB, Niyogi KK (2009) Sensing and responding to excess light. Annu. Rev. Plant Biol. **60:** 239–260

Lindorfer D, Müh F, Renger T (2017) Origin of non-conservative circular dichroism of the CP29 antenna complex of photosystem II. Phys. Chem. Chem. Phys. **19:** 7524–7536

Lindorfer D, Renger T (2018) Theory of anisotropic circular dichroism of excitonically coupled systems: Application to the baseplate of green sulfur bacteria. J. Phys. Chem. B **122:** 2747–2756

Linnanto J, Martiskainen J, Lehtovuori V, Ihalainen J, Kananavicius R, Barbato R, Korppi-Tommola J (2006) Excitation energy transfer in the LHC-II trimer: a model based on the new 2.72 Å structure. Photosynth. Res. **87:** 267–279

Liu C, Gao Z, Liu K, Sun R, Cui C, Holzwarth AR, Yang C (2016) Simultaneous refolding of denatured PsbS and reconstitution with LHCII into liposomes of thylakoid lipids. Photosynth. Res. **127:** 109–116

Liu ZF, Yan HC, Wang KB, Kuang TY, Zhang JP, Gui LL, An XM, Chang WR (2004) Crystal structure of spinach major light-harvesting complex at 2.72 Å resolution. Nature **428:** 287–292

Long SP, ZHU XG, Naidu SL, Ort DR (2006) Can improvement in photosynthesis increase crop yields? Plant, Cell Environ. **29:** 315–330

Marin A, van Stokkum INM, Novoderezhkin VI, van Grondelle R (2012) Excitation-induced polarization decay in the plant light-harvesting complex LHCII. J. Photochem. Photobiol. A: Chem. **234:** 91–99

Mascoli V, Liguori N, Xu P, Roy LM, van Stokkum IH, Croce R (2019) Capturing the Quenching Mechanism of Light-Harvesting Complexes of Plants by Zooming in on the Ensemble. Chem **5:** 494–495

Mazor Y, Borovikova A, Nelson N (2015) The structure of plant photosystem I super-complex at 2.8 Å resolution. eLife **4:** e7433

Melkozernov AN, Kargul J, Lin S, Barber J, Blankenship RE (2004) Energy coupling in the PSI–LHCI supercomplex from the green alga *Chlamydomonas reinhardtii.* J. Phys. Chem. B **108:** 10547–10555

Melkozernov AN, Kargul J, Lin S, Barber J, Blankenship RE (2005) Spectral and kinetic analysis of the energy coupling in the PS I–LHC I supercomplex from the green alga *Chlamydomonas reinhardtii* at 77 K. Photosynth. Res. **86:** 203–216

Melkozernov AN, Lin S, Blankenship RE (2000) Femtosecond transient spectroscopy and excitonic interactions in photosystem I. J. Phys. Chem. B **104:** 1651–1656

Miloslavina Y, Lambrev PH, Jávorfi T, Várkonyi Z, Karlický V, Wall JS, Hind G, Garab G (2012) Anisotropic circular dichroism signatures of oriented thylakoid membranes and lamellar aggregates of LHCII. Photosynth. Res. **111:** 29–39

Miloslavina Y, Wehner A, Wientjes E, Reus M, Lambrev P, Garab G, Croce R, Holzwarth AR (2008) Far-red fluorescence: A direct spectroscopic marker for LHCII oligomers forming in non-photochemical quenching. FEBS Lett. **582:** 3625–3631

Mizusawa N, Wada H (2011) The role of lipids in photosystem II. Biochim. Biophys. Acta. **1817:** 194–208

Moffitt W (1956) Optical rotatory dispersion of helical polymers. J. Chem. Phys. **25:** 467–478

Moya I, Silvestri M, Vallon O, Cinque G, Bassi R (2001) Time-resolved fluorescence analysis of the photosystem II antenna proteins in detergent micelles and liposomes. Biochemistry **40:** 12552–12561

Mukamel S (1995) Principles of nonlinear optical spectroscopy. Oxford University Press

Muller P, Li X-P, Niyogi KK (2001) Non-photochemical quenching. A response to excess light energy. Plant Physiol. **125:** 1558–1566

Mustárdy L, Buttle K, Steinbach G, Garab G (2008) The three-dimensional network of the thylakoid membranes in plants: quasihelical model of the granum-stroma assembly. Plant Cell **20:** 2552–2557

Mustárdy L, Garab G (2003) Granum revisited. A three-dimensional model – where things fall into place. Trends Plant Sci. **8:** 117–122

Mustárdy L, Jánossy AG (1979) Evidence of helical thylakoid arrangement by scanning electron microscopy. Plant Sci. Lett. **16:** 281–284

Müh F, Madjet ME-A, Renger T (2010) Structure-based identification of energy sinks in plant light-harvesting complex II. J. Phys. Chem. B **114:** 13517–13535

Müh F, Renger T (2012) Refined structure-based simulation of plant Light-harvesting complex II: linear optical spectra of trimers and aggregates. Biochim. Biophys. Acta **1817:** 1446–1460

Müller MG, Lambrev P, Reus M, Wientjes E, Croce R, Holzwarth AR (2010) Singlet energy dissipation in photosystem II light-harvesting complex does not involve energy transfer to carotenoids. Chem. Phys. Chem. **11:** 1289–1296

Müller MG, Niklas J, Lubitz W, Holzwarth AR (2003) Ultrafast transient absorption studies on photosystem I reaction centers from *Chlamydomonas reinhardtii*. 1. A new interpretation of the energy trapping and early electron transfer steps in photosystem I. Biophys. J. **85:** 3899–3922

Müller MG, Slavov C, Luthra R, Redding KE, Holzwarth AR (2010) Independent initiation of primary electron transfer in the two branches of the photosystem I reaction center. Proc. Natl. Acad. Sci. U.S.A. **107:** 4123–4128

Nagy G, Kovács L, Ünnep R, Zsiros O, Almasy L, Rosta L, Timmins P, Peters J, Posselt D, Garab G (2013) Kinetics of structural reorganizations in multilamellar photosynthetic membranes monitored by small-angle neutron scattering. Eur. Phys. J. E **36:** 69

Nagy G, Posselt D, Kovács L, Holm JK, Szabó M, Ughy B, Rosta L, Peters J, Timmins P, Garab G (2011) Reversible membrane reorganizations during photosynthesis in vivo: revealed by small-angle neutron scattering. Biochem. J. **436:** 225–230

Nagy G, Szabó M, Ünnep R, Kali G, Miloslavina Y, Lambrev PH, Zsiros O, Porcar L, Timmins P, Rosta L, Garab G (2012) Modulation of the multilamellar membrane organization and of the chiral macrodomains in the diatom Phaeodactylum tricornutum revealed by small-angle neutron scattering and circular dichroism spectroscopy. Photosynth. Res. **111:** 71–79

Nagy G, Ünnep R, Zsiros O, Tokutsu R, Takizawa K, Porcar L, Moyet L, Petroutsos D, Garab G, Finazzi G, Minagawa J (2014) Chloroplast remodeling during state transitions in *Chlamydomonas reinhardtii* as revealed by noninvasive techniques *in vivo*. Proc. Natl. Acad. Sci. U.S.A. **111:** 5042–5047

Nakayama K, Mimuro M (1994) Chlorophyll forms and excitation energy transfer pathways in light-harvesting chlorophyll *a*/*b*-protein complexes isolated from the siphonous green alga, *Bryopsis maxima*. Biochim. Biophys. Acta **1184:** 103–110

Nakayama K, Okada M (1990) Purification and characterization of light-harvesting chlorophyll *a*/*b*-protein complexes of photosystem II from the green alga, *Bryopsis maxima*. Plant Cell Physiol. **31:** 253–260

Natali A, Gruber JM, Dietzel L, Stuart MC, van Grondelle R, Croce R (2016) Light-harvesting complexes (LHCs) cluster spontaneously in membrane environment leading to shortening of their excited state lifetimes. J. Biol. Chem. **291:** 16730–16739

Nelson N (2011) Photosystems and global effects of oxygenic photosynthesis. Biochim. Biophys. Acta **1807:** 856–863

Nelson N, Ben-Shem A (2004) The complex architecture of oxygenic photosynthesis. Nature Reviews Molecular Cell Biology **5:** 971–982

Nelson N, Junge W (2015) Structure and energy transfer in photosystems of oxygenic photosynthesis. Annu. Rev. Biochem. **84:** 659–683

Nevo R, Charuvi D, Tsabari O, Reich Z (2012) Composition, architecture and dynamics of the photosynthetic apparatus in higher plants. Plant J. **70:** 157–176

Nield J, Barber J (2006) Refinement of the structural model for the photosystem II supercomplex of higher plants. Biochim. Biophys. Acta **1757:** 353–361

Nielsen JT, Kulminskaya NV, Bjerring M, Linnanto JM, Ratsep M, Pedersen MO, Lambrev PH, Dorogi M, Garab G, Thomsen K, Jegerschold C, Frigaard NU, Lindahl M, Nielsen NC (2016) *In situ* high-resolution structure of the baseplate antenna complex in *Chlorobaculum tepidum*. Nat. Commun. **7:** 12454

Nilkens M, Kress E, Lambrev P, Miloslavina Y, Müller M, Holzwarth AR, Jahns P (2010) Identification of a slowly inducible zeaxanthin-dependent component of non-photochemical quenching of chlorophyll fluorescence generated under steady-state conditions in *Arabidopsis*. Biochim. Biophys. Acta. **1797:** 466–475

Niyogi KK (1999) Photoprotection revisited: Genetic and molecular approaches. Annu. Rev. Plant Physiol. Plant Mol. Biol. **50:** 333–359

Niyogi KK, Grossman AR, Björkman O (1998) Arabidopsis mutants define a central role for the xanthophyll cycle in the regulation of photosynthetic energy conversion. Plant Cell **10:** 1121–1134

Novoderezhkin V, Marin A, van Grondelle R (2011) Intra- and inter-monomeric transfers in the light harvesting LHCII complex: the Redfield–Förster picture. Phys. Chem. Chem. Phys. **13:** 17093–17103

Novoderezhkin VI, Croce R, Wahadoszamen M, Polukhina I, Romero E, van Grondelle R (2016) Mixing of exciton and charge-transfer states in light-harvesting complex Lhca4. Phys. Chem. Chem. Phys. **18:** 19368–19377

Novoderezhkin VI, Palacios MA, van Amerongen H, van Grondelle R (2004) Energy-transfer dynamics in the LHCII complex of higher plants: Modified Redfield approach. J. Phys. Chem. B **108:** 10363–10375

Novoderezhkin VI, Palacios MA, van Amerongen H, van Grondelle R (2005) Excitation dynamics in the LHCII complex of higher plants: Modeling based on the 2.72 Å crystal structure. J. Phys. Chem. B **109:** 10493–10504

Novoderezhkin VI, Rutkauskas D, van Grondelle R (2006) Dynamics of the emission spectrum of a single LH2 complex: interplay of slow and fast nuclear motions. Biophys. J. **90:** 2890–2902

Novoderezhkin VI, van Grondelle R (2010) Physical origins and models of energy transfer in photosynthetic light-harvesting. Phys. Chem. Chem. Phys. **12:** 7352–7365

Nussberger S, Dekker JP, Kuhlbrandt W, van Bolhuis BM, van Grondelle R, van Amerongen H (1994) Spectroscopic characterization of three different monomeric forms of the main chlorophyll *a*/*b* binding protein from chloroplast membranes. Biochemistry **33:** 14775–14783

Oliver TA (2018) Recent advances in multidimensional ultrafast spectroscopy. Royal Soc. Open Sci. **5:** 171425

Ostroumov EE, Götze JP, Reus M, Lambrev PH, Holzwarth AR (2020) Characterization of fluorescent chlorophyll charge-transfer states as intermediates in the excited state quenching of light-harvesting complex II. Photosynth. Res. **144:** 171–193

Paillotin G, Swenberg CE, Breton J, Geacintov NE (1979) Analysis of picosecond laserinduced fluorescence phenomena in photosynthetic membranes utilizing a master equation approach. Biophysics Journal **25:** 513–534

Palacios MA, Standfuss J, Vengris M, van Oort BF, van Stokkum IHM, Kuhlbrandt W, van Amerongen H, van Grondelle R (2006) A comparison of the three isoforms of the light-harvesting complex II using transient absorption and time-resolved fluorescence measurements. Photosynth. Res. **88:** 269–285

Páli T, Garab G, Horváth LI, Kóta Z (2003) Functional significance of the lipid-protein interface in photosynthetic membranes. Cell. Mol. Life Sci. **60:** 1591–1606

Pålsson LO, Spangfort MD, Gulbinas V, Gillbro T (1994) Ultrafast chlorophyll *b*–chlorophyll *a* excitation energy transfer in the isolated light harvesting complex, LHC II, of green plants. Implications for the organisation of chlorophylls. FEBS Lett. **339:** 134–138

Pan X, Li M, Wan T, Wang L, Jia C, Hou Z, Zhao X, Zhang J, Chang W (2011) Structural insights into energy regulation of light-harvesting complex CP29 from spinach. Nat. Struct. Mol. Biol. **18:** 309–315

Pan X, Ma J, Su X, Cao P, Chang W, Liu Z, Zhang X, Li M (2018) Structure of the maize photosystem I supercomplex with light-harvesting complexes I and II. Science **360:** 1109–1113

Paolillo D (1970) The three-dimensional arrangement of intergranal lamellae in chloroplasts. J. Cell Sci. **6:** 243–253

Pascal AA, Liu ZF, Broess K, van Oort B, van Amerongen H, Wang C, Horton P, Robert B, Chang WR, Ruban A (2005) Molecular basis of photoprotection and control of photosynthetic light-harvesting. Nature **436:** 134–137

Paschenko V, Protasov S, Rubin A, Timofeev K, Zamazova L, Rubin L (1975) Probing the kinetics of photosystem I and photosystem II fluorescence in pea chloroplasts on a picosecond pulse fluorometer. Biochim. Biophys. Acta **408:** 143–153

Peterman EJG, Monshouwer R, van Stokkum IHM, van Grondelle R, van Amerongen H (1997) Ultrafast singlet excitation transfer from carotenoids to chlorophylls via different pathways in light-harvesting complex II of higher plants. Chem. Phys. Lett. **264:** 279–284

Peters FALJ, van Wielink JE, Wong Fong Sang HW, De Vries S, Kraayenhof R (1983) Studies on well coupled photosystem I-enriched subchloroplast vesicles. Content and redox properties of electron-transfer components. Biochim. Biophys. Acta **722:** 460–470

Petti MK, Lomont JP, Maj M, Zanni MT (2018) Two-Dimensional Spectroscopy Is Being Used to Address Core Scientific Questions in Biology and Materials Science. J. Phys. Chem. B **122:** 1771–1780

Pieper J, Rätsep M, Irrgang K-D, Freiberg A (2009) Chromophore– Chromophore and Chromophore–Protein Interactions in Monomeric Light-Harvesting Complex II of Green Plants Studied by Spectral Hole Burning and Fluorescence Line Narrowing. J. Phys. Chem. B **113:** 10870–10880

Pieper J, Schödel R, Irrgang K-D, Voigt J, Renger G (2001) Electron– Phonon Coupling in Solubilized LHC II Complexes of Green Plants Investigated by Line-Narrowing and Temperature-Dependent Fluorescence Spectroscopy. J. Phys. Chem. B **105:** 7115–7124

Pollard WT, Friesner RA (1994) Solution of the Redfield equation for the dissipative quantum dynamics of multilevel systems. J. Chem. Phys. **100:** 5054–5065

Pospíšil P (2012) Molecular mechanisms of production and scavenging of reactive oxygen species by photosystem II. Biochim. Biophys. Acta **1817:** 218–231

Pribil M, Labs M, Leister D (2014) Structure and dynamics of thylakoids in land plants. J. Exp. Bot. **65:** 1955–1972

Qin XC, Suga M, Kuang TY, Shen JR (2015) Structural basis for energy transfer pathways in the plant PSI–LHCI supercomplex. Science **348:** 989–995

Quaranta M, Borisov SM, Klimant I (2012) Indicators for optical oxygen sensors. Bioanalytical Reviews **4:** 115–157

Redfield AG (1957) On the theory of relaxation processes. IBM J. Res. Dev. **1:** 19–31

Remelli R, Varotto C, Sandona D, Croce R, Bassi R (1999) Chlorophyll binding to monomeric Light-harvesting complex - A mutation analysis of chromophore-binding residues. J. Biol. Chem. **274:** 33510–33521

Renger G, Renger T (2008) Photosystem II: the machinery of photosynthetic water splitting. Photosynth. Res. **98:** 53–80

Renger T, Madjet ME-A, Knorr A, Müh F (2011) How the molecular structure determines the flow of excitation energy in plant light-harvesting complex II. J. Plant Physiol. **168:** 1497–1509

Renger T, Marcus R (2002) On the relation of protein dynamics and exciton relaxation in pigment–protein complexes: an estimation of the spectral density and a theory for the calculation of optical spectra. J. Chem. Phys. **116:** 9997–10019

Renger T, Marcus R (2003) Variable-range hopping electron transfer through disordered bridge states: Application to DNA. J. Phys. Chem. A **107:** 8404–8419

Renger T, Trostmann I, Theiss C, Madjet ME, Richter M, Paulsen H, Eichler H, Knorr A, Renger G (2007) Refinement of a structural model of a pigment–protein complex by accurate optical line shape theory and experiments. J. Phys. Chem. B **111:** 10487–10501

Richter M, Renger T, Renger G, Knorr A (2007) Non-perturbative theory for the optical response to strong light of the light harvesting complex LHC II of plants: saturation of the fluorescence quantum yield. J. Chem. Phys. **127:** 075105

Rochaix J-D (2011) Reprint of: Regulation of photosynthetic electron transport. Biochim. Biophys. Acta **1807:** 878–886

Rochaix J-D (2014) Regulation and Dynamics of the Light-Harvesting System. Annu. Rev. Plant Biol. **65:** 287–309

Rogl H, Schodel R, Lokstein H, Kuhlbrandt W, Schubert A (2002) Assignment of spectral substructures to pigment-binding sites in higher plant light-harvesting complex LHC-II. Biochemistry **41:** 2281–2287

Romero E, Augulis R, Novoderezhkin VI, Ferretti M, Thieme J, Zigmantas D, Van Grondelle R (2014) Quantum coherence in photosynthesis for efficient solar-energy conversion. Nature Physics **10:** 676–682

Romero E, Mozzo M, Van Stokkum IH, Dekker JP, Van Grondelle R, Croce R (2009) The origin of the low-energy form of photosystem I light-harvesting complex Lhca4: mixing of the lowest exciton with a charge-transfer state. Biophys. J. **96:** L35–L37

Romero E, Novoderezhkin VI, van Grondelle R (2017) Quantum design of photosynthesis for bio-inspired solar-energy conversion. Nature **543:** 355–365

Ruban AV (2015) Evolution under the sun: optimizing light harvesting in photosynthesis. Journal of Experimental Botany **66:** 7–23

Ruban AV (2016) Nonphotochemical chlorophyll fluorescence quenching: mechanism and effectiveness in protecting plants from photodamage. Plant Physiol. **170:** 1903–1916

Ruban AV, Berera R, Ilioaia C, van Stokkum IHM, Kennis JTM, Pascal AA, van Amerongen H, Robert B, Horton P, van Grondelle R (2007) Identification of a mechanism of photoprotective energy dissipation in higher plants. Nature **450:** 575–578

Ruban AV, Calkoen F, Kwa SLS, van Grondelle R, Horton P, Dekker JP (1997) Characterisation of LHC II in the aggregated state by linear and circular dichroism spectroscopy. Biochim. Biophys. Acta **1321:** 61–70

Ruban AV, Horton P (1992) Mechanism of ΔpH-dependent dissipation of absorbed excitation-energy by photosynthetic membranes. 1. Spectroscopic analysis of isolated light-harvesting complexes. Biochim. Biophys. Acta **1102:** 30–38

Ruban AV, Horton P (1994) Spectroscopy of non-photochemical and photochemical quenching of chlorophyll fluorescence in leaves; evidence for a role of the light harvesting complex of photosystem II in the regulation of energy dissipation. Photosynth. Res. **40:** 181–190

Ruban AV, Horton P (1995) Regulation of nonphotochemical quenching of chlorophyll fluorescence in plants. Aust. J. Plant Physiol. **22:** 221–230

Ruban AV, Horton P, Robert B (1995) Resonance Raman spectroscopy of the photosystem II light-harvesting complex of green plants: A comparison of trimeric and aggregated states. Biochemistry **34:** 2333–2337

Ruban AV, Johnson MP, Duffy CD (2012) The photoprotective molecular switch in the photosystem II antenna. Biochim. Biophys. Acta **1817:** 167–181

Russo M, Petropoulos V, Molotokaite E, Cerullo G, Casazza AP, Maiuri M, Santabarbara S (2020) Ultrafast excited-state dynamics in land plants Photosystem I core and whole supercomplex under oxidised electron donor conditions. Photosynth. Res. **144:** 221–233

Rutkauskas D, Chmeliov J, Johnson M, Ruban A, Valkunas L (2012) Exciton annihilation as a probe of the light-harvesting antenna transition into the photoprotective mode. Chem. Phys. **404:** 123–128

Salverda JM, Vengris M, Krueger BP, Scholes GD, Czamoleski AR, Novoderezhkin V, van Amerongen H, van Grondelle R (2003) Energy transfer in light-harvesting complexes LHCII and CP29 of spinach studied with three pulse echo peak shift and transient grating. Biophys. J. **84:** 450–465

Savikhin S, Xu W, Chitnis PR, Struve WS (2000) Ultrafast primary processes in PS I from *Synechocystis sp.* PCC 6803: roles of P_{700} and A_0. Biophys. J. **79:** 1573–1586

Savikhin S, Xu W, Martinsson P, Chitnis PR, Struve WS (2001) Kinetics of charge separation and $A_0^- \rightarrow A_1$ electron transfer in photosystem I reaction centers. Biochemistry **40:** 9282–9290

Savikhin S, Xu W, Soukoulis V, Chitnis PR, Struve WS (1999) Ultrafast primary processes in photosystem I of the cyanobacterium *Synechocystis sp.* PCC 6803. Biophys. J. **76:** 3278–3288

Schaller S, Latowski D, Jemiola-Rzeminska M, Dawood A, Wilhelm C, Strzalka K, Goss R (2011) Regulation of LHCII aggregation by different thylakoid membrane lipids. Biochim. Biophys. Acta. **1807:** 326–335

Schatz GH, Brock H, Holzwarth AR (1988) Kinetic and energetic model for the primary processes in photosystem II. Biophys. J. **54:** 397–405

Schlau-Cohen GS, Calhoun TR, Ginsberg NS, Ballottari M, Bassi R, Fleming GR (2010) Spectroscopic elucidation of uncoupled transition energies in the major photosynthetic light-harvesting complex, LHCII. Proc. Natl. Acad. Sci. U.S.A. **107:** 13276–13281

Schlau-Cohen GS, Calhoun TR, Ginsberg NS, Read EL, Ballottari M, Bassi R, van Grondelle R, Fleming GR (2009) Pathways of energy flow in LHCII from two-dimensional electronic spectroscopy. J. Phys. Chem. B **113:** 15352–15363

Schmid VH, Cammarata KV, Bruns BU, Schmidt GW (1997) *In vitro* reconstitution of the photosystem I light-harvesting complex LHCI-730: heterodimerization is required for antenna pigment organization. Proc. Natl. Acad. Sci. U.S.A. **94:** 7667–7672

Scholes GD, Fleming GR (2000) On the mechanism of light harvesting in photosynthetic purple bacteria: B800 to B850 energy transfer. J. Phys. Chem. B **104:** 1854–1868

Schödel R, Hillmann F, Schrötter T, Voigt J, Irrgang K-D, Renger G (1996) Kinetics of excited states of pigment clusters in solubilized light- harvesting complex II: Photon density-dependent fluorescence yield and transmittance. Biophys. J. **71:** 3370–3380

Searle G, Barber J, Harris L, Porter G, Tredwell C (1977) Picosecond laser study of fluorescence lifetimes in spinach chloroplast photosystem I and photosystem II preparations. Biochim. Biophys. Acta **459:** 390–401

Shen L, Huang Z, Chang S, Wang W, Wang J, Kuang T, Han G, Shen J-R, Zhang X (2019) Structure of a C2S2M2N2-type PSII–LHCII supercomplex from the green alga Chlamydomonas reinhardtii. Proc. Natl. Acad. Sci. U.S.A. **116:** 21246–21255

Siligardi G, Hussain R (2015) CD spectroscopy: an essential tool for quality control of protein folding. *In* Structural Proteomics. Springer, pp 255–276

Simidjiev I, Barzda V, Mustárdy L, Garab G (1997) Isolation of lamellar aggregates of the light-harvesting chlorophyll a/b protein complex of photosystem II with long-range chiral order and structural flexibility. Anal. Biochem. **250:** 169–175

Simidjiev I, Barzda V, Mustárdy L, Garab G (1998) Role of thylakoid lipids in the structural flexibility of lamellar aggregates of the isolated light-harvesting chlorophyll *a/b* complex of photosystem II. Biochemistry **37:** 4169–4173

Simidjiev I, Várkonyi Z, Lambrev PH, Garab G (2011) Isolation and characterization of lamellar aggregates of LHCII and LHCII-lipid macro-assemblies with light-inducible structural transitions. *In* R Carpentier, ed, Photosynthesis Research Protocols. Humana Press, Totowa, NJ, pp 127–138

Slavov C, Ballottari M, Morosinotto T, Bassi R, Holzwarth AR (2008) Trap-limited charge separation kinetics in higher plant photosystem I complexes. Biophys. J. **94:** 3601–3612

Standfuss J, van Scheltinga ACT, Lamborghini M, Kühlbrandt W (2005) Mechanisms of photoprotection and nonphotochemical quenching in pea light-harvesting complex at 2.5 Å resolution. EMBO J. **24:** 919–928

Stingaciu L-R, O'Neill H, Liberton M, Urban VS, Pakrasi HB, Ohl M (2016) Revealing the Dynamics of Thylakoid Membranes in Living Cyanobacterial Cells. Sci. Rep. **6:** 19627

Su X, Ma J, Wei X, Cao P, Zhu D, Chang W, Liu Z, Zhang X, Li M (2017) Structure and assembly mechanism of plant C2S2M2-type PSII-LHCII supercomplex. Science **357:** 815–820

Suga M, Akita F, Hirata K, Ueno G, Murakami H, Nakajima Y, Shimizu T, Yamashita K, Yamamoto M, Ago H, Shen J-R (2015) Native structure of photosystem II at 1.95 Å resolution viewed by femtosecond X-ray pulses. Nature **517:** 99–103

Sumi H (1999) Theory on rates of excitation-energy transfer between molecular aggregates through distributed transition dipoles with application to the antenna system in bacterial photosynthesis. J. Phys. Chem. B **103:** 252–260

Tachibana Y, Vayssieres L, Durrant JR (2012) Artificial photosynthesis for solar water-splitting. Nature Photonics **6:** 511–518

Tan HS (2008) Theory and phase-cycling scheme selection principles of collinear phase coherent multi-dimensional optical spectroscopy. J. Chem. Phys. **129:** 124501

Telfer A (2005) Too much light? How beta-carotene protects the photosystem II reaction centre. Photochem. Photobiol. Sci. **4:** 950–956

Thyrhaug E, Tempelaar R, Alcocer MJP, Žídek K, Bína D, Knoester J, Jansen TLC, Zigmantas D (2018) Identification and characterization of diverse coherences in the Fenna-Matthews-Olson complex. Nature chemistry **10:** 780–786

Tikkanen M, Aro E-M (2012) Thylakoid protein phosphorylation in dynamic regulation of photosystem II in higher plants. Biochim. Biophys. Acta **1817:** 232–238

Tikkanen M, Grieco M, Aro EM (2011) Novel insights into plant light-harvesting complex II phosphorylation and 'state transitions'. Trends in Plant Sciences **16:** 126–131

Tinoco Jr I (1963) The exciton contribution to the optical rotation of polymers. Radiat. Res. **20:** 133–139

Tóth TN, Rai N, Solymosi K, Zsiros O, Schröder WP, Garab G, van Amerongen H, Horton P, Kovács L (2016) Fingerprinting the macro-organisation of pigment-protein complexes in plant thylakoid membranes in vivo by circular-dichroism spectroscopy. Biochimica et Biophysica Acta-Bioenergetics **1857:** 1479–1489

Towell JF, Manning MC (1994) Analysis of protein structure by circular dichroism spectroscopy. *In* N Purdie, HG Brittain, eds, Analytical Applications of Circular Dichroism. Elsevier Science B.V., pp 175–205

Triantaphylides C, Havaux M (2009) Singlet oxygen in plants: production, detoxification and signaling. Trends Plant Sci. **14:** 219–228

Triantaphylides C, Krischke M, Hoeberichts FA, Ksas B, Gresser G, Havaux M, Van Breusegem F, Mueller MJ (2008) Singlet oxygen is the major reactive oxygen species involved in photooxidative damage to plants. Plant Physiol. **148:** 960–968

Trissl H, Lavergne J (1995) Fluorescence induction from photosystem II: analytical equations for the yields of photochemistry and fluorescence derived from analysis of a model including exciton-radical pair equilibrium and restricted energy transfer between photosynthetic units. Funct. Plant Biol. **22:** 183–193

Tutkus M, Akhtar P, Chmeliov J, Görföl F, Trinkunas G, Lambrev PH, Valkunas L (2018) Fluorescence microscopy of single liposomes with incorporated pigment–proteins. Langmuir **34:** 14410–14418

Umena Y, Kawakami K, Shen JR, Kamiya N (2011) Crystal structure of oxygen-evolving photosystem II at a resolution of 1.9 Å. Nature **473:** 55–60

Ünnep R, Nagy G, Markó M, Garab G (2014) Monitoring thylakoid ultrastructural changes in vivo using small-angle neutron scattering. Plant Physiol. Biochem. **81:** 197–207

Ünnep R, Zsiros O, Solymosi K, Kovács L, Lambrev PH, Tóth T, Schweins R, Posselt D, Székely N, Rosta L, Nagy G, Garab G (2014) The ultrastructure and flexibility of thylakoid membranes in leaves and isolated chloroplasts as revealed by small-angle neutron scattering. Biochim. Biophys. Acta. **1837:** 1572–1580

Vaitekonis S, Trinkunas G, Valkunas L (2005) Red chlorophylls in the exciton model of photosystem I. Photosynth. Res. **86:** 185–201

Valkunas L, Liuolia V, Dekker JP, Grondelle R (1995) Description of energy migration and trapping in photosystem I by a model with two distance scaling parameters. Photosynth. Res. **43:** 149–154

van Amerongen H, Croce R (2007) Structure and function of photosystem II light-harvesting proteins (Lhcb) of higher plants. *In* G Renger, ed, Primary Processes of Photosynthesis, Part 1: Principles and Apparatus. The Royal Society of Chemistry, Cambridge, UK, pp 329–367

van Amerongen H, Croce R (2013) Light harvesting in photosystem II. Photosynth. Res. **116:** 251–263

van Amerongen H, Valkunas L, van Grondelle R (2000) Photosynthetic Excitons. World Scientific, Singapore

van Amerongen H, van Grondelle R (2001) Understanding the energy transfer function of LHCII, the major light-harvesting complex of green plants. J. Phys. Chem. B **105:** 604–617

van Bezouwen LS, Caffarri S, Kale RS, Kouřil R, Thunnissen A, Oostergetel GT, Boekema EJ (2017) Subunit and chlorophyll organization of the plant photosystem II supercomplex. Nat. Plants **3:** 17080

van Oort B, Roy LM, Xu P, Lu Y, Karcher D, Bock R, Croce R (2018) Revisiting the Role of Xanthophylls in Nonphotochemical Quenching. J. Phys. Chem. Lett. **9:** 346–352

van Stokkum IHM, Larsen DS, van Grondelle R (2004) Global and target analysis of time-resolved spectra. Biochim. Biophys. Acta **1657:** 82–104

Vass I (2011) Role of charge recombination processes in photodamage and photoprotection of the photosystem II complex. Physiol. Plant. **142:** 6–16

Vass I (2012) Molecular mechanisms of photodamage in the Photosystem II complex. Biochim. Biophys. Acta. **1817:** 209–217

Vinyard DJ, Ananyev GM, Dismukes GC (2013) Photosystem II: The reaction center of oxygenic photosynthesis. Annu. Rev. Biochem. **82:** 577–606

Visser HM, Kleima FJ, van Stokkum IHM, van Grondelle R, van Amerongen H (1996) Probing the many energy-transfer processes in the photosynthetic light-harvesting complex II at 77 K using energy-selective sub-picosecond transient absorption spectroscopy. Chem. Phys. **210:** 297–312

Vrandecic K, Rätsep M, Wilk L, Rusevich L, Golub M, Reppert M, Irrgang K-D, Kühlbrandt W, Pieper Jr (2015) Protein dynamics tunes excited state positions in light-harvesting complex II. J. Phys. Chem. B **119:** 3920–3930

Wahadoszamen M, Margalit I, Ara AM, van Grondelle R, Noy D (2014) The role of charge-transfer states in energy transfer and dissipation within natural and artificial bacteriochlorophyll proteins. Nat. Commun. **5:** 5287

Wang W, Qin X, Sang M, Chen D, Wang K, Lin R, Lu C, Shen J-R, Kuang T (2013) Spectral and functional studies on siphonaxanthin-type light-harvesting complex of photosystem II from *Bryopsis corticulans*. Photosynth. Res. **117:** 267–279

Wei X, Su X, Cao P, Liu X, Chang W, Li M, Zhang X, Liu Z (2016) Structure of spinach photosystem II–LHCII supercomplex at 3.2 Å resolution. Nature **534:** 69–74

Weier TE, Stocking CR, Thomson WW, Drever H (1963) The grana as structural units of chloroplasts of mesophyll of Nicotiana rustica and Phaseolus vulgaris. J. Ultrastruct. Res. **8:** 122–143

Wells KL, Lambrev PH, Zhang ZY, Garab G, Tan HS (2014) Pathways of energy transfer in LHCII revealed by room-temperature 2D electronic spectroscopy. Phys. Chem. Chem. Phys. **16:** 11640–11646

Wientjes E, Drop B, Kouřil R, Boekema EJ, Croce R (2013) During State 1 to State 2 Transition in *Arabidopsis thaliana*, the photosystem II Supercomplex Gets Phosphorylated but Does Not Disassemble. J. Biol. Chem. **288:** 32821–32826

Wientjes E, van Amerongen H, Croce R (2013) LHCII is an antenna of both photosystems after long-term acclimation. Biochim. Biophys. Acta **1827:** 420–426

Wientjes E, Van Stokkum IH, Van Amerongen H, Croce R (2011) Excitation-energy transfer dynamics of higher plant photosystem I light-harvesting complexes. Biophys. J. **100:** 1372–1380

Wientjes E, van Stokkum IH, van Amerongen H, Croce R (2011) The role of the individual Lhcas in photosystem I excitation energy trapping. Biochem. J. **101:** 745–754

Wilk L, Grunwald M, Liao PN, Walla PJ, Kühlbrandt W (2013) Direct interaction of the major light-harvesting complex II and PsbS in nonphotochemical quenching. Proc. Natl. Acad. Sci. U.S.A. **110:** 5452–5456

Williams WP (1998) The physical properties of thylakoid membrane lipids and their relation to photosynthesis. *In* P-A Siegenthaler, N Murata, eds, Lipids in Photosynthesis: Structure, Function and Genetics, Vol 6. Springer, Dordrecht, pp 103–118

Wollman F-A (2001) State transitions reveal the dynamics and flexibility of the photosynthetic apparatus. EMBO J. **20:** 3623–3630

Woody RW (1968) Improved calculation of the $n\pi^*$ rotational strength in polypeptides. J. Chem. Phys. **49:** 4797–4806

Woody RW (2005) The exciton model and the circular dichroism of polypeptides. Monatsh. Chem./Chem. Mon. **136:** 347–366

Woody RW, Tinoco Jr. I (1967) Optical rotation of oriented helices. III. Calculation of the rotatory dispersion and circular dichroism of the alpha - and 3_{10} - helix. J. Chem. Phys. **46:** 4927-4945

Wu Y, Huang HW, Olah GA (1990) Method of oriented circular dichroism. Biophys. J. **57:** 797–806

Yang C, Boggasch S, Haase W, Paulsen H (2006) Thermal stability of trimeric light-harvesting chlorophyll *a*/*b* complex (LHCIIb) in liposomes of thylakoid lipids. Biochim. Biophys. Acta **1757:** 1642–1648

Yang M, Fleming GR (2002) Influence of phonons on exciton transfer dynamics: comparison of the Redfield, Förster, and modified Redfield equations. Chem. Phys. **282:** 163–180

Zhang S-J, Wang S-C, He J-F, Chen H (2006) Energy transfer among chlorophylls in trimeric light-harvesting complex II of *Bryopsis corticulans.* Acta Biochimica et Biophysica Sinica **38:** 310–317

Zhang S, Scheller HV (2004) Light-harvesting complex II binds to several small subunits of photosystem I. J. Biol. Chem. **279:** 3180–3187

Zhang WM, Meier T, Chernyak V, Mukamel S (1998) Exciton-migration and three-pulse femtosecond optical spectroscopies of photosynthetic antenna complexes. J. Chem. Phys. **108:** 7763–7774

Zhang Z, Wells KL, Hyland EWJ, Tan H-S (2012) Phase-cycling schemes for pump–probe beam geometry two-dimensional electronic spectroscopy. Chem. Phys. Lett. **550:** 156–161

Zhou F, Liu S, Hu ZH, Kuang TY, Paulsen H, Yang CH (2009) Effect of monogalactosyldiacylglycerol on the interaction between photosystem II core complex and its antenna complexes in liposomes of thylakoid lipids. Photosynth. Res. **99:** 185–193

Zucchelli G, Santabarbara S, Jennings RC (2012) The Q_y absorption spectrum of the light-harvesting complex II as determined by structure-based analysis of chlorophyll macrocycle deformations. Biochemistry **51:** 2717–2736